HTS high current cable for fusion application
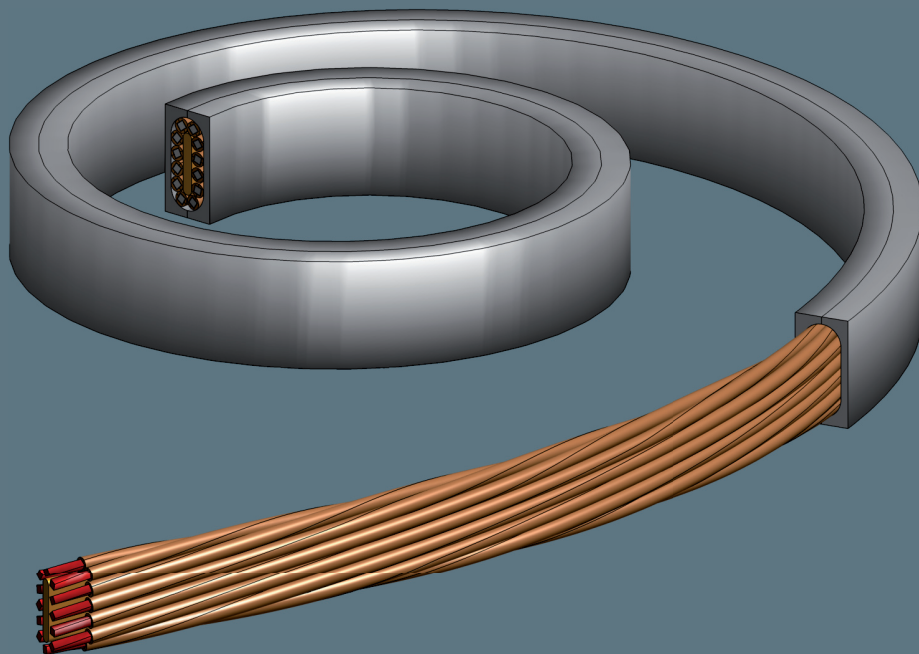
PAR

Nikolay BYKOVSKIY

EPFL

ÉCOLE POLYTECHNIQUE
FÉDÉRALE DE LAUSANNE

Suisse
2017

Nikolay Bykovsky

HTS high current cable for fusion application

2017

Abstract

State-of-the-art magnets of fusion devices, which are based on low temperature super-conductors (LTS), have almost reached their technological limits in terms of generated magnetic fields. Further progress can be made using novel high temperature super-conductors (HTS). Although HTS have been discovered several decades ago and in present time are ready for the long-length production, the feasibility of HTS cables for fusion magnets is not yet demonstrated. The main challenge toward HTS fusion cables is posed by essentially different geometry of conductors. While LTS conductors can be manufactured in a favorable geometry of round wires, the most promising HTS materials are only available as thin tapes. Thus, new cabling concepts suitable to arrange hundreds of thin tapes should be identified and developed.

In this research we aim at demonstrating experimentally the applicability of HTS materials for fusion magnets. This task starts from the development of an intermediate cabling 'solution' – the strand – where a stack of ten to forty tapes is encased between two semicircular copper profiles. Then, the components are twisted and soldered together. Investigations of the strand electrical and electromechanical properties are of key importance to assess the potential application to fusion magnets.

Thanks to its round geometry, the HTS strand can be used in conventional cabling methods. The Rutherford-like cable design, with the inclusion of central copper core, is investigated for use with the round strands. As a result of full-scale R&D activity at the Swiss Plasma Center, 60 kA-class HTS cable prototypes have been manufactured and successfully tested at low temperatures, from 5 K to 40 K, and high background magnetic fields, up to 12 T. Results and implications of these measurements constitute the backbone of this thesis.

The AC loss and quench properties of the proposed cable design are also studied. Experimental data for the AC loss have separately been acquired on the tape, strand and cable stages at operating conditions relevant for fusion magnets. This allowed us to validate the numerical tools developed to assess the hysteresis loss in stacks and coupling current losses in the strand and cable. The quench studies – mostly the protection issues – are addressed in this thesis via numerical modeling.

Application of the HTS cables to fusion magnets leads to various improvements in the magnet system such as an access to magnetic fields above 15 T limit and increased temperature margins at the cable operation. When applied to the central solenoid, the

use of the HTS cables may either reduce its dimensions at a given generated magnetic flux, or increase the flux when the dimensions are kept fixed.

Although presently the price of HTS materials is still at least 5 to 10 times higher than of 'classic' LTS materials, use of HTS at high fields is fully justified being the only available option for such application. Manufacturers of the HTS materials keep improving the price to performance ratio of their product, which also increases the chance that the HTS conductor technology can soon be used for fusion magnets.

Key words: Fusion magnets, Forced flow superconducting cables, High temperature superconductors.

Zusammenfassung

Hochmoderne Magnete von Fusionsanlagen, die Tieftemperatursupraleiter (LTS) benutzen, haben ihre technologischen Grenzen in Bezug auf die erzeugten Magnetfelder nahezu erreicht. Weitere Fortschritte können mit den neuartigen Hochtemperatursupraleitern (HTS) erzielt werden. Obwohl HTS, die vor einigen Jahrzehnten entdeckt wurden, in der heutigen Zeit in grossen Längen hergestellt werden können, ist die Machbarkeit von HTS Kabeln für Fusionsmagnete noch nicht demonstriert worden. Die größte Herausforderung für HTS Fusionskabel ist die sehr unterschiedliche Geometrie der Leiter. Während LTS Leitern in einer günstigen Geometrie von Runddrähten hergestellt werden können, sind die vielversprechendsten HTS Materialien nur als dünne Bänder erhältlich. So sollten neue Verkabelungskonzepte, die geeignet sind, Hunderte von dünnen Bändern anzuordnen, identifiziert und entwickelt werden.

In dieser Forschung streben wir an, die Anwendbarkeit von HTS Materialien für Fusionsmagnete zu demonstrieren. Diese Aufgabe beginnt mit der Entwicklung einer Zwischenverkabelungslösung – der Superdraht – wo ein Stapel von zehn bis vierzig Bändern von zwei halbkreisförmigen Kupferprofilen umhüllt ist. Dann werden die Komponenten verdrillt und miteinander verlötet. Untersuchungen der elektrischen und elektromechanischen Eigenschaften diese Superdraht sind von zentraler Bedeutung, um die mögliche Anwendung auf Fusionsmagnete zu beurteilen.

Dank seiner runden Geometrie kann der HTS Superdraht bei konventionellen Verkabelungsverfahren eingesetzt werden. Die zu einem Rutherford analoge eine Kabelkonstruktion mit der Aufnahme des zentralen Kupferkerns wird für den Einsatz mit den Rundsträngen untersucht. Durch die umfangreichen F&E Aktivitäten am Swiss Plasma Center wurden 60 kA HTS Kabelprototypen hergestellt und erfolgreich bei niedrigen Temperaturen von 5 K bis 40 K und hohen Hintergrundmagnetfeldern bis zu 12 T getestet. Ergebnisse und Implikationen dieser Messungen bilden das Rückgrat dieser Arbeit.

Die Wechselstromverluste und die Quench-Eigenschaften des vorgeschlagenen Kabeldesigns werden ebenfalls untersucht. Die experimentellen Daten für den Wechselstromverlust wurden separat auf den Band-, Superdraht- und Kabelstufen bei Betriebsbedingungen für Fusionsmagnete erfasst. Damit konnten wir die numerischen Werkzeuge validieren, die entwickelt wurden, um den Hystereseverlust in den Stapeln zu beurteilen und Stromverluste im Superdraht und Kabel zu koppeln. Die Quench-Studien – besonders die Schutzprobleme – werden in dieser Arbeit durch

numerische Modellierung angesprochen.

Die Anwendung der HTS Kabel für Fusionsmagnete führt zu verschiedenen Verbesserungen des Magnetsystems, wie zum Beispiel ein Zugang zu Magnetfeldern über 15 T und erhöhte Temperaturmargen im Kabelbetrieb. Bei Anwendung auf das zentrale Solenoid kann die Verwendung der HTS Kabel entweder die Abmessungen bei einem gegebenen erzeugten magnetischen Fluss verringern oder den Fluss erhöhen, wenn die Abmessungen fixiert sind.

Obwohl derzeit der Preis von HTS Materialien immer noch mindestens 5 bis 10 mal höher ist als bei 'klassischen' LTS Materialien, ist die Verwendung von HTS bei hohen Feldern die einzige verfügbare Option für diese Anwendung. Die Hersteller der HTS Werkstoffe verbessern das Preis-Leistungs-Verhältnis ihres Produktes, was auch die Chance erhöht, dass die HTS Leitertechnologie bald für Fusionsmagnete eingesetzt werden kann.

Stichwörter: Fusionsmagnete, Supraleitende Kabel mit Zwangströmungskühlung, Hochtemperatursupraleitern.

Contents

1 Introduction

The development of alternative energy sources based on non-fossil fuels is one of the key global tasks of the present century for several reasons. Fossil fuels (i.e. coal, gas, oil) are a finite resource, they have impact on climate change and they make economy vulnerable for countries that don't have direct access to sources [1]. Given the present trend of energy production, both the global energy demand and the carbon emissions will double by 2050 if new policies won't be adopted [2]. Economic, environmental and social aspects should be considered as highest priorities in order to maintain a sustainable development.

The energy production from fusion nuclear reactions of light elements has unique advantages over wind, solar and other options, including nuclear fission: a high energy density, practically infinite fuel reserves, no seasonal dependence, no military implication and no chain reactions [3]. Unlike nuclear fission, the fusion reaction is intrinsically safe. The required fuel mass is very small and any unforeseen circumstances completely stop the reactions.

These advantages come at the cost of an extreme complexity of fusion technology. As realized in the 1950s, at the dawn of fusion energy research, the criterion to operate a fusion reactor can be formulated in terms of the 'triple product' of the plasma temperature T, density n and confinement time τ, which should be maintained above a certain value (this is known as the Lawson criterion). For instance, the basic deuterium–tritium (D–T) reaction must be heated up to $T = 150$ millions °C, at a density of about $n \sim 10^{20}\,\mathrm{m}^{-3}$ and a macroscopic confinement time, $\tau \sim 1\,\mathrm{s}$. At such high temperatures the elements of the reaction tend to fly apart, thus a strong confinement should also be applied in order to keep the required values for n and τ.

In principle, there are two methods to confine the plasma: the magnetic confinement, based on use of high magnetic fields in a relatively large chamber volume (i.e. low n, high τ), and the inertial confinement, where ultra high compression of a fuel capsule is achieved, directly or indirectly, e.g. by focused laser beams (i.e. high n, low τ). Only the magnetic method will be addressed in the discussion below. The high magnetic fields required by this method can be achieved at low energy consumption using superconducting magnets operating at cryogenic temperatures. As a result, an enormous temperature gradient is inherently present in the system.

The products of the D–T reaction are one alpha particle with 3.5 MeV energy and one

neutron with 14.1 MeV energy. While the positively charged helium nucleus will be trapped by the magnetic field, collide with other particles and heat up the plasma, the neutron will eventually escape the plasma and hit the chamber wall, the 'blanket', where its energy will be absorbed and tritium fuel will be bred using nuclear reactions with lithium. The neutron flux induces radiation damage in the blanket during the plasma burn, which requires a remote handling equipment to inspect, repair and change the plasma-facing components. Detailed discussions of the scientific and technological challenges of the fusion technology can be found in [3, 4].

Fusion devices – machines where a full cycle of the fusion reaction can be performed – are at the cutting edge of the science and technology. Basically, there exist two main concepts of magnetic fusion devices: the Tokamak concept, proposed in the Soviet Union in 1950, and the Stellarator, proposed in the US at about the same time. While both concepts are based on a toroidal geometry of the chamber, the magnetic field is generated in different ways. The plasma in a Tokamak is confined using the field generated by external magnets and by the current induced in plasma. The Stellarator generates the required field only by means of 3D shaped magnets (see details on the magnetic flux configurations in [4]), with no plasma current.

The largest fusion device based on the Tokamak concept, the multi-national ITER project [5], is under construction in Cadarache, France. The main goal of this project is to demonstrate the scientific and technological feasibility of fusion technology. A plasma volume of about $800 \, m^3$ located in $5 \, T$ magnetic field should be confined during $4 \, s$. The expected fusion power in ITER is $\approx 500 \, MW$, corresponding to a power gain $Q \sim 10$. Although ITER is the first project that will demonstrate a significant power gain, the device is still not foreseen to produce electrical power.

Electrical energy can be generated in a fusion power plant from the flux of neutrons. As illustrated in figure 1.1, the heat produced from the collisions of neutrons with the blanket is transferred by a water circuit embedded into the blanket. The energy in the water, typically in a superheated phase, is converted to electrical energy through a steam turbine, which can finally be transmitted to the power grid. The fusion power for a typical reactor is expected to be from $2.5 \, GW$ to $5 \, GW$, corresponding to a net electricity power $\approx 1.5 \, GW$ [6].

Even if the feasibility of the fusion technology will be demonstrated, its competitiveness in terms of the cost of electricity (COE) with other methods of electricity production remains to be proved. High capital cost of fusion power plants would result in a relatively high COE [4]. The main motivations for fusion energy are rather of strategic nature, e.g. sustainability and environmental impact. As a next step beyond ITER, the design studies are already on-going for the DEMO project, which is considered to be a representative fusion power station in terms of predictable power production, fuel cycle self-sufficiency and plant performance.

The magnet system has a key impact on the overall performance of fusion device. It
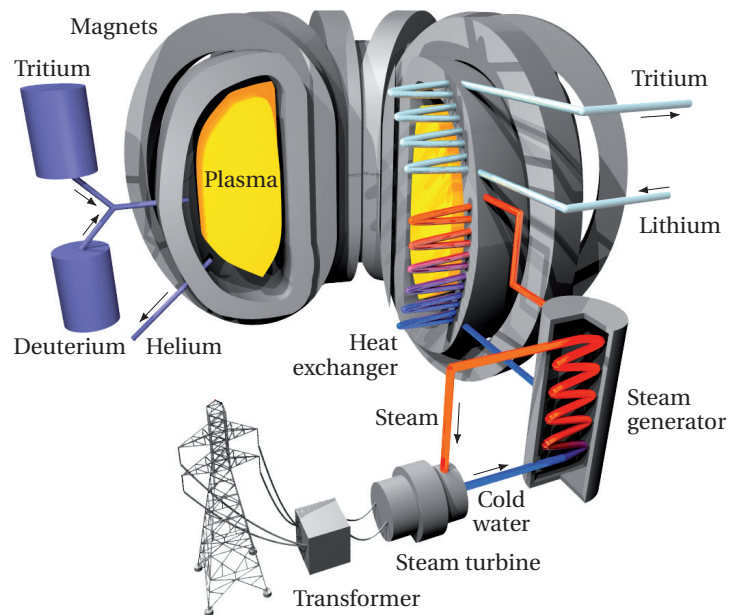
Figure 1.1: Sketch of a fusion power plant based on the Tokamak concept (picture from [7]).

defines the main plasma properties and constitutes a high fraction in the total cost of the device ($\sim 30\,\%$). Taking the ITER magnets as a reference, two main paths can be identified for further advances in fusion magnets: reducing the overall cost and increasing the generated magnetic field. Note that these two paths are not necessarily mutually exclusive, since higher magnetic fields may potentially lead to more compact and cheaper devices. Higher magnetic fields would also enhance plasma confinement and increase the fusion power.

The technology developed so far for fusion magnets is based on low temperature superconductors (LTS) and still has a large margin for economical improvements. However, the LTS fusion magnets are almost at the limit in terms of the maximum generated fields (about $15\,\mathrm{T}$ on coil). Higher fields are not accessible using LTS conductors because the maximum current that they can carry without energy dissipation is too low at such fields. Therefore, the path for higher magnetic fields in fusion is a very challenging task for the science of superconductivity, requiring both fundamental and applied studies.

In this respect, high expectations are raised for novel high temperature superconductors (HTS), which demonstrate superior current capacity at high fields. A long-term effort in the development of the HTS conductor technology has finally led to the possibility of using HTS materials in fusion magnets. Unlike the round LTS wires, the most promising HTS 'candidates' are only available as thin tapes, which makes it difficult to transfer cable technology from LTS to HTS, requiring the development of

new cabling concepts for the flat-tape geometry of the conductor.

The question rises if a breakthrough toward higher magnetic fields in fusion is in fact possible by using HTS. And of which cabling concept is most suitable for HTS in fusion. Would this be economically beneficial or at least acceptable? The motivation of this Thesis is to contribute to answering these questions. Based on the conducted research, answers will be provided as concluding recommendations to this work.

2 Technical background

2.1 Magnet systems of fusion devices

The state-of-the-art magnet system of ITER is presented in figure 2.1. In order to hold the plasma in equilibrium, the magnetic field lines have a toroidal helical shape including a toroidal component generated by the toroidal field (TF) coils and a poloidal component due to a toroidal current in plasma, induced in turn by a central solenoid (CS) and directly produced by poloidal field (PF) coils. The correction coils located outside the vacuum vessel (CC) are needed to reduce inaccuracies of the generated magnetic field. In-vessel coils can also be used to provide rapid feedback-control or to alleviate plasma edge instabilities. In total, there are 18 TF coils, 6 CS modules, 6 PF coils, 18 CC coils and 29 in-vessel coils. Details of the manufacturing of the coils and, of mechanical support structures are given in [8].

The coils are made of low temperature superconducting (LTS) cables, except the in-vessel coils, which are made of copper. The CS and TF cables are based on Nb_3Sn superconducting wires, the PF and CC cables – on NbTi superconducting wires, see corresponding photographs in figure 2.1. The maximum operating current and peak magnetic field are set for the cables as follows: 68 kA/11.8 T for the TF cables, 45 kA/13 T for the CS cables, 52 kA/5.7 T for the PF cables, 10 kA/4.1 T for the CC cables. In order to protect the magnets against a potential thermal runaway ('quench'), pure copper wires are embedded in the TF, CS and PF cables. The ratio between the copper and superconductor cross-sections is about 2.2 for TF, 2.0 for CS, from 1.6 to 4.7 for PF and 2.3 for CC cables. The total magnetic energy stored in the ITER system is about 50 GJ.

The ITER cables are so-called cable-in-conduit (CIC) conductors (see overview of the cabling concept in [9, 10]). A bundle of superconducting and copper wires is fully contained inside a steel jacket, which prevents accumulation of mechanical stresses in the cable from the adjacent turns of the coil. The He-4 coolant flows through the voids contained by the cable space inside the jacket. High heat removal is achieved by forcing the flow in a supercritical state at high pressure. As shown in figure 2.2, a typical pressure range for the CIC conductors is from 4 bar to 10 bar, such that a phase transition of He-4 will not occur during transient temperature rises. Crossing the two-phase boundary at lower pressures would result in a very unstable mass-flow, because of a rapid change of the coolant properties. While the inlet temperature of
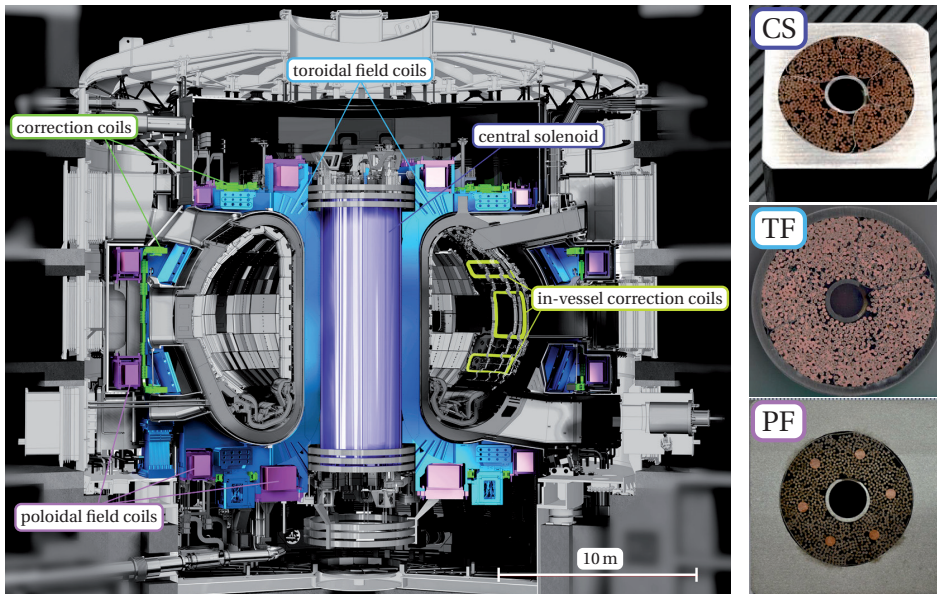
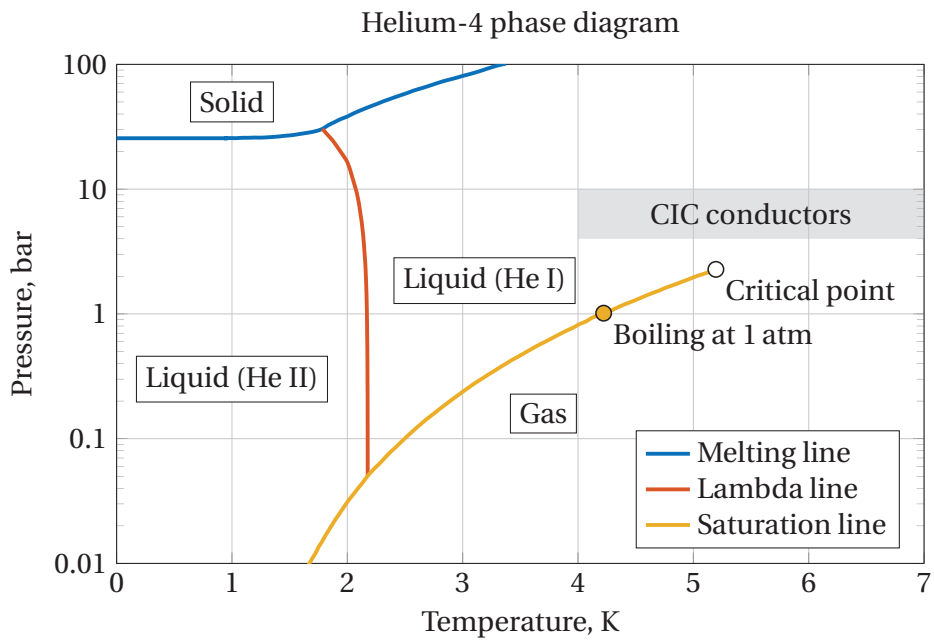**Figure 2.1:** Magnet system of ITER (pictures from [5]).

Figure 2.2: Phase diagram of helium-4. Hydraulic operating conditions for the CIC conductors are also indicated.

the cables is 4.5 K, this may slightly increase along the cable length up to 5 K, due to various heat loads in the system such as radiation and AC losses. The mass-flow rate of the coolant is between 8 g/s and 14 g/s, depending on the heat load that has to be removed.

The electric field along the cables at the operating conditions is negligible and as a function of temperature is usually expressed by a power law: $E(T) = E_c(T/T_{cs})^m$. The current-sharing temperature T_{cs} defines the situation when the electric field threshold E_c is reached and m characterizes the steepness of the transition. Typically, $E_c = 0.1\,\mu V/cm$ for the LTS testing. Then, the temperature margin can be defined as $\Delta T = T_{cs} - T_0$, where T_0 is the local operating temperature. In ITER, the TF cables have the lowest temperature margin, of about 0.7 K.

Measurements of the full-size ITER cables are carried out in the SULTAN test facility at the Swiss Plasma Center (SPC). The main parameters and an external view of SULTAN are given in appendix A.4. Even though all the measured cables have successfully passed the acceptance criterion for T_{cs} (see statistics of the test results in [11]), only about 50 % of the single wire performance is retained in the cables [12]. An estimated average strain of –0.5 % is expected on the TF cables and the performance of those conductors is expected to be twice as much compared to what measured experimentally in SULTAN.

This degradation is mostly due to an accumulation of compressive strains during the cable manufacturing and operation, which results in a relatively broad strain distribution [13] and fracture of a significant fraction of superconducting filaments [14]. The degradation is partially reversible and can be reduced when the cables experience tensile hoop stress in the coils [15]. These issues have already been addressed in the LTS fusion cables for DEMO. Design and full-size R&D studies of 80 kA/12 T prototypes resulted in significantly improved retention of the superconducting properties in the cables [16, 17].

Based on the ITER experience, the typical requirements for the forced-flow conductors of fusion magnets (as foreseen by the EUROfusion roadmap [18]) can be outlined as follows:

1. Temperature margin $\gtrsim 2\,K$ at operating conditions (typically $I \gtrsim 50\,kA$, $B \gtrsim 10\,T$).

2. Copper current density $\lesssim 100\,A/mm^2$.

3. Stability against a high transverse loading during the cable operation and against thermal stresses originating from a warm-up-cool-down of a magnet:
   no reduction of the cable performance by irreversible degradation is allowed.

4. Critical bending radius of the cable $\lesssim 2\,m$ (i.e. minimum radius of the coil).

5. Pressure drop of the coolant flow in the entire coil $\Delta p \lesssim 1\,bar$.

6. For the application in CS coils: minimized total AC loss.

In most of the cable designs these requirements result in a relatively low engineering current density of the cables j_{eng}, i.e. the ratio between the operating current and the cable space. In order to maintain acceptable compactness, usually $j_{\mathrm{eng}} \gtrsim 50\,\mathrm{A/mm^2}$. Although additional requirements can be imposed on the heat removal rate and radiation resistance of the cable, they will not be considered in the following discussion.
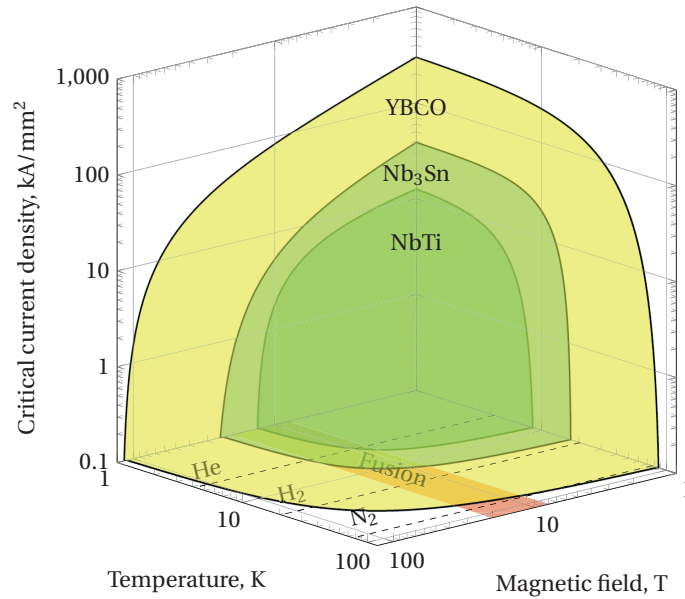
2.2 High temperature superconductors

High temperature superconductors (HTS), first discovered in 1986 [19], became commercially available about two decades ago. Although a large variety of HTS materials have been discovered since that time, at present only three of them can be considered suitable for large scale applications: two bismuth strontium calcium copper oxide compounds, $Bi_2Sr_2CaCu_2O_{8+x}$ and $Bi_2Sr_2Ca_2Cu_3O_{10+x}$, and a rare-earth barium copper oxide compound, $ReBa_2Cu_3O_{7-x}$, where Re stands for Rare Earth, typically yttrium (Y) or gadolinium (Gd). These materials are usually abbreviated as Bi2212, Bi2223 and ReBCO.

The main parameter of superconductors – the critical current density j_c – is defined from the voltage-current transition, which can be expressed per unit length by a power-law dependence:

$$E = E_c \left(\frac{j}{j_c(T,B,\theta,\varepsilon)} \right)^{n(j_c)} \tag{2.1}$$

where E_c is the electric field threshold: $E(j_c) = E_c$, j is the current density and n the exponent of the transition. A value of $E_c = 1\,\mu V/cm$ is commonly accepted for the HTS testing. Similar to the LTS superconductors, j_c is a function of temperature T, magnetic field B and mechanical strain ε (though j_c of NbTi has a weak dependence on ε). In addition, a strongly anisotropic crystal structure of the HTS materials (the unit cell is composed of parallel atomic ab planes, the c-axis is the direction perpendicular to ab [20]) results in a dependence of j_c over the angle of orientation θ of the magnetic field B with respect to the c-axis. For a given B, the lowest value of j_c is typically at $\theta = 0°$, the highest one at $\theta = 90°$. Although the value of n is also a function of T, B, θ and ε, usually it can be simplified to a single-valued dependence upon j_c.

A comparison of the j_c field-temperature dependence for the NbTi, Nb_3Sn and YBCO materials is presented in figure 2.3, where each axis is shown on a logarithmic scale. In a field range of fusion magnets, the j_c dependence upon T, in a range close to 5 K, is much weaker for YBCO than for NbTi and Nb_3Sn. Consequently, HTS materials can be operated closer to j_c than LTS, still retaining sufficient temperature margin. Or the other way around, the higher temperature margin can be easily gained by a smaller reduction of the relative operating current.

Figure 2.3: Critical current density as a function of magnetic field and temperature for YBCO, Nb$_3$Sn and NbTi superconductors. Orientation of the magnetic field is taken along the c-axis for YBCO ($\theta = 0°$). Typical range of magnetic fields in fusion magnets and normal boiling points of liquid helium, hydrogen and nitrogen are also reported.

Comparing the j_c surfaces with the boiling temperatures of common cryogenic liquids (helium, hydrogen, nitrogen), the 'low' temperatures can be defined as $T \lesssim 20\,$K, the 'high' temperatures as $T \gtrsim 77\,$K. These definitions will be used throughout this document.

From a practical point of view, the operating conditions at which the critical current becomes zero define a top limit for application of the superconductor. This condition for the field-temperature j_c surface reads as $j_c(B_{\mathrm{irr}}(T), T) = 0$, where $B_{\mathrm{irr}}(T)$ is a so-called irreversibility line. By definition, $B_{\mathrm{irr}}(T_c) = 0$, where T_c is the critical temperature. Note that in the HTS superconductors a magnetic field at which the superconducting state is destroyed (B_{c2}) is significantly higher than B_{irr}, while in the LTS superconductors they are almost identical [20]. For intermediate fields between B_{irr} and B_{c2}, the superconducting state in terms of Cooper pairing is still present but there is no flux pinning, i.e. the electrical resistance is no longer zero.

The irreversibility lines for most of the practical superconductors are reported in figure 2.4. Similar to MgB$_2$, the iron-based superconductors (discovered in 2008 [22]) have the critical temperature around 40 K. Sometimes they are referred to as 'medium' temperature superconductors (MTS). For the three reported HTS materials, the approximated values of B_{irr} at 0 K are larger than 100 T. As can be seen from the plot, the HTS materials provide an enabling technology for applications either at high
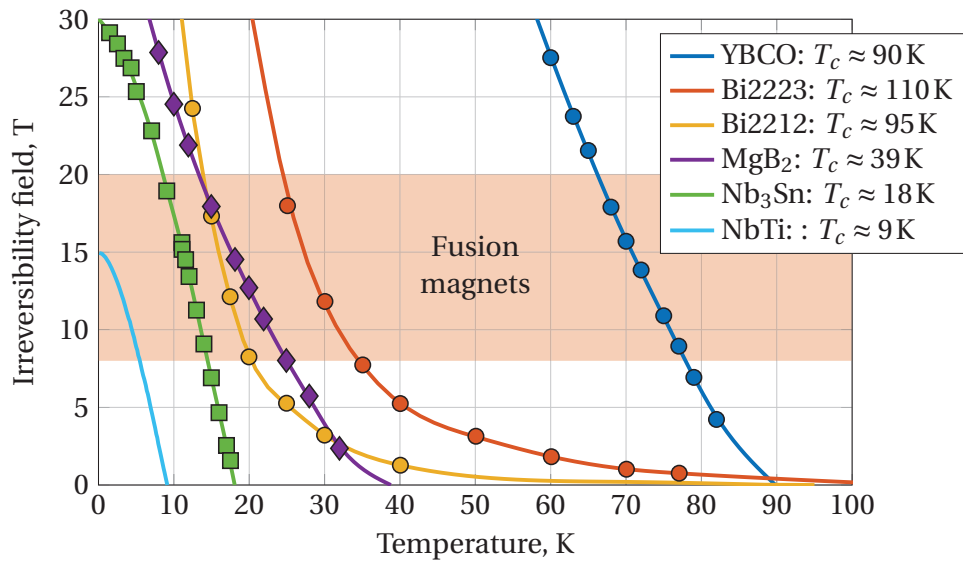
Figure 2.4: Irreversibility lines for the practical superconductors (adapted from [21]).

temperatures or at very high magnetic fields.

In the case of fusion magnets, the high critical currents of HTS can only be achieved in the low temperature range. Beside other features of HTS discussed below, the possibility of cooling the HTS materials with liquid nitrogen is also very advantageous for preliminary tests.

For YBCO at low temperatures there is a large margin between the operating temperature and the critical one defined from $B_{\mathrm{irr}}(T)$, typically about 70 K. This feature has twofold implications. On one hand, stabilization against various thermal perturbations is no longer an issue since the energy required to induce a thermal runaway ('quench') is three orders of magnitude larger than in LTS [23]. A so-called 'training' effect – a situation when series of quenches occur at relatively low operating currents in the LTS magnets before reaching the full operating current – is not expected in the HTS magnets. On the other hand, if by some reasons the HTS has been quenched, the high temperature zone will propagate at a very low speed. The corresponding voltage will rise also slowly. When the quench will be detected based on that signal, the hot-spot temperature can already exceed the permissible values. In order to prevent such situations, the HTS magnets should still be protected by a proper amount of stabilizing materials, which increase the heat capacity and thermal conductivity of superconducting cables.

Similar to the LTS, Bi2212 composite conductors can be manufactured in a round wire shape as precursor, meaning that a heat treatment to form the superconducting phase is still needed. Significant increase of the wire critical current can be obtained by applying the heat treatment at a very high pressure, ~ 100 bar [21]. The Bi2223 and
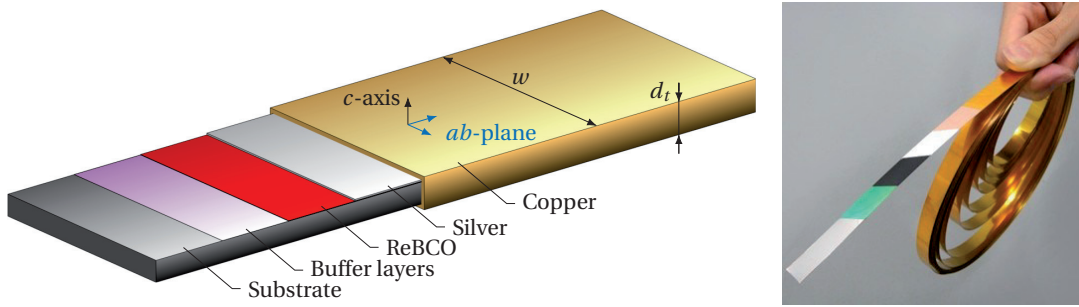
Figure 2.5: Composition and photograph of the ReBCO tape.

ReBCO conductors so far are only available in the form of thin tapes, in order to ensure alignment of the material grain boundaries [20]. For both conductors a heat treatment after the manufacturing is not needed. The powder-in-tube production method is used for the Bi2212 and Bi2223 conductors, while layer deposition methods are employed for the ReBCO conductors. In the terminology of applied superconductivity, the Bi2223 tapes are the first generation conductors (1G), the ReBCO tapes the second generation (2G) or 'coated conductors'.

A schematic composition and a photograph of the ReBCO tape are presented in figure 2.5. The width of the tape w is in the range from 2 mm to 12 mm. The total thickness $d_t \approx 100\,\mu$m is typically comprised of ~ 1 μm ReBCO layer, ~ 50 μm substrate, ~ 40 μm copper coating and the rest for the silver and buffer layers. Note that the fraction of the ReBCO material in the cross-section is only about 1 %, while for the Bi2223 tapes with a similar current capacity and having 4.30 mm width and 0.23 mm thickness, the superconductor occupies about 40 % of the cross-section. A high potential for improvements is still available for the coated conductor technology.

The mechanical properties of the ReBCO tapes such as the critical values of the stress or strain are mostly dominated by those of the substrate material. Hastelloy, stainless steel or Ni-based materials are commonly used. If compared with the Bi2223 tapes, the ReBCO tapes have from 2 to 3 times higher values of the critical axial strain, in the range from 0.4 % to 0.6 % [24]. The critical axial stress for the Bi2223 tape is up to 250 MPa, while for the ReBCO tape is more than 700 MPa. However, a high mechanical anisotropy is present in the ReBCO tapes due to weak 'adhesive' properties of the thin layers between the substrate and copper. The critical transverse tensile and peel stresses are about 10 and 100 times lower than the axial one [25].

The coated conductors are produced by several companies around the world: Super-Power, SuperOx, SuNAM, Fujikura, AMSC, SST, Bruker HTS, Theva, STI. The manufacturers are still constantly improving the tape performances by increasing the tape critical current and its homogeneity along the tape length, reducing the substrate thickness and the overall product price. Presently, the maximum length of a single tape piece with quite uniform transport properties is about 1 km. The critical current
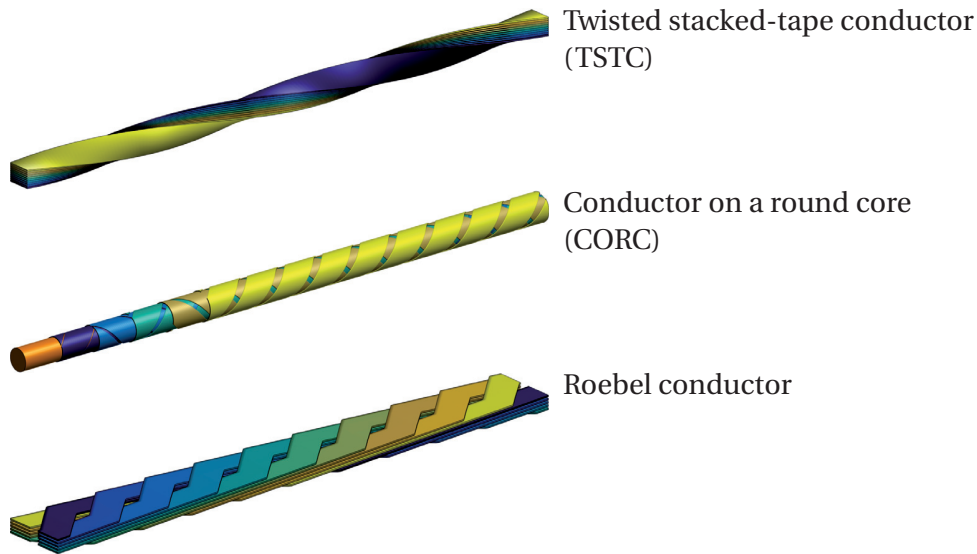
Figure 2.6: Illustration of 10 tapes assembled in the TSTC, CORC and Roebel cable layouts.

of a 4 mm-wide tape at 77 K / self-field is from 100 A to 200 A. Due to a variety of layer deposition techniques, the performance of the tapes can be optimized for a specific operating range. For instance, the SuNAM tapes have one of the highest critical currents at 77 K / low field application, but relatively low values at low temperature / high field, which is exactly the opposite with respect to the Bruker HTS tapes.

2.3 Coated conductor cabling concepts

Conventional cabling concepts are based on a round wire geometry. New design approaches are required for the HTS applications due a thin tape geometry. At present, there exist three cabling layouts, which are depicted in figure 2.6. Basically, these pictures represent general topological methods accounting for the flat tape geometry for cable manufacturing. Considering real applications, the inclusion of additional components for enhancing the mechanical, electrical and thermal properties with respect to the target requirements might be necessary.

The twisted stacked-tape conductor proposed at MIT [26] is a simple and economical design. The tapes are stacked along the c-axis and then twisted along a longitudinal direction. Material loss is negligible in this design. From a total tape length l one can produce n_t-tape conductor of l/n_t length. Note that in terms of strain distribution, the twisting of the stack is equivalent to that of a single tape, due to a tape slippage effect.

In the conductor on a round core cable design (CORC) the tapes are wound around a

central former at $\approx 45°$ to the cable axis [27]. The tapes are oriented with the superconducting side facing a central former, i.e. the ReBCO layers are under compression. The CORC design takes advantage of the fact that the in-plane mechanical strain applied at 45° to the a- or b-axis of the ReBCO crystal has a minimal impact on the critical current [28]. Consequently, the CORC cable should benefit of improved isotropic bending properties.

The most sophisticated option – Roebel conductor [29] – requires the tape surface to have a special meandering shape. This can be achieved by cutting the undesired regions out of a wide 12 mm tape. Even though almost half of the manufactured material is not used, the Roebel conductor is the only option with the full transposition of tapes and completely aligned orientations of the c-axes both along the conductor and between the tapes. As a result, improved in-field performance of the conductor can be achieved if a component of magnetic field along the c-axis is excluded. This idea has been recently elaborated and implemented in the design of the HTS accelerator magnet (see full details in [30]).

Comparative investigations of the cabling concepts at low temperatures and high fields have been carried out in the FBI test facility at KIT [31–35]. In principle, all the three concepts can be considered for high field applications in fusion magnets. Due to the high Lorentz force at high current and high field, the need for enhanced mechanical supports for tapes has been identified for the TSTC and Roebel samples. Relatively poor thermal properties have been observed for one of the CORC samples, which was burned during the quench at 10 T and 9.4 kA, before reaching the critical current. As a result, design iterations are still needed to finalize the flat-tape cabling layout for fusion.

2.4 Scope and outline of the thesis

The novel HTS materials have various advantages for fusion compared with the 'classic' LTS, such as an access to magnetic fields above 16 T, larger temperature margin and potential to operate at high temperatures. Even though low temperatures are still needed to achieve high currents in HTS at high magnetic fields, the possibility of a relatively simple preliminary testing of HTS in liquid nitrogen is an advantageous feature. Between the three main HTS conductors – Bi2212 wire, Bi2223 tape and ReBCO tape – we will mostly focus on ReBCO, which has superior axial mechanical properties. The coated conductor technology is still in the developing stage and employs relatively low cost raw materials. This implies that there is a high potential for the improvement of the price to performance ratio. While the prospects for HTS materials in fusion have been stated at least about a decade ago, a full-scale testing of HTS cables for fusion at the relevant operating conditions has not yet been performed.

In this research we aim at demonstrating the feasibility of HTS conductors for fusion magnets. One of the key challenges that has to be addressed is the development of the flat-tape cabling concept for fusion magnets. According to past experience, a high attention needs to be given to the mechanical and thermal properties of the HTS cables, with the high currents ($\gtrsim 50\,\text{kA}$) and magnetic fields ($\gtrsim 10\,\text{T}$) required in fusion magnets. Any design of HTS cables should take into account the main issues present in the HTS technology, such as highly anisotropic mechanical and electrical properties of the tapes, and protection against the quench that is intrinsically difficult to detect in HTS. The influence of defects in the tapes on the overall cable performance should also be minimized.

Full-scale measurements of the HTS cable prototypes are planned to experimentally demonstrate the feasibility of the proposed cable concept for fusion and validate if the developed design tools are adequate to predict the cable properties.

Keeping in mind that the ultimate goal of fusion technology is the production of electricity from fusion reactions, the cost implications of using HTS in fusion magnets should also be considered. Therefore, we will attempt to identify a suitable application for the HTS cables in the magnet system based both on the technical and economical aspects.

This thesis is organized as schematically illustrated in diagram 2.7. The initial steps in the project are dedicated to the design and technology development of the cabling concept proposed at the Swiss Plasma Center. These will be followed in the second half of the thesis by addressing the physical properties of the HTS cable. Due to the iterative nature of this research, the results from each main step of the project may lead to the necessity of repeating the previous steps, leading to a better understanding of the underlying phenomena. All the obtained results are considered to form a 'design document' for HTS fusion cable, i.e. a collection of knowledge required to construct the cables for fusion applications.

Chapter 3 presents the results of the electrical and mechanical investigations (experimental and numerical) of the basic component of the cable – the strand. The pros and cons of the proposed strand design will be highlighted.

Chapter 4 describes the parametric study of the cable design and the results of the full-scale R&D activity, including the construction of 60 kA/12 T HTS cable prototypes and their high field-low temperature measurements in EDIPO.

In chapter 5, a detailed analysis of the main AC losses contributions in the cable is discussed. An effective analytical parametrization of the developed models is proposed as a fast tool to assess the AC performance of the cable.

Chapter 6 deals with the analysis of thermal behaviour of the cable against local heat pulses, performed using the heat balance and coolant flow equations. Forced flow and adiabatic conditions are considered. Recommendations to reduce the hot-spot
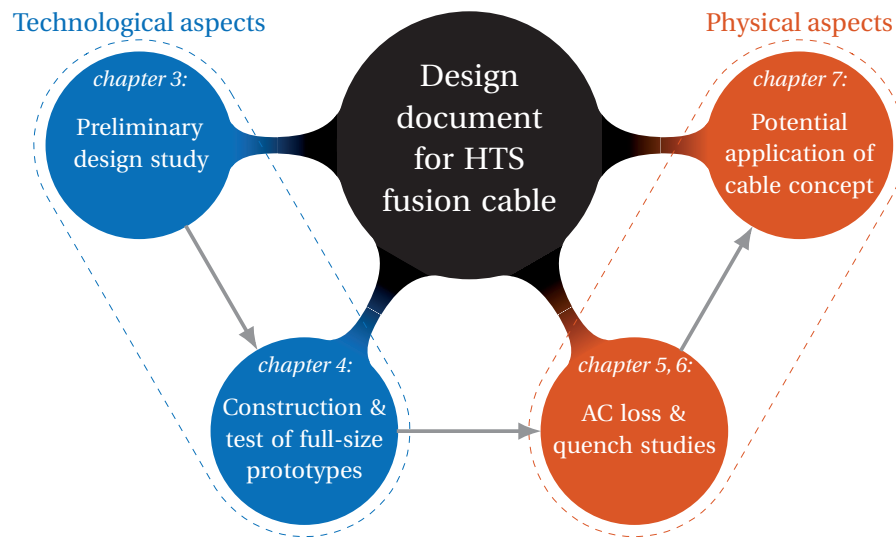
Figure 2.7: Mind map of the thesis objectives.

temperature during the quench are also provided.

In chapter 7 the potential applications of the cable concept in fusion magnets and its technical and economical implications are debated. The design and properties of the two elaborated options are presented.

Finally, the implications of this work on the development of HTS cables for fusion magnets are discussed in the conclusion section, along with recommendations for further investigations.

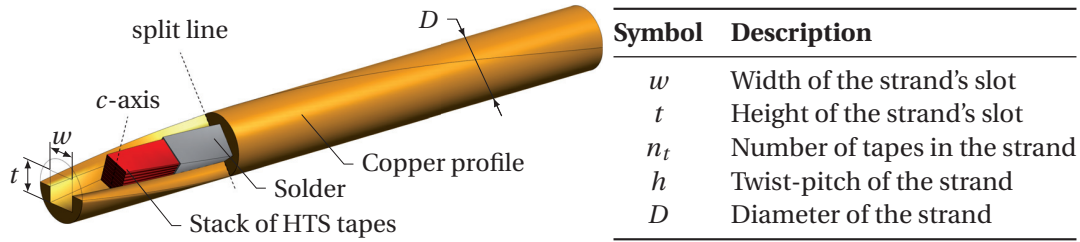# 3 Round strands made by twisted stacks of HTS tapes

Taking as a reference the ITER TF cables carrying 68 kA at 12 T, first considerations on the manufacturing of high current fusion cable based on HTS tapes suggest that hundreds of tapes are needed. In order to efficiently deal with an arrangement based on such a large number of tapes, the development of an intermediate cabling solution for tens of tapes is envisaged. Aiming the design studies primarily at fulfilling the requirements relevant for fusion, the arrangement of tapes should be mechanically rigid against the Lorentz force and thermally stabilized against the overloading conditions, as the cables are operated in high current and high field conditions. Among the HTS cabling concepts discussed in the previous chapter, a modified twisted stacked-tape conductor (TSTC) is selected.

In this chapter we discuss what are the pros and cons of the proposed modifications. We will focus on electrical and electromechanical studies, which are carried out in most cases both experimentally and numerically. Assuming that the mechanical limits such as critical values of the twist-pitch, bending radius and transverse pressure, are weakly dependent on temperature, they are inferred from electromechanical studies performed at 77 K, in a liquid nitrogen bath.

3.1 Design of the strand

A twisted stack of HTS tapes soldered between two copper semi-circular profiles is proposed at SPC as a basic component of high current cables for fusion magnets [36]. Similarly to the terminology of LTS conductors, next we call the proposed component design as a 'strand'. The tapes in the strand are partially transposed by longitudinal twisting: this can be done in general before or after the soldering. An artistic view with the definition of the geometrical parameters of the strand is outlined in figure 3.1.

Compared with the original TSTC concept, which is illustrated in figure 2.6, the outer copper shells and soldering of the components are embedded in the strand design. These features reduce the inter-tape resistance r_{it} and reinforce the mechanical properties of the strand against the Lorentz force at high field operation. Low values of r_{it} provide uniform current distribution in DC operation, which allows us to achieve full

| Symbol	Description
w	Width of the strand's slot
t	Height of the strand's slot
n_t	Number of tapes in the strand
h	Twist-pitch of the strand
D	Diameter of the strand

Figure 3.1: Sketch of the strand and definition of the geometry parameters. The split line between the copper profiles is perpendicular to the c-axis of the stack.

current capacity of the strand. Typical values of r_{it} at 77 K and 4.2 K are reported in the next section; the DC performance of the strand at low and high magnetic fields will be presented in sections 3.3 and 3.4. The possibility of current transfer between tapes at low voltage results in a high strand tolerance against defects in tapes and also in a high thermal stability at overloading conditions. The so-called 'cascade' burning of the tapes – the situation when the tapes are burnt one after another because the overloading current cannot be efficiently redistributed between them – is unlikely to happen during a quench in the strand. These two aspects will be further discussed in section 3.5 and in chapter 6.

On the negative side, mechanical tolerances on the strand bending are reduced compared with those of a single free-standing tape due to an effect of strain accumulation in the soldered structure. If the strand is first soldered and then twisted, the strain will also accumulate during the strand twisting. Twisting of a non-soldered stack of tapes is mechanically equivalent to single tape twisting [26]. Experimental and numerical parametric studies of the axial (twisting and bending) and transverse loading are summarized in sections 3.6 through 3.9. As it will be shown in these sections, preliminary annealing of the copper profiles and orientation of the split line between them with respect to the tape faces (can be either along or perpendicular to the tape faces), both have a strong impact on the strand mechanical properties and it should also be considered as part of the strand design.

As a result, the complete design of the strand is defined by set of 5 geometrical parameters, orientation of the split line and selected options for the preliminary profile annealing and twisting-soldering sequence. Since the improvement of one property of the strand may lead to the worsening of the other, an 'ideal' design of the strand is defined as the most balanced for the requirements of a specific application.
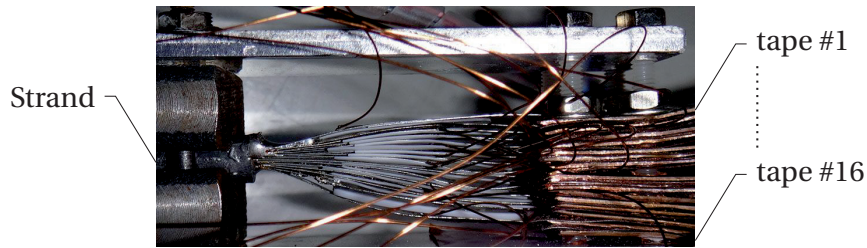
Figure 3.2: Terminal of the 16-tape strand for the inter-tape resistance measurements. The tapes have labels from 1 to 16 top-down.
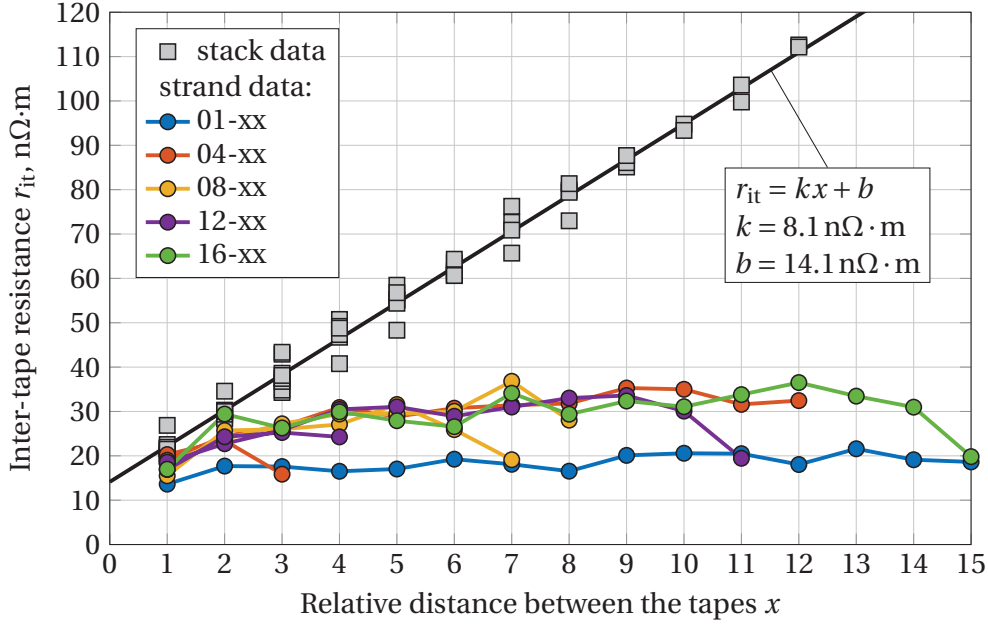
3.2 Inter-tape resistance

Several non-twisted samples have been prepared for the inter-tape resistance measurements: a soldered stack of 13 SuperPower tapes (without copper shells) and two identical 16-tape SuperOx strands. One of the two strands has been shipped to the University of Twente for measurements at 4.2 K in a background magnetic field. Other samples were measured in a liquid nitrogen bath.

The tapes in the stack are oriented such that the superconducting face of each tape is in contact with the substrate side of the next tape. The width of the tapes is 4 mm. The tapes were not soldered together at the terminal of the samples, so each tape has its own insulated current lead and voltage tap as shown for one strand in figure 3.2. This experimental setup allows us to select any pair of tapes and measure the resistance R between them. Then, the inter-tape resistance r_{it} can be obtained as $r_{it} = Rl$, where l is the soldered length of the sample ($l = 30$ cm for the stack and 16 cm for the strand). r_{it} can be considered as a function of the dimensionless 'distance' between the tapes $x = |i - j|$, where i and j are the tape labels of the selected pair (see figure 3.2). $x = 1$ for the adjacent tapes in the stack, $x = 12$ and 15 for the outermost tapes in the stack and strand.

The tapes #1, 4, 7, 10, 13 in the stack and #1, 4, 8, 12, 16 in the strand were selected as input. The voltage–current characteristics have been measured for each input tape and all other tapes in the sample, what results in 60 and 75 combinations of the input–output tapes in the stack and strand. The results of the r_{it} measurements for the stack and strand at 77 K are summarized in figure 3.3.

For all the measured tape pairs in the stack, r_{it} shows a linear dependence on x: $r_{it} = kx + b$, where the slope $k = 8.1$ nΩ·m and the offset $b = 14.1$ nΩ·m. Note that in general the values depend on the stack geometry and type of the solder.

In case of the strand a much different dependence of r_{it} on x has been obtained. Basically, two situations can be distinguished for the data presented in figure 3.3: either both tapes in the measured pair are oriented with the ReBCO layers facing another tape in the stack or one of them is in front of the copper profile. The values

Figure 3.3: Inter-tape resistance r_{it} at 77 K as a function of relative distance between tapes in the stack $x = |i - j|$, where i and j are the tape labels of the selected pair (see figure 3.2).

of r_{it} for the former situation are shown in figure 3.3 for the 04-xx, 08-xx, 12-xx and 16-xx connections, and 01-xx for the latter situation. For low values of x, r_{it} of the strand is close to the one measured in the stack, while at high values of x the difference between the strand and stack data becomes significant: r_{it} at $x = 12$ in the stack is 5.5 and 3 times larger than in the strand for the 01-xx and other connections, respectively. Although for the top and bottom tape in the stack it is also possible that both ReBCO layers are in direct contact with the copper profiles, this situation did not manifest in the measurements.

These results suggest that there are different current coupling paths between the tapes in the stack and in the strand. Since the specific resistivity at 77 K of the SnPb solder and Hastelloy substrate is ≈ 15 and ≈ 650 times higher than the one of copper, respectively, the following assumptions can be made on the coupling paths between the tapes (see corresponding illustration in figure 3.4):

- The tapes in the stack are coupled through the solder at the tape edges.

- The current between tapes in the strand flows first in the solder and then in the copper at the tape edges. If the superconducting side of the tape faces the copper profile the current enters the copper through the wide side of the tape.

Consequently, under these assumptions the inter-tape resistance in the stack reads as $r_{it} = 2r_{sc-so} + r_{so}(x)$, where $r_{sc-so} = b/2 \approx 7.1\,\text{n}\Omega\cdot\text{m}$ is the resistance between the
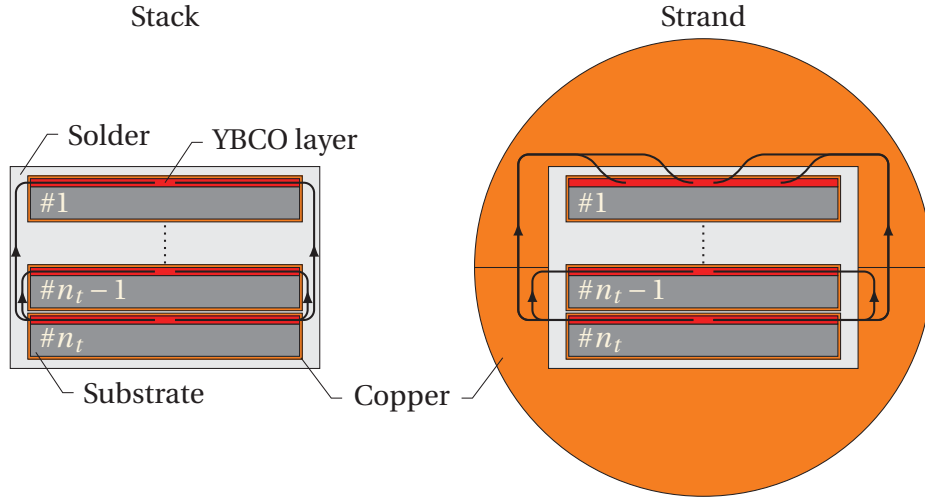
Figure 3.4: Sketch of the current coupling paths between tapes in the stack and strand. For simplicity, only the first and the last two tapes are shown in the stack and strand cross-section; the tapes are enlarged in the vertical direction.

superconductor and solder domains (i.e. sum of the ReBCO-silver, silver-copper, copper-solder interface resistances), and $r_{so}(x) = kx$ is the contribution from the solder domain. Using the specific resistivity of the SnPb solder $\rho_{so}(77\,\text{K}) \approx 31\,\text{n}\Omega\cdot\text{m}$ and thickness of the tape $d_t \approx 0.1\,\text{mm}$, the effective width of the solder domain that is involved in the current transfer can be estimated as $\rho_{so}(77\,\text{K})\cdot d_t/k \approx 0.4\,\text{mm}$.

Similarly, the inter-tape resistance in the strand reads as $r_{it} = 2r_{sc-cu} + r_{cu}(x)$. Taking into account the large aspect ratio of the tape (width/thickness ≈ 40), the resistance between the superconductor and copper domains r_{sc-cu} can be neglected for tape #1, i.e. $r_{it} = r_{sc-cu} + r_{cu}(x)$ for the blue line in figure 3.3. Then, the interface and distance-dependent resistance contributions are estimated as $r_{sc-cu} \approx 11.7\,\text{n}\Omega\cdot\text{m}$ and $r_{cu}(x) \approx kx$, $k = 0.84\,\text{n}\Omega\cdot\text{m}$. The effective width of the copper domain that is involved in the current redistribution can be estimated as $\rho_{cu}(77\,\text{K})\cdot d_t/k \approx 0.2\,\text{mm}$.

For the strand measured at the University of Twente, tape #1 was used as input, tapes #2 to 6 and 10 to 16 – as output (in total, 12 pairs). At 77 K the results for r_{it} fall in the range from 13 nΩ·m to 24 nΩ·m, which is in agreement with the corresponding data presented in figure 3.3 (the blue line). After the strand was cooled down to 4.2 K and a background magnetic field 1 T was applied (to eliminate superconductivity in the solder), the results for r_{it} fall in a narrower range, from 3.5 nΩ·m to 5.4 nΩ·m. At both temperatures, the minimum values were obtained for $x = 1$, the maximum values for $x = 13$. The effect of a background magnetic field on r_{it} was also studied for the outermost pair ($x = 15$): the results deviate by less than 0.2 nΩ·m as the field ranges from 0.3 T to 1.5 T .

Due to the weak dependence on the relative distance between tapes and the low
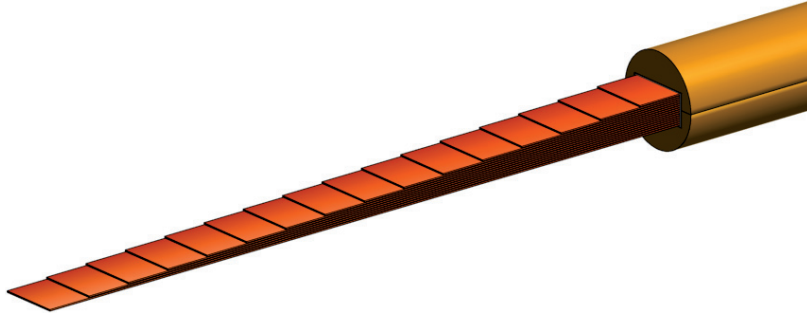
Figure 3.5: Artistic view of the staggered tapes at the strand terminal.

absolute values of the inter-tape resistance in the strand, the redistribution of the current and thermal stabilization between tapes should take place at low potential and temperature gradients in the strand cross-section. In other words, the strand cross-section can be considered essentially equipotential and isothermal.

The current distribution between tapes is also affected by the resistances at the strand terminals, except in the case of long strands in the AC operation, where the inductive voltage is dominant. The use of the staggered tapes at the strand terminals (see illustration in figure 3.5) and the symmetric arrangement ensure low and almost identical resistance for each tape of the strand. All the tapes are oriented with the superconductor side on top. Then, the copper plate is soldered on top of the staggered tapes; the current is injected in the plate in a direction perpendicular to the strand axis. This type of connection is used in most of the manufactured strands, as it will be discussed in the next sections.

3.3 DC performance at self-field

The electrical DC characterisation of the strand is based mainly on the determination of the critical current I_c. In case of equipotential cross-section of the strand, the electric field E developed in the longitudinal direction of the strand follows a power law dependence:

$$E = E_c \left(\frac{I}{I_c(B, T, \varepsilon, \theta)} \right)^{n(I_c)} \tag{3.1}$$

where E_c is the electric threshold at which I_c is defined: $E(I_c) = E_c$. Typically, $E_c = 1\,\mu V/cm$ for HTS testing. As for the tape properties, the values of I_c and n of the strand are also a function of the temperature T, the mechanical deformation ε, the magnitude of B and the orientation θ of the magnetic field.

As the n_t tapes can be considered as connected in parallel, I_c of the strand is a sum of the tape critical currents (see appendix A.2.1). In situations where the self-field

generated by the current in tapes cannot be neglected compared with the external magnetic field, a reduction of the tape critical current due to the self-field must be taken into account. For instance, all the electromechanical measurements discussed in sections 3.6 to 3.9 have been carried out in a self-field at 77 K. In general, the sum of the tape critical currents at given operating conditions without accounting for the self-field overestimates the strand I_c performance.

At a fixed temperature and mechanical strain, there are several analytical approaches to describe the field and angular dependences of the critical current density [37–41]. For example, the Kim-like relation [42] reads as:

$$j_c(B, \theta) = \frac{\alpha \, j_{c_0}}{\left(1 + \sqrt{k^2 \cos^2 \theta + \sin^2 \theta} \, \dfrac{B}{B_0}\right)^\beta} \tag{3.2}$$

where the values $\alpha = 1.08$, $k = 2.02$, $\beta = 0.65$ and $B_0 = 157\,\text{mT}$ have been set for the SuperPower SCS4050 tapes; j_{c_0} is the critical current density of the tape when no background field is applied. $\alpha > 1$ accounts for the fact that j_{c_0} is derived from measurements with the self-field of the tape. In other words, $\alpha \, j_{c_0}$ is the critical current density that would be measured in the absence of any field. For fixed temperature and tape geometry α is constant. Note that if the available experimental dataset is 'large enough', a direct interpolation of the values corrected for the self-field provides a high accuracy for the $j_c(B, \theta)$ dependence [43].

The analysis of the self-field effect can be simplified, as the twist-pitch of the strand $h \gg$ width of the tape $w \gg$ thickness of the tape d_t. Consequently, the tapes in the stack can be approximated as straight strips with a constant current density along the tape thickness. If each tape is divided into N_x elements along its width, the stack of n_t tapes can be considered as a set of $N_x \cdot n_t$ long straight conductors. The current density in each element is assumed constant.

The contribution of the element i to the total magnetic field at the location of the element k can be calculated as $\langle \Delta \vec{B} \rangle (x_k - x_i, y_k - y_i) = \{M_x, M_y, 0\} \cdot I_i$, where $I_i = j(x_i) w d_t / N_x$ is the current in the element i. Accurate expressions for M_x and M_y are given in (A.12) and (A.13) in the appendix. The total magnetic field at the element k is obtained as a sum of the contributions from all elements, excluding the k-th element itself. Note that the values of M_x and M_y can be calculated just once at the beginning of the calculation.

The initial distribution of I_i along the tape width is set constant and equal to $j_{c_0} w d_t / N_x$. After the corresponding field distribution is obtained, the values of I_i are recalculated using the selected $j_c(B, \theta)$ dependence. As a result, the calculation becomes self-consistent and runs until changes in I_i are smaller than a given tolerance. Typically, the process converges after about 4 iteration steps.
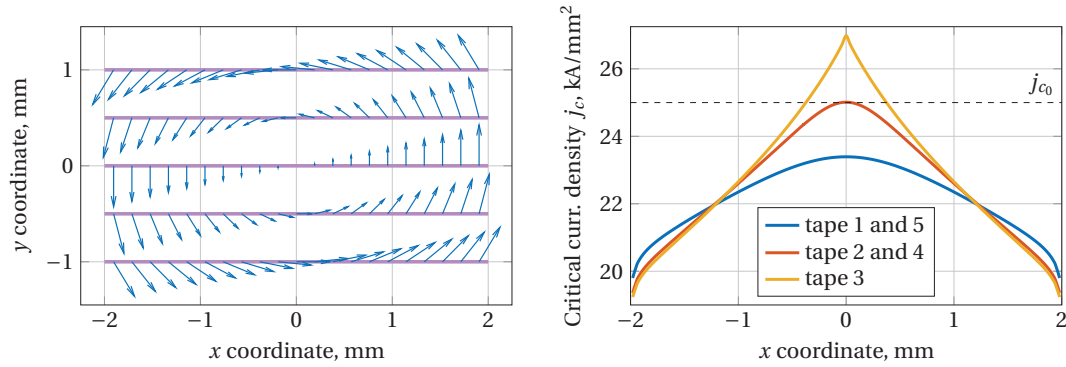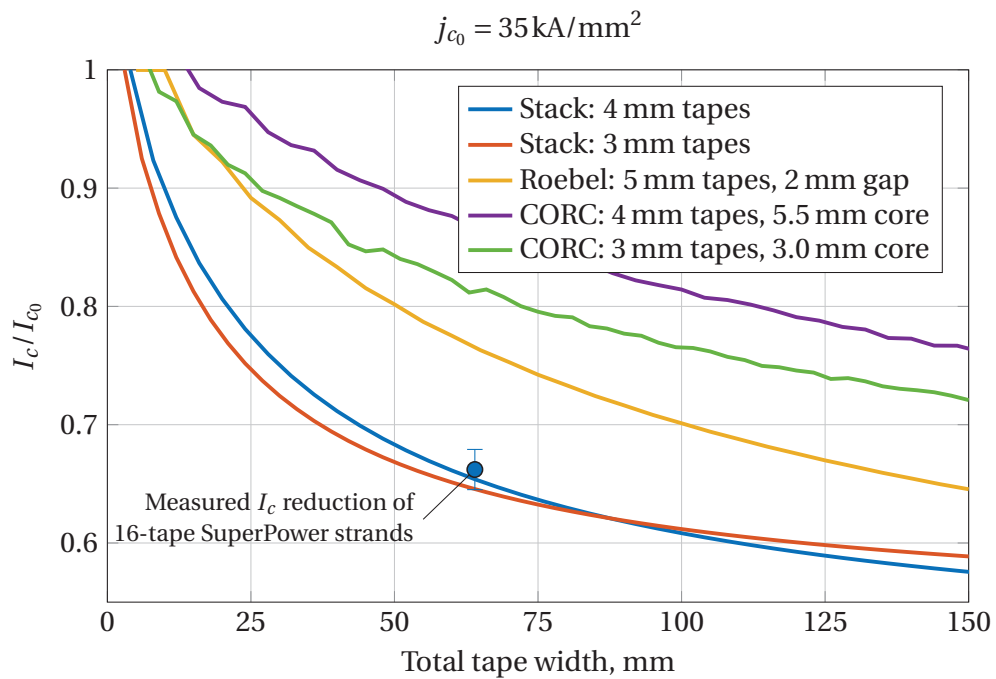
Figure 3.6: The self-field effect in the 5-tape stack. Left: distribution of the magnetic field along the tape width; the current is directed out of the page. Right: distribution of the critical current density along the tape width. Tapes are labelled 1 to 5 top-down.

As an example, the results of the calculation for a 5-tape stack are presented in figure 3.6. The current flows in the superconducting layers of 4 mm width and 1 μm thickness. The distance between the layers is set to 0.5 mm. The initial critical current of each tape was set to 100 A ($j_{c_0} = 25\,\text{kA/mm}^2$). The magnetic field shown on the left plot is generated by the j_c distribution from the right plot. The reduction of j_c is due to that field. The magnitude of the field is maximal at the tape edges (the peak field is about 50 mT) and minimal at the tape centers (zero field for the central tape). Note that j_c is even higher than j_{c_0} at the center of the stack due to the field screening in that region. The average critical current reduction is $\approx 11\,\%$ for the outer tapes and $\approx 9\,\%$ for the central one. The total critical current of the stack is $\approx 450\,\text{A}$.

The reduction of the strand critical current due to the self-field is strongly influenced by the number of tapes and the distance between tapes in the stack. The more the tapes in the stack, the higher the reduction (see dedicated experimental studies in [44]). For low field applications, such as superconducting power cables, the stacked-tape design is less suitable, especially if compared with the CORC design. As illustrated in figure 3.7, the magnetic field is directed along the tape face in the CORC design, while in the stacked-tape and Roebel designs the perpendicular component is present at the edges of the stacks (see 3D sketches of the cable concepts in figure 2.6). The reduction of the critical current as a function of the total tape width in the cross-section is summarized in figure 3.8. The average retention of the critical current for the 16-tape SuperPower strands (measured on 20 samples at 77 K, see section 4.4.3) is $66 \pm 2\,\%$. Since the self-field effect is inevitable, the stack of tapes should be preferably used in high field applications.
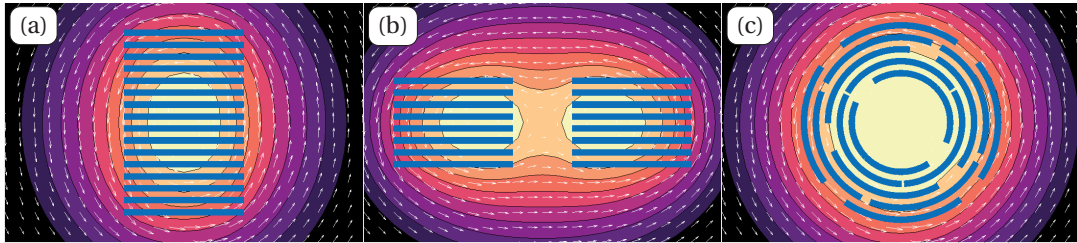
Figure 3.7: Illustration of the self-field generated in the stacked-tape (a), Roebel (b) and CORC (c) design (simplified 2-D analysis).

Figure 3.8: Reduction of the critical current due to the self-field effect as a function of total tape width in the cross-section of the various cable designs: 4 mm and 3 mm wide tapes are used for the stacked-tape and CORC designs, 5 mm – for the Roebel design.

3.4 DC performance at high field

High field – low temperature tests have been carried out at KIT with the non-twisted SuperPower 16-tape strand and the SuperOx 16-tape strand, which was twisted at $h = 320\,\text{mm}$ before soldering. The strands are made of 4 mm-wide tapes and 6.2 mm diameter copper profiles. The measurements of the SuperPower sample (performed in November'13) are the first high field tests of the strand aiming to demonstrate the feasibility of the proposed conductor design for fusion. The total length of the samples is 1160 mm. The terminals – two copper blocks with a semicircular groove – were soldered over 160 mm length at both ends of the samples.

The electric field developed in the SuperPower sample was measured by three pairs of voltage taps over 15 cm, 30 cm and 50 cm centered around a high field zone of the FBI (F force, B magnetic field, I current) test facility [45]. The external magnetic field, which has 3 % homogeneity over $\approx 10\,\text{cm}$ length, was applied perpendicular to the tape faces of the sample. For the SuperOx sample the distance between the voltage taps is 16 cm and 32 cm, i.e. respectively corresponding to half and the full twist-pitch. Note that the distribution of the local critical current along the length of the twisted strand in a background magnetic field is strongly non-uniform, with a period corresponding to the half twist-pitch. However, it is expected that the angular dependence of the strand I_c measured over at least half the twist-pitch is negligible.

In order to assess the critical current of the strands, the results of the short tape measurements in a perpendicular field at 12 T/4.2 K have been used: $I_c \approx 180\,\text{A}$ for the SuperPower tapes (M4-152-2FS production batch), $I_c \approx 195\,\text{A}$ for the SuperOx tapes (2014-4-L production batch). The field and temperature dependence of these values is taken according to the $j_c(B, T)$ scaling laws presented in appendix A.1. In order to match the measured tape performance at 12 T/4.2 T, the prefactor A is set to $1840\,\text{kA/mm}^2$ and $1853\,\text{kA/mm}^2$ for the SuperPower and SuperOx tapes. At high magnetic field, the self-field effect in the stack is negligible and the critical current of the strand can be evaluated simply as $j_c(B, T) \cdot S_{\text{sc}}$, where the total cross-section of the superconductor is $S_{\text{sc}} = 0.064\,\text{mm}^2$ for both strands.

The obtained data are summarized for both strands in figure 3.9: the round markers show the FBI test results, the solid lines the expected performance of the samples. At 12 T, 4.2 K the critical current of the two strands is around 3 kA, resulting in a transverse Lorentz load of 36 kN/m. No evident effects due to the twisting of the SuperOx sample have been observed. Although the mechanical strains due to the twisting and variation of the local critical current along the length are present in the SuperOx sample, the I_c performance behaves according to the simple scaling of the tape properties in the perpendicular field.

High n-values were also obtained from the measured voltage–current transitions, from 30 to 40 for the SuperPower strand and around 30 for the SuperOx one at 4.2 K.
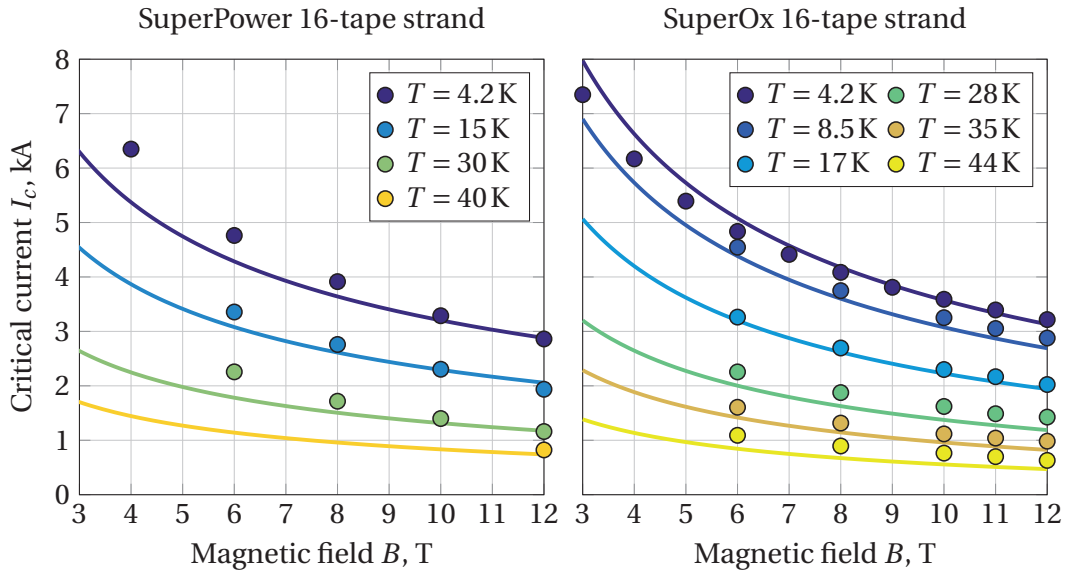
Figure 3.9: Field and temperature dependence of the critical current for the SuperPower and SuperOx 16-tape strands: round markers are for the values measured in the FBI test facility, solid lines – expected performance of the strand.

At higher temperatures, the n-values gradually decrease. The dependence of the n-values on the field strength is very weak. Full details about the test results are given in [35].

The agreement between the experimental and numerical results at 12 T, 4.2 K, conditions in which the short tape measurements have been carried out to deduce the prefactor A for the scaling law, and the high values of n suggest that the tape performance is fully retained in the strands. Minor deviations between the measured and predicted I_c of the strands at high temperature and at low magnetic field is most likely due to a low accuracy of the scaling laws in these regions.

3.5 Effect of embedded defects

An important issue remaining in the HTS tape technology is that it is very likely that for a long piece of tape (hundreds of meters), regions with relatively low critical current ('defects') will exist. As the tape manufacturers usually provide the distribution of the critical current along the tape length, it can be decided before the tapes are used in the cable manufacturing whether the presence of the defective regions is permissible or not. When it is necessary to cut the defective regions out of the tape, the obtained segments of the tape with rather uniform I_c distribution might be too short to use in the cable manufacturing. On the other hand, those defects which are present in the
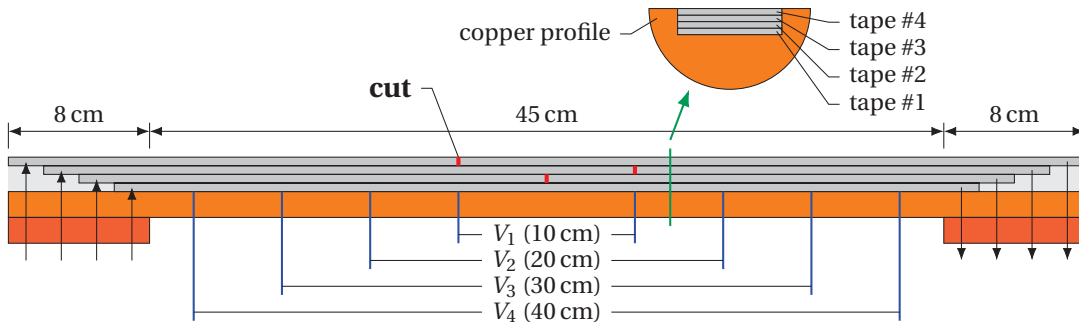
Figure 3.10: Schematic of the experimental assembly of the tapes with the embedded defects.

cable are in general a limiting factor in reaching the full operating current and are also potentially weak points with respect to the quench initiation.

As it will be shown in this section, if the defects are eventually present in the strand by any reason, the soldering of the tapes and copper profiles strongly mitigates the influence of the defects on the overall I_c performance of the strand.

For simplicity, only a limit case of the defect – a tape cut – is investigated in this section. In this case the current in the cut tape is forced to bypass the defect through the surrounding materials. This process can be performed in the strand at a low voltage due to the low values of the inter-tape resistance (see section 3.2).

The measurements have been carried out using the assembly shown in figure 3.10. First, the single tape of 4 mm width without the defects was soldered into the copper profile. Then, the second tape that is cut in the middle was soldered on top of the first one. The third and fourth tapes that have the defects shifted to the left and right by 5 cm from the center were assembled the similar way. The length of the tapes is gradually increased such that at both terminals of the stack a staggered type connection with the current leads is formed. The superconducting side of each tape faces the copper block.

After the assembly of every next tape, the voltage–current transitions measured on the four regions – V_1, V_2, V_3 and V_4 in figure 3.10 – were measured in a liquid nitrogen bath. The results of the measurements are shown in figure 3.11. When only the first tape was soldered, the electric field measured at each of the four regions was practically identical, resulting in 168±1 A of the critical current. When the defects were introduced in the measurements, the same total voltage was measured at each of the regions. As a result, the electric field becomes effectively lower for the longer regions.

The critical current and n-value of the transitions were obtained using the threshold value $E_c = 1\,\mu\text{V/cm}$. The results are summarized in figure 3.12. The critical current increases slowly with the number of tapes despite the presence of defects. Nonet-
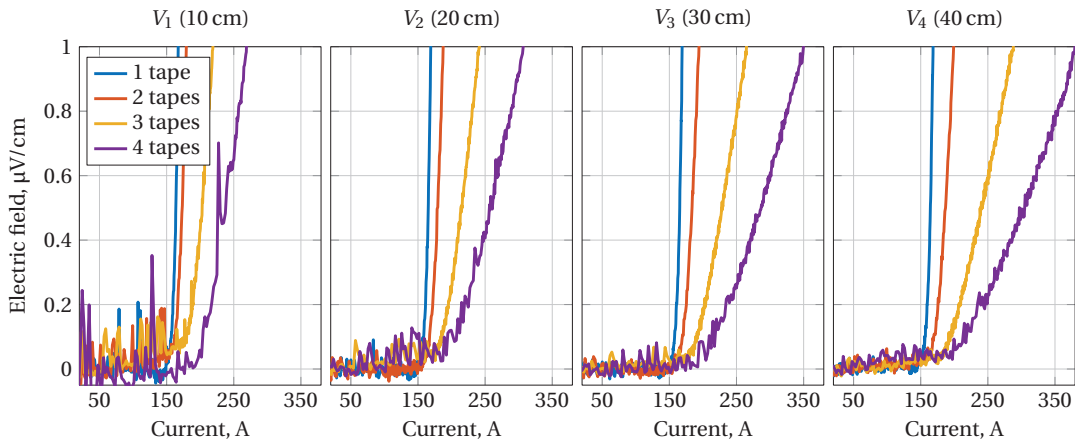
Figure 3.11: The voltage–current transitions measured at 77 K on the four regions of the assembly with the various number of tapes.
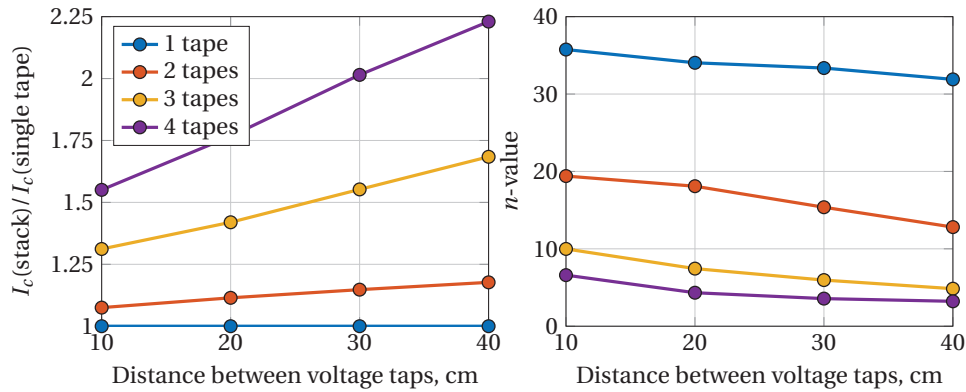
Figure 3.12: Critical current and n-value at 77 K as a function of the distance between the voltage taps for the various number of tapes in the assembly.

heless, a reduced steepness of the transition results in a stable thermal behaviour at overloading currents with respect to I_c of the first tape, which is the only one without defects.

As a result, in a more realistic situation when the defects have only the partially reduced critical current, the overall I_c performance of the strand is defined by the sum of the tape critical currents if the tapes and copper profiles are soldered together. The measured I_c performance of the strand can even overestimate the sum of the individual tape critical currents if the transition exhibits a low steepness, suggesting that the redistribution of currents is present. Consequently, non-uniformity of the tape I_c along the length is not a critical point for the strand, especially from a point of view of the quench protection. Note that if the strand components are not soldered and the uniform current distribution is established between the tapes, the total critical

current will be driven by the worst tape. In addition, the situation when the tapes are burnt one after another, because the overloading current cannot be efficiently redistributed between them, may occur.

3.6 Twisting of the strand

The twisting of the single tape and of the stack of tapes was studied in details in [26]. The expression for the axial strain along the tape's cross-section in the stack of tapes can be written as:

$$\varepsilon_{\text{twisting}} = \frac{1}{2}\left(\frac{2\pi}{h}\right)^2 \left(u^2 + v^2\right) - \varepsilon_0 \tag{3.3}$$

where (u, v) are the coordinates of the cross section, u is along the wide side of the tape: $-w/2 \leq u \leq w/2$, and they should not be confused with the notations conventionally used for displacements in continuum mechanics. The relaxation strain ε_0 represents the 'sliding effect' during the twisting: tapes have a mechanical ability to release a net longitudinal force in the cross-section. Mathematically, the axial force resulting from the sliding effect can be expressed as:

$$F_{\text{axial}} = \int_S E(u, v)\varepsilon_{\text{twisting}}(u, v)\,\mathrm{d}u\,\mathrm{d}v = 0 \tag{3.4}$$

where E is the Young's modulus and S the cross-section of the relaxation region.

When soldering is used, there are two options to manufacture the stack or strand: first twist – then solder (TS) or first solder – then twist (ST) [36]. When the tapes in the stack are twisted before soldering, the relaxation regions are the cross-sections of each individual tape in the stack. The corresponding relaxation strain reads as $\varepsilon_0^{\text{TS}} = 1/2\left(2\pi/h\right)^2\left(w^2/12 + v_k^2\right)$, where v_k is the vertical position of the k-th tape in the stack (the finite thickness of the tape can be neglected). Substituting this expression in (3.3), the resulting strain in a non-soldered twisted stack (TS option) can be written as:

$$\varepsilon_{\text{twisting}}^{\text{TS}} = \frac{1}{2}\left(\frac{2\pi}{h}\right)^2 \left(u^2 - \frac{w^2}{12}\right) \tag{3.5}$$

The central region of the tapes is under compression: $\varepsilon < 0$ for $|u| < \frac{w}{2\sqrt{3}}$. The tape edges are under tension: $\varepsilon > 0$ for $\frac{w}{2\sqrt{3}} < |u| \leq \frac{w}{2}$. Since there is no dependence over the vertical coordinate v, this result suggests that in terms of axial strain the non-soldered stack behaves during the twisting as a single tape.

In contrast with the TS option, the ST option has an unfavorable effect on the strain accumulation: the region of relaxation is the full cross-section of the stack or strand. The soldered stack can be considered in the calculation as a combination of two materials: HTS tapes and solder, while for the strand the copper profiles represent a

third domain. Using the axial strain approach, the relaxation strain for the ST stack and ST strand is obtained from (3.3) and (3.4):

$$\varepsilon_0^{\text{ST stack}} = \frac{E_1 I_1 + E_2 I_2}{E_1 S_1 + E_2 S_2}$$

$$\varepsilon_0^{\text{ST strand}} = \frac{E_1 I_1 + E_2 I_2 + E_3 I_3}{E_1 S_1 + E_2 S_2 + E_3 S_3} \tag{3.6}$$

$$I_j = \frac{1}{2} \left(\frac{2\pi}{h} \right)^2 \int_{S_j} \left(u^2 + v^2 \right) \mathrm{d}u\,\mathrm{d}v$$

where S_j is the cross-section of the j-th domain: 1 – HTS tapes, 2 – solder, 3 – copper profiles. The Young's moduli for the materials at 77 K are set to $E_1 = 157\,\text{GPa}$ [46], $E_2 = 45\,\text{GPa}$ [47], $E_3 = 120\,\text{GPa}$ [48].

Once the dependence of the critical current density over the axial strain $j_c(\varepsilon)$ is defined, one can finally calculate reduction of the critical current of the n_t-tape stack. As there is no variation of the strain along the stack length, a simple parallel connection of superconductors with varying j_c can be considered (see appendix A.2.1):

$$\frac{I_c(h)}{I_{c_0}} = \frac{1}{n_t} \sum_{k=1}^{n_t} \frac{1}{w} \int_{-w/2}^{w/2} \frac{j_c(\varepsilon_{\text{twisting}}(u, v_k))}{j_{c_0}} \, \mathrm{d}u \tag{3.7}$$

where $I_{c_0} = n_t w d_{\text{sc}} j_{c_0}$ is the initial critical current of the stack, i.e. $I_{c_0} = I_c(h = \infty)$.

The I_c/I_{c_0} values calculated for the single tape, TS stack, TS strand, ST stack and ST strand ($w = 4\,\text{mm}$, $t = 2\,\text{mm}$, $n = 13$, $D = 6.2\,\text{mm}$) are shown as a function of the twist-pitch h in the left plot of figure 3.13. The $j_c(\varepsilon)$ dependence is that of the SuperPower tapes [26]. Note that in the axial strain approach, the curves for the single tape, TS stack and TS strand are identical. A degradation of the critical current for the ST strand starts at higher values of h due to an increased compressive strain in the tapes. In the ST stack the increase of the axial strains is small and does not significantly reduce the critical current if compared with the single tape.

The degradation of the critical current of the ST stack and ST strand was also studied experimentally using the SuperPower SCS4050 tapes. A straight 13-tape soldered stack and strand were prepared for the twisting test. Before assembling the samples, 5 tapes from each sample were measured individually. These tapes were located at the positions #1, 4, 7, 10 and 13 in the stack. The test results are presented in the right plot of figure 3.13. While the calculated reduction of the twisted single tape is in good agreement with the experimental data, the influence of the twist-pitch h obtained for the ST stack and strand is much stronger than that calculated from the axial strain analysis. The green crossed circle refers to the results obtained in the next section: no degradation was observed in the several 15-tape TS strands twisted down to 300 mm twist-pitch (samples A, B, C and D in table 3.1).
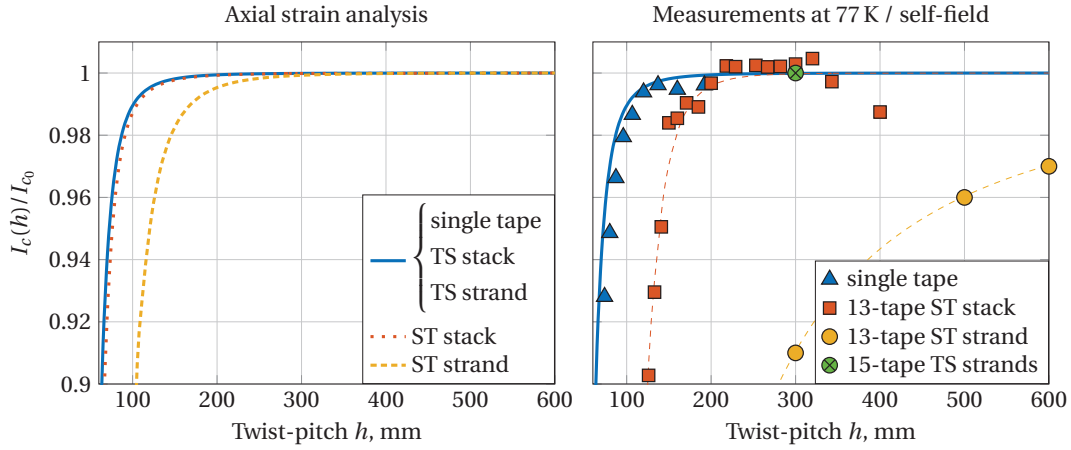
Figure 3.13: Reduction of the critical current as a function of the twist-pitch h. Left: calculation for the single tape, TS stack, TS strand, ST stack and ST strand ($w = 4\,\text{mm}, t = 2\,\text{mm}, n_t = 13, D = 6.2\,\text{mm}$). Right: measurements of the single tape, ST stack, ST and TS strands at 77 K / self-field.

The five initially measured tapes were carefully extracted from the stack and strand at the end of the measurements, at around 10 % of the I_c degradation. For both samples the same 10 % degradation was obtained for the central tape (at the position #7), while the degradation of the outer tapes (#1 and 13) was the smallest: from 2 % to 6 %.

The shear strain is another important component of the strain during the twisting. While the minimum and maximum of the axial strain are at the center and corners of the stack, respectively (according to the strain distribution (3.3)), the shear strain components γ_{uz} and γ_{vz} have their extrema at the middle of the external sides of the stack [49], with the absolute values estimated as $2\pi t/h$ [26]. Corresponding illustration is provided for the top and middle tape in the stack in figure 3.14. Unfortunately, even for the calculated distribution of the shear strains in the stack, the dependence of the critical current density on these components is not available (though 1G and steel laminated 2G tapes were measured at KIT [50]). The shear strain could be at the origin of the difference between the measured and calculated I_c degradation for the ST stack and ST strand. Also, the γ_{vz} component, providing the shear stress between the tape layers, has the highest impact on the central tape of the stack, which can explain the highest degradation measured for the tape #7 in the stack.

From the axial strain analysis it was also obtained that for the relatively low I_c degradation ($\lesssim 1\,\%$), the twist-pitch h_c, at which this degradation is reached, is proportional to the tape width w. For instance, 0.1 % I_c degradation corresponds to $h_c \approx 40w$ for the TS option. More results on this subject is given in [51]. As a confirmation, several TS strands presented in the following sections have no mechanical degradation at twist-pitches down to 300 mm.
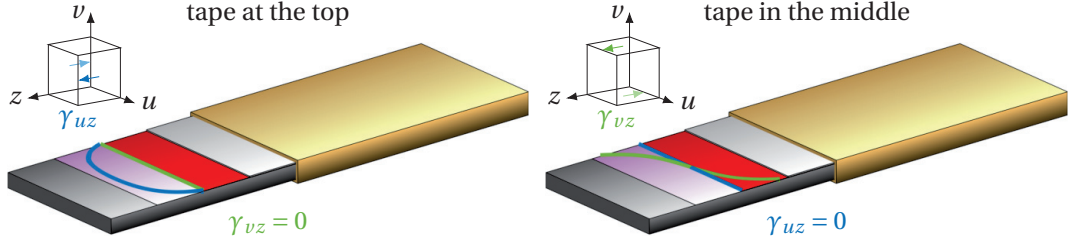
Figure 3.14: Distribution of the shear strains – blue lines for γ_{uz} and green lines for γ_{vz} – for the top (left picture) and central tape in the twisted stack (right picture). The tapes are shown straight since local coordinates (u, v), rotating together with the tape cross-section, are used instead of global (x, y).

3.7 Bending of the strand

Bending of the strands typically occurs during cable manufacturing (due to the transposition requirement) and coil winding. When the twisted strand has a round centerline of radius R (in xy plane), the position of the tapes can be described by the system of coordinates:

$$\begin{cases} x = \left(R + u \cos\left(\frac{2\pi}{h}s\right) + v \sin\left(\frac{2\pi}{h}s\right) \right) \cos\frac{s}{R} \\ y = \left(R + u \cos\left(\frac{2\pi}{h}s\right) + v \sin\left(\frac{2\pi}{h}s\right) \right) \sin\frac{s}{R} \\ z = -u \sin\left(\frac{2\pi}{h}s\right) + v \cos\left(\frac{2\pi}{h}s\right) \end{cases} \tag{3.8}$$

where (u, v) are the coordinates of the cross-section: $-w/2 \leqslant u \leqslant w/2$, $-t/2 \leqslant v \leqslant t/2$, s is the longitudinal coordinate, h is the twist-pitch.

An illustration of equation (3.8) is given in figure 3.15. Depending on the stack orientation, one can define two regions along the stack length: the easy-bending region (EB), where the tape faces are perpendicular to the bending plane, and the hard-bending region (HB), where the tape faces are parallel to the bending plane. $s = h/2 \cdot (k + 1/2)$ for EB and $s = h/2 \cdot k$ for HB, where $k = 0, 1, 2, \ldots$ and so on.

The axial strain can be obtained by definition as $\varepsilon = (\mathrm{d}l - \mathrm{d}s)/\mathrm{d}s - \varepsilon_0$, where $\mathrm{d}l = \sqrt{\mathrm{d}x^2 + \mathrm{d}y^2 + \mathrm{d}z^2}$, ε_0 is due to the sliding effect in the stack discussed in the previous section (net force is released before applying the bending). Assuming that $h, R \gg t, w$, the total axial strain can be simplified to the following expression:

$$\varepsilon_{\text{total}} = \varepsilon_{\text{twisting}} + \varepsilon_{\text{bending}}$$
$$\varepsilon_{\text{bending}} = \frac{u \cos\left(\frac{2\pi}{h}s\right) + v \sin\left(\frac{2\pi}{h}s\right)}{R} \tag{3.9}$$
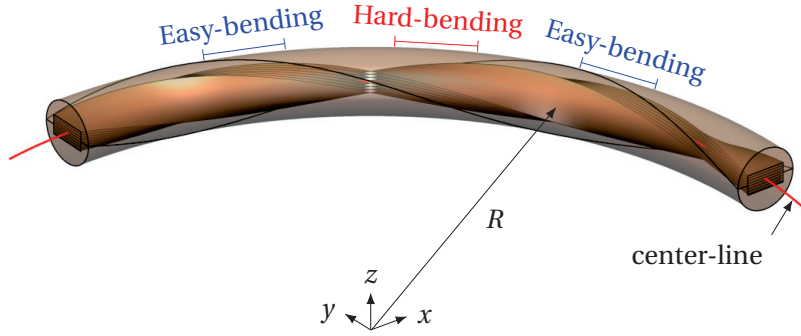
Figure 3.15: Artistic view of the strand bending: position of the tapes is described by equation (3.8).

where $\varepsilon_{\text{twisting}}$ for the first-twisted-then-soldered strands was already obtained in equation (3.5).

The expression (3.9) has a simple structure: the first term expresses the contribution from the twisting and the second that from the bending. The limit cases of $h = \infty$ or $R = \infty$ give the correct results for the bent non-twisted or straight twisted tapes. From (3.9), the distribution of the total axial strain in five selected tapes of the 15-tape strand twisted at $h = 300\,\text{mm}$ and bent at $R = 200\,\text{mm}$ is shown in figure 3.16. Note that at the HB region the strain distribution is highly non-uniform along the width of each tape and is similar between the different tapes, while at the EB region it is the opposite: uniform along the width but varying between the tapes.

Using the $j_c(\varepsilon)$ dependence for the SuperPower SCS4050 tape from [26], the value of the critical current of the strand I_c at the given bending radius R can be obtained from the strain distribution. Since the strain varies along the width and along the length of the tapes, the calculation of I_c must deal with both parallel and serial connection of the superconducting elements. First, the given strand length l is divided into N_s elements and for each one the critical current of the cross-section I_{c_i} is obtained according to appendix A.2.1. Then, the average critical current of the strand I_c is calculated from the N_s serial connected superconducting regions, see appendix A.2.2. In general, for the elements connected in series the n-values are also required in the calculation. These are taken as a function of the reduced critical current density: $n = n_0^{j_c/j_{c0}}$, where $n_0 = 25$. The variation of n_0 was found to have a minor effect on the calculated I_c. The results of the bending model for the SuperPower 4 mm-wide tapes with various parameters of the strand geometry are presented in the left plot of figure 3.17.

In total 8 types of TS strands were studied in the bending test, as presented in table 3.1. The I_c degradation of each strand as a function of bending radius R at 77 K and in self-field is presented in the right plot of figure 3.17. By comparing the calculation and test results for the B and C cases proves that the axial strain is the dominant factor for
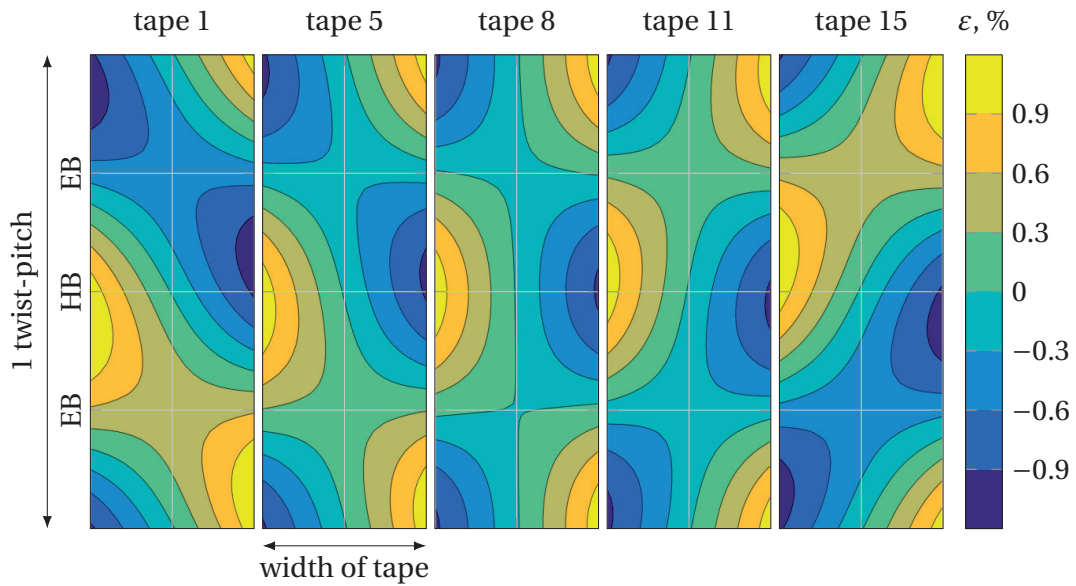
Figure 3.16: Distribution of the axial strain in the 15-tape strand twisted at $h = 300\,\text{mm}$ and bent at $R = 200\,\text{mm}$.

the I_c degradation during the strand bending. Deviations between the calculation and measurements can be explained by the real shape of the strand center-line: unlike a pure circle shape of the strand center-line assumed in the model, the local bending radius of the HB region is higher than that of EB since the HB regions are stiffer than EB. On top of that, EB regions are quite tolerant against the bending since an in-plane tape bending is not present. Consequently, slightly higher I_c values are expected in the measurements. The origin of the high deviation for the F case is not well understood.

Several aspects for the strand geometry and manufacturing procedure can be concluded from the bending test:

1. *Preliminary annealing of the copper profiles*: A vs B.
   The effectively softened copper profiles by annealing (1 hour at 300 °C) provide improved bending properties of the strand (i.e. smaller critical bending radius). The profiles with a lowered yield strength ensure less stress concentration, so the influence of the encasing copper on the bending properties is minimized. More discussion on the copper annealing is given in the next section.

2. *Geometry of the copper profiles*: B vs C vs D.
   In the C and D samples the soldered section between the copper profiles is larger. As a result, no cracks between the profiles of these samples were observed, while for the B sample 'opening' of the profiles happens at around 240 mm. Nevertheless, the relatively complicated fabrication procedure of the D sample and reduced current density of both C and D samples make them less attractive. Higher j_e can

Table 3.1: Main properties of the strands used in the bending test. The samples are first twisted then soldered.

Abbreviation	A	B	C	D	E	F	G	H
Tape's manufacturer	SuperPower						SuperOx	Sumitomo
Cross section								
Tape's width w, mm	4	4	4	4	3	4	4	4.3
Diameter D, mm	6.2	6.2	7	7	6	8	6.2	8
Number of tapes n	15	15	15	15	26	32	15	13
Twist-pitch h, mm	300	300	300	300	240	340	300	400
Profile annealing	No			Yes				
j_e^*, A/mm^2	94	94	74	74	131	121	90	114
Copper area, mm^2	25 (81 %)	25 (81 %)	33 (85 %)	33 (85 %)	22 (79 %)	39 (78 %)	25 (81 %)	33 (66 %)
R_c^{**}, mm	420	180	190	190	205	360	275	920

* Engineering current density at (12 T, 4.2 K); ** Critical bending radius @ 5 % I_c degradation
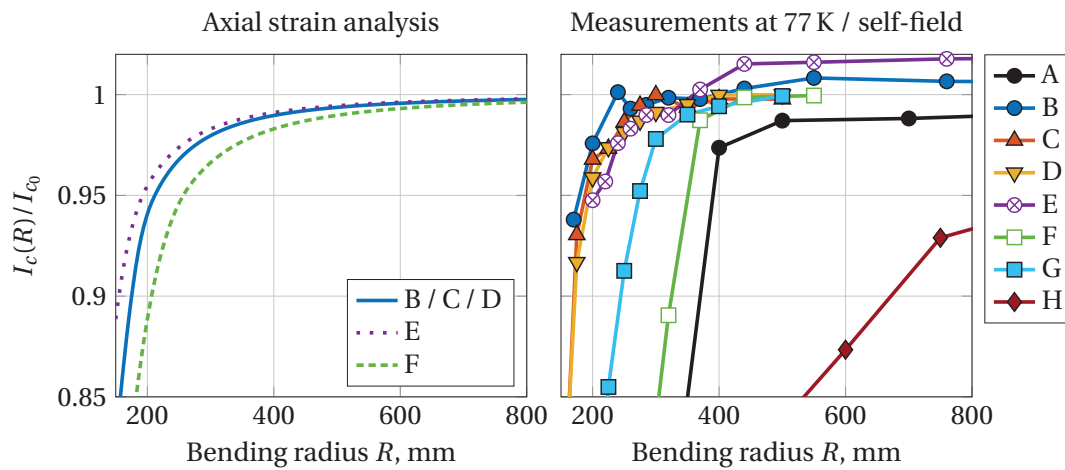
Figure 3.17: Reduction of the strand critical current as a function of the bending radius R. Left: results of the axial strain analysis. Right: measurements at 77 K / self-field. Definition of the strand abbreviations is given in table 3.1.

be achieved with the C and D samples by reducing the diameter, which was chosen as 7 mm only due to the easier fabrication at the laboratory scale.

3. *Effect of the stack aspect ratio*: C vs F.
The current density of the F sample is sufficiently increased, but at the same time, the critical bending radius R_c is almost twice as large compared to the C sample. Even though from the axial strain analysis the F sample is expected to be more sensitive against the bending than the C sample, a large deviation between the measured results is not understood. A compromised solution between the C and F samples might be needed.

4. *Effect of the tape width w*: E vs F.
Both E and F samples have a square stack, the only difference is the tape width (though the twist-pitch for both samples is different, it was chosen conservatively – an influence on the bending properties is not expected). While the current density of the two samples is comparable and noticeably higher than for the other samples, the bending properties of the E sample are far superior due to the narrower tapes. So far, the E-type geometry is the most balanced and favourable in electro-mechanical terms.

5. *Manufacturer of REBCO tapes*: B vs G.
The difference obtained between the B (SuperPower) and G (SuperOx) samples corresponds to the difference in the critical strain of various REBCO coated conductors [24]. Though R_c of the SuperOx strand is higher, it is still applicable for construction of relevant high current cable based on such strands.

6. *REBCO vs Bi2223 tapes*: F vs H.
The H sample, manufactured with 1G Sumitomo H-type tapes, is the weakest in terms of bending: $R_c = 920\,\mathrm{mm}$. This value, representing a relatively low critical strain of the 1G tapes itself, is too high to allow construction of high current cables. Another strand design must be considered for the application of the BISCCO tapes in fusion.

As a result of the bending tests, the configuration E was selected for further electromechanical investigations, which are discussed below in this chapter.

3.8 Transverse loading

The strands in the cable are subjected to the transverse mechanical load due to the acting Lorentz force. This is a typical 'plane strain' problem of continuum mechanics. With the assumption that $\varepsilon_z = \gamma_{xz} = \gamma_{yz} = 0$, the in-plane stress-strain elastic relation

simplifies to the following form [52]:

$$
\begin{bmatrix} \sigma_x \\ \sigma_y \\ \tau_{xy} \end{bmatrix} = \frac{E}{(1+\nu)(1-2\nu)} \begin{pmatrix} 1-\nu & \nu & 0 \\ \nu & 1-\nu & 0 \\ 0 & 0 & {}^{1}\!/_{2}-\nu \end{pmatrix} \begin{bmatrix} \varepsilon_x \\ \varepsilon_y \\ \gamma_{xy} \end{bmatrix}
\tag{3.10}
$$

where $(\sigma_x, \sigma_y, \tau_{xy})$ and $(\varepsilon_x, \varepsilon_y, \gamma_{xy})$ are the stress and strain components, E and ν are the Young's modulus and Poisson's ratio of the material domain. The strand is simply considered as a combination of two domains: copper (c-domain) and 'solid' stack of tapes (s-domain). The Poisson's ratio is taken as 0.34 for the c-domain and 0.3 for the s-domain. Three cases corresponding to the geometry of the A, G and E samples (see table 3.1) have been studied in the plane strain FEM model using MATLAB PDE Toolbox.

The effect of the annealing on the stress-strain curve of the copper is shown in figure 3.18 (data are adapted from [48, 53, 54]). While the Young modulus is almost the same for both the annealed and cold drawn copper, the yield stress σ_y is much lower after the annealing: at 76 K it drops from $\approx 380\,\text{MPa}$ to $\approx 60\,\text{MPa}$ (see the intersections of the curves in the left plot with the thin grey line). As can be seen from the right plot, the annealed copper is also more ductile than the cold drawn. The materials become slightly 'harder' (i.e. higher stress is needed for the same strain) when the temperature is decreased from 76 K to 4 K.

For consistency, equation (3.10) is used also to address the plasticity effects, assuming that the presented stress-strain curves of copper can be introduced through the effective Young's modulus for the c-domain, defined as $E_c(\sigma) = \sigma/\varepsilon(\sigma)$. The blue solid curve in 3.18 is taken for the c-domain of sample A, the red solid curve for samples G and E. At relatively low stress, $E_c(\sigma < \sigma_y) = 120\,\text{GPa}$. At high stress, E_c drops very fast below 10 GPa.

The Young's modulus of the s-domain was obtained according to the mixture rule: $E_s = E_{\text{tape}} n_t d_t / t + E_{\text{solder}} (1 - n_t d_t / t)$, where $E_{\text{tape}} = 157\,\text{GPa}$ [46], $E_{\text{solder}} = 45\,\text{GPa}$ [47], n_t is the number of tapes in the stack, d_t is the thickness of tape and t is the height of the strand slot. The mechanical anisotropy and plasticity effects in the s-domain are not addressed in this calculation.

The solution of the problem is a distribution of horizontal and vertical displacements $(u(x, y), v(x, y))$, with the stress and strain components being spatial derivatives of the displacements over specific coordinates. In order to obtain the I_c degradation of the strand, the j_c dependence over the parallel and perpendicular (to the wide side of the tape) stress of the single tape would be needed, but this information is not available. Therefore, considering only the mechanical part of the problem, the in-plane principal stresses (σ_1, σ_2) and the longitudinal stress $\sigma_3 = \nu(\sigma_1 + \sigma_2)$ are combined in a single effective measure, the von Mises stress σ_v, which has the following definition in the
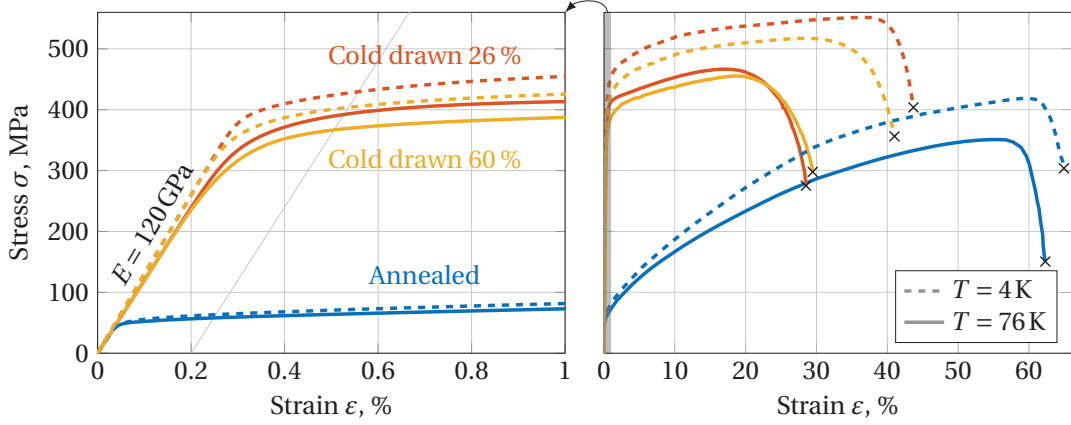
Figure 3.18: Comparison of the stress-strain curves for the annealed and cold drawn copper at 4 K and 76 K. In the left plot the curves are shown in the strain range from 0 % to 1 %, in the right plot – from zero till the fracture points (cross symbols).

'plane strain' case:

$$\sigma_v = \sqrt{\left(\sigma_1^2 + \sigma_2^2\right)\left(v^2 - v + 1\right) + \sigma_1 \sigma_2 \left(2v^2 - 2v - 1\right)} \tag{3.11}$$

The von Mises stress is used to have a scalar description of the mechanical state and also as the input argument for the effective Young's modulus of the copper E_s.

The transverse loading is applied as an external contact force F that allows us to define the midplane pressure as $p_{\text{midplane}} = F/(lD)$, where D is the strand diameter and l the longitudinal length. The loading will be studied in the pressure range from 0 to 100 MPa, meaning that the cold drawn copper will remain in the elastic regime where the problem is linear and the absolute values of the stress are proportional to p_{midplane}.

In the case of annealed copper, the plastic regime in the c-domain is assessed similarly to the calculation of the self-field effect (see section 3.3). Initially E_s is calculated at zero stress. Then, after the problem is solved, E_s is recalculated using the obtained σ_v distribution. After several iterations, the E_s and σ_v distributions become consistent. Although this method allows assessing the plastic deformations, a more complex algorithm is required if unloading of the material is of interest due to a hysteresis stress-strain behaviour in the material once it enters the plastic region (see [55, 56] for further reading).

By changing the angle between the c-axis and the direction of the applied force (see figure 3.19), the anisotropy of the strand mechanical properties can be studied. Three values of α were analysed in the FEM model and measurements: 0° (least loaded case), 60° (potentially dangerous case due to the possible shear breakage), 90° (most loaded
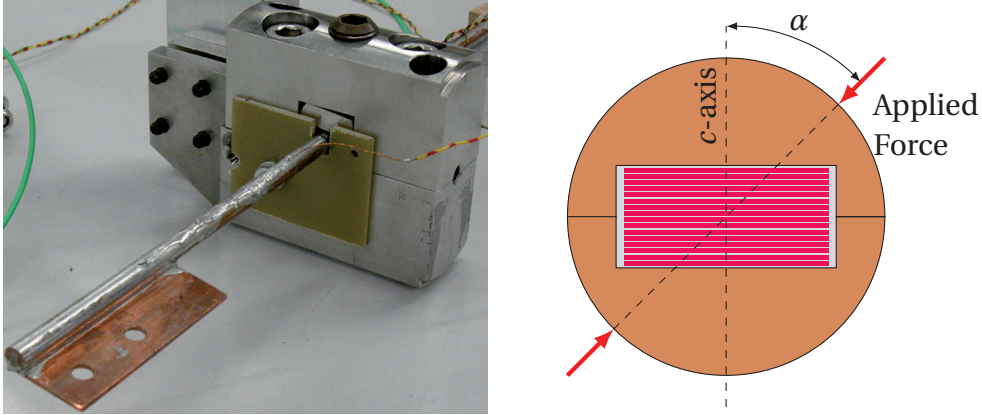
**Figure 3.19:** Left: experimental setup. Right: definition of the angle of orientation α.
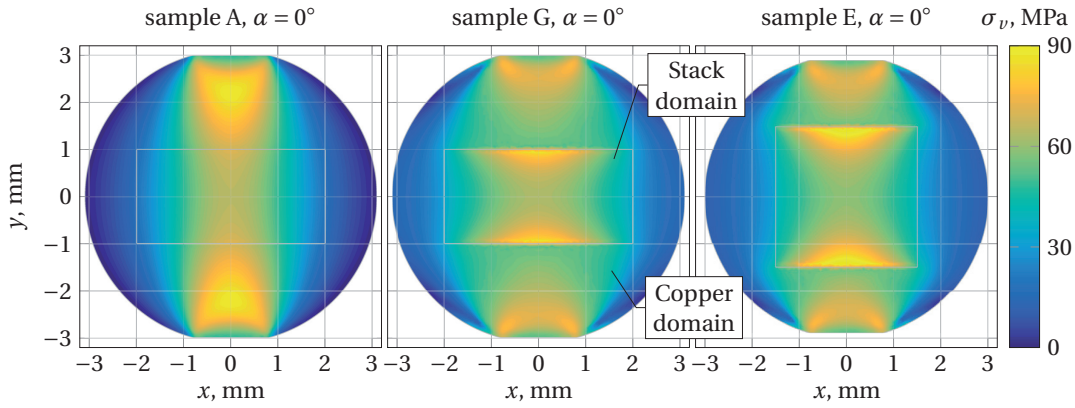
Figure 3.20: Calculated distribution of the von Mises stress σ_v for the A, G and E samples (see table 3.1) at $p_{\text{midplane}} = 30\,\text{MPa}$ and $\alpha = 0°$.

case).

As an example, the solution of the model in terms of the von Mises stress for the A, G and E samples (see table 3.1) at $p_{\text{midplane}} = 30\,\text{MPa}$ is given in figure 3.20. Note the higher values of σ_v in the stack domain in the annealed copper case. Focusing the attention on the s-domain, a statistical approach was applied to the distribution of the von Mises stress in order to have a clearer interpretation and comparison with the model results. Let us define a cumulative area function (CAF) for the given σ_v in the s-domain as a relative area of the stack that is subject to the von Mises stress less than σ_v (see also [57]). Similar to the cumulative distribution function in statistics, the CAF for the stack cross-section S can be written as:

$$\text{CAF}\left(\sigma_v\right) = \frac{1}{S} \int\limits_{\sigma'_v < \sigma_v} \mathrm{d}S' \tag{3.12}$$
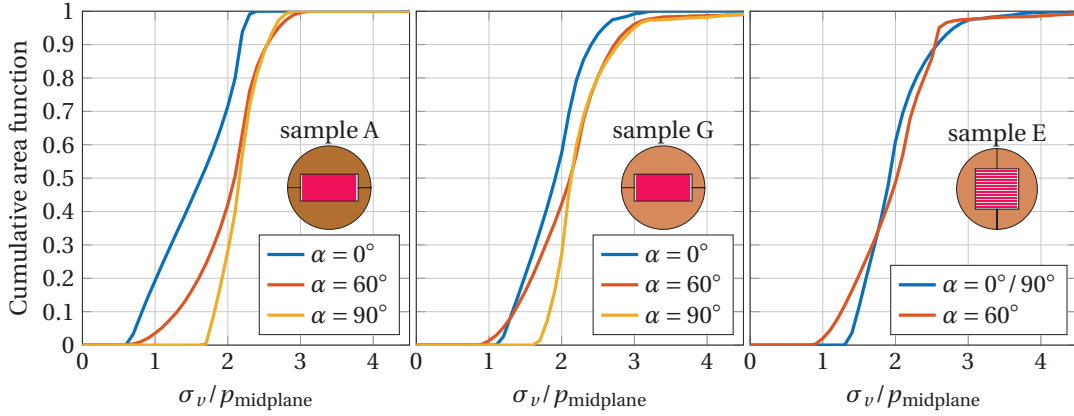
Figure 3.21: CAF of the s-domain for the A, G and E samples (see table 3.1) at $p_{\mathrm{midplane}} = 30\,\mathrm{MPa}$ as a function of normalised von Mises stress at various angles of orientation α.

The CAF is presented in figure 3.21 for the A, G and E samples at $p_{\mathrm{midplane}} = 30\,\mathrm{MPa}$ and three fixed angles of orientation α. A high mechanical anisotropy is present in the A case, i.e. the curves at 0°, 60° and 90° are far apart. Note that the results of the E case at 0° and 90° are identical. Tails at high $\sigma_v / p_{\mathrm{midplane}}$ ratio of the yellow ($\alpha = 90°$) and red ($\alpha = 60°$) curves indicate a presence of dangerous regions in the s-domain, which can be at the origin of the strand breakage. The shift to the right of the G-sample curves relatively to the ones of the sample A is an effect of the copper profile annealing: 'softer' profiles lead to higher stress concentration in the stack.

An average von Mises stress $\langle \sigma_v \rangle$ over the area of the s-domain S is calculated as follows:

$$\langle \sigma_v \rangle = \frac{1}{S} \int_S \sigma_v \, \mathrm{d}S = \int_0^{\sigma_{v\mathrm{max}}} \left(1 - \mathrm{CAF}\left(\sigma_v \right) \right) \mathrm{d}\sigma_v \tag{3.13}$$

$\langle \sigma_v \rangle$ as a function of α and p_{midplane} is given in figure 3.22: the annealing of the copper profiles (A vs G) increases the stress in the s-domain (but also improves the bending properties of the strand, see previous section). A modified geometry of the copper profiles (G vs E) eliminates the anisotropy of the mechanical properties. As long as the twisted geometry of the strand results in all possible angles of orientation in the cable, a reduction of the maximal average von Mises stress $\langle \sigma_v \rangle$ is the main advantage of sample E. σ_v deviates from the linear dependence over p_{midplane} in case of the annealed profiles starting from $\approx 20\,\mathrm{MPa}$.

An experimental study of the strand I_c degradation under the transverse pressure was performed on the three samples manufactured according to the parameters' set of the A, G and E samples of table 3.1, with only one difference: the sample A was non-twisted, while the samples G and E were twisted at $h = 300\,\mathrm{mm}$ and $h = 280\,\mathrm{mm}$,
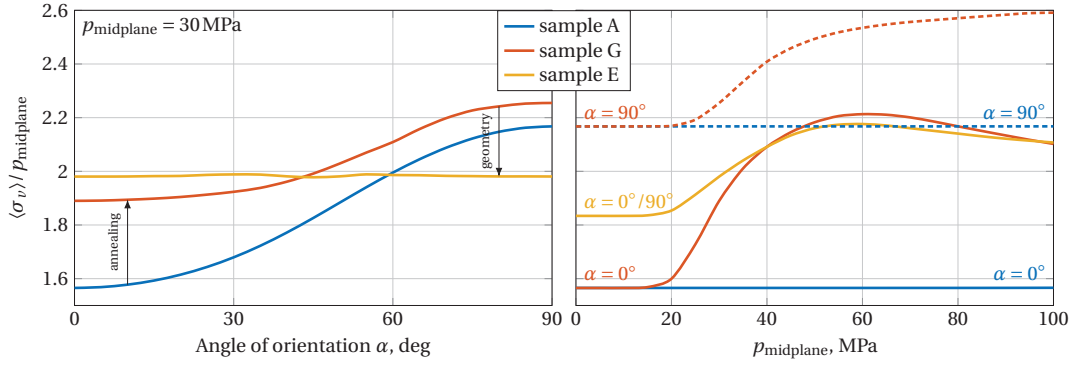
Figure 3.22: Average von Mises stress normalized by p_{midplane} as a function of α (left plot) and p_{midplane} (right plot) for the A, G and E samples (see table 3.1).

respectively. Twisting of the samples allows one to change α in the test simply by longitudinal shift, while in the non-twisted case the strand must also be rotated. Short regions of each sample, corresponding to the 0°, 60° and 90° orientations (variation due to the twisting is negligible), were subjected to the transverse force in a liquid nitrogen bath. The force was applied by tightening the bolt, which transfers the load to the steel anvil located on top of the strand (see figure 3.19). A piezoelectric sensor, located at the bottom of the strand, was used to measure the applied force. The midplane pressure p_{midplane} is obtained as the measured force divided by the diameter of the strand D and the length of the anvil l. Note that $l \sim D$ in the measurements, thus the main assumption of the plane strain analysis, that $l \gg D$, is not fulfilled.

A summary of the test results is presented in figure 3.23. The measured I_c degradation of the three strands qualitatively follows the results of the FEM model discussed above. The A and G samples are very tolerant to the applied force at 0° (up to 110 MPa). At 60° both samples have an abrupt I_c degradation in the region of 60 MPa, which corresponds to fracture effects in the strand (may result in cracks between copper profiles). Finally, the I_c degradation of these samples at 90° sets the operational limits: for 2 % I_c degradation 30 MPa for A and 25 MPa for G. Since the SuperOx tapes have slightly lower values of the critical strain than the SuperPower tapes [24], the sample B could have higher operational limit than the G one (see table 3.1).

In contrast with the A and G samples, measured curves for the E sample are very similar at 0° and 90°, while the degradation at 60° was obtained earlier. Fracture effects were not observed in this case. It is not clear why at 0° the degradation starts already at ≈ 70 MPa, since a free-standing tape is extremely tolerant against the compression along the c-axis, showing no degradation up to 300 MPa [46]. Presumably, edges of the profiles near the centers of the top and bottom tapes in the strand can provide an increased stress concentration. Operational limit for 2 % I_c degradation can be set as ≈ 40 MPa.
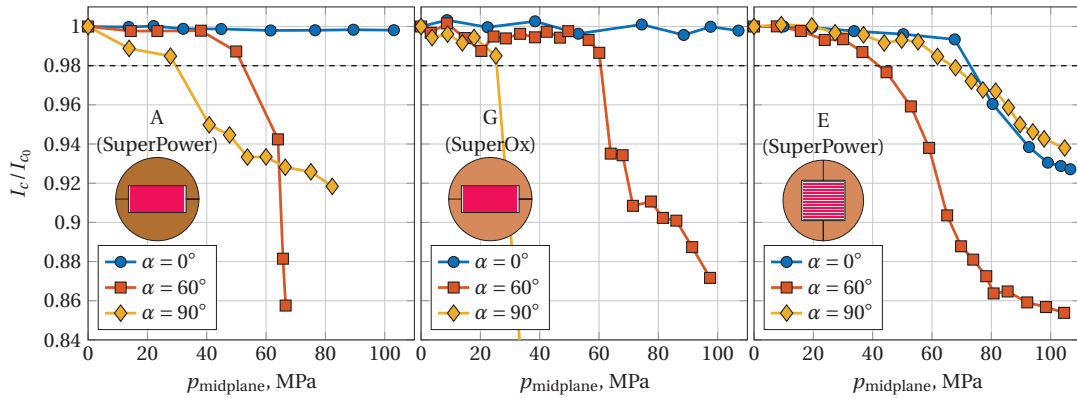
Figure 3.23: Measured I_c degradation of the A, G and E samples (see table 3.1) as a function of $p_{midplane}$ at various angles of orientation α (77 K, self-field).

If the strands are used in the Rutherford-type cable representing a flat two layered assembly of strands, midplane pressure can be estimated as $p_{midplane} \approx 2IB/D$ (see details in section 4.2.2). The strand carrying 2.5 kA at 12 T will be subjected to roughly 10 MPa making the proposed strand design appropriate for this cable option.

3.9 Effect of cyclic transverse load

This section addresses the potential degradation of I_c at relatively low transverse loads applied in a cyclic manner, i.e. fatigue failure. Although the importance of these phenomena was realized only after the measurements of the full-size cable prototypes (see next chapter), this study is a natural continuation of the transverse loading investigation discussed in the previous section. Therefore the reader should not be confused that the results obtained in this section were not addressed in the first cable prototypes.

The original press assembly that was used in the transverse load tests of the strands (shown in figure 3.19) was upgraded for an automatic control, see figure 3.24. The signal from the piezo sensor is used to control the DC motor. A worm gear installed on the top plate of fiberglass support serves as a reduction drive (20:1) for the motor and prevents release of the applied force at a system idle.
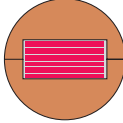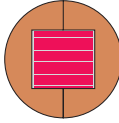
During the system operation, the strand in the press is immersed in a liquid nitrogen bath. In order to reduce heat transfer from the cooling region of the system the steel shaft is composed of three pieces with a hollow part in the center. An external force is applied in a cyclic manner from 0 to the maximum value F corresponding to the pressure $p_{max} = F/(lD)$, where $l = 15$ mm is the length of the anvil. Note that the actual body force acting on strands in the cable is simulated by the contact force
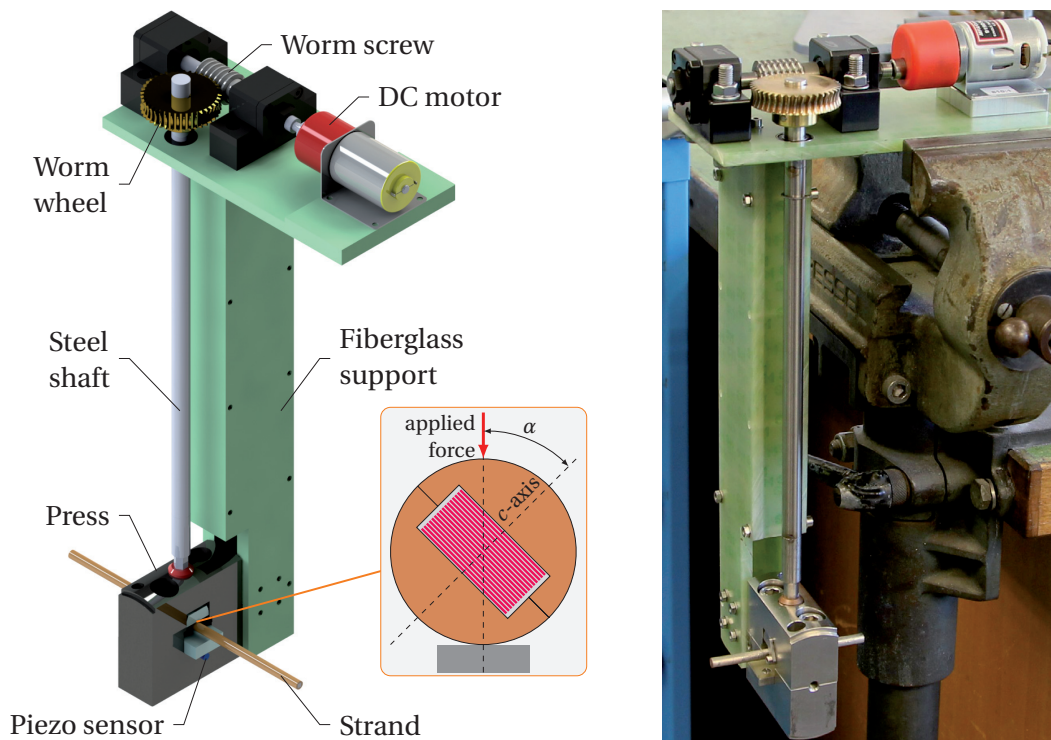
Figure 3.24: Experimental setup for the cyclic transverse load test at 77 K: left – CAD drawing; right – photograph.

Table 3.2: Parameters of strands used for the sample manufacturing.

Tape's manufacturer	SuperOx	SuperPower
Cross-section		
Width of tape w, mm	4	3
Thickness of tape d_t, μm	110	93
Number of tapes n	16	26
Diameter D, mm	6.2	6
Slot width/height, mm	4.3/2	3.3/3
Strand I_c at 77 K/sf, A	≈ 1600	≈ 1000

between the strand and anvil.

The two types of strand that have been selected for the cyclic load tests are presented in table 3.2. The SuperOx strands correspond to those used in the 60 kA cable prototype and aimed to reproduce the fatigue properties obtained during the cable measurements (see 4.6.4). The SuperPower strand composed of 3 mm-wide tapes has demonstrated promising results in the bending and transverse load tests and was selected for the measurements to further validate as a possible candidate for the next cable prototype.

In total six strands have been manufactured: 3 SuperOx and 3 SuperPower. One of the SuperPower strands has non-annealed copper profiles, while the other samples were manufactured with the ones preliminary annealed at 300 °C. This strongly reduces the yield strength of copper. Aiming at better reproducing the mechanical state in the cable, two samples were also bent before the cyclic loading at radius ≈ 360 mm, which corresponds to strand bending around the cable edge in the prototypes (as discussed in 4.4.1). Each sample is about 30 cm long and contains 4 regions with the voltage taps at a distance 2 cm to be tested in the press (see figure 3.25). The transverse load was applied on the region from 0 to p_{max} up to 1000 cycles, with intermediate measurements of the strand I_c as a function of number of cycles n_c at zero and maximum load p_{max}.

The accuracy for the applied load p_{max} has been set conservatively to ±1 MPa in order to increase the frequency of operation. After tuning of the PID control, the system can operate up to 6 cycles per minute, which allows to perform a full cycling test on the strand region within one day. The maximum force that can be transmitted in the assembly is ≈ 10 kN, what corresponds to $p_{max} \approx 110$ MPa.

The obtained test results are normalized to the critical current of the strand measured after the first load cycle $I_c(1)$ (see typical values in table 3.2). The data are summarized in figure 3.26 (estimated error bar is $\approx 0.5\%$).
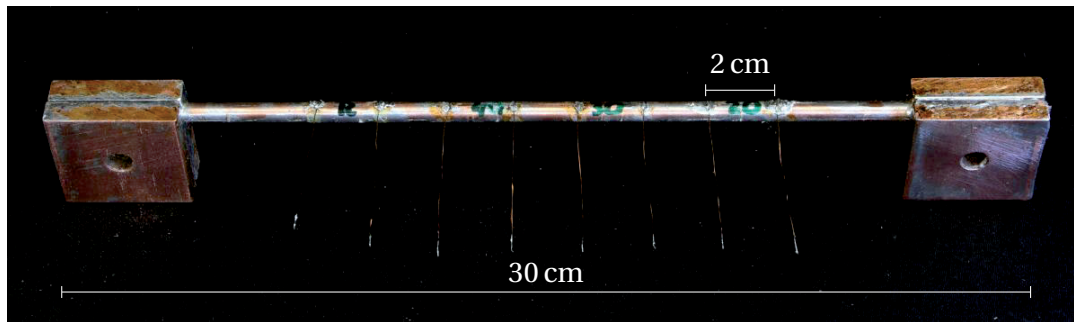
Figure 3.25: Photo of one of the strands used in the measurements.

A degradation of the strand performance during the cyclic loading has been observed. Similar results have been obtained for the different load directions studied on the straight SuperOx strands (0° vs 90°). Applied bending at 360 mm radius on the SuperOx strand does not cause weakening of the fatigue properties for the cyclic load at 20 MPa and 30 MPa, but at 40 MPa the strand performance degrades by 5 % already at 800 cycles. Nevertheless, the I_c evolution of the SuperOx cable prototype during the cycling test (see section 4.6.4) was not reproduced in the performed measurements of the SuperOx strands. In addition, there is no data correlation for the different pressures. The loading at 20 MPa results typically in the higher degradation than at 30 MPa. Possible reasons for these issues will be addressed later in this section.

The performance of the SuperPower strands with the annealed copper profiles is worse than for the SuperOx. Higher degradation has been obtained on both the straight and bent samples, with a higher impact of the bending on the fatigue properties. Similar to the SuperOx strands, no data correlation for the different p_{max} has been observed. For the bent SuperPower sample, better fatigue properties were obtained at 30 MPa than at 20 MPa. On the other hand, the sample with the non-annealed copper profiles has demonstrated a very stable performance for the load amplitudes up to 40 MPa. The strand I_c was almost not affected after 1000 load cycles. As a preliminary conclusion, annealing of the copper profiles could be responsible for the strand performance degradation in the cyclic load measurements.

Comparing $I_c(1)$ to the value measured before the loading, a noticeable irreversible degradation for some of the tested regions has been obtained (up to 5 %). This may indicate a presence of voids in the cross-section of the strand. In order to validate this assumption the strands were cut after the measurements at the locations of the test regions. The corresponding cross-sections that were subjected to 90° load at $p_{max} = 20$ MPa of the straight SuperOx and SuperPower strands (with annealed and non-annealed copper profiles) are presented in figure 3.27.

All three pictures show an issue with the strand manufacturing: the slot space is not completely filled with solder. This leads to a higher stress concentration at the
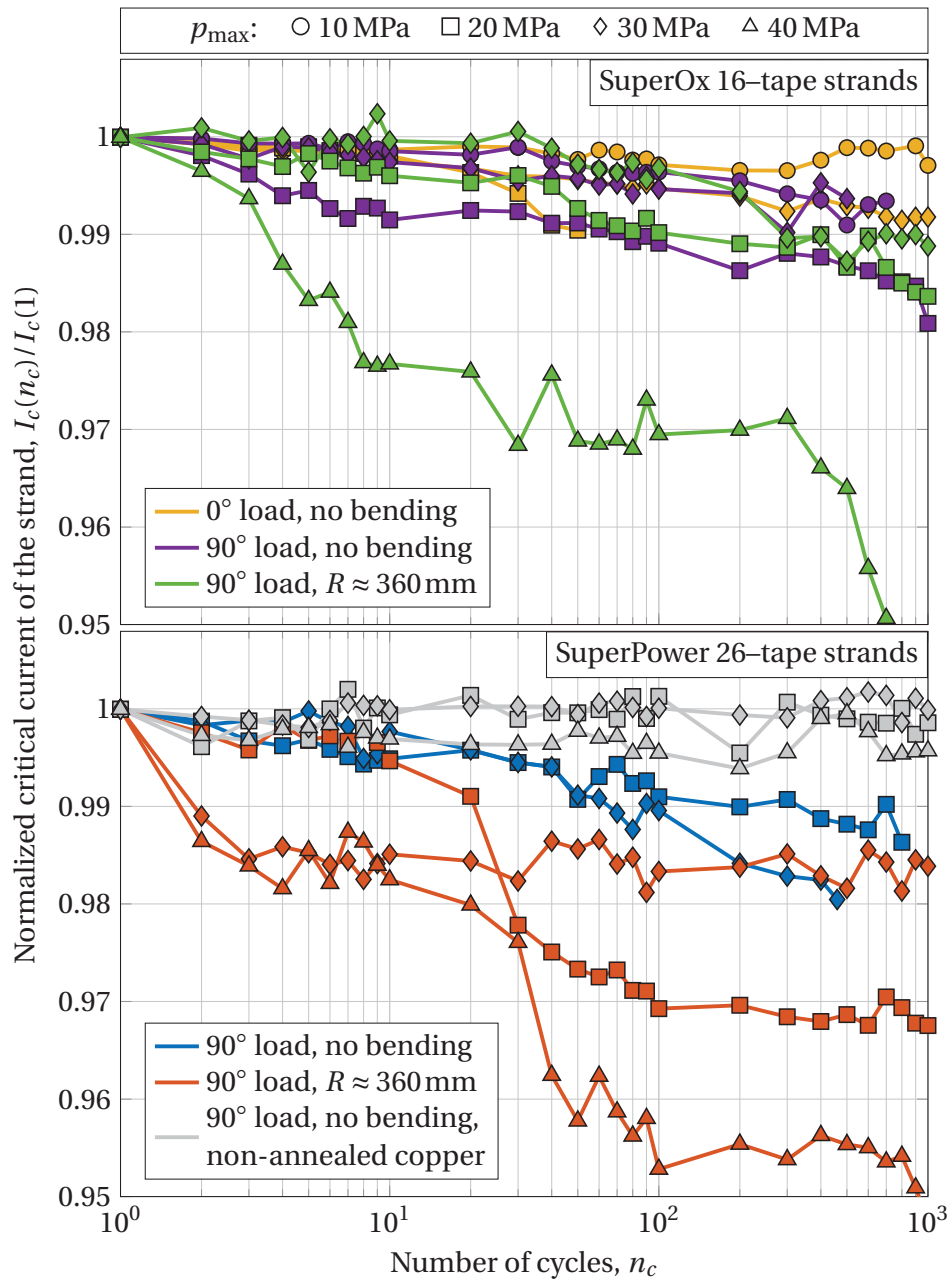
Figure 3.26: Evolution of I_c (at 77 K/sf) against the number of cycles n_c for SuperOx (top plot) and SuperPower strands (bottom plot) for different amplitudes of cyclic load p_{max}. Each individual color corresponds to one sample tested at selected bending and direction of the transverse load.
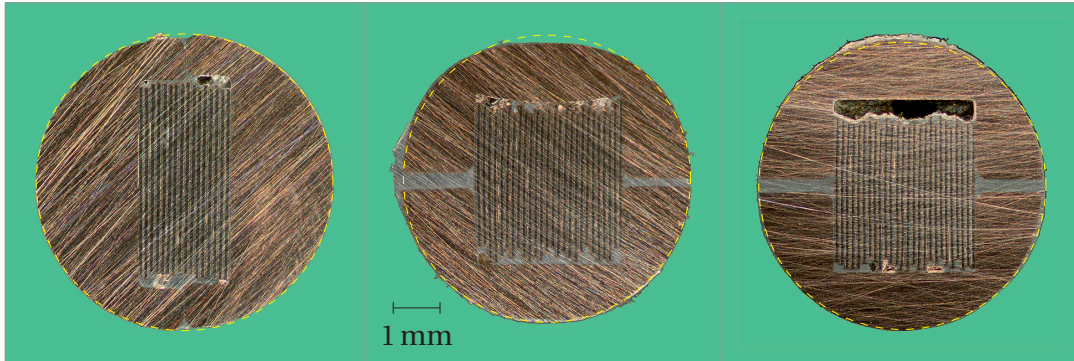
Figure 3.27: Cross-section of the straight strands after 1000 load cycles (90° load, $p_{max} = 20\,\text{MPa}$): left – SuperOx, center – SuperPower, right – SuperPower (non-annealed copper). Dashed circles are drawn from the strand centers with radii corresponding to each strand.

location of voids during the transverse loading. Comparing the cross-sections of the SuperPower strands, one can see the effect of the annealing. The annealed profiles, being a 'softer' material, have a highly deformed shape, while the non-annealed ones are not deformed. This is compatible with the difference in the test results between the two SuperPower samples (see figure 3.26). Nevertheless, by improving the strand manufacturing process, the effect of copper annealing on the fatigue properties could be reduced if voids will not be presented in the strand volume.

3.10 Conclusion

A twisted stack of HTS tapes soldered between the two copper profiles – strand – is investigated for the potential application to fusion magnets. As expected, the inter-tape resistance is very low, about 15 nΩ·m at 77 K and 4 nΩ·m at 4.2 K for the adjacent tapes in the stack. In DC applications the strand exhibits a pure power-law voltage–current transition, suggesting that the current distribution between tapes is uniform. A high tolerance against the potential defects in tapes is also observed. While the strand I_c is strongly reduced in the self-field conditions if compared with the single tape properties, no reduction of I_c is obtained at high fields, making the strand design relevant for high field applications in fusion.

The strand should be first twisted and then soldered, in order to reduce effect of the strain accumulation during the manufacturing. This process allows to produce the strand with the twist-pitch limited only by the properties of the single tape. The critical bending radius of the strand, R_c, is relatively high, about 400 mm when annealing of the copper profiles is not used. By annealing the profiles, R_c is reduced by about factor of 2. In order to prevent cracks of soldering between the copper profiles when getting

closer to the critical bending, it is advisable to set the split line between the profiles along the c-axis of the stack.

Unfortunately, when it comes to the transverse mechanical properties, the situation with the copper annealing is basically the opposite. When the profiles are annealed, the transverse pressure, resulting in 2 % degradation of I_c, decreases from 30 MPa to 25 MPa and also the fatigue issues arise, leading to several percent reduction of I_c after 1000 cycles at the moderately low amplitude of the cyclic loading. Additional investigations, presumably at the cable stage, are still needed in order to make a decision whether copper annealing should be used or not.

4 Coated conductor cable prototypes

The round strands discussed in the previous chapter comprise typically 10 to 40 HTS tapes and can carry several kA in high magnetic fields ($\gtrsim 10\,\mathrm{T}$). It is necessary to use about ten of them or more to construct an ITER-like high current cable for fusion. Thanks to the round geometry of the strands, conventional cabling techniques used in LTS applications can be considered to design and manufacture such cable.

In the present chapter we intend to introduce a suitable cable design based on the round HTS strands and investigate its mechanical and electrical properties. It is planned to support these design studies by R&D activities, including the manufacture and test of the full-size cable prototypes. The prototypes will be measured in the EDIPO test facility at SPC, which provides the opportunity to perform a typical test program of fusion cables (T_{cs}, I_c, AC loss and cycling tests) in a broad range of the operating field and temperature, up to 12 T and from 5 K to 40 K, respectively.

Measurements of HTS cables at operating conditions relevant for fusion magnets will be carried out for the first time, thus the results are of high interest to clarify potential applications of HTS in fusion.

4.1 Design of the cable

Based on the round geometry of the strand, the copper-cored Rutherford design has been selected for the cable layout, see figure 4.1. The two-layered fully transposed assembly prevents an accumulation of the transverse loading on strands when the cable operates at high current and high field, directed along the wide cable side. Improved out-of-plane bending properties are also expected due to a relatively low thickness of the cable. The intrinsic modularity of this concept allows addressing various demands on high current cables for fusion magnets by proper selection of the design parameters. The Rutherford cables are typically used in accelerator magnets with thin-diameter LTS strands, $D \sim 1\,\mathrm{mm}$, and very thin (or without) central core.

Among the parameters described in figure 4.1, only three are independent. In order to obtain a relation between the parameters let us consider the developed view of the

Symbol	Description
N	Number of strands in the cable
g	Thickness of the cable core
f	Width of the flat part of core
θ	Twist-angle of the cable
L	Twist-pitch of the cable
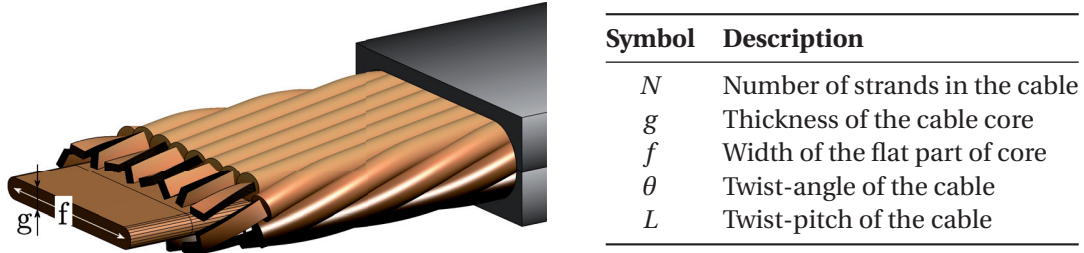
Figure 4.1: Artistic view of the cable design (left) and definition of the design parameters (right).
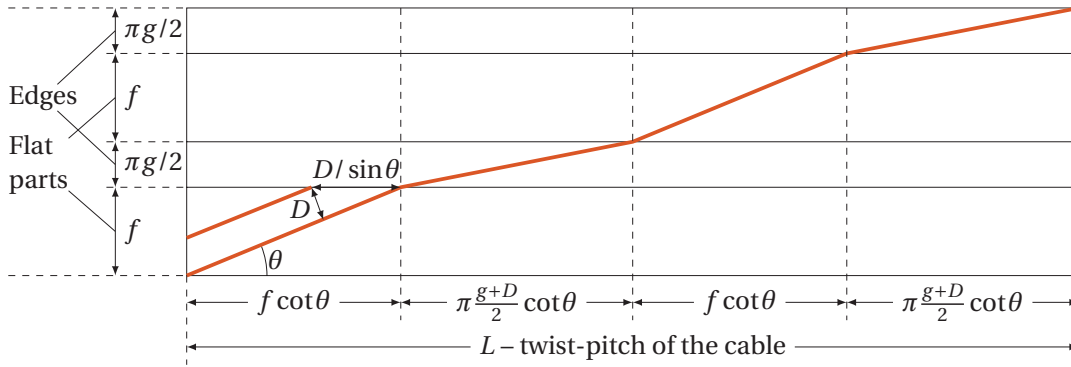
Figure 4.2: Flat pattern of the cable core and developed view of the contact line between the strand and cable core.

contact path between the strand and cable core presented in figure 4.2. This path is divided in four sections: two sections correspond to the strand position on flat parts of the cable, the other two – on the cable edges. Note that the helical contact line at the cable edges transforms into a straight line in the developed view. Thus, the cable twist-pitch L can be written as follows:

$$L = \left(2f + \pi\left(g + D\right)\right)\cot\theta$$
$$L = N\frac{D}{\sin\theta}$$

(4.1)

Considering (N, g, L) as independent cable parameters, one can express θ and f from (4.1) as:

$$\theta = \arcsin\frac{ND}{L}$$
$$f = \frac{\pi}{2}\left(g_c - g\right), \quad \text{with}$$
$$g_c = \left(\frac{N}{\pi\cos\theta} - 1\right)D.$$

(4.2)
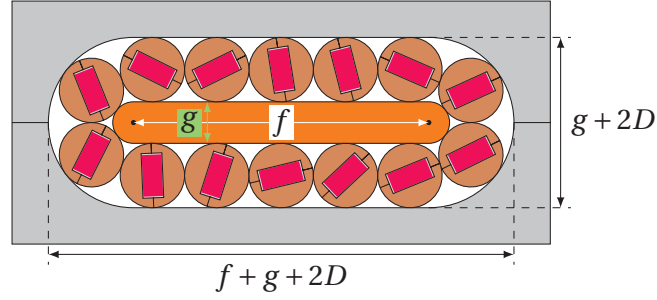
Figure 4.3: Cross-section of the 14-strand cable.

The cable core becomes round ($f = 0$) by setting $g = g_c$, i.e. in this notation g_c corresponds to the diameter of the round core. This is the maximum value for g: $0 \leqslant g \leqslant g_c$. Note that the precise expression for the diameter of round cable reads as $g_c = \left(\sqrt{1 + \frac{\cot^2(\pi/N)}{\cos^2\theta}} - 1\right) D$ (a derivation is given in [58]). The result obtained for g_c in (4.2) from the simplified analysis is a good approximation of the general expression if $\pi/N \ll 1$.

In the drawing 4.2 the strands are assumed in contact with each other at equatorial points of the cross-section. This assumption is strictly valid for the flat parts of the core and is an acceptable approximation for the edges if $g \gtrsim D$. In case of $g \lesssim D$ the result is less accurate: at the cable edge the strands contact each other at the points located lower than equator of the strand. After this effect was studied numerically, the more accurate expression for f (including the thin-core cases, $g \lesssim D$) has been obtained:

$$f = \frac{\pi}{2}\left(g_c - g\right) + 0.28\frac{D^2}{g + D} \tag{4.3}$$

This expression for f deviates from the numerical one by less then 1 % in a wide range of the parameters: $6 \leq N \leq 30$, $0 \leq g/D \leq 2.67$, $L \geq 0.2\,\text{m}$.

An example of the cross-section of 14-strand cable is depicted in fig. 4.3. According to the drawing, the cable space S_{cable} and the total copper cross-section S_{cu} can be expressed as:

$$\begin{aligned}
S_{\text{cable}} &= f\left(g + 2D\right) + \pi\left(g/2 + D\right)^2 \\
S_{\text{cu}} &= fg + \pi g^2/4 + N\left(\pi D^2/4 - w(t - n_t d_{\text{cu}})\right)
\end{aligned} \tag{4.4}$$

where d_{cu} is the thickness of the copper layers in a single tape (typically $40\,\mu\text{m}$). Engineering and copper current densities are written as: $j_{\text{eng}} = I/S_{\text{cable}}$, $j_{\text{cu}} = I/S_{\text{cu}}$, where I is the operating current of the cable. Note that the lower limit on j_{eng} and the upper limit on j_{cu} specified in section 2.1 have opposite effects: a reasonable compromise between the cable compactness and amount of copper should be achieved.

The space available for the coolant flow (i.e. cross-section of voids in the cable) S_{flow}

and wetted perimeter of the cable P_{wetted} are:

$$S_{\text{flow}} = 2fD + \pi gD + \pi D^2(1 - N/4)$$
$$P_{\text{wetted}} = 4f + 2\pi g + \pi D(N + 2) \tag{4.5}$$

which allows one to estimate the effective hydraulic diameter D_h and the void fraction of the cable cross-section: $D_h = 4S_{\text{flow}}/P_{\text{wetted}}$, vf $= S_{\text{flow}}/S_{\text{cable}}$ – the geometrical parameters used in hydraulic analyses. The main hydraulic property of a forced flow conductor – the pressure drop per unit length $\Delta p/l$ – can be estimated with the Darcy-Weisbach equation [59]:

$$\frac{\Delta p}{l} = \frac{\lambda \dot{m}^2}{2\rho S_{\text{flow}}^2 D_h} \tag{4.6}$$

where $\dot{m}$ and ρ are the mass flow rate and density of the coolant, λ – Darcy-Weisbach friction factor. More details about the hydraulic and thermal properties of the cable design will be presented in chapter 6.

Last but not least, a full transposition feature is presented in the cable design: translating each strand by L/N along the longitudinal direction results in a position identical to another strand. During a charge of the long cables, where the inductive voltage is dominant over the resistive component at the joints, the fully transposed cables have a uniform current distribution between the strands. Consequently, the full current capacity of the cable can be achieved. The limitations on the strand cabling and cable bending imposed by mechanical properties of the strand will be discussed in the next section.

4.2 Mechanical properties of the cable

4.2.1 Cable manufacturing

During the cable manufacturing bending deformations are applied to the strand at the cable edges, see figure 4.4. The helical trajectory of a center-line of the strand can be expressed as:

$$\gamma(s) = \left\{ a\cos\frac{s\sin\theta}{a}, a\sin\frac{s\sin\theta}{a}, s\cos\theta \right\}, \tag{4.7}$$

where $a = (g + D)/2$ is radius of the helix and s the arc length of the trajectory (natural coordinate). The local bending radius of the helix R can be deduced from the trajectory curvature $k = 1/R = |\ddot{\gamma}(s)| = \sin^2\theta/a$ (see [60] for further reading):

$$R = \frac{g + D}{2\sin^2\theta} \tag{4.8}$$

center-line
$\gamma(s)$

θ

$a = \dfrac{g+D}{2}$
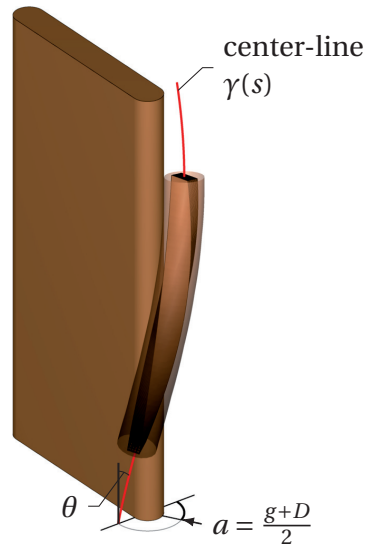
Figure 4.4: Artistic view of the strand cabling.

$\varphi = 0$

r

$\varphi = \pi$

φ
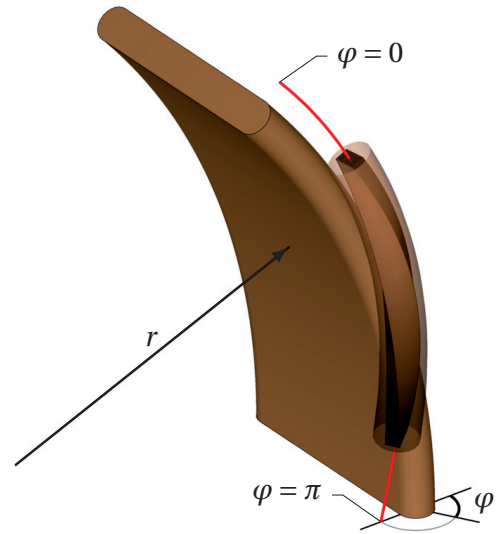
Figure 4.5: Artistic view of the cable bending.

To prevent a reduction of the strand critical current, the bending radius should be larger than the critical value: $R > R_c$, where R_c is a matter of chosen criterion for the I_c reduction. The values of R_c for a 5 % I_c reduction measured on several strands at 77 K are summarized in table 3.1. From the condition $R = R_c$ and equation (4.1) one can also estimate the minimal permissible twist-pitch of the cable $L_{\min}$:

$$L_{\min} = ND\sqrt{\frac{2R_c}{g+D}} \qquad (4.9)$$

Thus, the mechanical limit on the strand cabling stage can be formulated as: $L > L_{\min}$. The presence of the central core in the cable design (i.e. $g > 0$) allows a reduction of $L_{\min}$ and smaller values of L available – one of the key reasons for using the central core in this cable design. Other parameters in (4.9) do not have explicit effect on $L_{\min}$: for instance, for the fixed current capacity of the cable reducing the number of strands N would increase the strand diameter D (in order to reduce transverse load, see next subsection), what in turn increases R_c being a function of the strand design.

In addition, to obtain a specified coil geometry, the cable should be bent in a plane perpendicular to the flat side of the core, see figure 4.5. The friction coefficient between the cable elements – strands, core and steel jacket – is an important unknown for the mechanical analysis of the cable bending. Similar to the tape or stack twisting (see section 3.6), two limit cases can be considered: zero friction, where the sliding effect takes place, and high friction, which leads to complete accumulation of axial strains. In the case of zero friction, the neutral axis of each cable element is located at

its center, while in the case of high friction there is only one neutral axis in the center of the cable.

In the former situation, it is enough in practice to estimate the final bending radius of the strand. The edge of the bent cable will have the torus geometry, as illustrated in figure 4.5. The principal curvatures of this surface – k_1 and k_2 in the poloidal and toroidal planes – one can write as (see [60] for further reading):

$$k_1 = \frac{1}{a} \qquad k_2 = \frac{\cos\varphi}{r + a\cos\varphi} \tag{4.10}$$

where r is the bending radius of the cable, φ is the torus angle in the poloidal plane: $\varphi = 0/\pi$ defines outer/inner side of the core with respect to the bending center. The strand center-line follow this surface at the angle θ to the toroidal direction. The curvature of the curve on the surface can be obtained from the Euler formula: $k_\theta = k_1 \sin^2\theta + k_2 \cos^2\theta$. Consequently, the minimum bending radius of the strand, $1/k_\theta(\varphi = 0)$, is:

$$R_1 = \frac{(r + a)a}{(r + a)\sin^2\theta + a\cos^2\theta} \tag{4.11}$$

In the second situation, the axial strains in the superconducting layers will accumulate. The peak value occurs at the strand cross-section located at the outer side of the core, on the border between the edge and flat part of the core. It can be estimated as:

$$\varepsilon_{\text{peak}} = \frac{d}{2R_2} = \varepsilon_{\text{cabling}} + \varepsilon_{\text{bending}} = \frac{d}{2R} + \frac{(g + D + d)\cos^2\theta}{2r} \tag{4.12}$$

where $d = \sqrt{w^2 + t^2}$ is the diagonal of the stack.

The critical bending radius of the cable in the first and second approach can be obtained from the conditions $R_1 = R_c$ and $R_2 = R_c$. In terms of the (N, g, L) parameters, the result reads as:

$$\begin{aligned} r_{c_1} &= R_c \frac{L^2 - N^2 D^2}{L^2 - L^2_{\text{min}}} \\ r_{c_2} &= R_c \frac{L^2 - N^2 D^2}{L^2 - L^2_{\text{min}}} \left(1 + \frac{g + D}{d}\right) \end{aligned} \tag{4.13}$$

r_{c_1} and r_{c_2} are the bottom and top limits of the critical bending radius r_c in the cable with intermediate friction: $r_{c_1} < r_c < r_{c_2}$. In order to provide a qualitative illustration, the dependence over L and g of r_c that was taken as $(r_{c_1} + r_{c_2})/2$ is shown in figure 4.6. Note that $r_c = \infty$ in case of $L = L_{\text{min}}$, which means that such cable cannot be bent otherwise the critical strain on the ceramic is exceeded. The mechanical limit on the cable bending stage can be formulated as: $r_c < r^{\text{min}}_{\text{coil}}$, where $r^{\text{min}}_{\text{coil}}$ is the minimum radius of the coil.
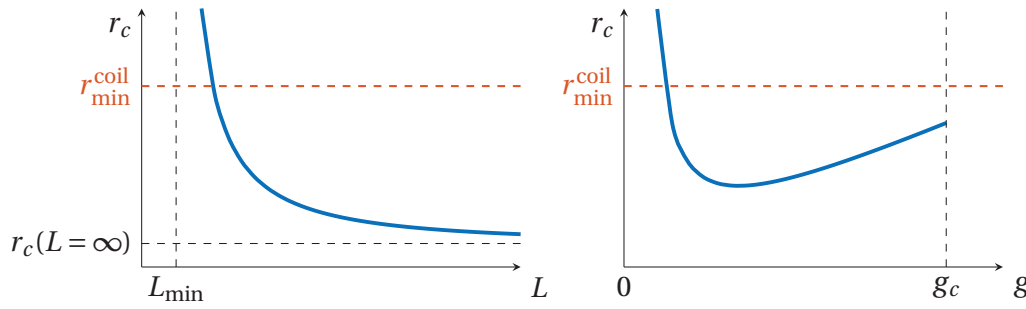
Figure 4.6: Illustration of the critical bending radius r_c dependence over the cable twist-pitch L (left) and thickness of the cable core g (right).

4.2.2 Cable operation

The mechanical issues during high current operation of the cable at high external magnetic field are originated from the Lorentz body forces. The strand properties against the transverse loading have been already discussed in section 3.8. For the flat two-layered assembly of strands in the cable peak transverse load can be estimated as $p = 2I_{op}B/(ND)$, I_{op} is the operating current of the cable. This load should not be larger than the pressure limit p_c: $p < p_c$. p_c is a function of the strand design, typically in the range from 20 MPa to 40 MPa.

More detailed analyses of mechanical stresses for a geometry of the first cable prototypes (to be discussed later in the chapter) have been performed in a 2D 'plane strain' FEM model, similar to the one used for single strands in 3.8. The model includes the steel jacket domain with a Young's modulus of 207 GPa. Each stack of the cable carries $I = 3$ kA at $B = 12$ T background field directed along the wide side of the cable. The self-field produced by the cable is also taken into account. Considering the Lorentz body force acting on the stack domain and assuming zero-displacement for the bottom side of the jacket, the distributions of the von Mises stress in the cable space were calculated. These shown in the left plot of figure 4.7 for the different orientations of the stacks in the cable. The cases (a) and (c) represent the limit cases for the transverse loading on stacks. The case (b) contains random orientations of the stacks, which are expected in a real sample.

The average von Mises stress in the stack domains is calculated according to equation (3.13). The results are presented in the right plot of figure 4.7. The labels of curves and strand numbers correspond to those in figure 4.7. Although a rough estimation of the transverse load as $p = 2I_{op}B/(ND)$ is close to the average stress obtained for the bottom layer of the strands (strand numbers from 11 to 20) in the case (c), significantly higher stress was obtained in the case (a). The peak transverse pressure stays below 20 MPa.

Comparing the calculated stress with the performance of the single strands under the
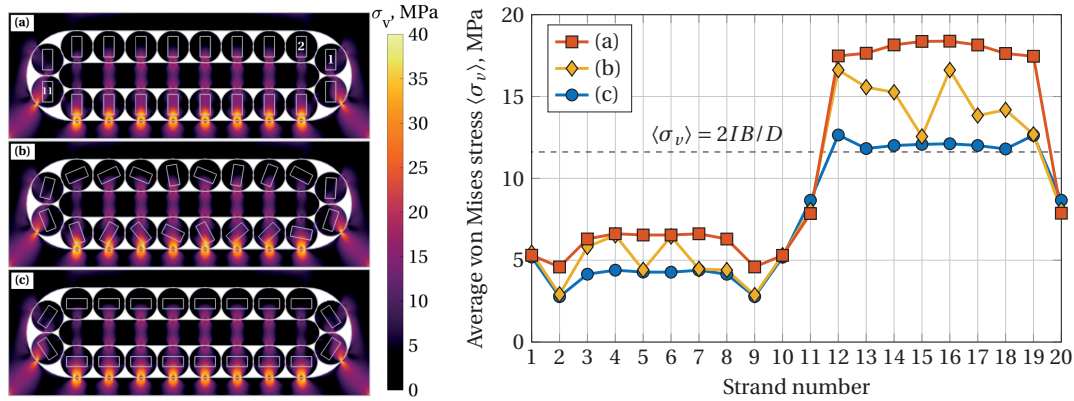
Figure 4.7: left – distribution of the von Mises stress, right – average von Mises stress as a function of the strand number. Indices of the strands are shown in the top left plot (a).

transverse load (see figure 3.23), significant degradation is not expected for the full current measurements of 60 kA cable at 12 T. However, in contrast with the calculation where all the strands are identical, a difference in the strand dimensions due to finite manufacturing tolerances will result in a higher non-uniformity of the transverse load. The strands of slightly larger diameter, located in the bottom cable layer, will experience higher load till they are deformed to the dimensions of the smaller ones. In addition, for the cable operation, when transport current is applied in a cyclic manner, fatigue properties of the strands may still result in a performance reduction, especially if the strands are made of annealed copper profiles (see details in section 3.9).

4.3 Inter-strand resistance

A short cable for the inter-strand resistance measurements (see figure 4.8) has been prepared with the following parameters: $N = 20$, $g = 5$ mm, $n_t = 16$, $D = 6.2$ mm, with no twisting at the strand and cable stages. This assembly of the SuperOx 10 cm-long strands is encased between the two steel jackets and spot welded along a split line. Voltage taps are placed on the strands near the border with the jackets, 3 cm away from the end of the strand terminal.

At the ends of the strands, 1 cm-long sections of the strands are machined to a smaller diameter. Thin-wall copper tubes of 2 cm length and 6 mm outer diameter are inserted and soldered at these locations. Then, insulated copper wires are soldered into the tubes over 1 cm length. Finally, in order to prevent current transfer between the strands outside the voltage taps, the regions between the strand voltage tap and terminals were additionally varnished.
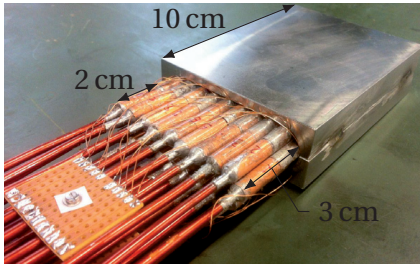
Figure 4.8: Experimental assembly for the inter-strand resistance measurements.
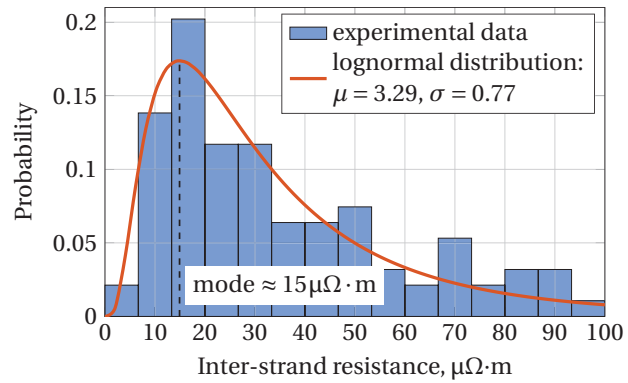
Figure 4.9: Distribution of the inter-strand resistance at 77 K. Lognormal function, being not in scale with vertical axis, illustrates a mode of the distribution.

This experimental setup allows measuring the inter-strand resistance over 8 cm of transfer length between any input–output pair of the strands. The measurements were carried out at 77 K for the input strands #1, 6, 11, 16 – all other output strands, and also for the all possible adjacent pairs of the strands. The obtained results are very scattered and not directly related with the distance between strands. While some of the lowest resistances were obtained for the strands located at the opposite edges of the core, some of the very high values correspond to the adjacent strands. Most likely, a major coupling path between the strands is through the central core (note that the strands and core are pressed by the steel jackets). On top of that, the quality of the strand surface significantly affects the measurements, making it difficult to interpret the results properly.

By neglecting another coupling path directly between the adjacent strands, all the results can be treated in a statistical way: the histogram of the results in the range from 0 and $100\,\mu\Omega{\cdot}m$ is presented in figure 4.9. This follows roughly the lognormal distribution with the mode (i.e. most probable resistance) of about $\approx 15\,\mu\Omega{\cdot}m$. The obtained form of the distribution reflects the situation, where requirements on several factors, such as applied transverse force, roughness and oxidation of the strand surface, need to be fulfilled simultaneously in order to obtain a low value of the inter-strand resistance. High values are obtained if any of these factors is not fulfilled. In this case a non-symmetric distribution of the results highlights the increased probability for higher values.

At low temperature conditions ($T \sim 5K$), the expected inter-strand resistance is in the range from $1\,\mu\Omega{\cdot}m$ to $4\,\mu\Omega{\cdot}m$ assuming a similar scaling as it was measured in case of the inter-tape resistance (see section 3.2). These results will be used in the analysis of inter-strand coupling loss, section 5.2.
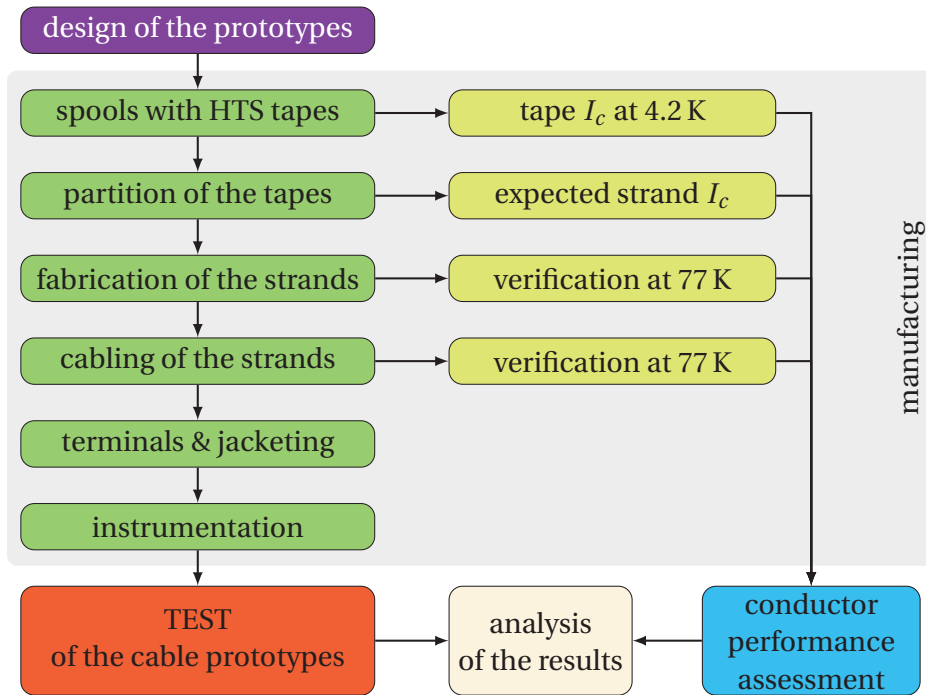
Figure 4.10: Scheme of the R&D steps performed on the full-size cable prototypes.

4.4 Manufacturing of 60 kA cable prototypes

In order to demonstrate the feasibility of the proposed HTS cable concept for fusion magnets, it was decided to fabricate two full-size cable prototypes with the target current capacity 60 kA at 12 T (taking ITER TF cables as a reference) for measurements in the EDIPO test facility. The main parameters and an external view of EDIPO are given in appendix A.4. The following discussion in this chapter is organized as schematically illustrated in figure 4.10: the design and manufacturing of the prototypes will be presented below in this section; the assessment of the cable performance, test in EDIPO and analysis of the test results will be discussed then in each individual section.

4.4.1 Design of the prototypes

Similar to the samples measured in the FBI test facility (see section 3.4), the strands for the cable prototypes are made of 16-tape stacks of the SuperPower and SuperOx 4 mm-wide tapes encased between the annealed copper profiles of 6.2 mm diameter. The dimensions of the strand slot are 4.3 mm × 2 mm. The expected critical current of the strands is around 3 kA at 12 T/4.2 K, which results in 20 strands per cable in order to reach the target current capacity. As illustrated in the upper sketch in figure 4.11,
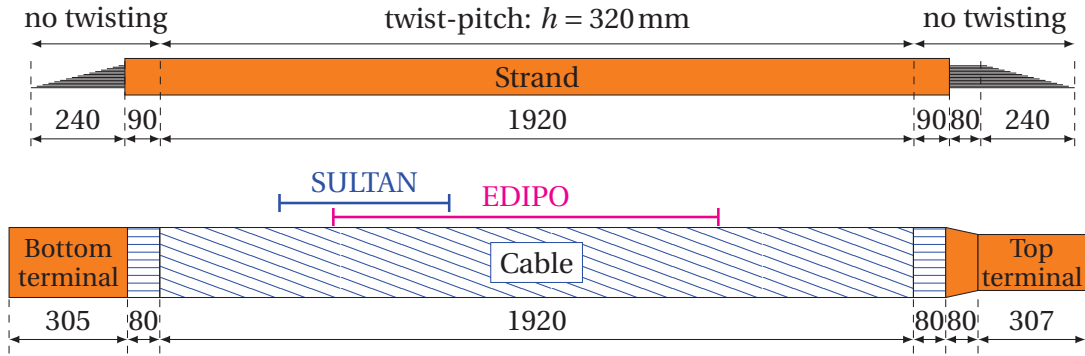
Figure 4.11: Dimensions of the strand (upper drawing) and cable (bottom drawing) used in the fabrication of the cable prototypes. Lengths of the field homogeneity of the SULTAN ($\approx 440\,\text{mm}$) and EDIPO ($\approx 1000\,\text{mm}$) test facilities are also indicated.

there are three regions along the length of the strands: a central region twisted at 320 mm (6 twist-pitches in total) and two non-twisted regions at the ends. A staggered arrangement of the tapes at the strand ends was used to reduce the terminal resistance of the prototypes, as will be discussed in details in section 4.4.4. The total length of the strands is 2660 mm. The length of the tapes in the strand ranges from 2.21 m to 2.66 m with 3 cm step, requiring 39 m of total tape length per strand.

As the number of strands $N = 20$ is already defined, the only free parameters in the cable design are the thickness of the cable core g and the twist-pitch of the cable L. There are two main restrictions imposed on the values of L: $L > L_{\text{min}}$ in order to maintain bending of the strand within acceptable limits (see equation (4.9)) and $L \lesssim 1.1\,\text{m}$ in order to have at least one full twist-pitch in the field homogeneity zone of EDIPO (see bottom illustration in figure 4.11). If the critical bending radius of the strand is taken conservatively as $R_c = 300\,\text{mm}$ (see for details section 3.7), both requirements can be fulfilled simultaneously if $g \gtrsim 3\,\text{mm}$. As a result, g and L have been set as: $g = 5\,\text{mm}$, $L = 1000\,\text{mm}$, corresponding to $\approx 360\,\text{mm}$ of the strand bending radius at the cable edge. The design parameters of the prototypes and their cross-section are outlined in figure 4.12. Although shorter L would also lower the AC losses of the prototypes, this factor was not included in the design considerations for the first cable prototypes, meant as TF prototypes.

The twist-angle of the cable θ and the width of the flat part of the core f can be obtained from equation (4.2) and (4.3): $\theta = 7.1°$, $f = 45.9\,\text{mm}$. The total width of the cable core is $f + g = 50.9\,\text{mm}$. A manufacturing tolerance due to minor variations of the strand diameter can be applied to f, which will affect only L. The other parameters are kept constant, including the bending radius of the strand at the cable edge. A cable core that is wider by Δf increases the cable twist-pitch by $\Delta L = 2\Delta f \cot\theta$.

Stage	Parameter	Value
Tape	Width of tape w	4.0 mm
	Thickness of tape d_t	0.1 mm
Strand	Number of tapes n_t	16
	Slot width	4.3 mm
	Slot height	2.0 mm
	Split line	$\perp$ to c-axis
	Diameter D	6.2 mm
	Twist-pitch h	320 mm
	Annealing of profiles	Yes
Cable	Number of strands N	20
	Thickness of core g	5.0 mm
	Twist-pitch L	1000 mm
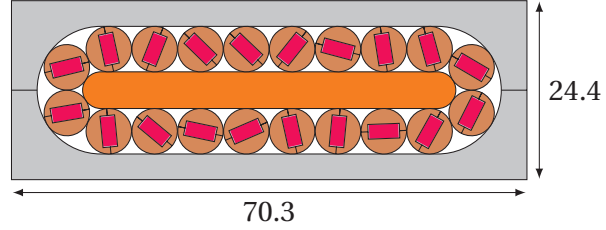
Figure 4.12: Design parameters and cross-section of the prototypes.

4.4.2 Spools with HTS tapes

The total required length of the tapes to manufacture the two cable prototypes is 1.56 km (780 m per each cable). The tapes were purchased from SuperPower for the first cable ('1st leg') and from SuperOx for the second one ('2nd leg'). Photographs of the received material are presented in top row in figure A.4 in appendix. The distribution of the critical current of the full tapes along the length at 77 K (provided by the manufacturers) was not uniform. Because of that, the tapes were cut in shorter segments with approximately constant critical current.

23 spools were purchased from SuperPower. A characterization of all spools was considered excessively time consuming, therefore samples from 11 spools, corresponding to 65 % of the total tape length, were tested in self-field (s.f.) at 77 K and in 12 T perpendicular field at 4.2 K. Note that the lift factor (i.e. $I_c(12\,\text{T}, 4.2\,\text{K})/I_c(\text{s.f.}, 77\,\text{K})$ ratio) is assumed constant along the length of each spool from the same production run. For the remaining 12 spools (35 % of the total tape length), the average lift factor was taken as the most probable value from the distribution of the measured ones (the values follow a log-normal distribution). This value is used to extrapolate the values of I_c from s.f., 77 K to 12 T, 4.2 K operating conditions.

The tape from SuperOx came in four spools, corresponding to four production runs. Short samples were cut from each spool and the I_c value was also measured at s.f., 77 K and at 12 T, 4.2 K. Results of the measurements for SuperPower and SuperOx spools are reported in appendix in table A.2. Note that the high spread in the lift factors for SuperPower is due to the doping in the tapes used by the manufacturer, while there are no artificial pinning centers in the SuperOx tapes, leading to a much weaker scattering of the results.
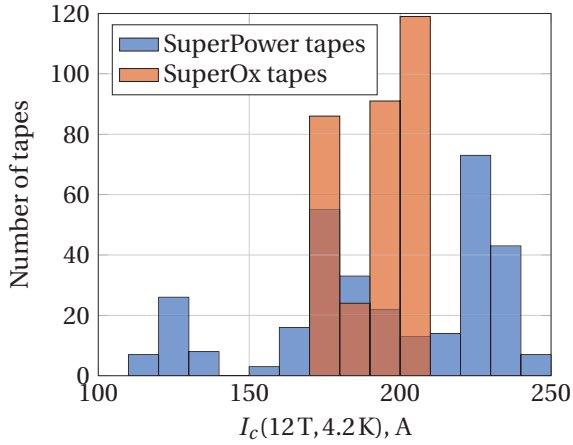
	Expected critical current I_c^{expected}, A			
	SuperPower		SuperOx	
Strand	s.f., 77 K	12 T, 4.2 K	s.f., 77 K	12 T, 4.2 K
1	1165	3094	1600	3104
2	1187	3074	1593	3104
3	1170	3130	1592	3105
4	1137	3117	1592	3105
5	1182	3092	1600	3104
6	1180	3094	1600	3104
7	1174	3094	1600	3104
8	1164	3116	1592	3105
9	1129	3073	1593	3104
10	1143	3055	1600	3104
11	1124	3112	1592	3105
12	1144	3130	1592	3105
13	1162	3151	1593	3104
14	1167	3153	1600	3104
15	1153	3113	1592	3105
16	1172	3128	1599	3104
17	1156	3170	1600	3104
18	1129	3087	1599	3106
19	1144	3129	1598	3104
20	1167	3140	1598	3104

Figure 4.13: Distribution of the critical current at 12 T/4.2 K for 320 SuperPower and 320 SuperOx tapes selected for the prototypes.

Table 4.1: Expected critical current of the SuperPower and SuperOx strands.

Due to a highly non-uniform distribution of the tape I_c values, the arrangement of the tapes in the strands ('partition map') should be carefully specified in order to obtain uniform critical current among the strands. In case the strands have non-uniform I_c value and the inter-strand resistance is low, current redistribution between the strands occurs, reducing the steepness of the transition. For the high inter-strand resistance, the current capacity of the cable can be defined as the lowest value of the strand I_c multiplied by the number of strands. To avoid such situations, the partition maps for the SuperPower and SuperOx tapes have been obtained according to their individual critical currents at 12 T, 4.2 K. The results are shown in tables A.3 and A.4 in appendix. The numbers in the tables correspond to the spool indices. As a result, 320 tapes were distributed in 20 strands, such that a standard deviation of the strand critical current is about 1 % for the SuperPower strands and about 0.02 % for the SuperOx strands, even if the standard deviation of the tape I_c is 20 % for SuperPower and 5.5 % for SuperOx tapes. The distribution of the critical current at 12 T, 4.2 K of the SuperPower and SuperOx tapes selected for manufacturing of the cable prototypes is presented in figure 4.13. The average critical current of the obtained distribution is 195 A and 194 A for the SuperPower and SuperOx tapes, respectively.

Finally, the critical currents of the strands for both prototypes have also been assessed, see table 4.1. At s.f., 77 K the average expected critical currents of the SuperPower

and SuperOx strands are 1160 A and 1600 A, including an I_c reduction due to a self-field effect (see section 3.3). The current capacity of the strands is reduced by $\approx 30\%$ compared to a sum of the I_c of the individual tapes. At 12 T, 4.2 K, the expected values are 3113 A and 3105 A. No self-field reduction of I_c is expected in the high field. Note that the variation in I_c among the strands at s.f. and 77 K is larger than the one at 12 T and 4.2 K, since the tapes were distributed based on the I_c values at low temperature.

4.4.3 Fabrication of strands and cables

The whole fabrication process of the two cable prototypes was carried out at laboratory scale, but there should be no technological obstacles preventing an industrialization. After assembling the stack of tapes and copper profiles, the strands were first twisted and then soldered using standard Sn60Pb40 solder. Each set of 20 strands was cabled around a flat copper core (see photographs in figure A.4 in appendix). Although the design dimensions of the copper core are 5 mm × 50.9 mm, in case of the SuperPower cable a copper core 56 mm wide and 5 mm thick was used. The size was a bit larger than the actual space required for arranging all the 20 strands, because it was unclear whether the required tolerance should be kept large or small. After cabling all the strands there were relatively large gaps between strands. Therefore, copper strips 0.5 mm thick and 6 mm wide were inserted between the strands in order to fill up the voids and limit the strand movements under electromagnetic forces. For the manufacturing of the SuperOx cable, the copper core was machined down to 51.5 mm of width, and the strands were placed around the core without any gap. The tolerances used for the width of the cable core $\Delta f =5.1$ mm and 0.6 mm increased the cable twist-pitch by $\Delta L =82$ mm and 10 mm for the SuperPower and SuperOx cables. The twist-angle and bending radius of the strands were not changed.

The critical currents of all strands were measured in a liquid nitrogen bath just after the fabrication (the strands were straight) and, for some of them, after the cabling (strands were bent around the edge of the flat copper core) as intermediate verification stages. For the SuperPower cable seven strands were measured after the cabling, while for the SuperOx cable ten strands were measured. The $E-I$ curves before and after the cabling for three strands from each manufacturer are plotted in figure 4.14. The values of the critical current normalized to the expected ones (see table 4.1) are given in figure 4.15.

For both manufacturers the I_c of the straight strands (gray bars in figure 4.15) are slightly lower than the expected values: up to 3 % lower for SuperOx and up to 8 % lower for SuperPower. For both manufacturers a systematic increase (less than 4 %) in I_c is observed after the strands are cabled. This was further studied at 77 K on a single tape soldered into the copper profile, where a reduction of I_c of about 2 % was obtained after the soldering. Such reduction disappears after the tape is extracted
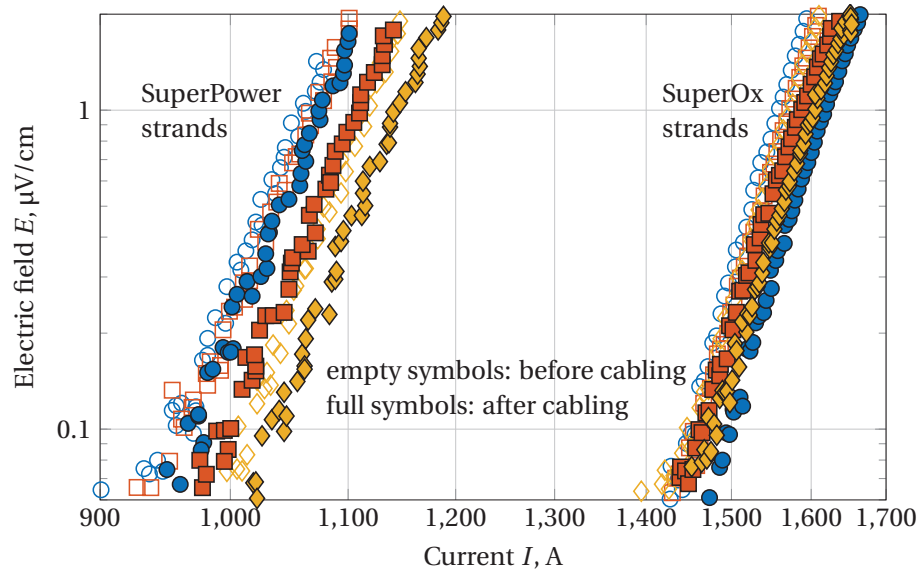
Figure 4.14: Electric field versus current for three SuperPower and SuperOx strands, measured before and after cabling at 77 K / self-field.
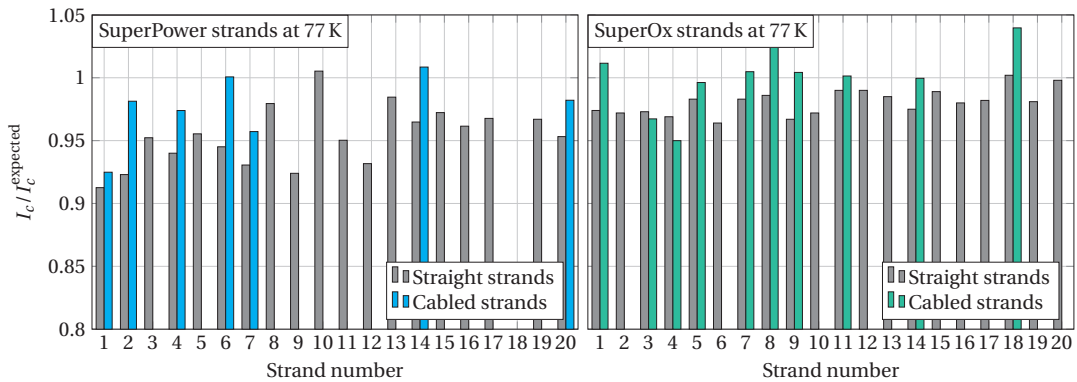
Figure 4.15: Ratio between measured and expected critical current for the strands made with SuperOx (left) and SuperPower tapes (right); the distance between the voltage taps was 150 cm. The grey bars are for the I_c measured in straight strands, while the blue/green bars are for the I_c measured in cabled strands.
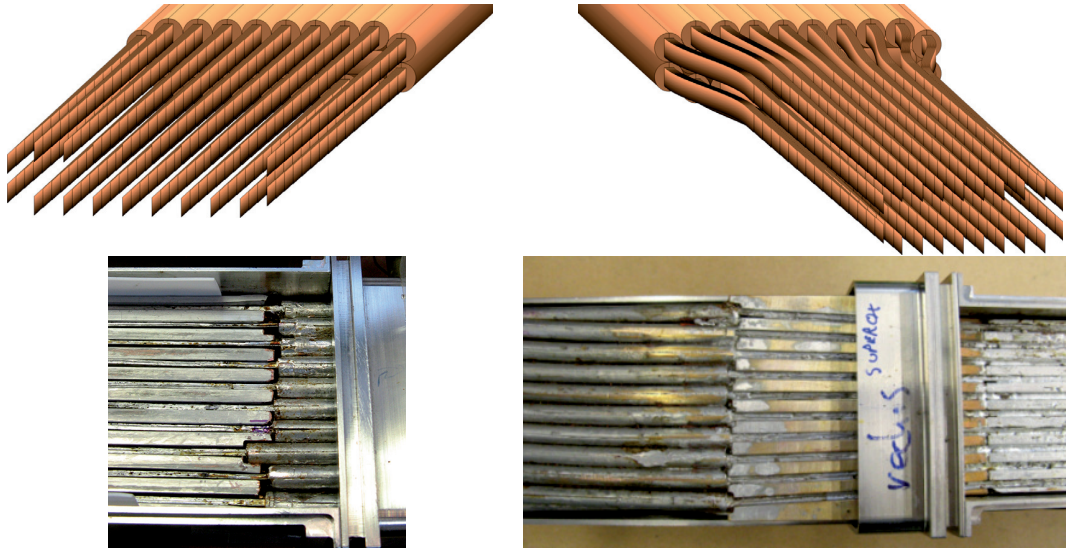
Figure 4.16: Bottom (left column) and top terminals (right column) of the prototypes.

from the profile. This indicates that the pre-compression exerted from the copper profiles on the coated conductors can be at the origin of the increment. The pre-compression is released after the strands are cabled on the copper core because of bending and plastic deformations. $j_c(B,\theta)$ dependence accurately matching the tape properties is also needed if higher accuracy between the measurements and calculations is required.

4.4.4 Terminals and jacketing

The operating current in the EDIPO / SULTAN test facilities is generated by an inductive coupling of a primary coil of the NbTi superconducting transformer with a secondary coil connected to the sample. Hence, the duration and the maximum value of the operating current are directly linked with the total resistance of the secondary loop R_s (see details in [61]). R_s includes all joints and terminals between the transformer, the HTS adapter (to be discussed in the next section) and the prototypes. A step-like operation for the transport current or temperature is possible in the facilities if $R_s \lesssim 10\,\mathrm{n\Omega}$.

The staggered ends of the strands at the terminals allow connecting in parallel all the 320 tapes at the cable terminal as it is illustrated in figure 4.16. Each tape is in contact with the copper of the terminal over a $4\,\mathrm{mm} \times 15\,\mathrm{mm}$ area. Assuming a specific contact resistance of the tape on copper is $6\,\mathrm{\mu\Omega{\cdot}mm^2}$ at $4.2\,\mathrm{K}$ (values between $2\,\mathrm{\mu\Omega{\cdot}mm^2}$ and $6\,\mathrm{\mu\Omega{\cdot}mm^2}$ were typically measured), the total contact resistance of each terminal can be estimated as $6\,\mathrm{\mu\Omega \cdot mm^2}/(4\,\mathrm{mm} \times 15\,\mathrm{mm})/320 \approx 0.3\,\mathrm{n\Omega}$.

Copper blocks with 10 groves (3 mm wide and 10 mm deep) machined into it are used as terminals of the cable. In the trapezoidal part of the top terminal a specially shaped copper block is used to provide thermal and mechanical stability to the stacks, where they are not encased with the copper profiles. The width of the top terminal is reduced by $\approx 30\%$ compared to the bottom one.

A steel casing was braised on the copper block. Each staggered stack was soldered to the copper terminal using Sn60Pb40 solder at a temperature of about 200 °C. Copper strips were inserted vertically in the grooves on the Hastelloy side of the stack in order to push the side of the tape with the superconducting ceramic in direct contact with the copper of the terminal. After soldering a steel cover is welded on top and steel pipes are also welded to the terminals for cooling.

Each cable was enclosed in a rectangular steel jacket (3.5 mm thick on the wide side and 2 mm thick on the narrow side). The jacket is composed of two machined steel profiles welded around the cable. A photograph of the cross section of a trial assembly is shown in bottom left photograph in figure A.4 in appendix. Tests were carried out to verify that during welding the temperature of the strands does not exceed the melting temperature of the solder alloy (188 °C); a thermocouple inserted in a dummy strand measured a maximum temperature of less than 100 °C.

4.4.5 Instrumentation and cryogenic circuit

After jacketing the cables and soldering the terminals, the two prototypes were assembled in an EDIPO sample. Two legs are connected in series at the bottom joint and with left and right sides of the HTS adapter at the top joints. All joints were prepared using indium wires. The full instrumentation scheme is sketched in figure 4.17, where cross-section of the sample is also shown. The legs are positioned at 60 mm distance using fiberglass spacers and oriented such that the DC field of EDIPO is parallel to the broad side of the prototypes, the AC field – perpendicular.

On each leg, six pairs of voltage taps over 1 m distance centered with respect to a high field zone of EDIPO were spot welded to the steel jacket. By comparing the signals from each pair of voltage taps the equipotentiality of the cable cross-section can be checked. Three pairs of voltage taps were used on the bottom joint, and five pairs for each side of the sample between the prototypes and transformer.

Temperature sensors (marked red in figure 4.17) were attached to the steel conduit. The sensors allow measuring the temperature at inlet (T0R/T0L), outlet (T52/T50) and in the high field region (T2-T4/T1-T3, centered around the high field zone) of the prototypes.

The HTS adapter has a function similar to a current lead, providing a superconducting current flow with a relatively high thermal resistance, so that the NbTi supercon-
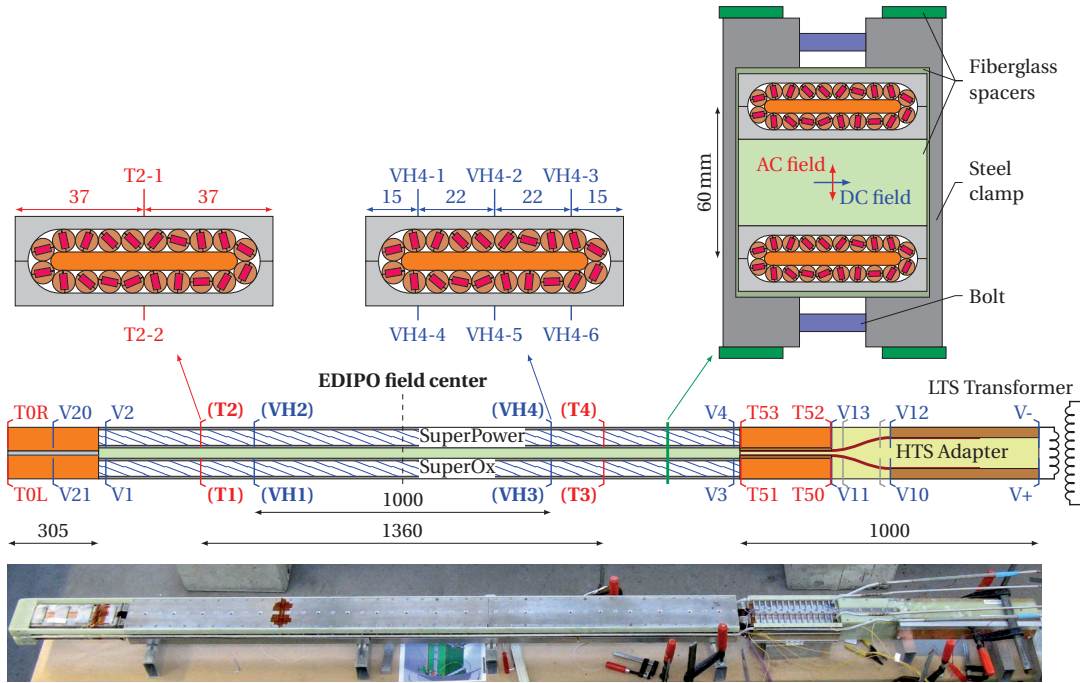
Figure 4.17: Instrumentation scheme of the EDIPO sample consisting of HTS adapter and SuperPower / SuperOx cable prototypes. Temperature sensors are shown in red, voltage taps – in blue and gray. Bold labels correspond to multiple sensors. Cross-section of the sample and orientations of DC and AC fields with respect to the sample are also shown.
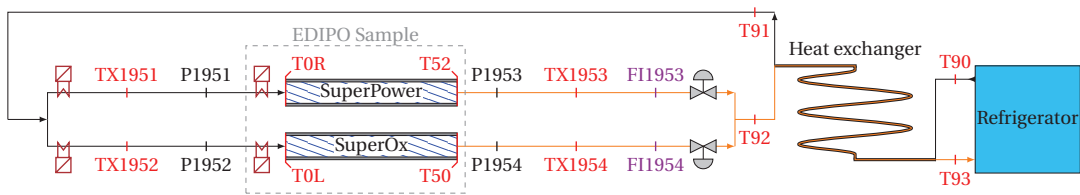
Figure 4.18: Cryogenic circuit of the EDIPO facility for HTS sample test. Temperature sensors are shown in red, pressure drop – in black, mass flow-rate – in violet. Valves and built-in / sample heaters are also indicated.

ducting transformer is thermally decoupled from the sample to be measured (see more details in [62]). The HTS adapter is also equipped with a set of potential contacts and thermometers.

The cryogenic circuit of the EDIPO test facility is sketched in figure 4.18. Each leg of the sample has a separate cryogenic path with temperature, pressure and mass flow-rate sensors. Built-in heaters and valves provide temperature and helium flow control. The inlet pipes of the sample were additionally equipped with two extra heaters just upstream of the inlet, in order to establish different operating temperatures in the two conductors, if needed. A counter flow heat exchanger was also installed in the circuit of the sample. The heat exchanger is required for high temperature operation of the facility to avoid sending warm helium back to the refrigerator. The temperature of helium returned to refrigerator should be maintained below 20 K.

4.5 Assessment of the prototype performance

The value of the critical current I_c at 12 T, 4.2 K of the two cable prototypes is obtained by summing up the expected I_c of the strands (see table 4.1). $I_c \approx 62.2 \, \text{kA} \pm 2.0 \, \text{kA} (\pm 3.3 \, \%)$ for SuperPower and $I_c \approx 61.9 \, \text{kA} \pm 1.5 \, \text{kA} (\pm 2.4 \, \%)$ for SuperOx. Once the values at 12 T, 4.2 K are determined, it is necessary to scale them to various temperatures and fields.

The current sharing temperature T_{cs} and the critical current of the cables I_c are calculated considering not only the background field, but also the self-field generated by the cable and the field generated by the return conductor. Calculation of these components of the magnetic field was performed in a simplified 2D approach using Biot-Savart law. By distributing the total current I_{cable} uniformly among the mesh elements (N_e in total), the contribution of the element i to the total magnetic field at the location of the element k can be calculated as $\langle \Delta \vec{B} \rangle (x_k - x_i, y_k - y_i) = \{M_x, M_y, 0\} \cdot I_i$, where I_i is the current in the element i: $|I_i| = I_{\text{cable}}/N_e$, I_i is negative for the elements of the return conductor. Accurate expressions for M_x and M_y are given in equation (A.12) and (A.13) in the appendix. The total magnetic field at the element k is obtained as a sum of the contributions from all elements excluding the k-th element itself. Note that the values of M_x and M_y are calculated only once, at the beginning of the calculation.

The comparison of the self-field distribution generated by one cable carrying 60 kA and by two cables carrying 60 kA in opposite directions and separated by 60 mm (i.e. corresponding to the EDIPO sample) is presented in figure 4.19. Due to symmetry, only a first quadrant of the full cross-section is shown.

The real orientations of the stacks in the cable and the angular dependence of the critical current were also considered. According to the orientation of every single tape
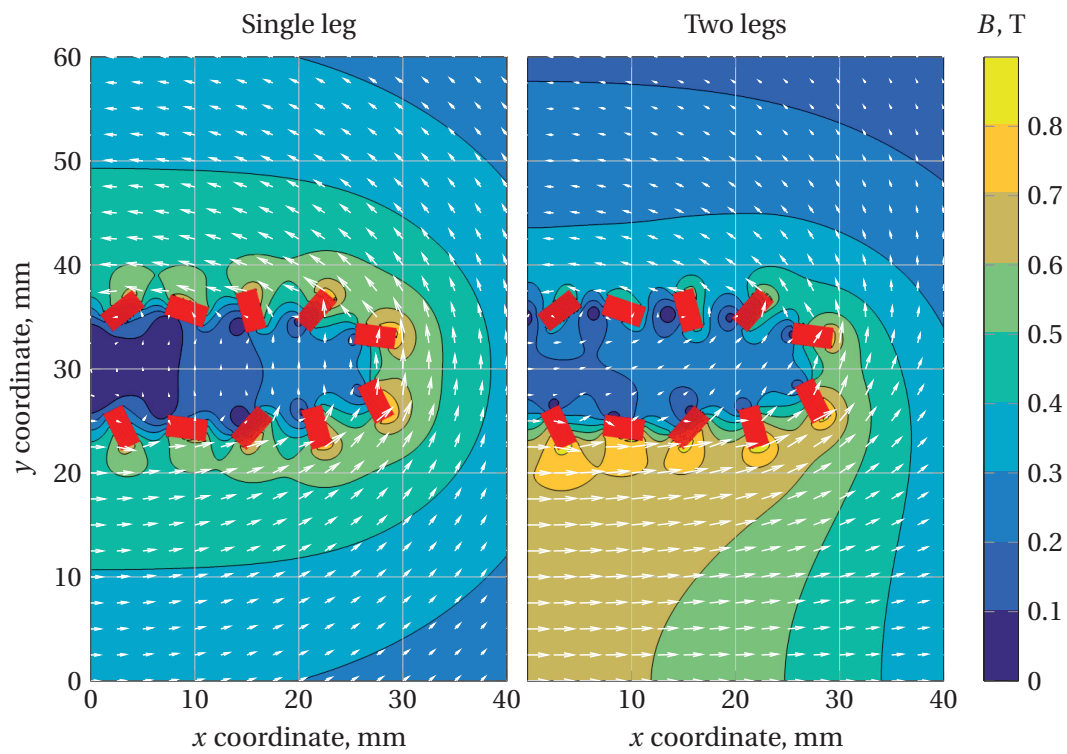
Figure 4.19: Left: Magnetic field profile generated by the conductor (self-field). Right: total magnetic field profile generated by the conductor (self-field) and by the return conductor.
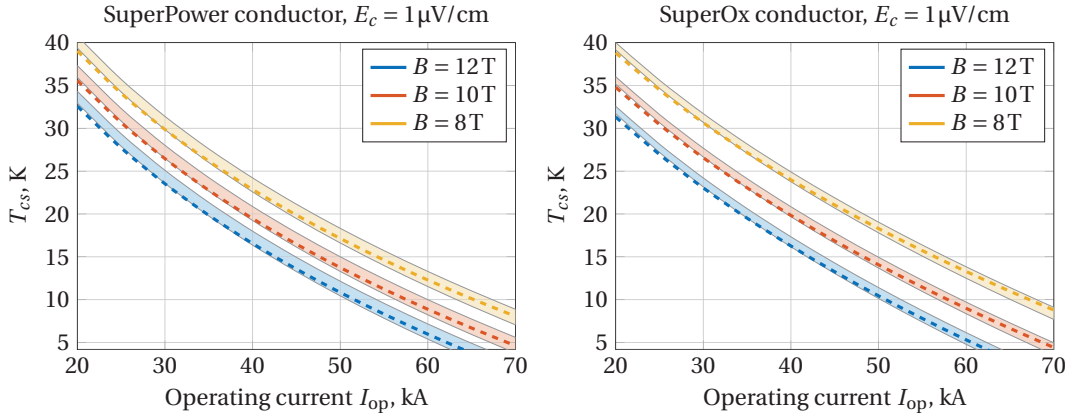
Figure 4.20: Current sharing temperature for the SuperPower (left plot) and SuperOx prototype (right plot) at various background magnetic fields and operating currents for voltage criterion $E_c = 1\,\mu\text{V/cm}$. Bands indicate uncertainty in I_c of 3.3 % for Super-Power and 2.4 % for SuperOx; dashed lines are for the direct scaling of the tape I_c in the perpendicular field.

in the cable, the total magnetic field is divided into parallel, $B_{\parallel}$, and perpendicular, $B_{\perp}$, components with respect to the wide face of the tape. The angle between the magnetic field and the c-axis of the tape is $\theta = \arctan(B_{\parallel}/B_{\perp})$. Consequently, one can obtain the average electrical field E of the cable cross-section as a function of the operating current I and temperature T:

$$\frac{E(I,T)}{E_c} = \frac{1}{N_{\text{mesh}}\,n_t N} \sum_{(i,j,k)=1}^{N_{\text{mesh}}\,n_t N} \left(\frac{I}{I_c^{\text{tape}}\left(B^{(i,j,k)}(I),T\right) f\left(\theta^{(i,j,k)}(I)\right)} \right)^{n\left(B^{(i,j,k)}(I),T\right)} \tag{4.14}$$

Here i is the index of the current element in the tape (from 1 to N_{mesh}), j the index of the tape position in the strand (from 1 to n_t), k the index of the strand in the cable (from 1 to N); $E_c = 1\,\mu\text{V/cm}$, and $B^{(i,j,k)}$ is the magnitude of the total magnetic field, which includes the background field, the self-field and the field of the return cable at the (i,j,k) position. $f(\theta)$ is an interpolation function of the I_c angular dependence, based on data from figure A.2. The field and temperature dependence of I_c^{tape} and n was taken proportional to the lift-factor, with coefficients 117 and 20 for SuperPo-wer, 129 and 25 for SuperOx, respectively. The scaling law for the lift factor of the SuperPower and SuperOx tapes is discussed in appendix A.1.

Finally, $T_{cs}(I)$ can be readily obtained from the equation $E(I, T_{cs}) = E_c$, $I_c(T)$ from the equation $E(I_c, T) = E_c$ or simply as an inverse function of the $T_{cs}(I)$ dependence. The results of the T_{cs} calculation for both prototypes are presented in figure 4.20. In general, the self-field and return field decrease the nominal critical current values. The angular dependence of I_c is an improving factor with respect to the measurements

71

Figure 4.21: The sequence of tests performed in the EDIPO test facility. WUCD stands for warm up-cool down test. Each line corresponds to a DC test.

done at $\theta = 0°$, i.e. in perpendicular field. By chance, the effects on T_{cs} of the generated magnetic field and angular dependence almost compensate each other (in general, this is not the case for other cable configurations). The total impact of both effects on T_{cs} is less than 2 % in the range from 8 T to 10 T and from 20 kA to 60 kA compared to a simple assessment based only on the scaling law in the perpendicular field: $I_c(B, T) = N n_t I_c^{\text{tape}}(B, T)$ (dashed lines in figure 4.20).

4.6 Measurements in the EDIPO test facility

The sequence of various tests performed with the HTS cable prototypes in EDIPO is listed in figure 4.21. Each line in the figure is a function of number of electromagnetic cycles n_c and corresponds to a high field – high current DC test on the prototypes. Two types of DC tests have been carried out: T_{cs} measurements, where the temperature is increased at fixed operating current and background magnetic field, and I_c measurements, where a current ramp is applied at fixed temperature (with only a minor temperature rise due to the joule heating in the sample) and background field.

Individual strand measurements at 77 K (as reported in 4.4.3) before the EDIPO test correspond to $n_c = 0$. Commissioning of the heat exchanger and the HTS adapter was required at the beginning of the test program, since these devices were used for the first time in the measurements. Series of 'cycling' tests, where the operating current was applied in a cyclic manner between 0 and 50 kA at 12 T, were carried out to reveal the influence of the electromagnetic loading on the performance of the prototypes. After about 1000 cycles, in one of the high temperature measurements, the HTS adapter quenched, which led to unrecoverable damage in the device. One of the halves of the adapter was burnt because the tapes in the adapter were not protected against the quench in the original design. The measurements were continued after a new HTS adapter has been manufactured (for protection, additional brass strips between tapes

Figure 4.22: Sample resistances at 5 K and zero background field.

were used in the new device). Before the second test campaign, minor improvements of the sample instrumentation have also been made: SuperPower voltage taps were re-twisted to reduce the relatively high noise present during the first campaign, and additional voltage taps were installed on the adapter (gray ticks in figure 4.17).

4.6.1 Performance of the heat exchanger and HTS adapter

The values of the resistances of the sample at various locations at 5 K and zero background field are illustrated in figure 4.22. The overall resistance of the sample of about 10.5 nΩ is composed of 0.9 nΩ at the bottom joint, 3.3 nΩ at the top joints and 6.3 nΩ of the first adapter interface. Step-like operation for the transport current and temperature, conventionally used in measurements of LTS cables in the SULTAN test facility, is not possible. Continuous ramps were used instead. A minor increase in the resistance of the top and bottom joints with the increasing number of cycles n_c has been detected, as it will be discussed in section 4.6.4.

The heat exchanger demonstrated an acceptable performance, operating up to 40 K of outlet temperature of the sample. The temperature of helium gas measured by the sensors T90, T93, T91 and T92 (see figure 4.18) during the T_{cs} test at 12 T background field and 20 kA operating current is given in figure 4.23. In this measurement, the temperature of the sample was increased above 40 K, while the temperature of the return flow to the refrigerator T93 is kept well below 20 K. The initial offset of 12 minutes is due to the current ramp to 20 kA.

4.6.2 DC test results

In order to obtain I_c or T_{cs} values from the DC measurements, we use average signals from the six pairs of voltage taps VH2-VH4/VH1-VH3 and from the set of four temperature sensors T2-T4/T1-T3 for SuperPower/SuperOx. In contrast with some Nb$_3$Sn ITER conductors, the variation among the six pairs of voltage taps was found to be very small. This is an indication that the cable cross-section is equipotential. For an electric field below 1 μV/cm, the temperature gradient along the length of the prototypes is lower than 0.25 K.
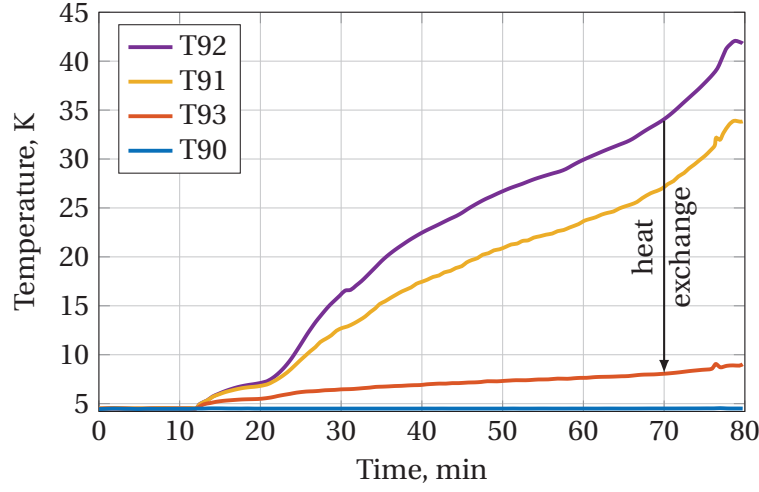
Figure 4.23: Inlet and outlet temperatures of the heat exchanger in the T_{cs} test at 12 T and 20 kA. Labels of the temperature sensors are from the cryogenic circuit presented in figure 4.18.

Examples of the $E - T$ transitions for the SuperOx prototype in a background field of 12 T and at operating currents I_{op} from 20 kA up to 60 kA are shown in figure 4.24. Similar curves are observed at 10 T and 8 T background fields. For the measurements performed at $I_{op} > 50$ kA the superconducting transition starts at temperatures lower than 4.5 K and the base line is not visible. Standard power-law dependences are used for the voltage-temperature $E(T)$ and voltage-current $E(I)$ transitions:

$$E(T) = E_c \left(\frac{T}{T_{cs}} \right)^m \qquad E(I) = E_{\text{offset}} + E_c \left(\frac{I}{I_c} \right)^n \qquad (4.15)$$

where $E_c = 1 \, \mu\text{V/cm}$, unless otherwise stated. E_{offset} is the inductive electric field due to the current ramp, and is considered as a fit parameter for the $E(I)$ transition.

The corresponding exponential m-values are also reported in figure 4.25. The results are plotted together with the expected m-values obtained by applying the scaling laws to the short sample measurements. The full transition can be calculated from (4.14) by increasing T, which allows extracting the m-value using the fit function (4.15). Relatively low m values are expected because of the intrinsic properties of coated conductors, i.e. very high critical temperature and operating currents. Only the operation at low currents can guarantee a sharper transition. While the m values measured at 12 T follow roughly the expected trend, the values measured at 8 T and 10 T are significantly lower than expected. Unlike Nb$_3$Sn conductors, it could be possible to operate HTS conductors at currents close to the critical current still retaining a sufficient temperature margin, but the superconducting transition will be relatively broad. During the $E - I$ test at 12 T the exponential n value was found to be about 12

SuperOx conductor at 12 T

SuperOx conductor
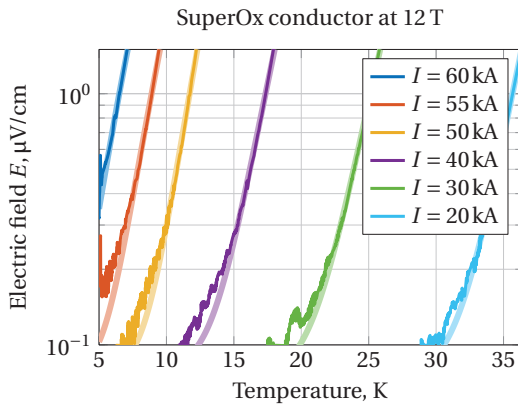
Figure 4.24: $E-T$ transitions of the SuperOx prototype at 12 T and operating current from 20 kA to 60 kA.
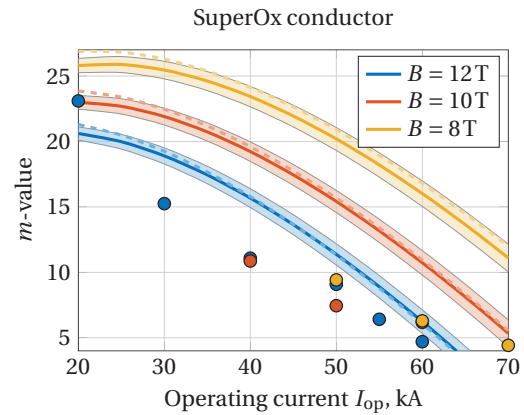
Figure 4.25: m-values of $E-T$ transitions of the Superox prototype at various fields and operating currents.

at a temperature of about 6 K.

Results of the T_{cs} and I_c measurements are summarized for the SuperPower leg in figure 4.26. Dashed and solid lines in the left plot are obtained from the assessment procedure of the conductor performance (details are in previous section 4.5). Results of the simple scaling of the tape properties in a perpendicular field are shown with the dashed lines. For the solid lines, the distribution of the generated magnetic field and the $I_c(\theta)$ angular dependence were taken into account. The bands indicate an error margin of ±3.3 %, which comes from the uncertainty on the assessed critical current of the cable at 12 T, 4.2 K due to the limited set of data available from the short tape measurements.

In the right plot of figure 4.26, the values at $E_c = 0.1\,\mu V/cm$ are also reported, but the assessment of the T_{cs} values at 0.1 μV/cm was not carried out because the data for the determination of the parameters at this criterion are not available.

Similar plots for the SuperOx prototype are presented in figure 4.27. The bands in the case of SuperOx indicate an error margin of ±2.4 %.

For both conductors the measured values are within a few percent from the expected values, at least in the region close to 12 T, 4.2 K, where the tapes were measured. The tape transport properties were fully retained after the full scale R&D activity. At much higher temperature or, in the case of the SuperPower conductor, at lower field, the deviation of the measured values from the expected ones is probably due to the inaccuracy of the fitting parameters of the scaling laws. Strictly speaking, the error bands of ±3.3 % for SuperPower and ±2.4 % for SuperOx correspond to the accuracy of the assessment only at 12 T / 4.2 K. At the other field-temperature conditions, where the short tape samples were not measured, the accuracy is significantly reduced.
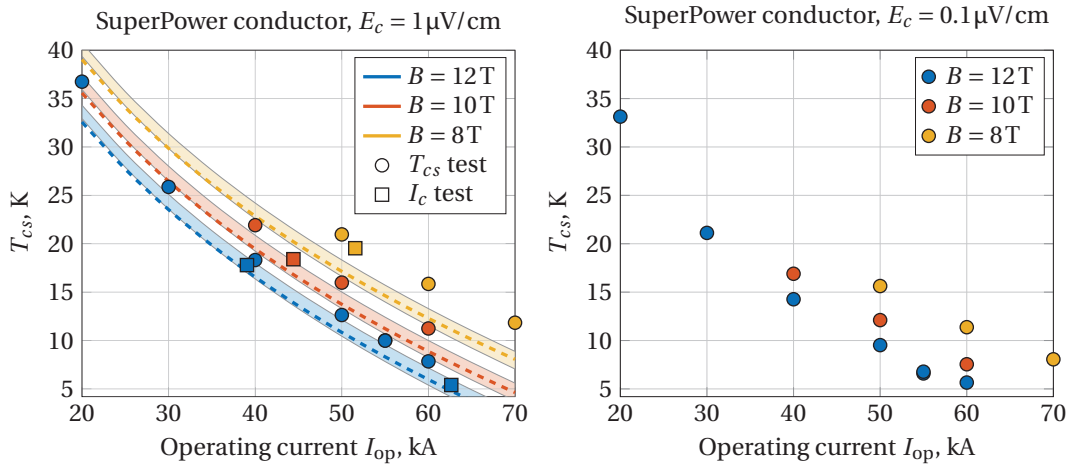
Figure 4.26: Current sharing temperatures and critical currents of the SuperPower prototype at various background magnetic fields and operating currents for voltage criterion $E_c = 1\,\mu\text{V/cm}$ (left) and $E_c = 0.1\,\mu\text{V/cm}$ (right).
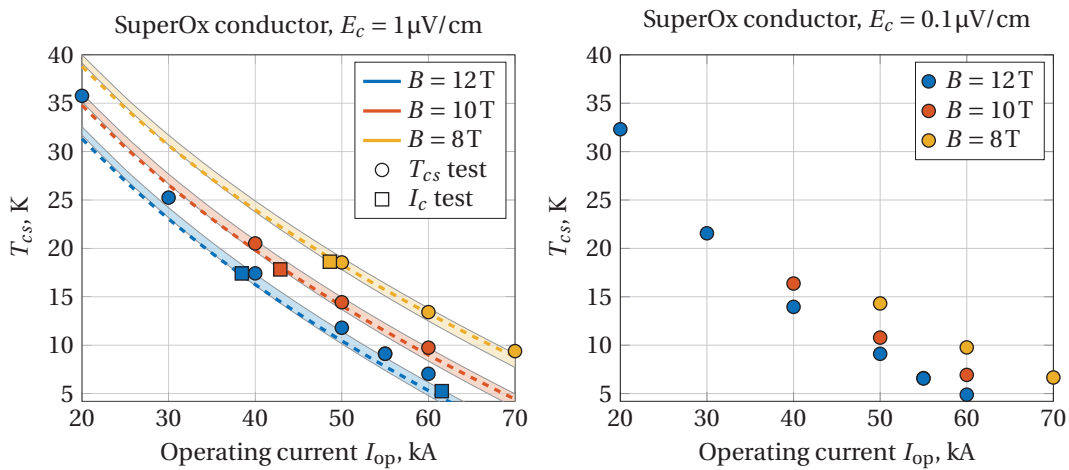
Figure 4.27: Current sharing temperatures and critical currents of the SuperOx prototype at various background magnetic fields and operating currents for voltage criterion $E_c = 1\,\mu\text{V/cm}$ (left) and $E_c = 0.1\,\mu\text{V/cm}$ (right).

4.6.3 AC test results

The total AC losses of the cables in the applied time-varying magnetic field have been measured using a calorimetric method. The power loss per unit length P released in the helium flow can be calculated as:

$$P = \left(h(T_{\text{out}}, p) - h(T_{\text{in}}, p)\right) \dot{m}/l \qquad [\text{W/m}] \qquad (4.16)$$

where T_{in} and T_{out} are the average inlet and outlet temperatures, T1/T2 and T3/T4 for SuperOx / SuperPower according to figure 4.17; $\dot{m}$ and p are the helium mass flow-rate and absolute pressure measured by FI1953/FI1954 and P1951/P1952 according to figure 4.18. The distance between the temperature sensors is $l = 1.36\,\text{m}$. The dependence of the helium enthalpy upon the temperature and pressure $h(T, p)$ is obtained by interpolating the tabulated data from [63]. The accuracy of this calorimetric method is poor at low frequencies, thus the lowest used frequency is 0.05 Hz.

After the AC field with amplitude B_a and frequency v is applied, the temperature of the helium flow increases and normally reaches a plateau. However, in some measurements only a partial stabilization of the temperature was reached, mostly at low frequency of the AC field. The value of the temperature plateau T_2 can be recovered by fitting the signal with the following regression function:

$$T(t) = \begin{cases} T_1, & t \leq t_1 \\ T_1 + \left(T_2 - T_1\right)\left(1 - e^{-\alpha_1(t-t_1)}\right), & t_1 < t \leq t_2 \\ T_3 + \left(T(t_2) - T_3\right)e^{-\alpha_2(t-t_2)}, & t > t_2 \end{cases} \qquad (4.17)$$

This function contains in total 7 input parameters: $t_1, t_2, \alpha_1, \alpha_2, T_1, T_2, T_3$. Examples of the temperature signals during an AC test with $B_a = 0.3\,\text{T}$, $v = 0.1\,\text{Hz}$ in a background field 2 T are shown for both conductors in figure 4.28. The corresponding fits (gray lines) are also reported. Although in most of the measurements the steady state conditions have been achieved and use of (4.17) may seem overcomplicated, this allows automatizing the AC loss calculation. The values obtained for T_2 at the inlet and outlet of each prototype are directly used in (4.16) to calculate the power loss P. Finally, the energy loss per cycle per unit length Q is obtained as P/v (in J/m/cycle).

Three operating conditions were studied: (a) $B = 0\,\text{T}, I = 0\,\text{kA}$, (b) $B = 2\,\text{T}, I = 0\,\text{kA}$ and (c) $B = 10\,\text{T}, I = 50\,\text{kA}$, where I is the transport current, B is the DC magnetic field parallel to the broad side of the cables (see figure 4.17). The DC joule power loss in the (c) condition was approximately 0.41 W/m and 1.49 W/m for the SuperPower and SuperOx prototypes respectively, i.e. (c) corresponds to an advanced current sharing in the cables. The values are slightly different, because these measurements were done after about 1500 electromagnetic cycles (see figure 4.21), at which a higher performance degradation was present in the SuperOx leg (to be discussed in the next
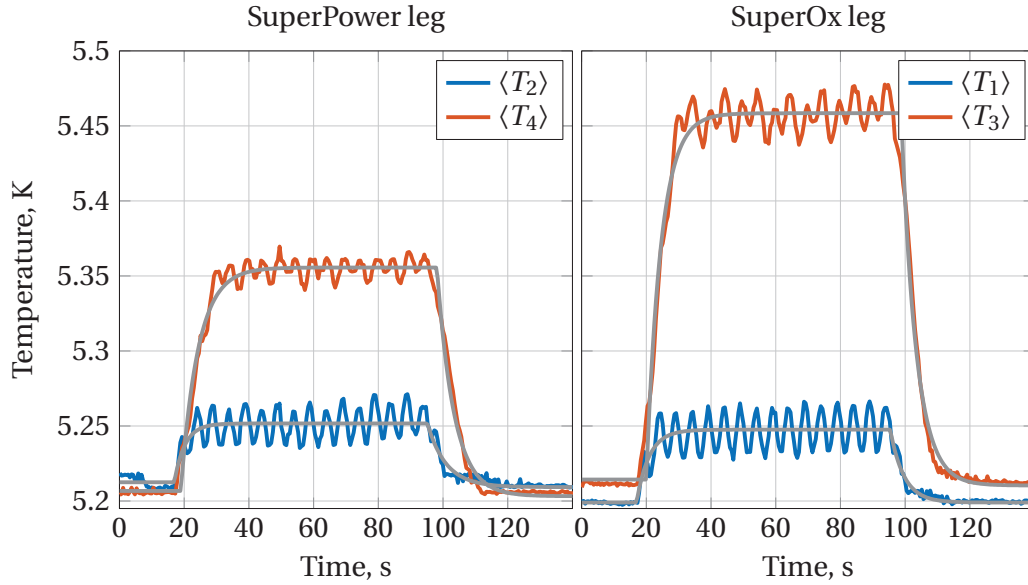
Figure 4.28: Average temperatures of the helium flow in the prototypes measured in background field $B = 2\,\mathrm{T}$ and AC field $B_a = 0.3\,\mathrm{T}$ at $\nu = 0.1\,\mathrm{Hz}$. The AC field is switched on at $t \approx 20\,\mathrm{s}$ and switched off at $t \approx 100\,\mathrm{s}$. Labels in legend correspond to the temperature sensors shown in figure 4.17.

section). These DC loss contributions were subtracted from the total power loss (4.16).

The results of the measurements are shown for both prototypes in figure 4.29. The data in the right plot were obtained during the second test campaign (see the test program in figure 4.21). The energy loss Q is proportional to B_a^2 for the different amplitudes used in the measurements: $0.1\,\mathrm{T}$, $0.2\,\mathrm{T}$ and $0.3\,\mathrm{T}$. Note that with increasing B_a the accuracy of the measurements also increases, but the frequency range where the measurements can be performed becomes narrower.

By comparing the results for the conditions (a) and (b) in the right plot of figure 4.29, we conclude that SnPb solder is responsible for the noticeable difference. For temperatures below $7\,\mathrm{K}$, SnPb is superconducting at $0\,\mathrm{T}$ (see section A3.9 in [64]), while at $2\,\mathrm{T}$ is already in a normal state. In the case (c), when the higher DC magnetic field and transport current were applied, the corresponding transverse Lorentz force ensures a better contact between the strands and the copper cable core (i.e. inter-strand resistivity ρ_{is} is decreased) and the cables are almost saturated with the transport current (i.e. a smaller margin is available for the induced currents). The impact of these factors on the AC performance will be further discussed in chapter 5.

The energy of the AC field stored in the cable cross-section can be roughly estimated as $Q_0 = \frac{B_a^2}{2\mu_0}S$, where $S = 74\,\mathrm{mm} \times 26\,\mathrm{mm}$ is the actual rectangular cross-section of the prototypes (the design value is $70.3\,\mathrm{mm} \times 24.4\,\mathrm{mm}$, see figure 4.12). The AC loss results
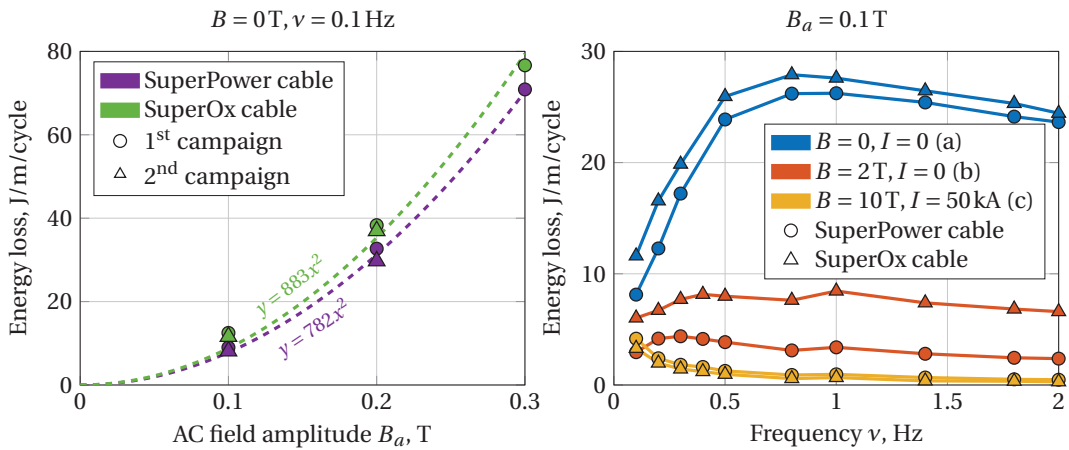
Figure 4.29: The energy loss for the SuperPower and SuperOx cables as a function of the AC field amplitude at $\nu = 0.1\,\text{Hz}$ and zero background field (left plot) and as a function of the frequency at $B_a = 0.1\,\text{T}$ (right plot).

obtained during the first and second campaigns are normalized to Q_0 in order to exclude dependence over B_a in the data representation. They are summarized for both cables in figure 4.30. Typical data for TF and CS ITER cables [16] at $B_a = 0.2\,\text{T}$ and normalized to $Q_0 = 30.6\,\text{J/m/cycle}$ are also reported for comparison. Note that the measurements at $B = 10\,\text{T}, I = 50\,\text{kA}$ were performed only in the second campaign. For the other two operating conditions, the data points of the first campaign have lighter colors. There is only a small influence of warm up-cool down and cycling tests on the AC performance of the cables.

Whether the obtained AC energy losses are acceptable or not depends on the cryogenic analysis of the whole magnet system, including the nuclear heating effect. The values of the hysteresis AC loss can be obtained by extrapolating the measured values down to zero frequency: at $B_a = 0.3\,\text{T}$ and $B = 2\,\text{T}$ they are estimated from $5\,\text{J/m/cycle}$ to $10\,\text{J/m/cycle}$ for the SuperPower cable and from $15\,\text{J/m/cycle}$ to $30\,\text{J/m/cycle}$ for the SuperOx one. The hysteresis loss represent only a fraction of the total losses, the main contribution coming from coupling losses. Coupling losses have two different sources: losses in the strands (coupling among tapes in the strand) and losses in the cable (coupling among strands). The lower total AC loss observed in the SuperPower cable can be due to the fact that the strands are only in loose contact, thus the higher contact resistance decreases the amplitude of the coupling currents. In the SuperOx cable the inter-strand resistance is somehow lower (the strands are tightly packed), and the inter-strand loss is larger than in the SuperPower cable.

The intra-strand coupling loss can be reduced by using a solder alloy with higher electrical resistance; the inter-strand coupling loss can be reduced by plating the copper core so that the strands cannot couple through the core. Detailed analyses of
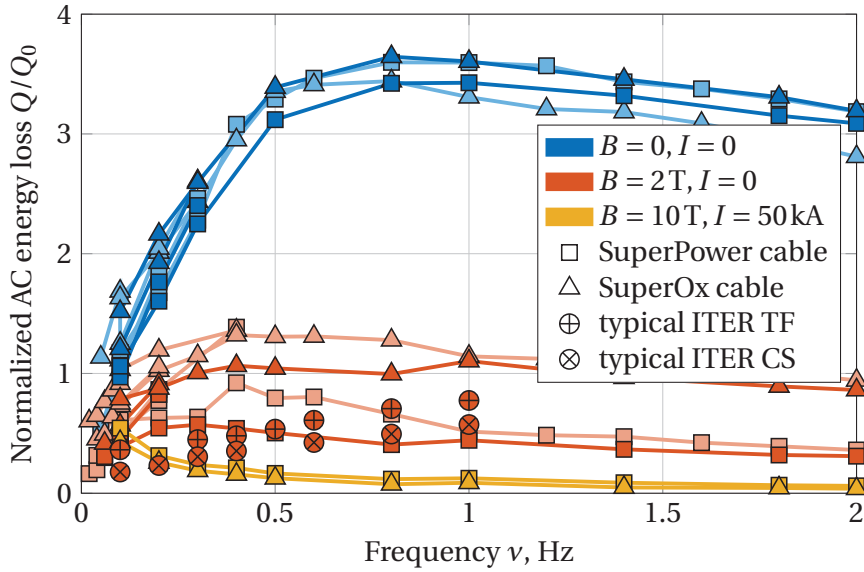
Figure 4.30: Comparison of AC test results obtained during the first (lighter colors) and second test campaigns (darker colors). Typical data for ITER TF and CS cables are also shown.

the hysteresis, intra- and inter-strand losses will be presented in chapter 5.

4.6.4 Cycling test results

After the initial set of DC measurements, during which the current in the conductors was ramped about 20 times at high magnetic field, the conductors went through electromagnetic cycling, consisting in ramping the current from zero to 50 kA and back to zero in a background field of 12 T. In this way transverse electromagnetic forces as large as 600 kN/m are applied to each conductor. After 100 cycles the T_{cs} at 12 T and 50 kA was measured again. Then, increasing the number of electromagnetic cycles n_c the DC measurements were repeated at intermediate steps. In total, 2005 test cycles have been carried out on the cable prototypes.

The resistances of the bottom joint, top joints and adapter interface were obtained for every DC measurement of the sample. The evolution of the sample resistances as a function of number of cycles n_c is presented in figure 4.31. The symbols in the figure correspond to different DC fields explained in the legend. While the current ramp for most of the measurements was done at ≈ 5 K, in some of them (such as $n_c = 502, 1003$ etc.) the initial temperature was higher, up to 18 K, leading to higher values of the resistance.

The resistances of the bottom and top joints tend to increase with n_c. The initial
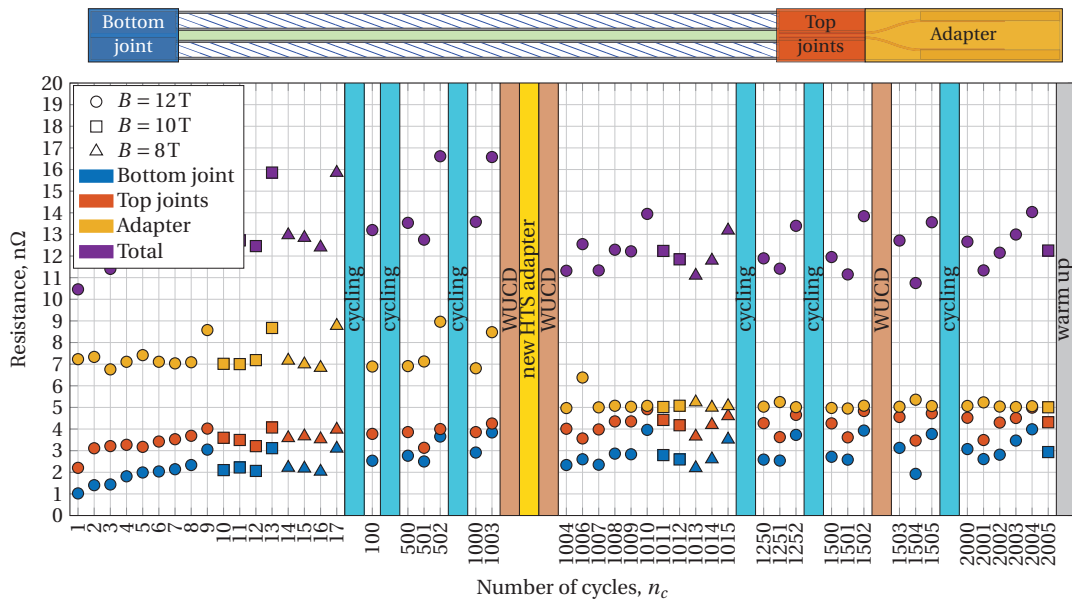
Figure 4.31: Resistances of the sample as a function of number of cycles n_c.

values of about $1\,\text{n}\Omega$ for the bottom joint and $2\,\text{n}\Omega$ for the top ones increase up to $3\,\text{n}\Omega$ and $4\,\text{n}\Omega$ at the end of the second test campaign. The increase of the resistance of the bottom joint was detected on the V20-V21 pair of voltage taps (see figure 4.17), while the resistance of the bottom terminals measured by V20-V2 and V21-V1 was in the range from $0.3\,\text{n}\Omega$ to $0.4\,\text{n}\Omega$, unaffected by the cycling.

Note that the resistance of the new adapter is lower than that used in the first test campaign. For the first adapter there was also a noticeable difference in the resistance of left and right sides ($\sim 2\,\text{n}\Omega$). When that adapter was burnt during the quench at the end of the first campaign, the side with higher resistance was the one that initiated this process. With the new HTS adapter the resistances of both sides are almost identical, what reflects a higher manufacturing quality of the new adapter. Since the HTS adapter is necessary for a high temperature operation in EDIPO or SULTAN, $\approx 5\,\text{n}\Omega$ are already 'used' out of total $10\,\text{n}\Omega$ requirement. This means that bottom and top joints of future HTS cable prototypes should be designed to meet $\approx 5\,\text{n}\Omega$ requirement, allowing to operate transport current and temperature in steps.

The performance of the cable prototypes during the cycling test was continuously degrading with increasing number of cycles n_c. The comparison of voltage-temperature curves for all the T_{cs} tests performed at $50\,\text{kA}$ and $12\,\text{T}$ for the both prototypes is shown in figure 4.32. In these plots the temperature is an average value for T2, T4 sensors for SuperPower and T1, T3 – for SuperOx. The electric field is an average between the six pairs of voltage taps (VH2-VH4; VH1-VH3) normalized by $1\,\text{m}$ length (according to figure 4.17). In the first test campaign, corresponding to n_c up to 1003, there was an
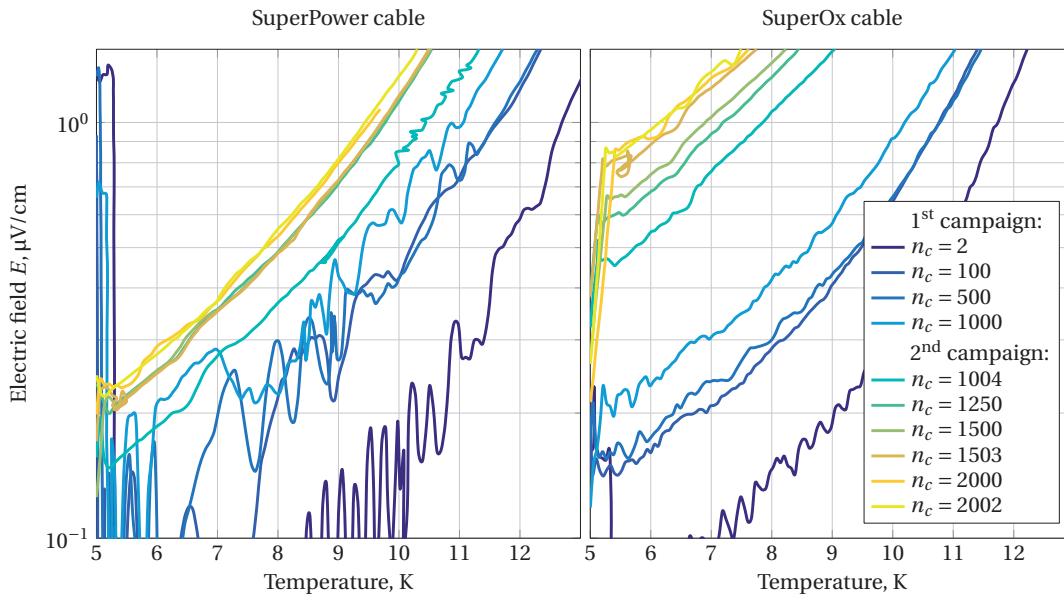
Figure 4.32: Smoothed voltage-temperature curves of SuperPower and SuperOx prototypes at 50 kA / 12 T for various number of electromagnetic cycles n_c.

instrumentation problem with voltage taps of the SuperPower leg resulting in a high signal noise. As one can see from figure 4.32, this was fixed in the second campaign, corresponding to n_c from 1004 to 2005. A strong performance drop of the SuperOx leg was observed at $n_c = 1004$ (beginning of the second campaign), which reflects presumably an influence of the warm up-cool down (WUCD) tests on the cable performance. For this and the following T_{cs} tests, the superconducting transition in the SuperOx leg starts already during the current ramp up to 50 kA.

The evolution of the T_{cs} values obtained at 50 kA and 12 T with the increasing number of cycles is reported in figure 4.33. The WUCD tests performed after 1003 and 1502 cycles have much stronger influence on T_{cs} of the SuperOx leg than that for the SuperPower. The reason for that is not clear. At the end of the measurements T_{cs} is degraded by about 25 % in the SuperPower cable and by 45 % in the SuperOx one. Presumably, saturation of the T_{cs} was not achieved right up to 2005 cycles.

In order to fully characterize the performance evolution of the cables, the expected values of T_{cs} and I_c were calculated from (4.14) using corresponding (B, I) or (B, T) operating conditions of each measurement. Then, both the numerical and experimental sets of data were considered as $I_c(B, T)$ data disregarding the type of test, which allows us to consider the simultaneous evolution of the cable performances as a function of n_c. Results for the SuperOx prototype are presented in figure 4.34. As in figure 4.31, different symbols correspond to different magnetic fields, while the colors represent a temperature range in which the E_c criterion was reached. It is
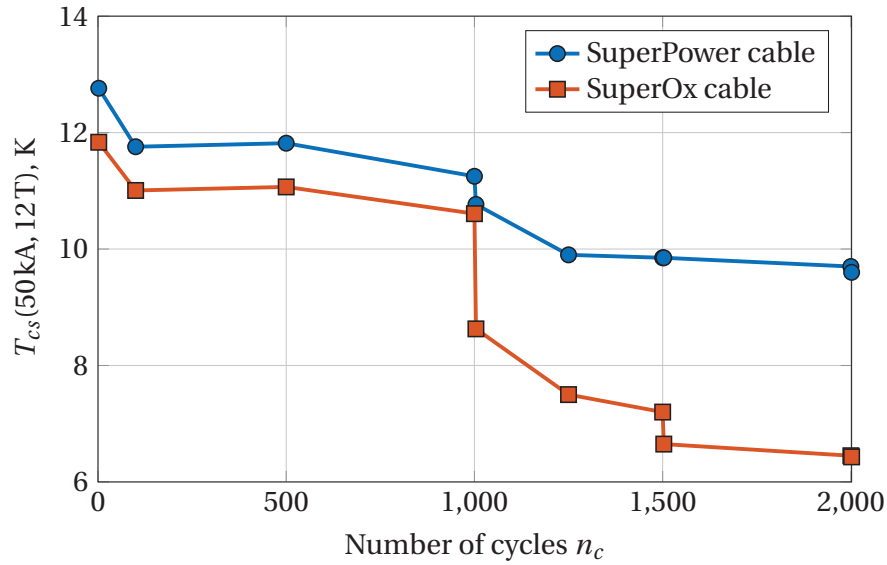
Figure 4.33: Current sharing temperature at at 50 kA / 12 T as function of number of cycles n_c for the SuperPower and SuperOx cables.

important to notice that the degradation of the cable performance progresses almost independently of the operating conditions, i.e. it moves as a function of cycles at the same rate for all conditions. For the temperature range from 30 K to 40 K, the obtained high values are due to the low accuracy of the scaling law for SuperOx at high temperature.

Average results of individual strand test at 77 K are also presented in figure 4.34 at $n_c = 0$ and $n_c = 2005$. These measurements were performed before the EDIPO test (as already discussed in section 4.4.3) and afterwards (to be discussed in section 4.7). The cable performance at self-field / 77 K follows the same trend as the one at lower temperatures and high magnetic fields. Roughly 20 % of the I_c performance degradation was observed with the SuperOx prototype at the end of the second test campaign.

The same data analysis was performed for the SuperPower prototype. As already stressed in section 4.6.2, the chosen scaling law parameters for SuperPower tapes are not well representative for the prototype. The measured T_{cs} and I_c values are typically higher than expected, especially at $B < 12$ T. Nevertheless, this scaling law was used in the calculation for consistency. As a result, the data for the evolution of the SuperPower prototype presented in figure 4.35 are much more scattered than that for the SuperOx. In spite of this, it is still possible to draw the same conclusion: the degradation of the SuperPower cable performance is almost independent of the operating conditions. The average I_c degradation observed at the end of the measurements is about 10 %.

Note that for the measurements in EDIPO, error bars in the figures are due to uncertainty in the cable I_c and the temperature gradient along the cables ($\lesssim 0.25$ K in the
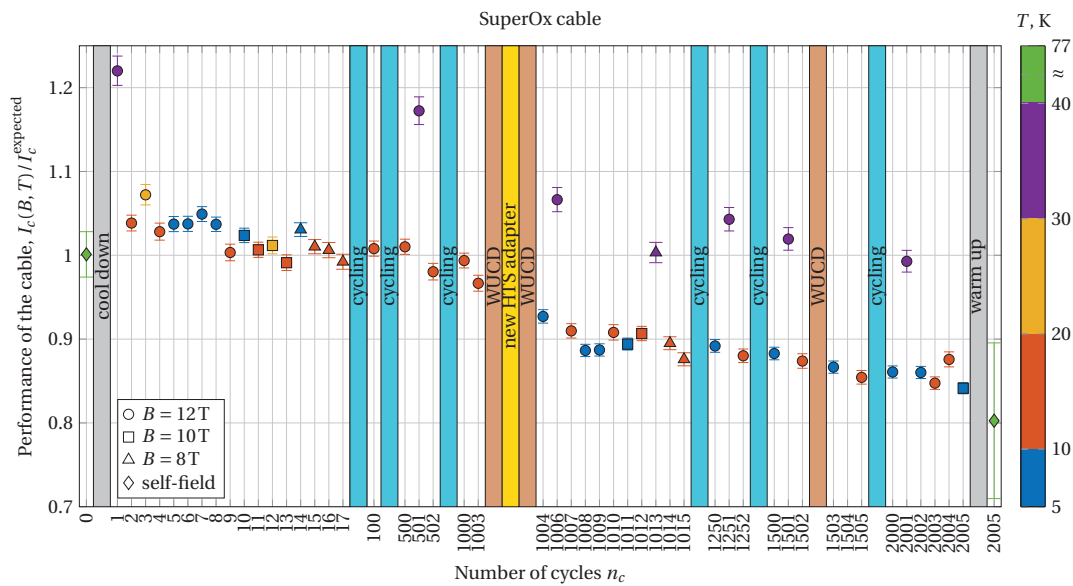
Figure 4.34: Performance evolution of the SuperOx prototype as a function of number of cycles n_c.
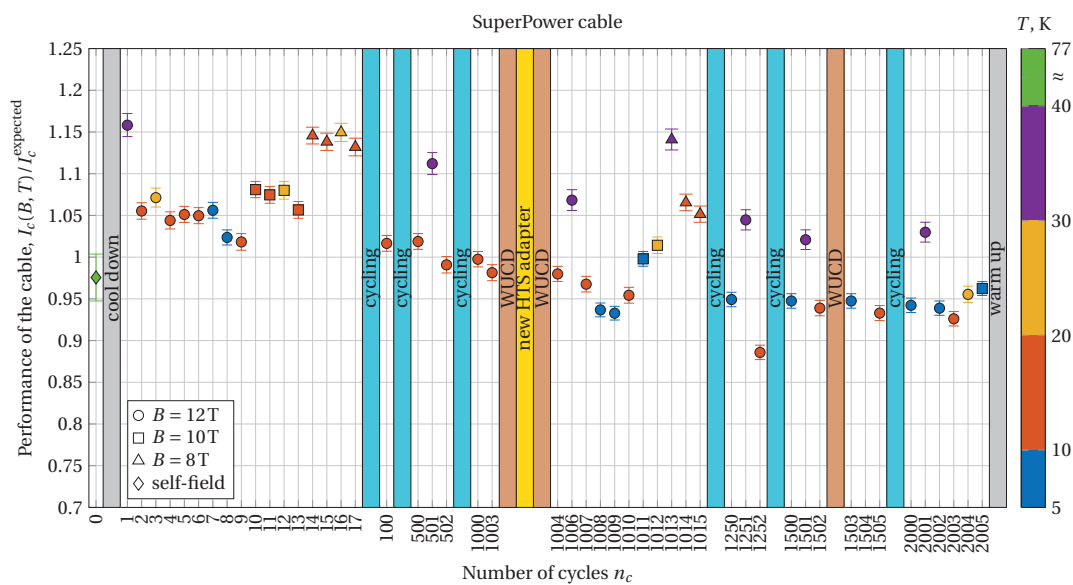
Figure 4.35: Performance evolution of the SuperPower prototype as a function of number of cycles n_c.
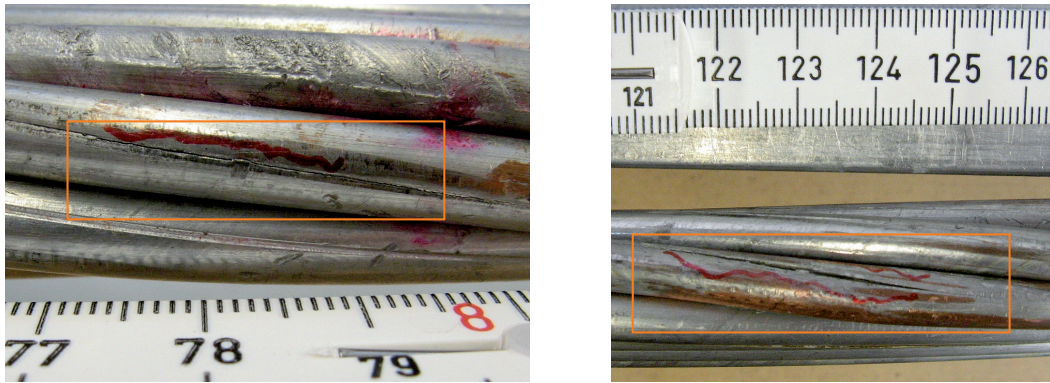
Figure 4.36: Photographs of the damaged regions at edges of the SuperOx cable after the test in EDIPO. Rectangles indicate the cracks between the copper profiles, caused by the transverse Lorentz force. The highest degradation of the strand I_c was also obtained at these regions.

DC tests). For the measurements at self-field / 77 K, the error bars are purely statistical, representing the I_c dispersion of the test results (see figure 4.15). It should also be noted that a more sensitive criterion E_c is desirable (i.e. 0.1 µV/cm, typical for LTS wires), since this may drastically increase the sensitivity of the test results.

4.7 Investigation of the cyclic load degradation

After the measurements in EDIPO it was decided to investigate further the reasons of DC performance degradation of the prototypes. The SuperOx conductor was chosen for disassembling since, after the cycling test, it has a degradation twice as high as the one observed with the SuperPower cable, so a larger performance reduction at 77 K is also expected. In addition, the Superox cable is slightly narrower than the Superpower, but the dimensions of the steel jacket are the same. Therefore, two steel curved profiles were inserted between the cable edges and the jacket in order to fill up the space. When the jacket is cut (by milling), the cable is protected by the steel profiles.

After disassembling the terminals, the jackets were cut and removed. The cable was visually inspected to identify possible defects. It was found that in four locations the soldering between the copper profiles that compose the strands cracked, as shown in figure 4.36. Based on our experience, such fractures usually extend into the stack of soldered tapes, causing the delamination of the superconducting layer and a drop in critical current [65]. The fractures were found in the high field region and in three cases out of four were located at the edges of the cable.

Considering as a reference point the results of the I_c measurements at 77 K after

Figure 4.37: Photograph of the strands after extraction from the SuperOx prototype.

the strands were cabled (see details in section 4.4.3), it was first decided to carry out similar measurements directly on the cable in a liquid nitrogen bath. In most of the measurements, regular VI curves have been recorded, showing on average a degradation of I_c of about 20 %.

However, a non-monotonic built-up of the voltage with increasing current or a negative slope of the voltage were observed for some of the strands. It was not possible to reliably measure the I_c of each individual strand directly on the cable because a large copper piece was soldered at the cable end, see right bottom photograph in figure 4.16. This copper piece caused advanced current sharing among the strands. In order to avoid this situation, the copper piece was de-soldered and removed. The whole cable was disassembled and all the strands were removed from the flat copper core, as shown in figure 4.37.

Small copper terminals were soldered on all twenty strands and the critical current was measured placing the voltage taps around bent sections (where the strands were bent around the edges of the flat copper core) and around the straight sections. Although these locations were not measured on the as-manufactured strands, the variation in I_c along the strands should be about 1 %. This was measured on three sections each 50 cm long for each strand, see section 4.4.3. Figure 4.38 shows the full distribution of the retained I_c in the SuperOx strands. The value of I_c after testing in EDIPO is normalized to the values measured before the strand cabling. The largest reduction is located at the cable edges. On the flat unloaded region the normalized I_c is close to unity.

The average values of the I_c retention at the flat regions and edges of the cable are
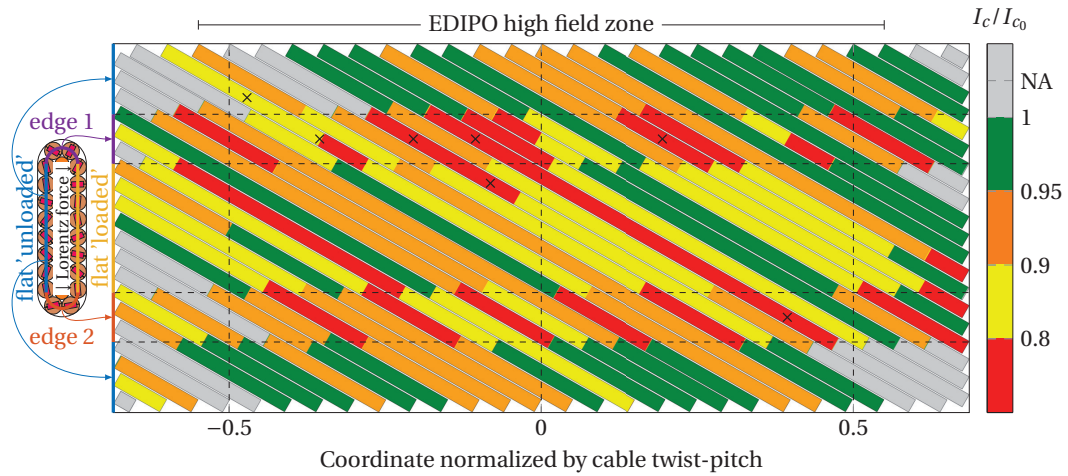
Figure 4.38: Distribution of I_c retention of the strands in the Superox leg. The sections with the highest I_c degradation at each region of the cable are shown with the crosses.

Table 4.2: Average retention of the strand I_c at 77 K after measurements in EDIPO.

Location	Flat 'unloaded'	Flat 'loaded'	Edge 1	Edge 2
I_c retention	0.96 ± 0.04	0.89 ± 0.11	0.84 ± 0.14	0.83 ± 0.14

given in table 4.2. The high standard deviation of the values is due to a high spread of the measured values at the every region. The only difference between the flat 'unloaded' and 'loaded' regions is the accumulation of Lorentz forces in the latter one, what is also reflected in the obtained I_c retention. This allows us to conclude that this transverse load is responsible for the performance degradation of the prototypes.

Absolute transverse Lorentz stresses during the cable operation are relatively low, as discussed in section 4.2.2. In other words, the I_c degradation is not expected if such loading is applied just once. Nonetheless, it was already demonstrated in section 3.9 that the strands may still fail under cyclic loading at low amplitudes, due to fatigue behavior of the strands made of annealed copper. The value of I_c in the bent strands (i.e. applied axial strains) is even more sensitive to the cyclic loading, which also agrees with the higher reduction obtained at the cable edges, where the strands are subjected to bending.

For each region of the cable, the strand sections where the highest I_c degradation was found were further investigated. The locations of 7 selected sections are shown in figure 4.38 with crosses. The sections of about 15 cm length were cut from the strands and the tapes have been carefully extracted by soldering. Finally, the critical current of all the 112 extracted tapes was measured in a liquid nitrogen bath.

An extremely non-uniform distribution of the critical currents was observed. For each
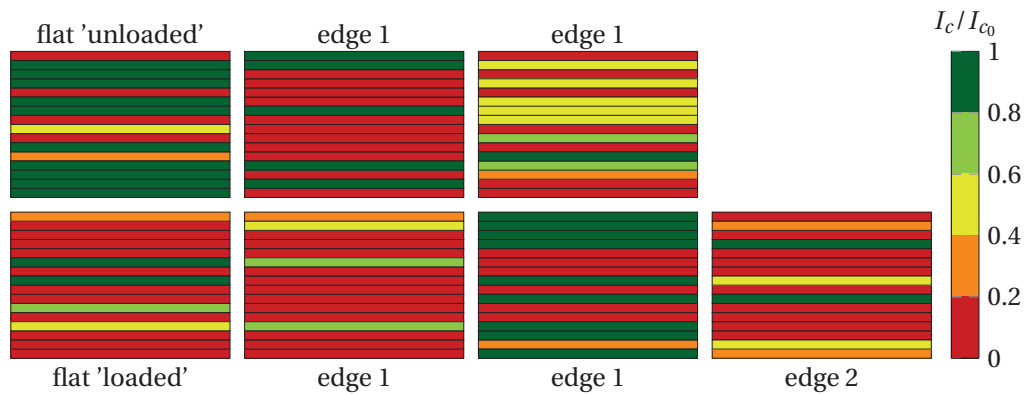
Figure 4.39: Sketch of a transverse view for the I_c retention in the tapes extracted from the strand sections with the highest overall degradation at each region of the cable (see cross markers in figure 4.38). Each stack comprises 16 tapes.

selected section there are at least several tapes with a critical current of about 1 A. In many cases such high degradation was localized within few millimeters, which was observed from an intensive boiling of the liquid nitrogen due to the high Joule heating in these regions. In few cases the damaged regions take more than 50 % of the tape length.

As can be seen from figure 4.39, a correlation between the I_c degradation and the position of the tape in the stack has not been observed on the extracted tapes. Thus, the obtained results are summarized in a statistical manner in figure 4.40. While the initial I_c (according to the specifications provided by the manufacturer) ranges from 140 A to 160 A and I_c for almost 20 % of the extracted tapes is still higher than 140 A, I_c for half of the extracted tapes is lower than 20 A.

Note that when localized defects are present in the strand, the I_c value of the strand can even be higher than the sum of I_c values of the tapes of which the strand is made of. As discussed in section 3.5, this is expected for strands with broad $V - I$ transitions (i.e. low n-value). The reasons for a high non-uniformity of the I_c degradation both in the longitudinal (i.e. figure 4.38) and transverse (i.e. figures 4.39 and 4.40) directions of the strand are not yet identified.

SuperOx tapes at 77 K
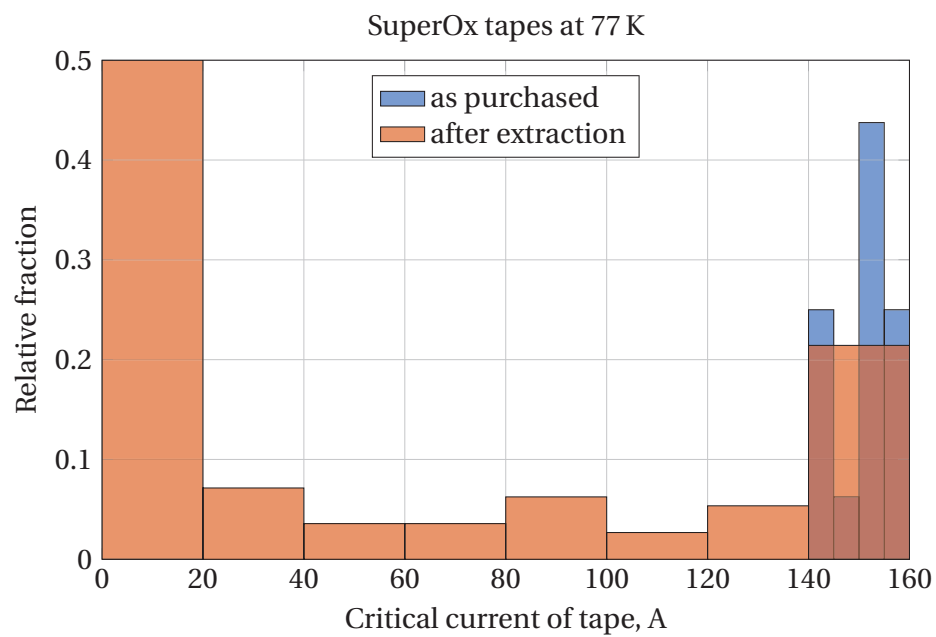
Figure 4.40: Distribution of the critical current measured at 77 K on the tapes extracted from the SuperOx strands at the selected locations (cross markers in figure 4.38). In total, 112 tapes have been measured; corresponding initial distribution provided by the manufacturer is also shown.

4.8 Conclusion

The Rutherford cable design with a central copper core has been investigated for use with round HTS strands. Analytical expressions are proposed for the main properties of the design. The obtained relations for the minimum permissible twist-pitch and bending radius of the cable and for the transverse pressure on strands due to the Lorentz force can be used to infer a first estimate of the cable mechanical properties.

No major technological issues arise during the manufacturing of the two full-size cable prototypes, made of the SuperPower and SuperOx tapes. For all the forty 16-tape strands (20 SuperPower and 20 SuperOx), each about 2.5 m long, the critical current measured at 77 K is within several percent from the expected values. Although the terminals of the prototypes have also been successfully manufactured, it is envisaged to simplify their design, eliminating the requirement for each stack to have a specified orientation.

The following conclusions can be made from the measurements in EDIPO:

- The feasibility of the proposed HTS cable concept for fusion magnets has been experimentally demonstrated from the performed DC tests, in which the transport properties of the tapes were fully retained. It is possible to operate the HTS cables with the temperature margin of about 5 K at the relatively high transport current, $I/I_c \sim 0.85$.

- The energy loss of the prototypes is relatively high if compared with the ITER cables, although it was not addressed during the design considerations of the prototypes. This aspect must be taken into account in the next prototypes.

- The degradation of the I_c performance for both cables is mainly driven by the cycling test. It progressively increased up to 10 % and 20 % after about 2000 electromagnetic and several warm-up-cool-down cycles for the SuperPower and SuperOx prototypes, respectively. The phenomenon is not yet fully understood. The preliminary results obtained during the cyclic loading on single strands (discussed in the previous chapter) suggest that the profile annealing is responsible for the degradation, especially when the strands are bent. However, a noticeable discrepancy between the two datasets (i.e. EDIPO cycling test and single strand measurements) and extremely non-uniform distribution of the I_c degradation detected on the SuperOx prototype are still a matter of further investigations.

In general, despite of the cyclic load issues, the results obtained from the EDIPO measurements encourage us to keep developing the proposed HTS cable design. A further improvement of the cable properties is anticipated for the next prototypes, based on the results already obtained and on the dedicated studies of the AC loss and quench properties. These aspects are a matter of discussion in the following chapters.

5 Analysis of AC losses

Although the superconducting cables are able to carry DC current without energy dissipation, energy losses are still present in transient situations. In fusion magnets, the AC losses affect mostly CS coils due to their pulsed operation. Even though the requirements on the AC losses are not specified for the DEMO CS cables at the present stage, loss minimization should be considered as a design criterion for these cables. As the use of HTS cables is also envisaged for the DEMO CS coils and the geometry of the studied cable design does not match the available AC loss models, in this chapter we investigate the AC properties of the cable and propose analytical tools for an assessment of AC losses.

The main assumption of the present study is that the different loss contributions to the overall losses – namely, the hysteresis loss in the stack Q_{hyst}, and the coupling current loss in the strand Q_{intra} and in the cable Q_{inter} – are independent from each other. Consequently, the total AC losses in the strand Q_{strand} and in the cable Q_{cable} can be expressed as:

$$Q_{strand} \approx Q_{hyst} + Q_{intra}$$
$$Q_{cable} \approx N Q_{strand} + Q_{inter},$$

(5.1)

where N is the number of strands in the cable. It is also assumed that the energy loss due to the currents flowing entirely within the normal conductor ('eddy' current loss) can be neglected. Therefore, the results of the following analyses are restricted to a relatively low frequency ν and low rate of field change, which corresponds to the case of fusion magnets.

At low ν the energy loss per cycle due to coupling currents is proportional to ν, while the hysteresis loss is practically independent of ν. This is originated from the different mechanisms involved in formation of the AC losses: the hysteresis loss originates from the rearrangement of the magnetic flux in the superconductor, the coupling losses are due to the Joule heating in the normal conducting paths connecting the superconducting ones. Thanks to the different frequency dependence, each type of loss can be identified directly from the measurements.

5.1 Hysteresis loss

Analytical formulae for the hysteresis loss in a thin superconducting tape in a time-varying field parallel and perpendicular to its surface are available since the 70's [66, 67]. However, in a tight stack with an aspect ratio of about 1, containing tens of tapes, a strong electromagnetic interaction between tapes is present. Such situation cannot be described by analytical methods and the results for a free-standing tape are not applicable. Because of that, the hysteresis loss in stacks will be studied numerically and experimentally in this section.

5.1.1 Description of the numerical model

A general variational approach for the electro-magnetic modeling of superconductors with a smooth $E(j)$ relation is summarized in [68], where it is demonstrated that the minimization of the certain scalar function L of many variables ('functional') is equivalent to solving the Maxwell equations. Depending on which variables are considered independent, two formulations have been proposed for L, based either on magnetic field or current density-scalar potential unknowns. The latter one is selected for the modeling of the hysteresis loss since it only requires meshing over the superconductor domain. Eliminating the grid over 'air' – a region where currents are not present – reduces the number of unknowns, thus it potentially increases the computational speed.

We start by locating the stack at the origin with the c-axis along the vertical y direction and assuming the stack to be infinitely long, without twisting in the z direction. Hence we consider only longitudinal currents in the stack induced by external magnetic field and/or transport currents. A sketch of the stack geometry used in the model is presented in figure 5.1. The superconducting layer of each tape in the stack is presented in the model as a thin rectangle of width w and thickness $d = 1\,\mu$m. Considering n_t tapes in the stack and dividing each tape by N_x cells along the width, the total number of mesh elements in the model becomes $N = n_t \cdot N_x$. We use a uniform grid, so each cell has a width $s = w/N_x$ and is centered at $x_i = s \cdot (i - (N_x + 1)/2)$, $y_j = v \cdot (j - (n_t + 1)/2)$, where $i = 1 \ldots N_x$, $j = 1 \ldots n_t$, v is the vertical distance between the mesh elements.

Implying zero background magnetic field and transport current at the initial time, the trivial solution for the current distribution in the stack is $I_k(t = 0) = 0$, where $k = 1 \ldots N$ is the linear index of the mesh elements. Then, at the following time step Δt, the external magnetic field is increased by $\Delta \vec{B}_a$ at angle θ_a to the c-axis of the stack (i.e. $\Delta \vec{B}_a = \Delta B_a \{\sin\theta_a, \cos\theta_a, 0\}$), which corresponds to a change of the vector potential $\Delta \vec{A}_a = \{0, 0, (-x\cos\theta_a + y\sin\theta_a)\Delta B_a\}$ in Coulomb's gauge. In order to find the distribution of the corresponding induced currents in the stack ΔI_k ($k = 1 \ldots N$),
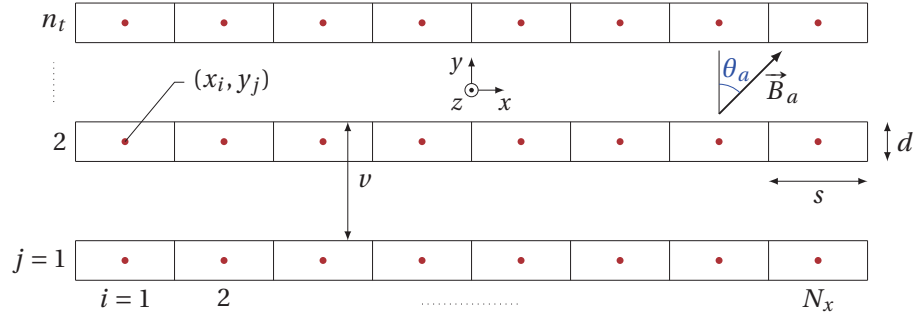
Figure 5.1: Sketch of the geometry and definitions used in the numerical model.

first the following functional (see eq. (27) in [68]) is minimized:

$$L(\Delta I) = \sum_{i=1}^{N} \left(\frac{\sum_{j=1}^{N} \frac{1}{2} C_{ij} \Delta I_j \Delta I_i + \Delta A_{a_i} \Delta I_i}{\Delta t} + \frac{E_c I_{c_i}^{cell}}{n+1} \left(\frac{|I + \Delta I|}{I_c^{cell}} \right)_i^{n+1} \right)$$ (5.2)

where the standard power law relation with $E_c = 1\,\mu V/cm$ and exponent n is used for the current-voltage transition (see equation (2.1)). $I_c^{cell} = j_c(B,\theta) \cdot s \cdot d$ is the critical current of the cell element and is a function of the magnitude and direction of the magnetic field (at a given temperature and zero strain). C_{ij} is the matrix of mutual inductances of the cell elements, which can be calculated analytically (see appendix A.3.1). Note that the original definition of L contains a term related to the transport current source ($\nabla \varphi$ in eq. (27) of [68]) that has been dropped in equation (5.2). We implement this term as a minimization constraint on ΔI: the sum of the induced currents in the stack should be equal to the applied ramp of the transport current ΔI_{tr}. Finally, in order to increase the computational speed of the numerical model, the following expression for the gradient of the functional L is used in the optimization routine:

$$\frac{\partial L}{\partial (\Delta I_i)} = \frac{\sum_{j=1}^{N} C_{ij} \Delta I_j + \Delta A_{a_i}}{\Delta t} + E_c \, \text{sgn}(I + \Delta I)_i \left(\frac{|I + \Delta I|}{I_c^{cell}} \right)_i^{n}$$ (5.3)

From the physical point of view, this expression represents the electric field that drives the current redistribution.

After the minimization of L is completed, the obtained solution ΔI (i.e. intermediate distribution of the induced currents) is used to calculate the total magnetic field $\vec{B} = \vec{B}_a + \vec{B}_{sf}$, $\vec{B}_{sf} = \{M_x, M_y, 0\}(I + \Delta I)$ (see appendix A.3.1). The obtained $\vec{B}$ allows recalculating the critical currents of the cell elements and repeating the minimization of L. After several iterations, the final distribution of the induced currents ΔI is obtained, which ensures consistency between the total magnetic field and the critical currents of the elements (within a given tolerance). As a result, the current distribution of the stack reads as $I(t + \Delta t) = I(t) + \Delta I$ and one can start the calculation of the
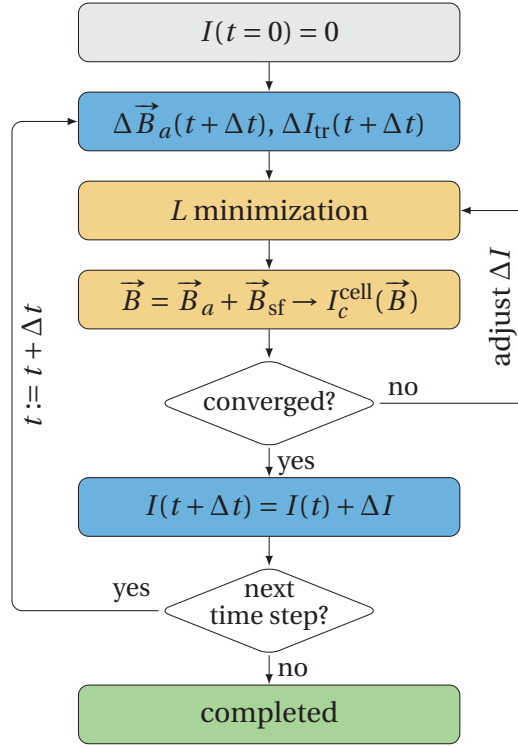
Figure 5.2: Scheme of the numerical model.

induced currents ΔI for the next time step. The diagram of the calculation procedure is illustrated in figure 5.2.

For each considered time step we calculate the magnetic moment of the stack m and instantaneous power loss P as follows (both – per unit length of the stack):

$$
m(t) = \sum_{k=1}^{N} x_k I_k(t)
$$

$$
P(t) = \sum_{k=1}^{N} E_k(t) I_k(t) = \sum_{k=1}^{N} E_c I_k(t) \left(\frac{|I(t)|}{I_c^{\text{cell}}} \right)_k^n
$$

(5.4)

Finally, we calculate the hysteresis loss per cycle using the general expression: $Q = \oint P(t)\,\mathrm{d}t$. In case of zero transport current, one can also calculate the magnetization loss of the stack from the area of the corresponding magnetization loop (see detailed discussion in [69]): $Q = \oint m\,\mathrm{d}B_a$.

5.1.2 Stack of tapes in the critical state model

There are two particular situations for the hysteresis loss that will be analyzed in the following discussion: the external AC field B_a is applied at zero transport current (pure 'magnetization loss') and the AC transport current I_{tr} is applied at zero external field (pure 'AC transport current loss'). Although these cases are not strictly relevant for fusion magnets, where both B_a and I_{tr} are non zero, the present study will help to understand what is the role of the stacking (i.e. of the parameter n_t) when either B_a or I_{tr} is applied.

The n value is set to 1000 in order to provide a direct comparison with several analytical solutions available for the superconductors in the critical state model [66], where a step-like voltage-current transition is used (i.e. $n = \infty$ in equation (2.1)) .

Magnetization loss

The presented numerical model was benchmarked against several analytical solutions for the magnetization behavior of a single tape. For instance, results of the single tape modeling with the parameters $w = 4\,\text{mm}$, $N_x = 100$, $j_c(B,\theta) = 40\,\text{kA/mm}^2$ (i.e. no field dependence, $I_c^{\text{cell}} = 1.6\,\text{A}$) are presented together with the thin-film behavior in the critical state model (see section III in [70]) in figure 5.3. The 'cusp' points in the left plot are due to the Meissner effect, which provides a specific response of superconductors on external excitation: currents are induced by an external field such that they saturate to j_c at the edges of superconducting domain and central region is at zero total magnetic field. When the field ramp is reversed, currents are first induced at the edges, providing again zero field in central region of the tape. As a result, the 'cusp' points are the edges of the zero field region.

Note that the curves in the left plot are labeled with the values of time that correspond to the field ramp in the right plot. The precise agreement between the results of the numerical model and Brandt's solution confirms the validity of the model for high n-values. Additional validation of the n-value in the model was successfully performed by considering a saturated state of the tape, which can also be expressed analytically (see section V in [71]).

It turns out that the effect of the cell width on the modeling results can be neglected already for $N_x \geq 30$. In order to decrease the computational time, $N_x = 30$ is retained for all the numerical results presented below for the magnetization loss.

There are two limit cases for the magnetization of the stacks in the perpendicular magnetic field (to the tape's face) that are solved analytically in the critical state model (i.e. assuming field independent j_c with $n \to \infty$): Brandt's solution for the single tape ($n_t = 1$) [70] and Mawatari's solution for the stack with infinite number of tapes ($n_t = \infty$) [72]. These solutions can be expressed for the magnetization loss per volume
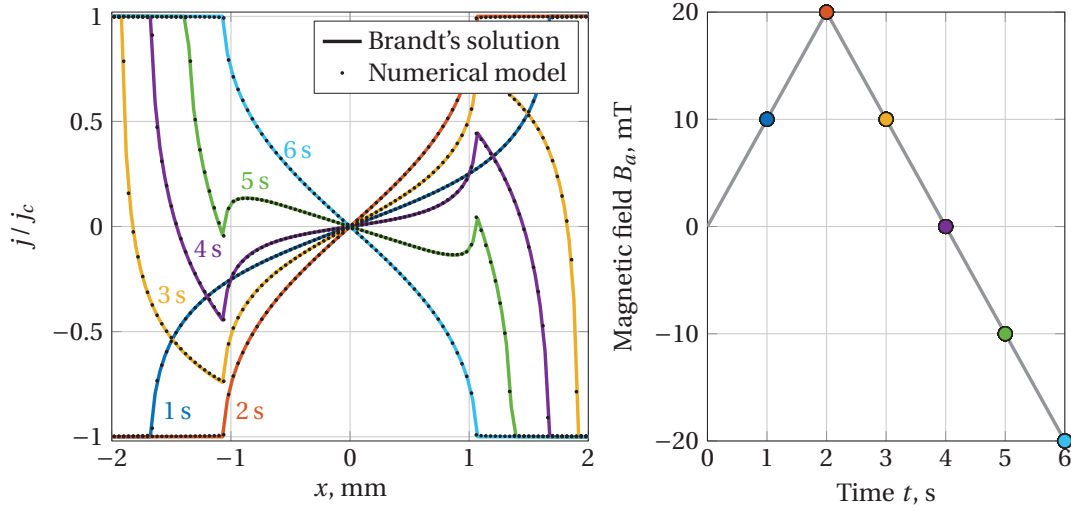
Figure 5.3: Left: analytical (solid lines) and numerical (dots) results for the current distribution in a single 4-mm width tape. The curves are labeled with the values of time. Right: applied magnetic field as a function of time.

per cycle (in $J/(m^3 \cdot cycle)$) as:

$$Q_{brandt} = w j_c B_c q_1 (B_a/B_c)$$
$$Q_{mawatari} = w j_c B_c q_\infty (B_a/B_c, 2v/\pi w)$$
$$B_c = \frac{\mu_0 j_c d}{\pi}$$
$$q_1(x) = 2\ln(\cosh x) - x \tanh x$$
$$q_\infty(x, a) = a^2 \int_0^x (x - 2\xi) \ln\left(1 + \frac{\sinh^2(1/a)}{\cosh^2 \xi}\right) d\xi$$

(5.5)

where the definition of the parameters is the same as used in the numerical model. Note that for the stacks with $v \gg w$, the Mawatari solution converges to the Brandt one, $q_\infty(x, a \gg 1) = q_1(x)$. For $v \ll w$ it converges to the slab solution: $q_\infty(x, a \ll 1) = q_{slab}(x, a) = a^2 x^3/3$ if $x \leq 1/a$ and $x - 2/(3a)$ if $x > 1/a$.

Using the numerical model, the magnetization loss in the stacks per volume of the superconductor per cycle with the finite number of tapes n_t can also be calculated. Results of the calculation for $w = 4$ mm, $v = 100$ μm and various n_t normalized by $w j_c B_c$ and by the Brandt's solution are presented in figure 5.4. The curves demonstrate a gradual decrease of the loss with increasing n_t, that represents the effect of the magnetic shielding in the stack (see also [73, 74]). This effect is more pronounced for a relatively low magnetic field, $B_a \sim B_c$, for which a contribution from the self-field plays a dominant role on distribution of the induced currents. When $B_a \gg B_c$, the generated self-field of the stack cannot shield anymore a volume of the stack against
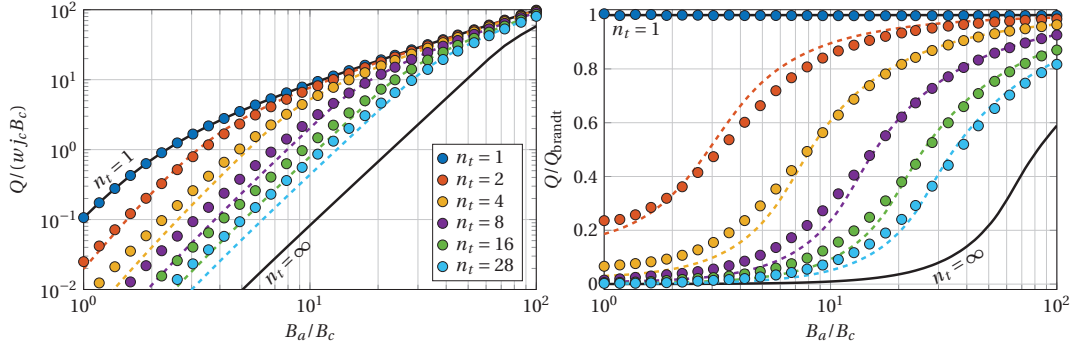
Figure 5.4: Magnetization loss for the stacks with various number of tapes n_t in the critical state model normalized by $w j_c B_c$ (left) and by the Brandt's solution (right). Round markers represent the modeling results; black lines are obtained from equation (5.5); dashed lines correspond to the proposed analytical approach in equation (5.6).

the applied field, such that the tapes in the stack become independent from each other. As a result, Q approximates the single tape loss Q_{brandt}.

By taking into account a similar shape of the curves in figure 5.4, the following approach is used to parametrize the numerical results: one can consider the n_t-tape stack as the stack with infinite number of tapes but with some effective distance between the tapes $v_{\text{eff}}(n_t)$. Applying the valid limits for this parameter: $v_{\text{eff}}(\infty) = v$ and $v_{\text{eff}}(1) = \infty$, the obtained analytical parametrization for the magnetization loss reads as:

$$Q_{n_t} = w j_c B_c q_{n_t} \left(B_a / B_c, 2v / \pi w \right)$$

$$q_{n_t}(x, a) \approx q_\infty \left(x, a + \frac{0.25}{n_t^{0.77} - 1} \right) \tag{5.6}$$

The selected parametrization of the numerical results (see the dashed lines in figure 5.4) provides a quite accurate data representation, with the maximum deviation $\lesssim 5\%$. This parametrization constitutes the key result of this section. On this basis, the magnetization loss in the stacks with an arbitrary number of tapes can in fact be calculated analytically. Expression (5.6) is valid for the ratio v/w in the range from 0.013 to 0.033.

AC transport current loss

The electromagnetic behaviour of the thin-film superconductor carrying the AC transport current in the critical state model was first calculated by Norris in [75]. For example, the current distribution in the 4 mm-wide and 1 μm-thick tape with the critical current of 100 A is shown in figure 5.5. The corresponding results obtained
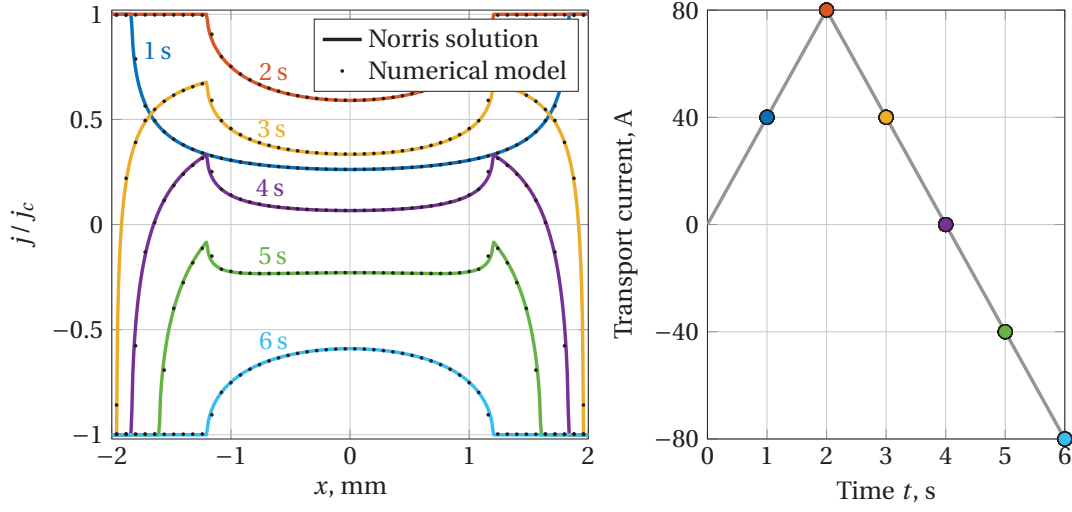
Figure 5.5: Left: analytical (solid lines) and numerical (dots) results for the current distribution in a single 4-mm wide tape. The curves are labeled with the values of time. Right: applied transport current as a function of time.

from the numerical model for $N_x = 50$ are also presented. The current ramp is given in the right plot. The magnetic field in the central region of the tape generated by the presented current distributions is zero.

If the cell width s is wider than a region at the tape edges where the current saturates to j_c, then the current in such cells will be effectively lower than j_c. Hence, calculation of the power loss using equation (5.4) would result in much lower values due to very high n. In such situations, the number of mesh elements should be increased: typically, $N_x \gtrsim 150$ for $I/I_c < 0.3$, where I is the total AC current in the stack, I_c the critical current of the stack.

Similar to the magnetization loss, there are two analytical solutions in the critical state model for the energy loss due to the AC current in a single tape [75] and a stack with infinite number of tapes [76, 77]. The energy loss per volume of the superconductor per cycle (in J/m^3/cycle) can be expressed as:

$$Q_{\text{norris}} = w j_c B_c q_1 \left(I/I_c \right)$$
$$Q_{\text{mawatari}} = w j_c B_c q_\infty \left(I/I_c, 2v/\pi w \right)$$
$$B_c = \frac{\mu_0 j_c d}{\pi}$$
$$q_1(x) = (1+x)\ln(1+x) + (1-x)\ln(1-x) - x^2$$
$$q_\infty(x,a) = \int_0^x (x-2\xi)\ln\left(\frac{\cosh^2(1/a)}{\cosh^2(\xi/a)} - 1 \right) d\xi.$$

(5.7)
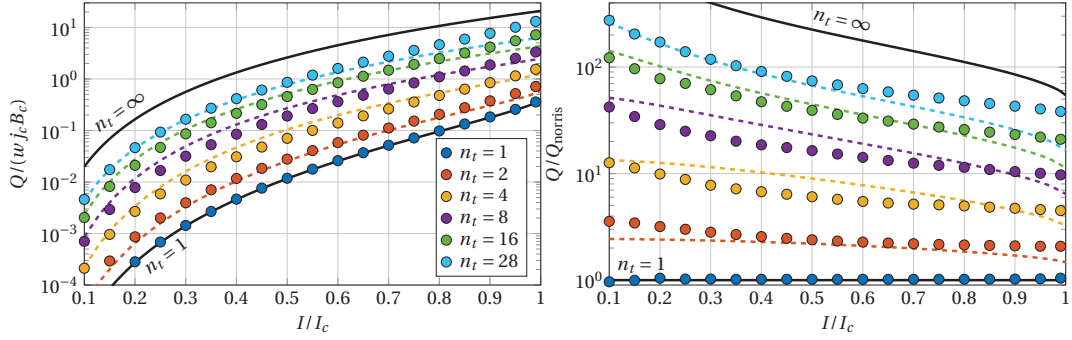
Figure 5.6: AC current loss for the stacks with various number of tapes n_t in the critical state model normalized by $w j_c B_c$ (left) and by the Norris solution (right). Round markers represent the modeling results; black lines are obtained from equation (5.7); dashed lines correspond to the proposed analytical approach in equation (5.8).

Here the parameters definition is the same as used in the numerical model. Note that for the stacks with $v \gg w$ the Mawatari solution converges to the Norris one, $q_\infty(x, a \gg 1) = q_1(x)$. For $v \ll w$ it converges to the slab solution, $q_\infty(x, a \ll 1) = q_{\text{slab}}(x, a) = x^3/(3a)$.

For the intermediate number of tapes n_t, the energy loss was calculated using the numerical model. The summary of the results is presented in figure 5.6 as a function of the normalized transport current I/I_c. Unlike the magnetization loss, the AC transport current loss increases with the increasing n_t. The significant increase in the energy loss is due to the superposition of the self-field generated by the tapes.

Based on the numerical results, it was attempted to parameterize the AC current energy loss for the stacks with the tape distance v using an approach similar to the magnetization loss. The stack of n_t tapes is considered as a stack with infinite number of tapes and some effective distance between the tapes $v_{\text{eff}}(n_t)$: $v_{\text{eff}}(\infty) = v$, $v_{\text{eff}}(1) = \infty$. The obtained parametrization reads as (see the dashed lines in figure 5.6):

$$Q_{n_t} = w j_c B_c q_{n_t}\left(I/I_c, 2v/\pi w\right)$$

$$q_{n_t}(x, a) \approx q_\infty\left(x, a + \frac{0.18 a^{-0.27}}{n_t^{0.84} - 1}\right)$$

(5.8)

Although the fit curves at $I/I_c \sim 1$ are intrinsically less steep than the numerical data (due a difference in the current distributions between the stacks with finite n_t and $n_t = \infty$), an acceptable accuracy for the data representation was obtained at lower currents. The fit parameters were derived for the ratio v/w in the range from 0.013 to 0.033.

5.1.3 Experimental results

As discussed above on the basis of the numerical and analytical studies, the magnetization loss per tape decreases with increasing number of tapes n_t. The magnetization behaviour of the stack is further studied experimentally using a vibrating sample magnetometer (VSM), used in a collaboration with ENEA, Frascati. The VSM measurements can be carried out for temperatures down to 5 K and magnetic fields up to 12 T, with a relatively small volume of field homogeneity. Experimental data will be used to conclude whether the proposed numerical tools are adequate for an assessment of the magnetization loss in stacks.

Samples for the VSM measurements

The parameters of the stack samples that were prepared for the magnetization measurements using a vibrating sample magnetometer (VSM) are summarized in table 5.1. The length of the sample should not exceed 10 mm due to a restricted volume of the VSM system at ENEA. SuperPower single tapes with different lengths (4 mm, 5 mm and 10 mm) and SuperPower 16-tape stacks (5 mm and 10 mm) can be used to investigate an edge effect of the short samples in the measurements. With the SuperPower 4-mm wide, 5-mm long stack samples the magnetic shielding and field orientation effects with the varied number of tapes are studied. The list of samples allows also evaluating the influence of the tape's manufacturer on the magnetization behavior by comparing the SuperPower and SuperOx single tapes and 16-tape stacks. Note that there are no artificial pinning centers in the SuperOx tapes, while the doping is used by the SuperPower company. The geometry aspect ratio of the stack can also be studied using the SuperPower stacks of different tape's width (3 mm vs 4 mm) and thickness: the 3 mm-wide tapes are 60 μm thick, while all the other tapes are 100 μm thick.

In order to manufacture the samples, only 3 different tape spools (production batches) are used: SuperPower 4 mm, SuperPower 3 mm and SuperOx 4 mm. Before the assembling, the critical currents and n-values of the tapes were measured in a liquid nitrogen bath (see results in table 5.2).

All the stacks were assembled using the soldering device shown in figure 5.7. Short

Table 5.2: I_c and n-value at 77 K / self-field of the tapes used to manufacture the samples.

HTS tape	I_c, A	n-value
SuperPower 4 mm	155 ± 2	33
SuperPower 3 mm	70 ± 1	29
SuperOx 4 mm	164 ± 1	34

HTS tape	Number of tapes, n_t	Orientation of the sample, θ_a
SuperPower width 4 mm length 4 mm	1	0°
SuperPower width 4 mm length 5 mm	1	0° / 45°
	8	0° / 45°
	16	0° / 45° / 90°
	28	0° / 45°
SuperPower width 4 mm length 10 mm	1	0°
	16	0°
SuperPower width 3 mm length 5 mm	1	0°
	8	0°
	16	0°
	28	0°
SuperOx width 4 mm length 5 mm	1	0°
	16	0°

Table 5.1: Description of the samples used in the VSM measurements.
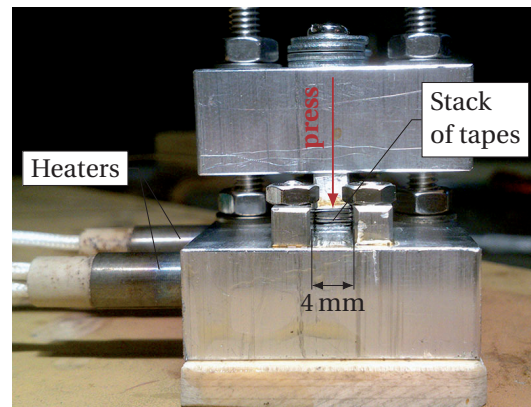
Figure 5.7: Device for the stack soldering. A thermocouple is inserted at the rear side of the bottom aluminum block to control the heaters.
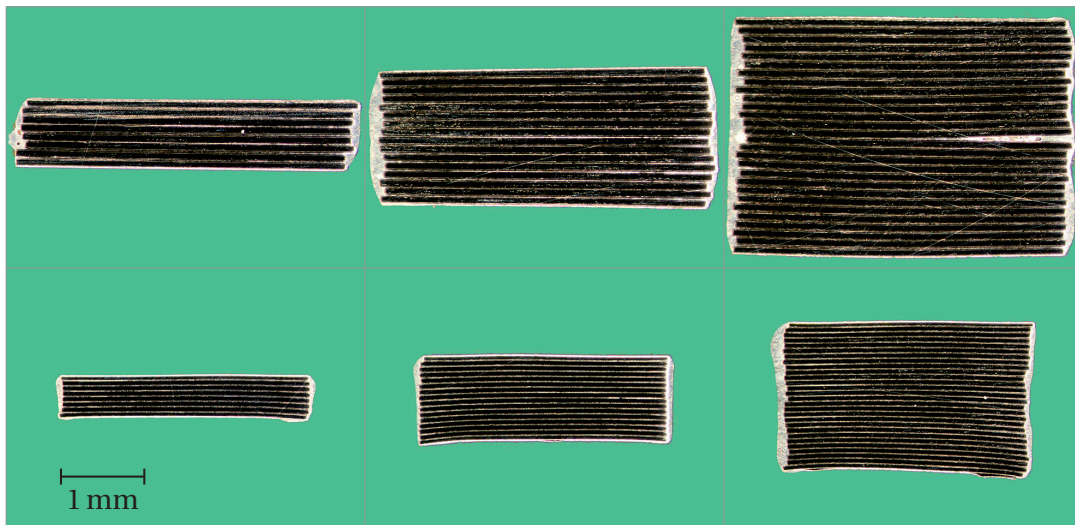
Figure 5.8: Cross-sections of the SuperPower tape stacks. Columns from left to right: 8, 16 and 28-tape stacks. Dimensions of the tapes: $4\,\text{mm} \times 0.1\,\text{mm}$ in the top row; $3\,\text{mm} \times 0.06\,\text{mm}$ in the bottom row.

sections of tapes are stacked in the central groove of the bottom block ($4\,\text{mm}$ wide) and pressed by the top block. The blocks are made of aluminum. Then the device is heated by two heaters up to $200\,°\text{C}$, and the temperature is monitored using a thermocouple inserted in the bottom block. During the melting of the solder an additional compression is applied to ensure a tight packing of the stack. In case of the $3\,\text{mm}$ wide tapes, the top block of a narrower size is used together with a teflon spacer to fill the width of the groove.

After the stack is soldered, the tapes in the stack are nicely packed in the cross-section, but slightly misaligned in the longitudinal direction. Therefore, the tape sections that are few mm longer than the target length have been used in the soldering: the extra length is cut away from the misaligned edges of the stacks by the wire erosion, resulting in a satisfactory geometry of the samples.

Cross-sections of the SuperPower stacks of $3\,\text{mm}$ and $4\,\text{mm}$ wide tapes are presented in figure 5.8. Presumably, the noticeable geometry artifact of the narrower stacks (parabolic shape of tapes at the bottom of the stack) is due to the bent surface of the pressing block. Since the solder thickness between the tapes is negligible, the distance between the superconducting layers (i.e. parameter ν of the numerical model, see previous section) reduces simply to the tape's thickness: $100\,\upmu\text{m}$ and $60\,\upmu\text{m}$ for the $4\,\text{mm}$ and $3\,\text{mm}$ width samples, respectively.
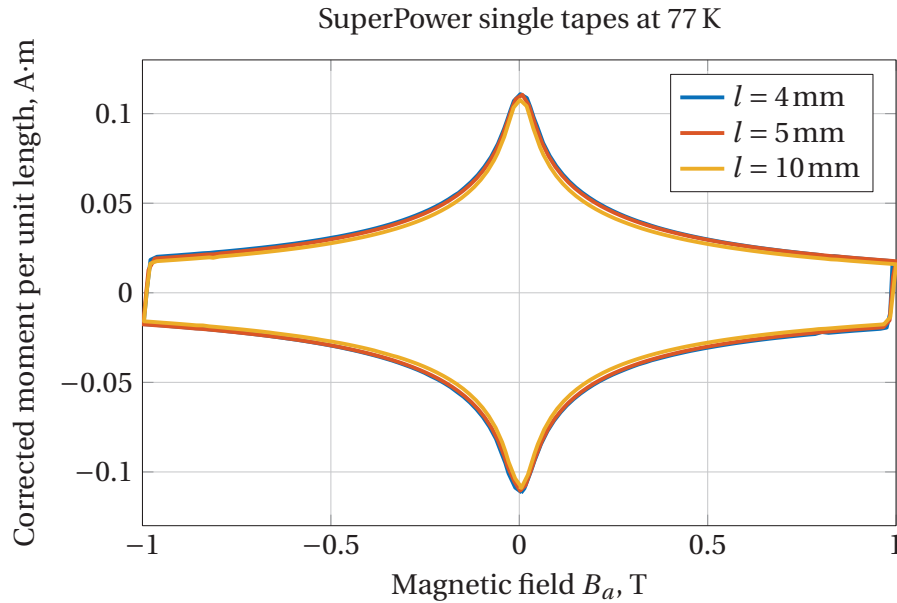
Figure 5.9: Measured negative magnetic moment per unit length scaled by the finite length factor $(1 - w/3l)$ for the SuperPower 4 mm-width single tapes of different lengths l at 77 K.

Finite length effect

The magnetic moment of the stacks m is influenced by the finite length and n-value of the tapes. For a single tape, the influence of each factor can be expressed analytically. The impact of the edge currents on m was considered in [78]. The solution for the saturated state of the tape with finite n-value was given in [71]. Combining the two methods together, one can express m for the single tape:

$$\frac{m_{\text{sat}}}{l} = \frac{1}{4} I_c w \left(1 - \frac{w}{3l}\right) \left(\frac{\dot{B}w}{2E_c}\right)^{1/n} \frac{2n}{2n+1} \tag{5.9}$$

To validate the finite length factor, the measured m is scaled by $(1 - w/3l)$ for the 4 mm-wide single tapes of the different length: 4 mm, 5 mm and 10 mm (see table 5.1). The results of the scaling at 77 K are presented in figure 5.9. Note that the difference in I_c of these samples is negligible according to the transport measurements at 77 K. The scaling is also applied to the 16-tape SuperPower stacks (5 mm and 10 mm long) with the same satisfactory agreement. Consequently, the scaling is justified and will be applied to obtain the magnetization behavior of long stacks from the measurements of the short samples. Due to the high n-values of the tapes (see table 5.2), their effect on the measurements is small.
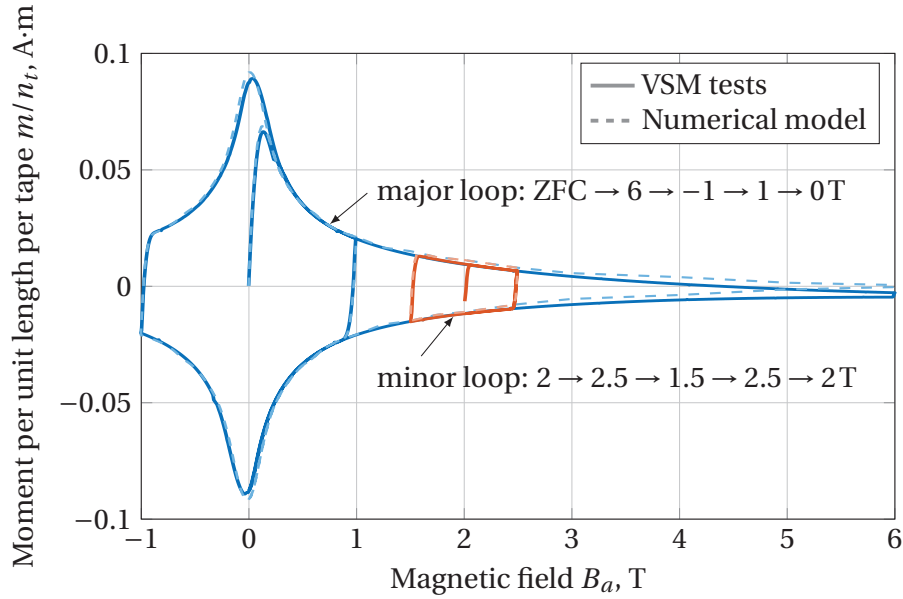
Figure 5.10: Negative magnetic moment per unit length for the SuperOx 16-tape stack at 77 K.

Magnetization loops

The magnetization behavior of the stacks (see description in table 5.1) was measured in the VSM system at 77 K and 5 K. For the measurements of the major magnetization loops the samples were cooled in zero field (ZFC) and then the following ramp of the magnetic field was applied: ZFC $\rightarrow 6 \rightarrow -1 \rightarrow 1 \rightarrow 0$ T at 77 K, ZFC $\rightarrow 12 \rightarrow -2 \rightarrow 2 \rightarrow 0$ T at 5 K. In the measurements of the minor loops the field ramp was set as $2 \rightarrow 2.5 \rightarrow 1.5 \rightarrow 2.5 \rightarrow 2$ T at 77 K and $10 \rightarrow 11 \rightarrow 9 \rightarrow 11 \rightarrow 10$ T at 5 K. The loops were performed at various ramp rates: 0.1, 0.2, 0.4, 0.6, 0.8 and 1.0 T/min. The minor loops are used to calculate the magnetization loss of the samples that will be discussed in the following section.

An example of the major and minor loops of the SuperOx 16-tape stack at 77 K is presented in figure 5.10 together with the corresponding modeling results. The angular dependence of the critical current $j_c(B, \theta)$ of the SuperOx tape at 77 K that was used in the modeling corresponds to the data presented in [79] and was provided by the authors of that article in the tabulated form. Due to the weak influence of the n-value on the calculation for $n \gtrsim 15$, a constant n is retained as in table 5.2. The developed numerical model (see section 5.1.1) provides an accurate representation of the experimental data if the material properties are well defined.

The major magnetization loops for the SuperPower stacks with the different number of tapes n_t at 5 K are summarized in figure 5.11. The overlapping of the curves in the
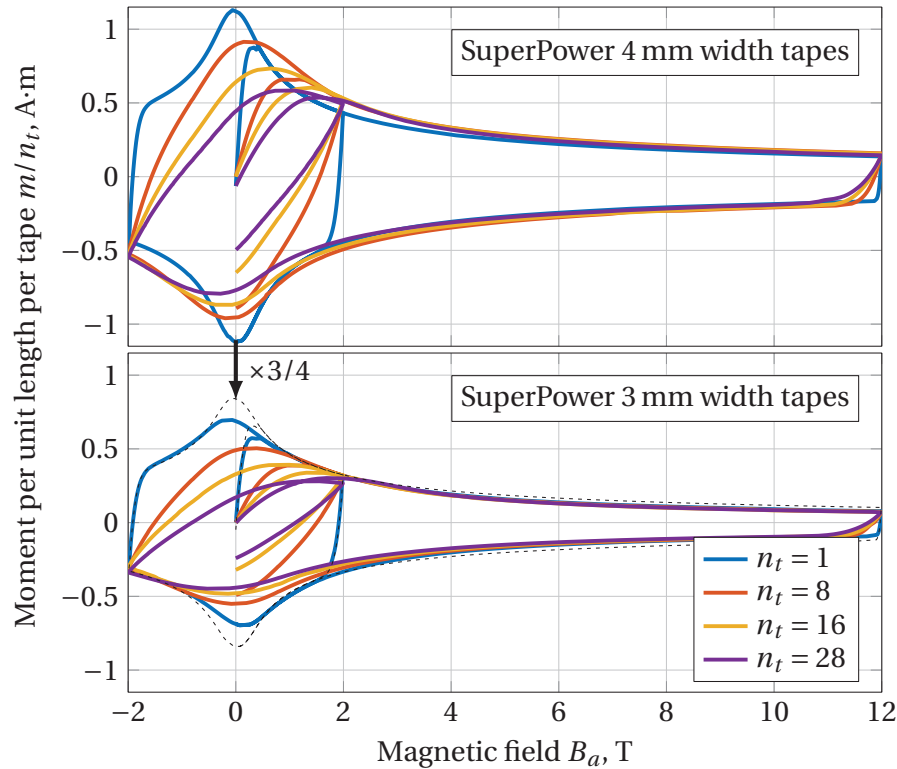
Figure 5.11: Negative magnetic moment per unit length normalized by the number of tapes n_t for the SuperPower 4 mm and 3 mm width stacks at 5 K.

high field zone ($B \gtrsim 6\,\text{T}$) suggests that the stack samples were not damaged during the manufacturing. In the low field zone the self-field of the stacks has a strong impact on the resulting magnetic moment: the induced currents in the outer tapes of the stack generate sufficient magnetic field to provide the shielding effect for the inner tapes. As a result, the magnetization loops become 'smoother' with the increasing number of tapes n_t. The bottom plot in figure 5.11 contains also the comparison for the single tapes of the different widths, which demonstrates a weaker I_c field dependence of the 4 mm wide tapes.

Orientation of the magnetic field

In order to apply the background magnetic field at $\theta_a = 45°$ and $90°$ to the c-axis of tapes, appropriate VSM sample holders were manufactured, see sketch in figure 5.12. Let us assume that the resulting magnetic moment $\vec{m}$ consists of components that are induced by the perpendicular ($\vec{B}_\perp$) and parallel ($\vec{B}_\parallel$) projections of the field with respect to the tape face. The component of $\vec{m}$ that is induced by $\vec{B}_\perp$ (or $\vec{B}_\parallel$) is proportional to the tape width w (or tape thickness d). Consequently, due to a
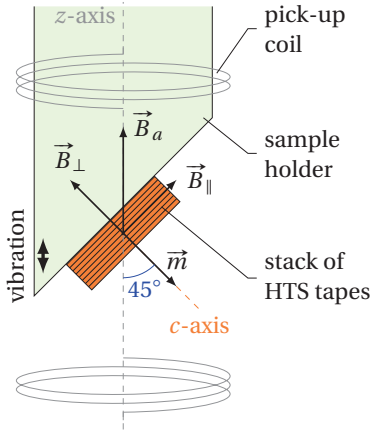
Figure 5.12: VSM sample holder for the field orientation $\theta_a = 45°$ with respect to the c-axis of tapes. The electromotive force induced on the pick-up coils is proportional to m_z.
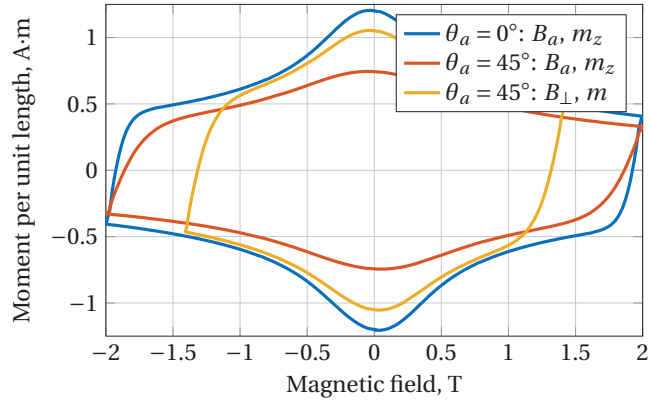
Figure 5.13: Magnetization loops of the SuperPower single tape at 5 K for different orientations of the applied magnetic field. For the 45° applied field the loop in transformed coordinates is also presented.

very high aspect ratio of the superconducting layer in the HTS tapes ($w/d \gtrsim 10^3$), the magnetic moment induced by the field with non-zero $\vec{B}_\perp$ (i.e. $\theta_a \neq 90°$) is directed essentially along the c-axis. As a consequence, a mechanical torque $\vec{\tau} = \vec{m} \times \vec{B}_a$ acting on the sample should be taken into account by inserting an appropriate reinforcement of the sample's support. The main effect of $\vec{B}_\parallel$ on the magnetization is the reduction of the critical current due to that component, what in turn reduces the area of the loop.

A comparison of the magnetization loops for the SuperPower single tape at 5 K for 0° and 45° applied magnetic field is given in figure 5.13. For the 45° case, m versus $B_\perp$ is also shown, which was obtained from the measurements as $m = m_z / \cos\theta_a$, $B_\perp = B_a \cos\theta_a$ (see figure 5.12). This transformation preserves the area of the loop and consolidates the conclusions that has been done above: in the presence of $\vec{B}_\parallel$ component the loop is similar to the one measured at 0° applied field, but slightly squeezed (see also [80, 81]). For the 90° orientation reliable results could not be obtained in the VSM system due to a weak magnetization of the sample. SQUID magnetometer should be used instead as a more sensitive technique.

Magnetization loss

Using the measured minor loops the magnetization loss of the stacks (see description in table 5.1) is calculated at 5 K and 77 K as an area of the closed loop: $Q = \oint m \, dB_a$. A minor effect of the field ramp-rate on the loss was found and can be expressed as

$Q \sim \dot{B}^{1/n}$ [82]. This relation is directly obtained from equation (5.9) for the sample considered only in the saturated state (a good assumption for the samples with a low penetration field).

The loss estimate at 5 K for the SuperPower stacks is presented in figure 5.14. The results normalized by the loss of the single tape in the perpendicular field are summarized in figure 5.15 for both temperatures. The effect of the magnetic field shielding by the tapes' stacking results in the reduction of the loss with the increasing number of tapes n_t. The same 20 % reduction was obtained for the SuperPower and SuperOx 16-tape stacks, which demonstrates a negligible influence of the tape's manufacturer. For the 4 mm and 3 mm wide SuperPower stacks the difference in results is in agreement with the analytical expression (5.6): a lower aspect ratio v/w leads to lower loss (v/w is 0.025 and 0.020 respectively).

A further reduction of the loss was obtained in the field applied at 45° to the c-axis of the SuperPower stacks. In the measurements at 5 K the field ramp 10 ± 1 T corresponds to a variation of the perpendicular and parallel components by 7.1 ± 0.7 T. These variations are high enough to saturate the single tape: the 33 % loss reduction is mainly due to the shorter field ramp. In contrast, the full saturation was not achieved on the other samples, which have penetration field higher than 0.7 T: starting the loop from the upper branch of the magnetic moment, the bottom one was not reached in these measurements. As a result, the loss is additionally lowered by the weak magnetization of the samples.

Similar results were obtained at 77 K (the right plot of figure 5.15), but the data are less smooth because of low absolute values of the loss ($\sim$ 30 times smaller than at 5 K). Note that the influence of n_t on the loss reduction at 77 K is much weaker than at 5 K. This can be explained by a low penetration field of the samples compared to the applied minor loops 2.0 ± 0.5 T: the tapes in the stack behave almost independent from each other. The loss reduction for 45° oriented field ($\approx$ 30 %) correspond mainly to the shorter field ramp of the perpendicular field component, which is 29 % shorter than the one oriented at 0°.

The solid lines in figure 5.15 represent the magnetization loss obtained from the developed numerical model (see section 5.1.1): the darker/lighter curve correspond to 0°/45° applied field respectively (for the both temperatures). At 5 K the modeling results correspond to the SuperPower tapes ($j_c(B, \theta)$ from [83]), at 77 K to the SuperOx tapes ($j_c(B, \theta)$ from [79]). In case of 45° applied field at 5 K, the progressing deviation between the experimental and numerical data is presumably originated from the discrepancy between the real and modeled angular dependence of the material. In this case, the full saturation was not obtained also in the modeling for $n_t > 8$ (loops are not closed). In other cases there is a good correlation between the measurements and modeling.

The magnetization loss of the 16-tape stacks was also estimated from the calori-
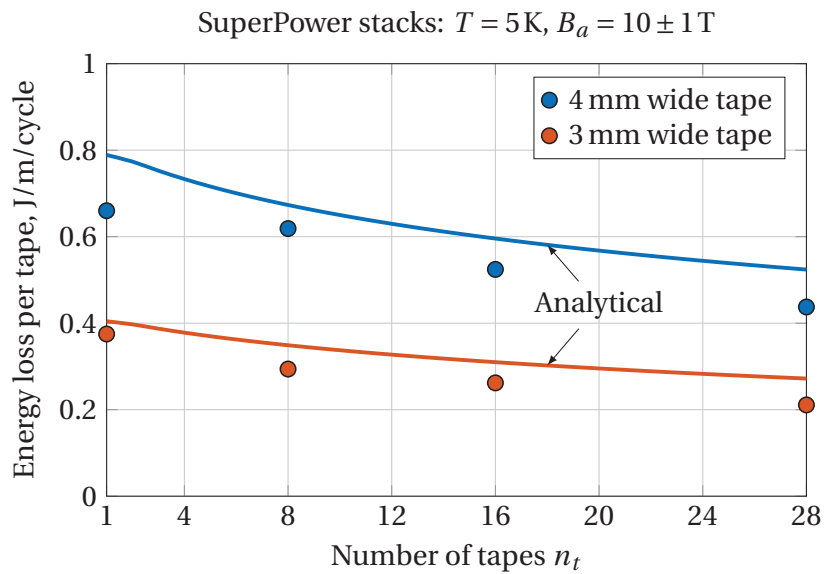
Figure 5.14: Magnetization loss of the SuperPower stacks per tape as a function of the number of tapes n_t. Analytical results are from equation (5.6).
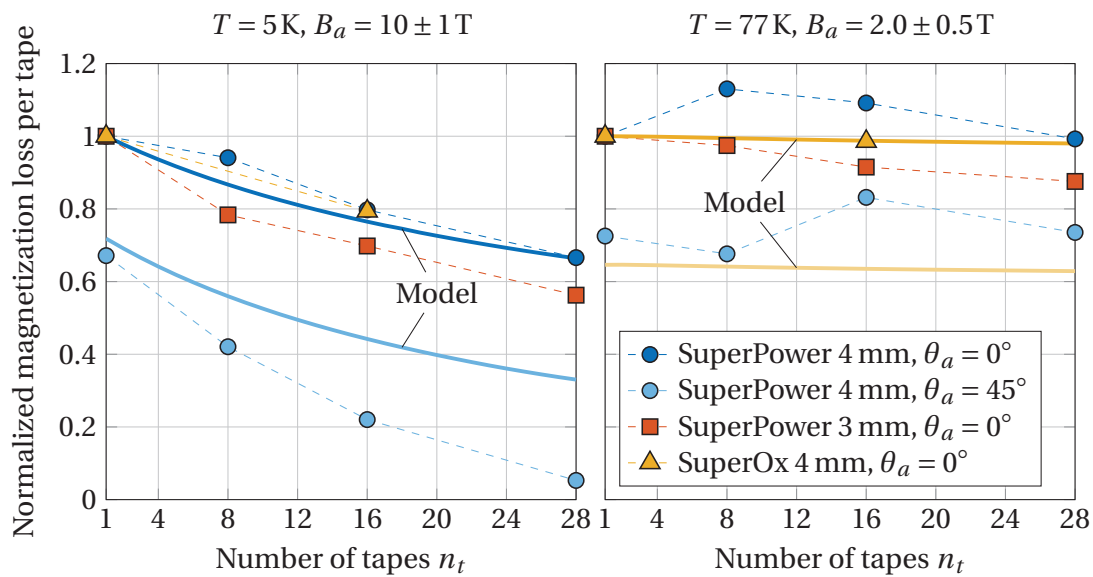
Figure 5.15: Magnetization loss of the stacks per tape as a function of number of tapes n_t normalized to the single tape loss in the perpendicular field.

metric AC loss tests performed with the 60 kA HTS cable prototypes in EDIPO (see section 4.6.3). The AC loss of the SuperPower and SuperOx prototypes was measured at $T = 5$ K against the frequency of the AC field from 0.1 Hz to 2 Hz, which allows assessing the magnetization loss by extrapolation to 0 Hz: at 2 T background field and $B_a = 0.3$ T the magnetization loss per tape is in the range from 13 mJ/m/cycle to 30 mJ/m/cycle. For these operating conditions the magnetization loss per tape is about 15 mJ/m/cycle from the numerical model and about 12 mJ/m/cycle from the analytical formula (5.6). The twisting of the stacks in the cables was accounted in the calculations in a simplified way: the loss was calculated as a function of field's orientation θ_a and then averaged over that parameter (this method was verified in [84]). Note that the corresponding single tape loss is estimated to ≈ 250 mJ/m/cycle, significantly overestimating the actual value.

Finally, the energy loss of the 15-tape SuperPower non-twisted stack was measured at the University of Twente. At $T = 5$ K and $B_a = 0.4$ T the reported results for the magnetization loss of the sample are in the range from 0.5 J/m/cycle to 0.6 J/m/cycle. Using the analytical formula (5.6), the corresponding loss is estimated to 0.45 J/m/cycle.

According to the qualitative data agreement, the analytical formula (5.6), 'extracted' from the numerical studies, is validated and can be used as a fast tool to estimate the magnetization loss of the stacked tapes.

5.2 Coupling loss

When superconductors are in electrical contact with each other via some normal conducting materials, applied changes in the magnetic flux induce currents between them according to Faraday's law. These currents release some energy through Joule heating. This type of loss is referred to as the coupling loss. Analytical methods available for this phenomenon explain mostly a general trend in the frequency dependence, while aspects of the specific geometry are usually captured using simplified effective parameters, such as the shape factor n and time constant τ. Unfortunately, the studied geometry of the cable is not the one for which n and τ are deduced. Therefore, it will be attempted to express them using the parameters of the strand and cable design by help of the numerical analysis. Available experimental datasets will be used to verify the obtained numerical results.

5.2.1 Description of the numerical model

The coupling loss in the strand and cable is studied using the electrical network model. The model is based on the Kirchhoff circuit laws and the current conservation law, where currents are taken as unknowns. Similar models have been extensively
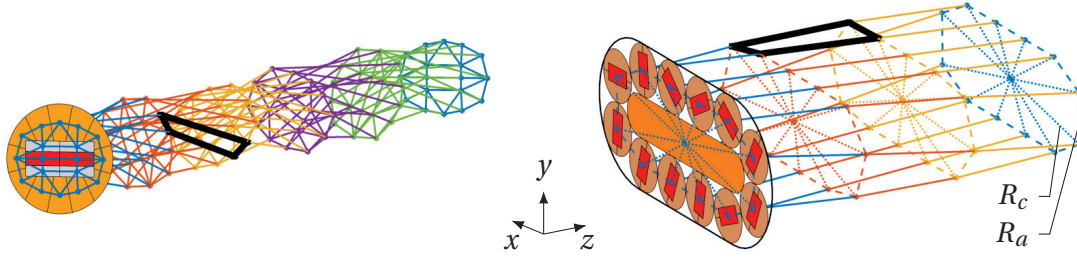
Figure 5.16: Mesh of the strand geometry with 5 bands (left) and of the cable geometry with 3 bands (right). The elements in the last plane are identical to the ones in the first plane due to the periodic boundary conditions (illustrated by the same color).

developed for the Rutherford cables [85–88]. Comparing with them, it will also be considered the finite thickness of the cable core (i.e. $g \neq 0$, see figure figure 4.1).

Assuming that the center-line of the given geometry is a straight line, the mesh is generated in a simplified way. The nodes are placed on equidistant parallel planes perpendicular to the center-line. Each plane contains the same number of nodes N_s. There are N_a connections (branches) between the nodes of the same plane and N_s connections between the nodes of the adjacent planes, i.e. one connection per node in the longitudinal direction. Each branch is the current path. A set of the in-plane nodes and the corresponding in-plane and inter-plane branches will be referred to as a calculation 'band'. For the N_b bands the total number of unknown currents is $N_t = (N_s + N_a)N_b$ assuming that the periodic boundary conditions can be applied for the first and the last planes.

An illustration of the mesh for the strand and cable is presented in figure 5.16. Periodic boundary conditions are applied to the nodes located at the distance of one full twist-pitch h for the strand and at the distance of the twist-pitch L divided by the number of strands N for the cable (due to the full transposition feature of the cable). Note the same color for the elements of the first and last planes in figure 5.16. The cable geometry is simplified such that each strand has one connection with the adjacent strand and with the central core, i.e. $N_a = 2N_s$.

Three types of equations describe the currents I induced in the mesh:

Kirchhoff's current law: the algebraic sum of the currents flowing into and out the every node is zero. Note that for the cable a 'circular shift' for the currents should be applied in the first and last band in order to account properly the periodic boundary conditions. For example, in the situation without the central core with 3 strands and 2 bands (see node diagram in figure 5.17) this condition reads for the bottom left node as: $I_{11}^1 + I_{12}^1 - I_{33}^2 - I_{31}^1 = 0$, where I_{ij}^k denotes the current flowing from i-th node to j-th node in k-th band (a special case $i = j$ is for the axial currents). For the cable it is assumed that there is no axial current flowing in the central core.
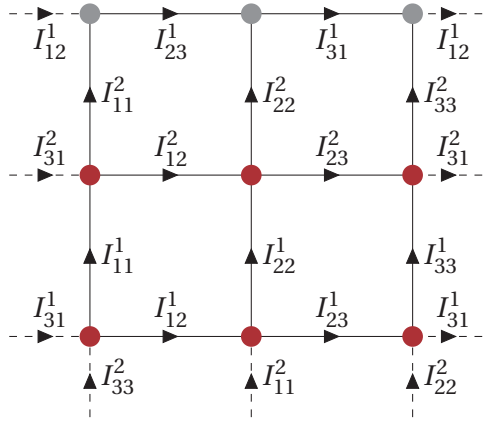
Figure 5.17: Diagram of the nodes for the cable with 3 strands and 2 bands. The currents are labeled as follows: first bottom label is the output strand, second bottom – input strand, top – index of the band.
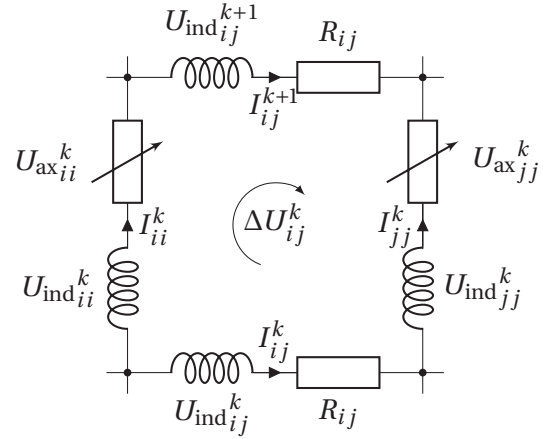
Figure 5.18: Circuit diagram for i-th and j-th nodes located in k-th band. The superconducting sections are shown as the variable resistors.

Kirchhoff's voltage law: for each branch in the cross-section there is a circuit (i.e. see thick black contours in figure 5.16), for which the algebraic sum of the voltage drops is equal to an externally induced voltage ΔU, see the corresponding circuit diagram in figure 5.18. Assuming that the AC field $\vec{B}_a = B_a\{\sin\theta_a, \cos\theta_a, 0\}$ is spatially uniform and using the Faraday's law lead to $\Delta U = -\dot{B}_a\left(S_{yz}\sin\theta_a + S_{xz}\cos\theta_a\right)$, where S_{yz} and S_{xz} are the projections of the circuit area onto yz and xz planes. The inductive voltage U_{ind} is computed by means of partial inductances [89]. Formulas for the straight segments are given in [90]. The axial voltage U_{ax} is either the one along the superconducting path described by the power law (see equation (2.1)) or along the solder and copper domains described by the Ohm's law. The transverse voltage is due to Ohm's law, using the specific resistance of the solder and copper for the strand and the strand-to-strand R_a and strand-to-core R_c resistances for the cable. R_a and R_c are attributed to the dashed and the dotted lines in the right plot of figure 5.16, respectively. For simplicity, the critical current is assumed constant in the model.

Current conservation: additional to the Kirchhoff's current law a term for the applied transport current I_{tr} should be specified explicitly: for the first band it reads as: $\sum_{k=1}^{N_s} I_{kk}^1 = I_{\text{tr}}$. For the transverse currents the following conditions have also been found: $\sum_{k=1}^{N_b} I_{ij}^k = 0$ for the strand and $\sum_{i=1}^{N_s} I_{i,i+1}^1 = 0$ for the cable, where $I_{N_s,N_s+1}^1 \equiv I_{N_s,1}^1$.

The required set of N_t independent equations (IE) can be written in a matrix form. The Kirchhoff's current law provides $N_s N_b - 1$ IE. For the cable $2N_s N_b - 1$ IE are due to the Kirchhoff's voltage law and 2 IE are from the current conservation law. In case

of the strand, IE are obtained by writing all the possible equations and extracting the linearly independent rows from the rectangular matrix: for these needs, the inductive terms in the Kirchhoff's voltage law are omitted and the axial ones are assumed linear.

A sinusoidal field ramp of the amplitude B_a and frequency ν is used in the model. After the equations are solved, the power loss is computed directly as the Joule heating along all the branches in the model. The energy loss per cycle is obtained by integration the power loss over time from $1/(4\nu)$ to $3/(4\nu)$ and multiplying by factor 2.

Note that the present study is focused only at investigating the coupling loss at the strand and cable levels. Hence, we neglect the hysteresis loss in stacks for the strand and the loss inside the strands for the cable.

5.2.2 Scaling laws for energy loss

From a general consideration of the coupling currents in the electrical models [91], expression for the energy loss per cycle per unit length due to a sinusoidal AC field reads as:

$$Q_{\text{coupling}} = \frac{B_a^2}{2\mu_0} \cdot S \cdot \frac{4\pi^2 n\tau\nu}{1 + 4\pi^2\tau^2\nu^2} \quad [\text{J/m/cycle}] \tag{5.10}$$

where n is the shape factor of the system and τ is the time constant. The effective cross-section S occupied by the coupling currents can hardly be determined and usually is set to the full cross-section of the system. In such a case, n should be taken as an effective value providing that $n \cdot S$ gives the correct result. As a function of the frequency ν, expression (5.10) has a bell-like shape with the maximum value at the frequency $1/(2\pi\tau)$, which is equal to $\frac{B_a^2}{2\mu_0} \cdot S \cdot \pi n$. These correlations are illustrated in figure 5.19.

At relatively low frequency $\nu \ll 1/\tau$, the coupling loss is a linear function of ν. This is used in the measurements to obtain the $n\tau$ product from the slope of the measured loss (i.e. as a fitting parameter). The power loss per unit length at the low frequency can be obtained from equation (5.10) as $P = \dot{B}^2 Sn\tau/\mu_0$. This expression allows to calculate the energy loss per cycle for an arbitrary ramp of the AC field: $Q = \int_{1/\nu} P\,dt = \langle\dot{B}^2\rangle Sn\tau/(\mu_0\nu)$. For the sinusoidal field ramp $\langle\dot{B}^2\rangle = 2\pi^2 B_a^2\nu^2$, for the triangular one $\langle\dot{B}^2\rangle = 16 B_a^2\nu^2$.

Given these correlations, it is only required to deduce the values of n and τ in order to estimate the coupling loss. Using the numerical model described in the previous section, parametric studies for n and τ have been performed for the strand and cable cases. For a given set of the geometrical parameters ('configuration') n and τ were extracted from the $Q(\nu)$ curve as the fitting parameters for equation (5.10). Based on a large set of calculated configurations (in total, 341 configurations for the strand and 350 for the cable), analytical dependencies have been built for n and τ. Obtained
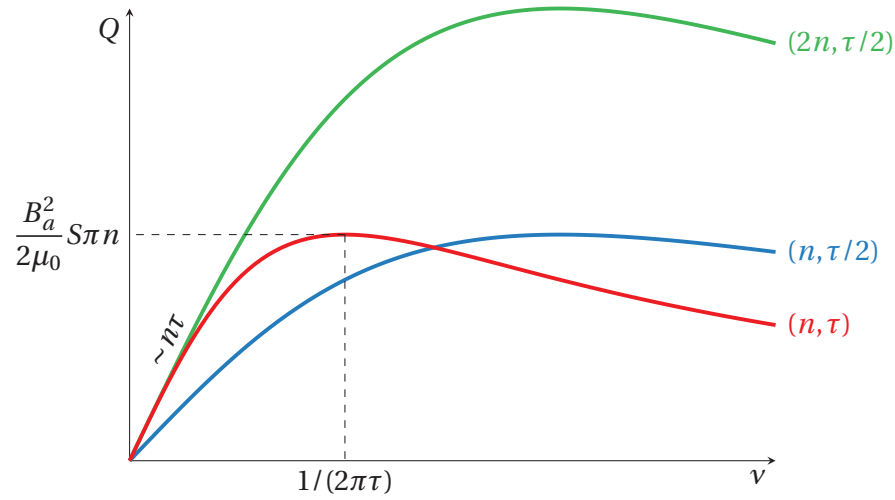
Figure 5.19: Frequency dependence of the coupling loss for various values of the time constant τ and shape factor n.

results from this procedure for the strand and cable are presented in the discussion below.

Intra-strand energy loss

There are four geometrical parameters of the strand, which were used in the parametric study of n and τ: diameter of the strand D, width of the slot w, height of the slot t and twist-pitch h (see figure 3.1). The cross-section is simply taken as $S = \pi D^2/4$. It was also attempted to vary the specific resistance for the solder and copper domains by changing the temperature, but it was not possible to obtain a reasonable parametrization. Because of that, the temperature was simply set to 5 K, roughly corresponding to the operating temperature of fusion magnets.

The obtained results for n and τ at 5 K are written as follows:

$$n \approx 0.2320$$

$$\tau = (p_1 D + p_2)\left(1 - \frac{d}{D}\right)^{p_3 \frac{w}{t} + p_4}\left(1 - \exp\left(-\left(p_5 \frac{h}{D}\right)^{p_6}\right)\right)$$

$$d = \sqrt{w^2 + t^2}$$

p_1 [s/mm]	0.2824
p_2 [s]	−1.0968
p_3 [-]	0.0883
p_4 [-]	0.1909
p_5 [-]	0.0226
p_6 [-]	1.4430

(5.11)

The confidence bounds for the proposed parametrization can conservatively be imposed as ±10 % for the computed values of n and τ. Although the classic result $\tau \sim h^2$ for the round multi-filament superconducting wire [92] is almost reproduced at the relatively low twist-pitches $(h \lesssim 50D)$, the $\tau(h)$ dependence saturates at the high values of h. The dependence of n on the strand parameters is weak and can simply
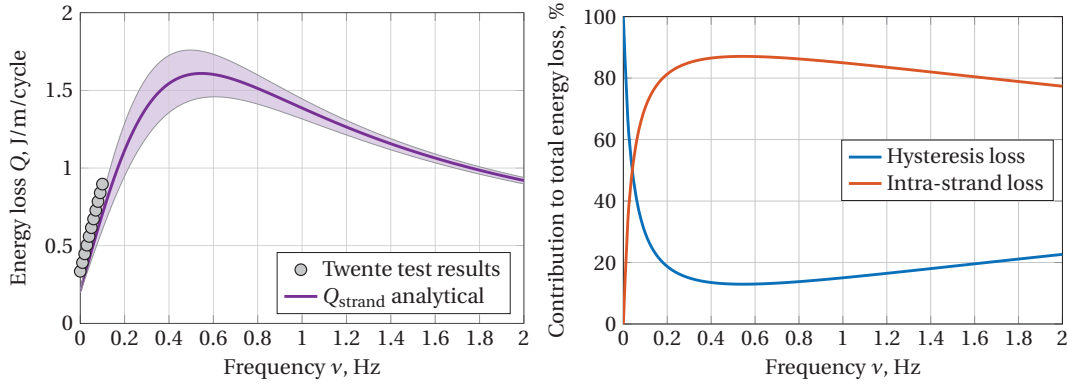
Figure 5.20: The total energy loss per cycle per length (left) and the relative contributions from the hysteresis and intra-strand loss (right) for the 16-tape SuperOx strand at $T = 5\,$K, $B = 1\,$T, $B_a = 0.4\,$T.

be represented by the constant value within the confidence bounds. Consequently, the peak value of the coupling loss, which reads as $\frac{B_a^2}{2\mu_0} \cdot S \cdot \pi n$, depends on the strand parameters simply as $\sim D^2$.

The measurements of the 16-tape SuperOx strand with the parameters $\{D, w, t, h\} = \{6.2\,\text{mm}, 4\,\text{mm}, 2\,\text{mm}, 320\,\text{mm}\}$ have been carried out at the University of Twente. The sample was tested at $T = 5\,$K in the collinear DC field $B = 1\,$T and AC sinusoidal field $B_a = 0.4\,$T. The results of the measurements are presented in the left plot of figure 5.20. For the given strand parameters the shape factor and the time constant are computed from equation (5.11) as $n = 0.232$ and $\tau = 0.292\,$s, which allows us to calculate the intra-strand loss Q_{intra} from equation (5.10). The hysteresis loss Q_{hyst} was obtained from equation (5.6). Thus, the total energy loss is evaluated simply as $Q_{\text{strand}} = Q_{\text{hyst}} + Q_{\text{intra}}$, applying also the confidence bounds $\pm 10\,\%$ for n and τ. The relative contribution of each component to Q_{strand} is presented in the right plot of figure 5.20. About 80 % of the total energy loss is due to the coupling loss for $v > 0.1\,$Hz.

Although a relatively good agreement between the experimental and numerical data has been obtained, it is necessary to obtain more experimental data in a wider frequency range in order to completely validate the proposed parametrization for n and τ.

Inter-strand energy loss

The parametric studies for n and τ have been performed using the network model for the following parameters: diameter of the strand D, number of the strands N, thickness of the copper core g, twist-pitch of the cable L, resistance times unit length between the adjacent R_a and crossing strands R_c and orientation of the magnetic field

θ_a with respect to the broad side of the cable ($\theta_a = 0°$ for the perpendicular direction). The cross-section of the cable is evaluated as $S = NS_{\text{strand}} + fg + \pi g^2/4$, where $S_{\text{strand}} = \pi D^2/4$ and f is the width of the flat part of the cable core (see equation (4.3)).

The obtained parametrization reads as follows:

$$n = 0.1049 \frac{ND}{f + g + 2D} (1 + x)$$

$$\tau = 0.0143 \mu_0 L^2 \left(\frac{f + g}{D}\right)^{0.434} \left(\frac{1}{R_a} + \frac{8.283}{R_c}\right) \left(1 - \frac{0.773}{1 + x}\right) \qquad (5.12)$$

$$x = f \cos^2 \theta_a / (g + 2D)$$

The confidence bounds for this parametrization can be conservatively taken as ±10 % for the computed values of n and τ. The anisotropy of the AC loss in the cable is described by the parameter x. $x = 0$ for the round cable ($f = 0$) regardless of the field orientation θ_a. Note also that for the cable with the large number of the strands, $N \gg 1$, and the thin cable core, $g \lesssim D$, the shape factor in a perpendicular field $(\theta_a = 0°)$ is a linear function of N, $n \sim ND/(g + 2D)$, while in a parallel field $(\theta_a = 90°)$ is independent of N, $n \approx 0.21$.

The maximum value of the coupling loss is independent of τ (see figure 5.19). It means that the values of R_a and R_c define the position of the maximum inter-strand loss as $1/(2\pi\tau)$ and do not change its magnitude. Consequently, relatively low energy loss at a given frequency of the sinusoidal sweep can be achieved both in case of high resistances, providing that the peak value is at much higher frequency, and of low resistances, providing that the peak value is at much lower frequency. For a linear or exponential current ramp in fusion magnets, the energy loss can be reduced only by increasing the inter-strand resistance. Similar to the results obtained from the network model for the Rutherford cable without the cable core ($g = 0$) [85], the influence of R_c on the coupling loss is much stronger than of R_a.

Substituting the parameters of the first cable prototype ($D = 6.2\,\text{mm}$, $N = 20$, $g = 5\,\text{mm}$, $L = 1000\,\text{mm}$, $\theta_a = 0°$, $R_a = 15\,\mu\Omega\cdot\text{m}$, $R_c = 1.5\,\mu\Omega\cdot\text{m}$) into equation (5.12) yields $n = 0.747$ and $\tau = 0.197\,\text{s}$, which allows us to calculate the inter-strand loss Q_{inter} from equation (5.10). The values of R_a and R_c are estimated with respect to the results discussed in section 4.3. The total energy loss for the given parameters is obtained as $Q_{\text{cable}} = NQ_{\text{strand}} + Q_{\text{inter}}$, where the calculation of Q_{strand} have already been discussed in the previous section.

The results of the calculation and the AC measurements performed in EDIPO for $B_a = 0.3\,\text{T}$, $B = 2\,\text{T}$, $T = 5\,\text{K}$ are presented in the left plot of figure 5.21. Some of the experimental data, which have been obtained at $B_a = 0.1\,\text{T}$ and 0.2 T, were rescaled to 0.3 T according to $Q \sim B_a^2$, see equation (5.10). This scaling was also confirmed in the measurements, see figure 4.29. The qualitative agreement between the numerical and experimental data suggests that the value of R_c taken as 1.5 μΩ·m is representative for
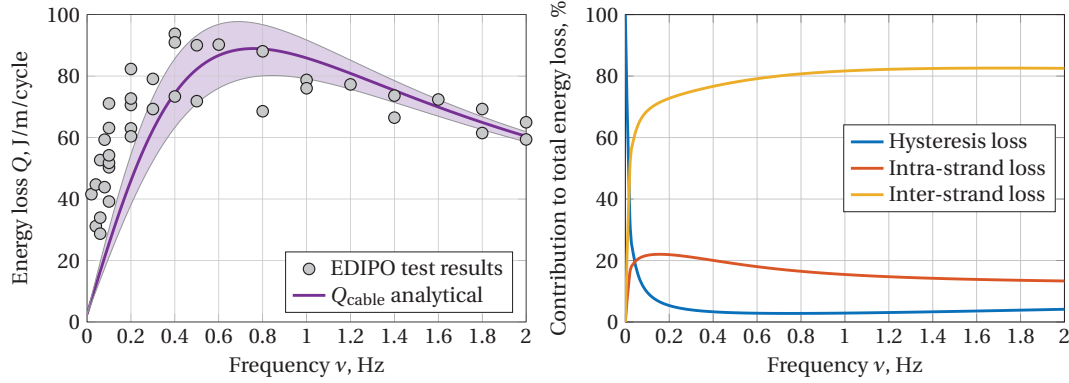
Figure 5.21: The total energy loss per cycle per length (left) and the relative contributions from the hysteresis, intra- and inter-strand loss (right) for the SuperOx cable prototype at $B_a = 0.3\,\text{T}$, $B = 2\,\text{T}$, $T = 5\,\text{K}$.

the cable prototype (influence of R_a is small). At the low frequencies, $v \lesssim 0.2\,\text{Hz}$, a relatively poor accuracy of the calorimetric method, which was used in the measurements, can be at the origin of the discrepancy.

As presented in the right plot of figure 5.21, about 80 % of the total loss is due to the inter-strand coupling currents for $v \sim 1\,\text{Hz}$. Thus, the AC performance of the next cable prototypes can efficiently be improved by adjusting the cable parameters in the following priority: (1) reducing the number of the strands N but also avoiding that the intra-strand loss becomes the dominant contribution, (2) increasing the inter-strand resistance R_c, (3) reducing the cable twist-pitch L. Lower values of R_c can be achieved by plating the copper core (i.e. a resistive barrier on the core surface) or by using the mixed matrix composite (i.e. resistive barriers are distributed throughout the entire cross-section). Both methods diminish the electrical and thermal properties of copper only in the transverse direction. Although R_c would also be increased by using materials with the high resistivity, use of copper is required to increase the heat conductivity in the cable, which will be discussed in the next chapter. Note that the mechanical limits should also be accounted for when choosing lower values of L (see section 4.2.1).

Finally, the effect of the transport current I on the AC loss has also been studied. When all other parameters of the cable are fixed, a relatively weak influence on the computed results was obtained for I/I_c up to 0.9 and $B_a = 0.1\,\text{T}$. The influence of I/I_c is expected to be more pronounced at higher values of B_a. Although the explicit effect of I is small, increasing the transport current at high field should strongly reduce the inter-strand resistance, due to the high Lorentz force acting on the strands, as discussed in section 4.3. The lower values of R_c lead to higher values of τ (see equation (5.12)).

Assuming that R_c drops from $1.5\,\mu\Omega\cdot\text{m}$ to $0.1\,\mu\Omega\cdot\text{m}$, when 50 kA is applied at 10 T, the
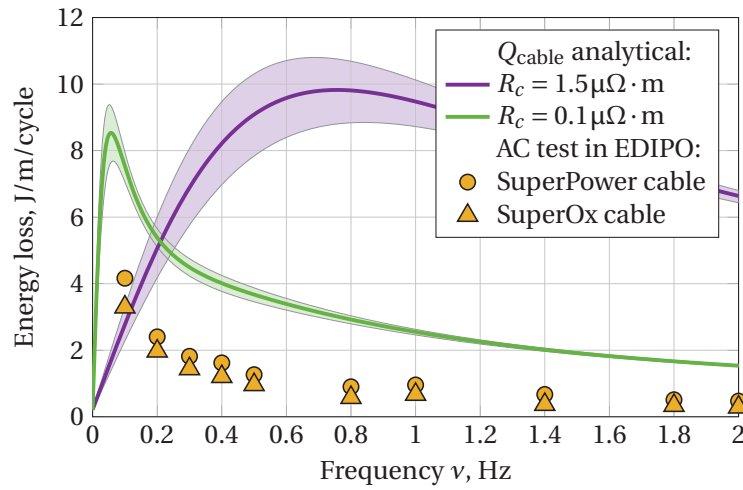
Figure 5.22: Calculated and measured energy loss as a function of frequency for the cable prototypes carrying $50\,\text{kA}$ at $B_a = 0.1\,\text{T}, B = 10\,\text{T}, T = 5\,\text{K}$.

time constant increases from $0.2\,\text{s}$ to $2.9\,\text{s}$. As a result, the maximum value of the total energy loss, being about $9\,\text{J/m/cycle}$ at $B_a = 0.1\,\text{T}$, is shifted from the frequency $0.8\,\text{Hz}$ to $0.05\,\text{Hz}$. As shown in figure 5.22, the results roughly follow the experimental data obtained during the AC test in EDIPO (the full test results are given in section 4.6.3). The energy loss due to the transport current is subtracted in this plot.

Note that the AC test with the transport current have been carried out after about 1500 electromagnetic load cycles, when the I_c performance was degraded by $\sim 10\,\%$ and $\sim 15\,\%$ for the SuperPower and SuperOx cables, respectively (see section 4.6.4). Due to the highly non-uniform distribution of the I_c degradation (see section 4.7), the inter-strand coupling paths through the low I_c regions might not be 'active', which leads to lower energy loss. This effect may explain the discrepancy between the measured and calculated data.

5.3 Conclusion

The main components of the energy loss in the cable have been investigated both experimentally and numerically. The numerical models developed for the hysteresis loss in stacks and coupling losses in the strand and in the cable provide predictions that are a fairly good agreement with the experimental data. Based on the analytical relations extracted from the numerical models, the AC performance of the cable can be assessed in a straightforward manner. The scaling laws obtained for the coupling loss are verified using only a single dataset for the strand and for the cable, so additional experimental data are still needed.

As already concluded from the previous chapter, the AC loss in the first cable prototypes is noticeably higher than for the ITER TF cables. This comes mainly from the inter-strand coupling loss, which is about 80 % of the total energy loss in the first cable prototypes. Hence, the AC performance can be efficiently improved in the next prototypes by reducing the number of strands, increasing the inter-strand resistance and reducing the cable twist-pitch. Unlike the first prototypes meant as TF cables, the AC loss will be included in the design considerations for the CS cables. This will be discussed in chapter 7.

6 Quench analysis

There are various thermal loads acting on superconductors in fusion magnets such as AC losses, Joule heating and heat radiation from the plasma. If the deposited energy is higher than the thermal stability margin of the cable, the evolution of the local operating temperature follows an avalanche-like process [93]. This is due a positive feedback in the system: a relatively small rise of the temperature at the initial moment locally reduces the critical current, such that a fraction of the operating current starts to flow in normal conducting materials inside the cable (stabilizer). This in turn contributes to the temperature rise by Joule heating. This process of the thermal runaway is called 'quench'.

Despite the fact that HTS are intrinsically much more stable than LTS due to a larger margin between the operating and critical temperatures [23], the possibility that a quench occur must be considered. The most severe situation is for a quench starting in the low field region or at reduced operating current during the charge, since a higher temperature margin along the cable complicates a rapid detection of the thermal runaway. Regardless of the underlying reasons, the magnet should be protected against local overheating during the quench. Quantitatively, the protection requirement is formulated in terms of the maximum allowable local temperature (hot spot) on the steel jacket of 150 K [94]. The criterion aims to avoid thermal mechanical stress in the electrical insulation, which may compromise the integrity of the winding pack.

A major concern about the quench process in HTS comes from a slow longitudinal expansion of the high temperature zone. The propagation velocity is order of 1 cm/s, about two orders of magnitude lower than in LTS. Nonetheless, the temperature of hot spot is still rapidly rising. In addition, the voltage measurements, which are typically used to detect quench in fusion magnets, are based on a relatively high threshold value – about 100 mV is the minimum affordable in a noisy fusion environment. Therefore, it should be verified whether this detection method is still capable to ensure a safe discharge of the magnet containing HTS cables.

Analysis of the quench properties for the proposed HTS cable design is addressed in this chapter by means of the numerical modeling, which is a multiphysics task, involving the heat, electrical and hydraulic equations. Design of the 60 kA/12 T prototypes with the steel cross-section relevant for TF coils will be taken as a reference to identify how the hot spot temperature depends on the operating conditions and parameters of the cable.

6.1 Description of the numerical model

Based on the cable design presented in figure 4.1, we distinguish three main domains (or components) in its cross-section: (1) cable bundle, composed of the strands and copper core, (2) steel jacket and (3) helium (i.e. cross-section of voids). For simplicity, in the following discussion the domain (1) is simply referred to as 'cable', which hopefully would not confuse the reader. The length of the components is assumed much larger than their cross-sectional dimensions. This justifies an analysis to based on 1-D geometry.

For the two solid components, cable and steel, the 1D heat equation is written as:

$$C_i \frac{\partial T_i}{\partial t} = \frac{\partial}{\partial x}\left(k_i \frac{\partial T_i}{\partial x}\right) + g_i, \quad i = 1 \text{ for cable, 2 for steel} \tag{6.1}$$

where C denotes the volumetric heat capacity (in J/(m^3·K)), k the thermal conductivity (in W/(m·K)) and g describes the total volumetric heat (in W/m^3), which includes the heat transfer from the other domains, Joule heating and external heat sources.

The cable domain comprises five materials: ReBCO superconductor, copper, Hastelloy, SnPb solder and silver. As they are considered at the same temperature T_1, the average properties of the cable are calculated as follows: $C_1 = \sum \gamma_j f_j c_j$, $k_1 = \sum f_j k_j$, where γ_j, c_j and k_j are the density, specific heat capacity and thermal conductivity of the materials, respectively, and f_j their fraction in the cable cross-section, $\sum f_j = 1$. Buffer layers of HTS tapes are omitted as their contributions to C_1 and k_1 are negligible.

The electrical resistivity of the superconductor is defined as $\rho_{\text{sc}}(B, T, j) = \frac{E_c}{j}\left(\frac{j}{j_c(B,T)}\right)^{n(B,T)}$, assuming that $E_c = 1\,\mu\text{V/cm}$, the magnetic field B is perpendicular to the tape face and the mechanical strain is zero (see equation (2.1)). It is neglected that ρ_{sc} should deviate from the power law to Ohm's law for $j \gg j_c$. At such overloading conditions the operating current will flow entirely in the stabilizer (i.e. normal conducting materials), which is also obtained from considering only the power-law dependence for ρ_{sc}. Anisotropy of j_c is also excluded as on average the cable performance is defined by the field perpendicular to the c-axis, see section 4.6.2.

The cable and steel domains are electrically connected in parallel. The sharing of the total operating current I between them is non-linear, as the superconductor is present in the cable domain. The total electrical resistivity of the stabilizer is written as $\rho_{\text{stab}} = 1/\left(\sum \frac{f_j}{\rho_j}\right)$, where the resistivity of Cu, Hastelloy, SnPb and Ag is taken at temperature T_1 and that of steel at T_2. By neglecting the transverse and inductive voltages due to the current sharing, the current in the superconductor, I_{sc}, can be

obtained from a balance of the DC electric fields, $E_{sc} = E_{stab}$, which leads to:

$$\xi^n + \frac{\rho_{stab} I_c}{S_{stab} E_c}\left(\xi - \frac{I}{I_c}\right) = 0, \quad \xi = \frac{I_{sc}}{I_c} \tag{6.2}$$

where S_{stab} is the cross-section of stabilizer, $I_c = j_c S_{sc}$ and n are the critical current and the power-law exponent of ReBCO at T_1, respectively. Using the value of ξ obtained from equation (6.2), the electric field can be calculated as $E = E_c \xi^n$, which allows us to obtain the total voltage $V = \int E \, \mathrm{d}x$, the current in the steel $I_2 = E S_2 / \rho_2$ and in the cable $I_1 = I - I_2$. Finally, we calculate the power of Joule heating in these components as $P_{1J} = I_1 E$ and $P_{2J} = I_2 E$. The effect of the transverse currents on the Joule heating is neglected.

The required properties of the solid materials – γ, c, k and ρ – as a function of temperature are adapted from various sources [48, 95, 96]. The calculation is terminated if the temperature rises above 300 K, as some of the material properties are not available above this limit. Note also that k and ρ for pure materials, i.e. copper and silver in the presented model, depend also on the magnetic field B and RRR.

Following an approach taken in the THEA package of CryoSoft [97], the state of the forced flow in helium is described by its temperature T_3, pressure p and velocity v. The governing equations can be obtained from the energy, continuity and momentum equations of the flow, respectively, as follows [98]:

$$
\begin{aligned}
\frac{\partial T_3}{\partial t} &= -\varphi T_3 \frac{\partial v}{\partial x} - v \frac{\partial T_3}{\partial x} + \frac{\gamma_h v F + g_3}{\gamma_h c_v}, \\
\frac{\partial p}{\partial t} &= -\gamma_h c^2 \frac{\partial v}{\partial x} - v \frac{\partial p}{\partial x} + \varphi\left(\gamma_h v F + g_3\right), \\
\frac{\partial v}{\partial t} &= -v \frac{\partial v}{\partial x} - \frac{1}{\gamma_h}\frac{\partial p}{\partial x} - F, \quad \text{where } F = 2f \frac{v|v|}{D_h}.
\end{aligned}
\tag{6.3}
$$

The hydraulic diameter of the coolant flow D_h is obtained as discussed in section 4.1. In addition, the hydraulic dimensionless numbers, namely the Reynolds number $\mathrm{Re} = \gamma_h |v| D_h / \mu$ and the Prandl number $\mathrm{Pr} = \mu c_p / k$, are also calculated.

The helium density γ_h, the speed of sound c, the specific heat capacities c_v and c_p, the viscosity μ and the thermal conductivity k as a function of p and T_3 are obtained from [63, 99]. The detailed discussion over the Gruneisen parameter φ is given in [100].

The Fanning friction factor f is usually determined from the empirical correlations. The Blasius expression $f = 0.079 / \mathrm{Re}^{0.25}$ is used in the model for the turbulent flow with $\mathrm{Re} \gtrsim 10^3$. For the lower values of Re, f is set to the constant value about 0.04, see [101] for more details.

Assuming that the external heating P_{ext} (in W/m) is applied only to the cable domain,

the volumetric heat terms in equations (6.1) and (6.3) are obtained as:

$$g_1 = \left(-P_{12} - P_{13} + P_{1J} + P_{ext}\right)/S_1$$
$$g_2 = \left(P_{12} - P_{23} + P_{2J}\right)/S_2 \tag{6.4}$$
$$g_3 = \left(P_{13} + P_{23}\right)/S_3$$

where $P_{ij} = h_{ij}p_{ij}\left(T_i - T_j\right)$ is the heat transfer between the i-th and j-th components, p_{ij} the contact perimeter between them and h_{ij} the heat transfer coefficient (in $W/(m^2 \cdot K)$). The external power per unit length, P_{ext}, is applied at the beginning of the calculation as a short pulse at the center of the cable over the length l_p and during the time t_p. Consequently, the energy of the heat pulse $Q = P_{ext}l_p t_p$ is deposited in the cable.

According to [102], the heat transfer coefficient between the cable and steel components, h_{12}, can be conservatively estimated as $h_{12} = 500\,W/(m^2 \cdot K)$. With regard to the heat transfer to the coolant flow, h_{13} and h_{23} are deduced from the Nusselt number, $Nu = hD_h/k$. The dependence of Nu upon the parameters of the helium flow is approximated as the constant value about 8 for the laminar flow [103] and using the Dittus-Boelter correlation $Nu = 0.023\,Re^{0.8}\,Pr^{0.4}$ for the turbulent flow [104, 105]. Although a slightly modified expression for Nu is proposed for the turbulent flow in the cable-in-conduit conductors [106], we will use the Dittus-Boelter expression, because it provides a slightly faster temperature rise (i.e. the results are more conservative).

As a result, equations (6.1) and (6.3), coupled by the volumetric heat terms (6.4), form a system of equations for T_1, T_2, T_3, p and v, which are a function of the time t and the longitudinal coordinate x. For N_x nodes along x, the system can be considered as a set of $5 \cdot N_x$ ordinary differential equations. This system can be directly integrated. This is performed using the built-in Matlab solver `ode15s`.

The following parameters are used to calculate the initial and boundary conditions for the system: the temperature T_0, the inlet pressure p_0 and the mass flow rate $\dot{m}_0$. The initial values for T_1, T_2, T_3 and v are set to T_0 and $v_0 = \dot{m}_0/(\gamma_h(p_0, T_0)S_3)$, respectively. The length of the components l is set to relatively high values, tens of meters. Therefore, at the first and the last nodes it is possible to use zero derivatives on the right hand side in equations (6.1) and (6.3), except those for p. The pressure drop per unit length can be evaluated from the Darcy-Weisbach equation [59], or considering the steady-state flow $v = const$ in the last equation in (6.3), as $p'_x = -2f_0\dot{m}_0^2/(\gamma_h(p_0, T_0)D_hS_3)$. The pressure at the initial moment is set to a linear function as $p(x, t = 0) = p_0 + p'_x \cdot (x + l/2)$, assuming that $x = 0$ for the center of the cable.

During the integration, an event of the quench detection is defined as a situation, when the total voltage along the cable is equal to the threshold value, $V = V_{th}$. Before this condition is met, the operating current I_0 is constant in the cable. As the quench is detected, the current stays constant during the time $t_{discharge}$, which simulates the

(1) cable: T_1, steel: T_2, helium: T_3, p, v (2) cable + steel: T (3) cable: T
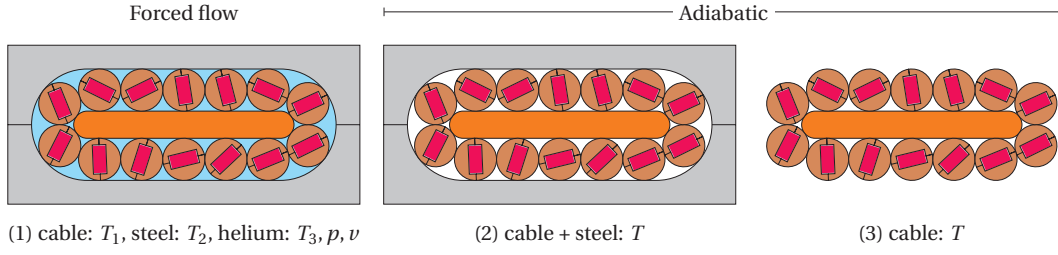
Figure 6.1: Studied cases for the presented model.

total delay required to trigger the circuit breakers. After that, the current decreases exponentially with the time constant τ, $I(t) \sim e^{-t/\tau}$, simulating the presence of a dump resistor in the system. A simple estimate of the electrical circuit at the moment of the breakers opening yields that $\tau = LI_0/V_{\max}$, where L is the inductance of the coil, $V_{\max}$ the maximum terminal voltage. τ is order of tens of seconds in large fusion coils. The external magnetic field is considered constant along the cable and proportional to the operating current, $B(t) = B_0 I(t)/I_0$.

For the specified material properties and design of the cable, the input parameters of the described model can be divided into the three categories:

1. Operating conditions: T_0, p_0, $\dot{m}_0$, I_0, B_0

2. Heat pulse: Q, t_p, l_p

3. Current decay: V_{th}, τ, $t_{\text{discharge}}$

Two simplified adiabatic cases will be considered: the cable and steel domains at the same temperature T and only the cable domain. As the helium cooling is excluded and the temperature evolution is obtained directly from equation (6.1), the peak temperature is overestimated in these cases, which can be considered as a conservative approach to fulfil the quench protection requirement. The differences between these two and the general case are illustrated in figure 6.1. A distinctive feature of the adiabatic cases is that the hot spot, the point where the temperature is maximum along the cable, is always at the center of the region where the heat pulse is applied. For the forced flow cooling, the location of the hot spot is slowly moving in the direction of the helium flow.

Although strictly speaking the model is 1-D, the heat transfer terms provide the possibility to effectively account for 3-D geometry of fusion coils using periodicity conditions, with a period of the one turn length l_1 in the winding pack. A set of points, located from each other at the distance l_1 along x, can be considered as located in the same cross-section of the winding pack, so the heat transfer between them can be included in g_3 for the steel domain to account the transverse heat propagation. As this is beyond the scope of the present study, only a straight cable situation is considered in the following discussion.
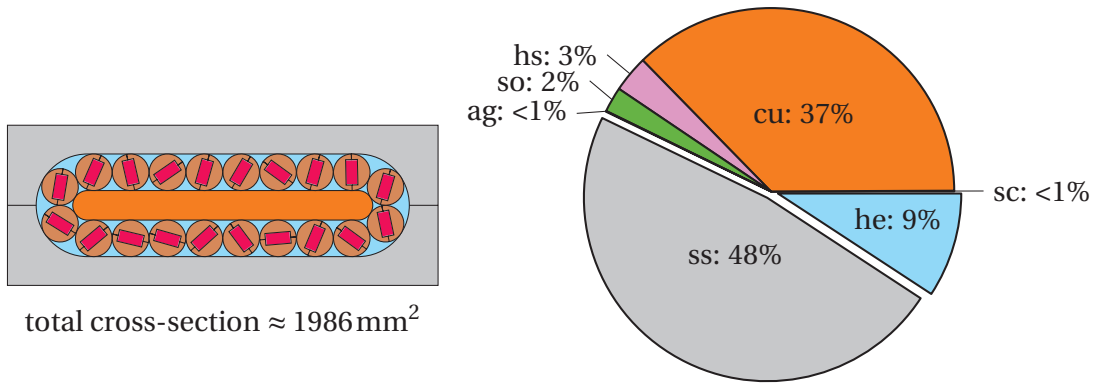
Figure 6.2: The cross-section of the first cable prototype with 950 mm^2 of steel (left) and relative fractions of ReBCO, stabilizing materials and helium in it (right).

6.2 Quench propagation

The geometry parameters of the first cable prototypes, which have been discussed in section 4.4.1, are selected for the present study except the cross-section of steel, which is increased from about 680 mm^2 to 950 mm^2, making it suitable for TF coils from a mechanical point of view [107]. This is achieved by increasing the minimum thickness of the steel jacket from 3.5 mm to 4.9 mm. As a result, about half of the total cross-section is occupied by the steel domain, see figure 6.2. The rest of the cross-section is due to the cable ($\sim$43 %) and the helium ($\sim$9 %) domains.

The length of the components is set to 25 m, along which about 300 mesh-elements are used, with the higher density at the center of the cable, where the quench is initiated. The initial values for the temperature, magnetic field and inlet pressure are set as $T_0 = 5$ K, $B_0 = 12$ T and $p_0 = 6$ bar, respectively. The field-temperature dependence of the critical current density $j_c(B, T)$ of the SuperOx tapes (see appendix A.1) is selected for the superconductor domain. With regard to the n-value of the voltage-current transition, two options are considered: (1) constant value, $n = 40$, and (2) dependence upon field and temperature, $n(B, T) = 1 + \alpha\, j_c(B, T)$, such that $n(B_0, T_0) = 40$, which yields $n(\mathrm{sf}, 77\,\mathrm{K}) \approx 27$. For the copper and silver domains, the value of RRR is set to 100 and 200, respectively.

The heat pulse is applied at the center of the cable over the length $l_p = 0.1$ m and during the time $t_p = 0.1$ s. The energy deposited during the pulse, Q, has a highly non-linear impact on the temperature evolution. At the end of the heater operation, the temperature and voltage start to decrease and it takes a relatively long time to obtain the system response upon Q. If Q is below a certain threshold, the temperature and voltage continue to decrease monotonically in time. Otherwise, at some moment they both start to increase very rapidly. The value of the energy threshold is called the
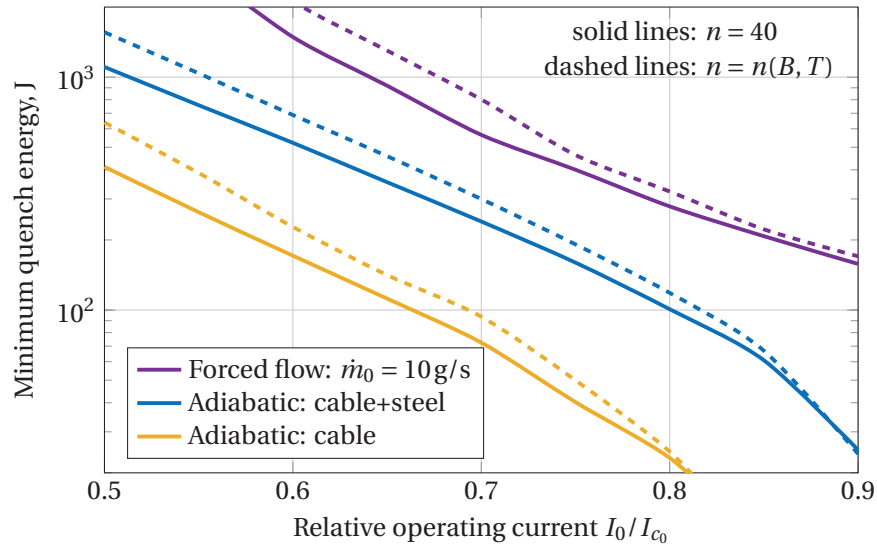
Figure 6.3: Minimum quench energy for the first cable prototype as a function of relative operating current at 5 K and 12 T. The dashed lines are obtained assuming that n-value depends upon $j_c(B, T)$.

minimum quench energy (MQE).

Defining the quench event as an increase of the hot spot temperature at the end of the calculation, one can find the MQE using, for example, the binary search algorithm over the given energy range. The obtained values of MQE for the three studied cases (see figure 6.1) are presented in figure 6.3 as a function of I/I_{c_0}, where $I_{c_0} = I_c(B_0, T_0) \approx$ 61 kA is the initial critical current of the cable.

Comparing the two adiabatic cases, the MQE is significantly increased, by a factor 3 to 4, when steel is present. This is mainly due to its high thermal capacity. A similar increase in MQE is obtained due to the forced flow of the helium coolant at $\dot{m}_0 = 10$ g/s. In general, higher values of MQE are obtained when the field and temperature dependent n-value is used (see dashed lines in figure 6.3), since lower values of n during the temperature rise reduce the Joule heating in the cable.

As proposed for DEMO magnets [94], the quench should be initiated by applying the heat pulse with the energy $Q = 2 \cdot \text{MQE}$. This condition is mostly a matter of agreement, since different values of Q (higher than MQE) have a minor impact on the peak temperature. A rather weak influence of the heat pulse parameters and the discharge time on the peak temperature was also observed for the DEMO LTS cables [108]. Note that the results presented in figure 6.3 are used as the input data for the following simulations.

Finally, let us investigate the quench situation in the cable operated at $I/I_{c_0} = 0.9$ and with $n = 40$. As discussed in the previous section, when $V = V_{\text{th}}$ is achieved, the
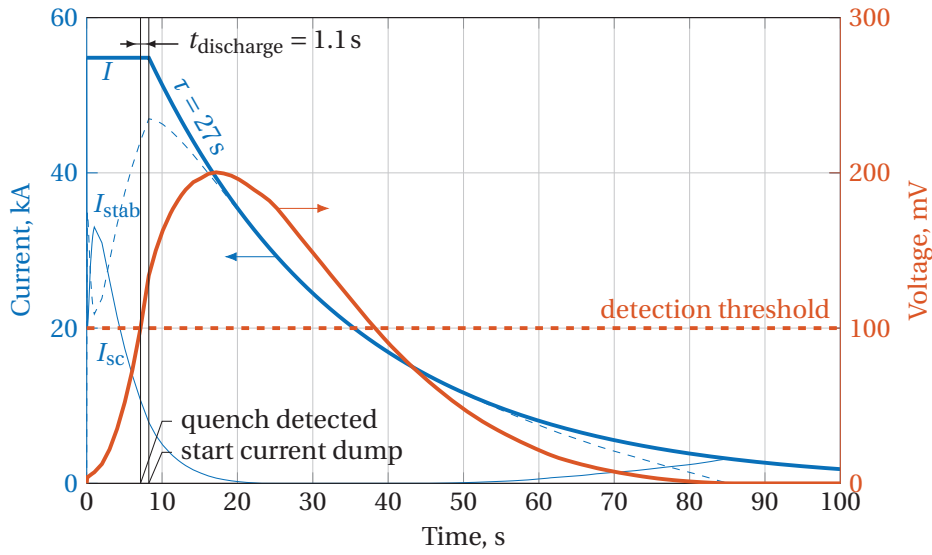
Figure 6.4: Evolution of current and voltage during quench in the cable operated at $I/I_{c_0} = 0.9$ and cooled by the forced flow of helium at $\dot{m}_0 = 10\,\text{g/s}$. Fractions of the total current flowing in the superconductor I_{sc} and stabilizer I_{stab} at the hot spot are also reported.

operating current I stays constant during $t_{\text{discharge}}$ and then exponentially decays with the time constant τ, which is necessary to avoid the overheating of the cable. According to common design values for DEMO TF coils [94], these parameters are taken as follows: $V_{\text{th}} = 100\,\text{mV}$, $t_{\text{discharge}} = 1.1\,\text{s}$, $\tau = 27\,\text{s}$.

The dependences upon time of V, I and the currents at the hot spot in the superconductor I_{sc} and stabilizer I_{stab} are shown in figure 6.4 for the forced flow of helium at $\dot{m}_0 = 10\,\text{g/s}$. Note that $I = I_{sc} + I_{stab}$. The I/I_c ratio at the location of the hot spot, which slowly moves in the direction of the helium flow, is 0.9 at the beginning of the calculation, about 3 at 0.1 s, when the heater is switched off, about 6 when the quench is detected and about 8 at the beginning of the current dump. The critical current of the hot spot finally drops to 0 at about 24 s and the operating current starts to flow entirely in the stabilizing materials. After that, the critical current slowly recovers starting from 45 s due to the current and field dump and at 80 s the operating current returns completely in the superconducting domain. The maximum voltage obtained during the simulation is about 200 mV.

The corresponding temperature distribution along the cable domain and the mass flow rate for the selected moments of time are presented in figure 6.5. In addition, the time evolution of the temperature and location of the hot spot is shown in the left plot. The high temperature zone at 0.1 s is relatively narrow, about the length of the heater $l_p = 0.1\,\text{m}$, and then it expands and moves towards the helium flow, reaching about several meters in width when the quench is detected. The hot spot temperature
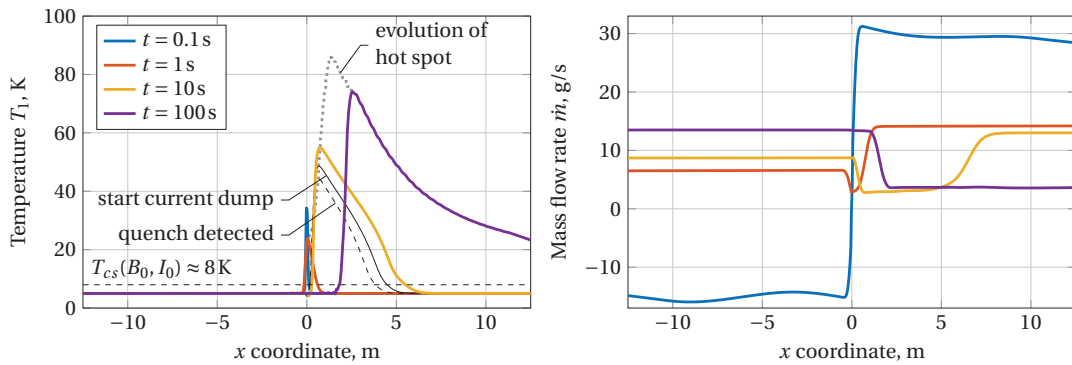
Figure 6.5: Temperature of the cable and mass flow rate of the coolant along x at certain moments of time for the forced flow cooling, $\dot{m}_0 = 10\,\text{g/s}$.

is $\approx 44\,\text{K}$ when the quench is detected, and $\approx 74\,\text{K}$ at the end of the calculation. The maximum temperature of the hot spot, T_{max}, is about 86 K.

The perturbations in the helium mass flow rate are distributed around its initial value of 10 g/s, which corresponds to the pressure drop from 6 bar at the inlet to about 5.94 bar at the outlet. The helium state at 0.1 s is characterized by the pressure rise at $x = 0$ of about 0.1 bar, resulting in a high gradient of $\dot{m}(x)$ at that point and the back flow (i.e. the negative values of $\dot{m}$) in the left half of the cable. It takes about 1 s for the main perturbation to die out, after which $\dot{m}$ deviates from 10 g/s much weaker. Then, the minor perturbations follow the high temperature zone, where the heat exchange between the cable and helium is still present.

Although a large variety of hydraulic phenomena are present in the calculations, the following discussion is mostly focused on the study of the hot spot temperature, the key figure for the quench analysis.

6.3 Hot spot temperature

First, let us compare the hot spot temperature calculated from the three approaches discussed so far: (1) the forced flow at $\dot{m}_0 = 10\,\text{g/s}$, (2) the adiabatic heating of the cable with the steel jacket and (3) standalone cable (see figure 6.1). For each case we also consider effect of the n-value: either $n = 40$ or $n = 1 + \alpha\,j_c(B, T)$ such that $n(B_0, T_0) = 40$. Using the same input parameters in the model as in the previous section and the values of MQE presented in figure 6.3, we arrive at the comparison of the six situations for the hot spot, presented in figure 6.6. Two characteristic values of the hot spot temperature will be used below: the maximum value, T_{max}, and the value when the quench is detected, T_q. The values of T_q are shown as round markers in figure 6.6.
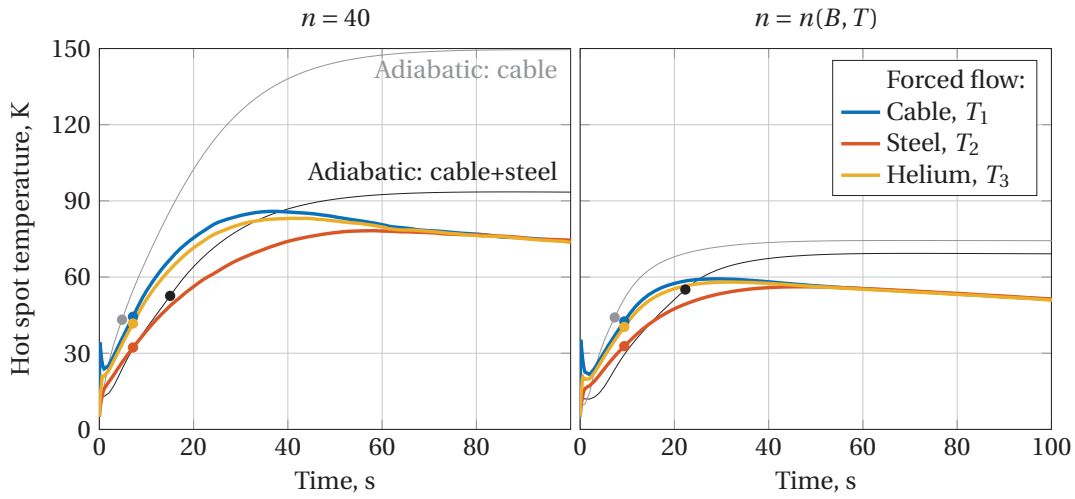
Figure 6.6: Hot spot temperature as a function of time calculated based on the three approaches, illustrated in figure 6.1, for the constant (left) and for the field and temperature dependent n-value (right). The moments when quench in detected (i.e. $V = V_{th}$) are shown by round markers.

The results obtained from the forced flow case are expected to be the most relevant, as this approach accounts for most phenomena during the temperature evolution. However, such calculation requires about 10 times longer computation time than in adiabatic cases. For all three cases the values of T_q are similar, around 40 K. T_{max} obtained from the case (3) is significantly larger than that of (1) as the steel jacket strongly increases the thermal capacity of the system. When the amount of the solid materials is identical, as in cases (1) and (2), the deviation between the results is much weaker. Hence, case (2) is selected to perform the parametric study of T_{max}.

As expected, the influence of the n-value dependence on T_q is relatively weak, as both options for n provide high values till the quench is detected, i.e. when the temperature is relatively low. However, a much stronger impact is obtained on T_{max}. This still requires additional investigations. In practice, a constant value of n is the common choice for the quench analysis. $n = 40$ is used for the following discussion as a conservative approach.

In order to better understand the main factors determining the value of T_{max}, we shall also compare the following results with even more simplified calculation, assuming that the energy dissipation due to the Joule heating is fully absorbed by the thermal capacity of the cable and steel jacket. Such situation can be achieved by neglecting the thermal conductivity and heat transfer terms in the heat transfer equation. Assuming also that the operating current flows entirely in the stabilizing materials and it decreases exponentially after being constant during $t_{discharge}$, these simplifications
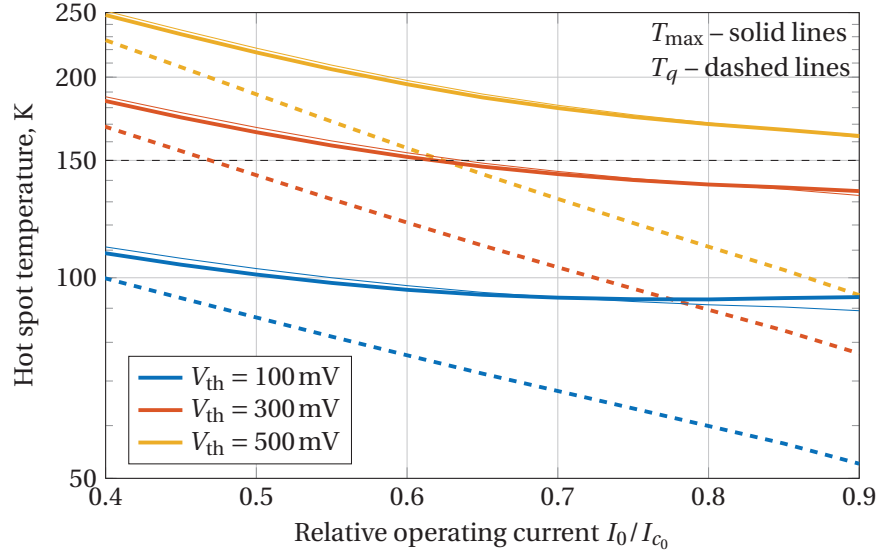
Figure 6.7: T_{max} (solid lines) and T_q (dashed lines) as a function of relative operating current for various voltage detection thresholds V_{th}. T_{max} is calculated using both the numerical model (thick lines) and equation (6.5) (thin lines).

allow us to directly integrate the heat equation by separation of variables [109]:

$$
C\frac{\partial T}{\partial t} = \rho\, j^2 \Rightarrow \int_{T_q}^{T_{\mathrm{max}}} \frac{C(T)}{\rho(T)}\, \mathrm{d}T = \int_{t_q}^{\infty} j(t)^2\, \mathrm{d}t = j_0^2\left(t_{\mathrm{discharge}} + \frac{\tau}{2}\right) \tag{6.5}
$$

where $j_0 = I_0/S_{\mathrm{stab}}$ and t_q is the time when quench is detected. Note that the magnetoresistivity effect is also omitted, i.e. ρ depends only on temperature and for copper and silver the values of ρ are taken at zero magnetic field. When T_q is defined, the integral expression (6.5) is an implicit equation for T_{max}. Due to its simplicity, this assessment is widely used as a simplest estimate of T_{max} and can be referred to as '0-D adiabatic' [110], 'Z-function' [23] or 'MIIT' [88, 111] calculation.

As a quench can occur at any moment of the cable operation, it should be verified that the cable design fulfils the requirement on steel temperature, that should stay below 150 K, even at low currents, i.e. during the charge of the magnet. The values of T_q and T_{max} are summarized in figure 6.7 as a function of I_0/I_{c_0} for various values of V_{th} (other parameters of the model are the same as used before).

Both T_{max} and T_q increase for higher values of V_{th} and for lower I_0. This is an expected result, as higher values of V_{th} lead to longer propagation of the quench process without the dump of the operating current. The stability margin over the cable length is higher for the lower values of I_0, so the longitudinal propagation of heat is highly reduced and more energy is 'spent' to raise T_{max}.
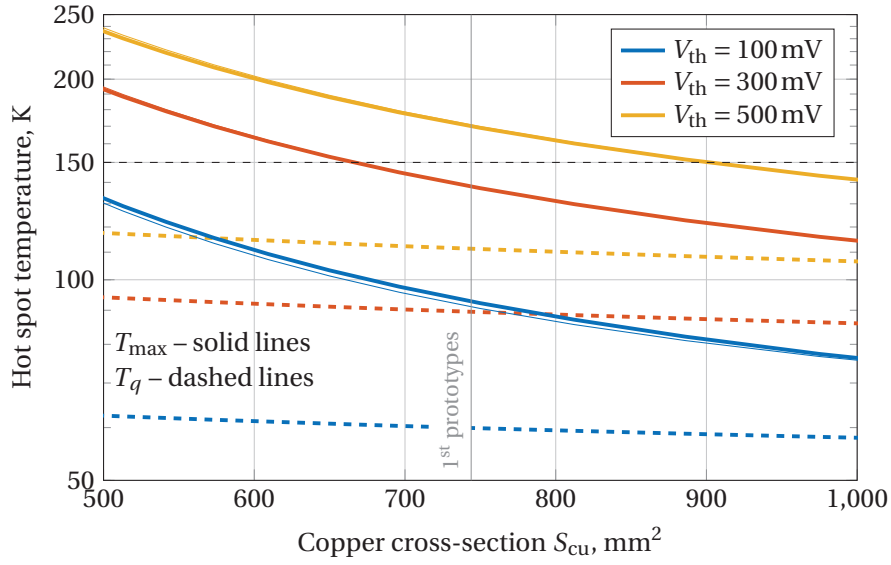
Figure 6.8: T_{max} (solid lines) and T_q (dashed lines) at $I_0/I_{c_0} = 0.8$ as a function of the copper cross-section S_{cu} for various voltage detection thresholds V_{th}. T_{max} is calculated using both the numerical model (thick lines) and equation (6.5) (thin lines). S_{cu} of the first prototypes is also shown.

In order to calculate T_{max} from equation (6.5), the values of T_q presented in figure 6.7 are used. Although T_q can be estimated for LTS as $(T_{cs} + T_c)/2$, such estimate for T_q is not applicable for HTS as the values even higher than T_c, which is about 70 K at 12 T, can be obtained depending on V_{th} (see dashed lines in figure 6.7). As T_{max} calculated from the numerical model and equation (6.5) are in good agreement (compare thick and thin solid lines in figure 6.7), we conclude that T_{max} is mostly defined by the adiabatic heating of the cable and steel from the Ohmic dissipation of energy. Hence, influence of the longitudinal heat propagation on T_{max} is negligible.

The analysed cable design (see figure 6.2) fulfils the protection requirement for $V_{th} = 100\,$mV over the entire range of the studied operating currents. The results at higher values of V_{th} are not acceptable according to the specified requirement. Note that the total voltage is measured over long sections on coil and it is unlikely to use $V_{th} < 100\,$mV for reliable measurements.

The obtained margin about 40 K between the protection requirement and T_{max} for $V_{th} = 100\,$mV suggests that the cross-section of copper in the cable, S_{cu}, can be reduced. This possibility is investigated in figure 6.8 for $I_0/I_{c_0} = 0.8$ and various values of V_{th}. The variation of S_{cu} is performed in a straightforward manner, regardless whether it corresponds to some design of the cable or not. The initial cross-section of copper, $S_{cu} \approx 738\,$mm^2, is indicated by a thin gray line in figure 6.8.

S_{cu} can be reduced down to 500 mm^2 at $V_{th} = 100\,$mV, still fulfilling the protection

requirement, where we also assume that the presented results for $I_0/I_{c_0} = 0.8$ depend on I_0/I_{c_0} in a similar way as presented in figure 6.7. For the other values of V_{th} the opposite direction for S_{cu} must be used: S_{cu} should be increased to $\approx 850 \, \text{mm}^2$ at $V_{\text{th}} = 300 \, \text{mV}$ and to even higher values at $V_{\text{th}} = 500 \, \text{mV}$. Hence, V_{th} is a crucial input parameter for the cable design studies.

6.4 Conclusion

A 1-D numerical model based on heat transfer and flow equations is developed for the quench analysis of the HTS fusion cables. If compared with the THEA package of Cryosoft, by which this model is heavily influenced, two distinctive features are envisaged as further advances: the implementation of the field and temperature dependent n-value of the superconductor, and the accounting for the 3-D geometry of fusion coils via the heat transfer between adjacent turns in the winding pack. When $n = n(B, T)$ is used, which is mostly relevant for HTS, a significant reduction of the hot spot temperature is obtained if compared with the simulation where the n-value is considered constant. However, the results are obtained only on a single design case and more studies are still needed. As regards the second feature, there is no obstacles preventing its implementation. This activity is left for future investigations.

The quench behaviour of the first cable prototype with $950 \, \text{mm}^2$ cross-section of steel, which is mechanically relevant for TF coils, fulfils the protection requirement for the operation at the peak field $12 \, \text{T}$ and in a wide range of the operating currents at $100 \, \text{mV}$ of the detection threshold. Using HTS cables at low field is not envisaged in the present study, as no advantages of such application are identified. Nonetheless, a substantial variation of field in the HTS section of the winding pack can be present, which should be accounted for in a further quench analysis. As a preliminary result, the margin between the required and actual values of the steel temperature of about $40 \, \text{K}$ allows reducing the copper cross-section in the prototype from $740 \, \text{mm}^2$ to $500 \, \text{mm}^2$. Note that this modification should also be validated by the mechanical considerations.

The quench detection based on the voltage measurements is feasible for the HTS fusion cables. Although use of the detection threshold of $100 \, \text{mV}$ is a challenging task of electrical engineering, higher values should only be considered as an ultimate measure, as they would lead to significant changes in the cable design.

7 Application of the cable concept to fusion magnets

Using HTS cables in fusion magnets provides an unique opportunity to increase the peak field on the coil above the 15 T limit, at values for which the LTS materials cannot carry sufficiently high currents. When applied to TF coils of tokamak reactors, an increase of magnetic fields potentially leads to higher fusion powers and better confinement of the plasma. For CS coils it becomes possible to reduce the size of the coils or increase the generated magnetic flux, i.e. produce a longer plasma burn. Although both options are of high interest, the former one is not currently envisaged in the EUROfusion roadmap, since in large tokamaks the TF coils are almost at the limit in terms of mechanical stresses in the jacket and thus the main benefit is expected by use of higher strength steels. Therefore, in the present discussion we focus on the application of HTS cables to the CS coils, corresponding to the current European DEMO design proposed in 2015 [112, 113].

In particular, we will address the main issue that remains from the previous discussion – whether preliminary annealing of the copper profiles is required or not in a design study of the CS cable prototypes. We will perform an assessment of the main cable properties, such as T_{cs}, AC losses and hot-spot temperature during quench. In addition, cost considerations associated with the presence of expensive HTS materials in the magnet system will be presented.

7.1 Central solenoid conceptual design

The poloidal field in the reference design of the DEMO magnet system is generated by the central solenoid, made of Nb_3Sn cables, and 6 PF coils, made of NbTi cables [114]. The central solenoid comprises 5 independently operated modules, which are of the same inner radius 2.5 m and radial thickness 0.8 m. The modules are stacked co-axially with 100 mm spacing and labelled top-down as CS3U, CS2U, CS1, CS2L and CS3L. The peak poloidal field is about 12 T at a so-called 'pre-magnetization' stage, right before the plasma discharge is initiated. The magnetic flux generated at that moment in the midplane of the system is about 320 Wb.

Let us analyze a situation, where the central solenoid is made of ReBCO, Nb_3Sn and
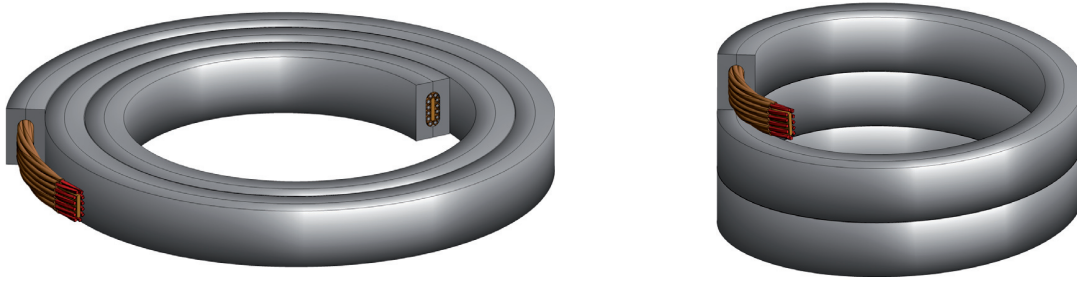
Figure 7.1: 2.5 turns of the cables, which are wound using the pancake winding (left) and the layer winding (right). For illustrative purposes, the radius of bending is reduced by about order of magnitude.

NbTi cables. The main goal is to demonstrate the possibility of reducing the radial dimensions of the solenoid while maintaining the same magnetic flux 320 Wb at the pre-magnetization. Below in this section we summarize the key results obtained in [115] and focus on coil sections made of HTS cables.

Topologically, there are two basic options to wind a solenoid: the 'pancake' and the layer windings, which are illustrated in figure 7.1. Note that bending deformations are applied in a plane perpendicular to the broad side of the cable. For a winding pack relatively thin in the radial direction and tall in the axial one, which is the case of the CS1 module, the layer winding provides with the possibility of superconductor grading between layers. Thus, the layer winding will be considered in the following discussion.

The preliminary study of the graded CS1 module resulted in a winding pack divided into 78 turns in the vertical direction and 20 layers in the radial [116]. The inner radius is reduced by about 25 %, down to 1.9 m, and the outer radius by 15 %, down to 2.9 m. The radial thickness is about 1 m. The inner 4 layers are occupied by the ReBCO cables, which requires in total about 4 km of the cable (≈ 1 km per layer). The subsequent 10 layers are occupied by Nb_3Sn and the last 6 layers by NbTi. The operating current of the cables is about 53 kA, which corresponds to the total current flowing in the cross-section of the CS1 module of about 83 MA. The estimated inductance of the CS1 module is about 6 H.

The distribution of the magnetic field is obtained by integrating the magnetic field produced by ring conductors, see details in appendix A.3.2. The results of the calculation for the baseline design of DEMO and for the graded CS solenoid with the original PF system are provided in figure 7.2. For the remaining CS modules the layer grading is simply taken from the CS1 module, and the total current is rescaled from the values of the baseline design by a factor of 1.447, obtained as the ratio between the total current of the CS1 cross-section in the graded and the baseline designs. The peak magnetic field is about 12.3 T for the baseline design and 17.9 T for the option
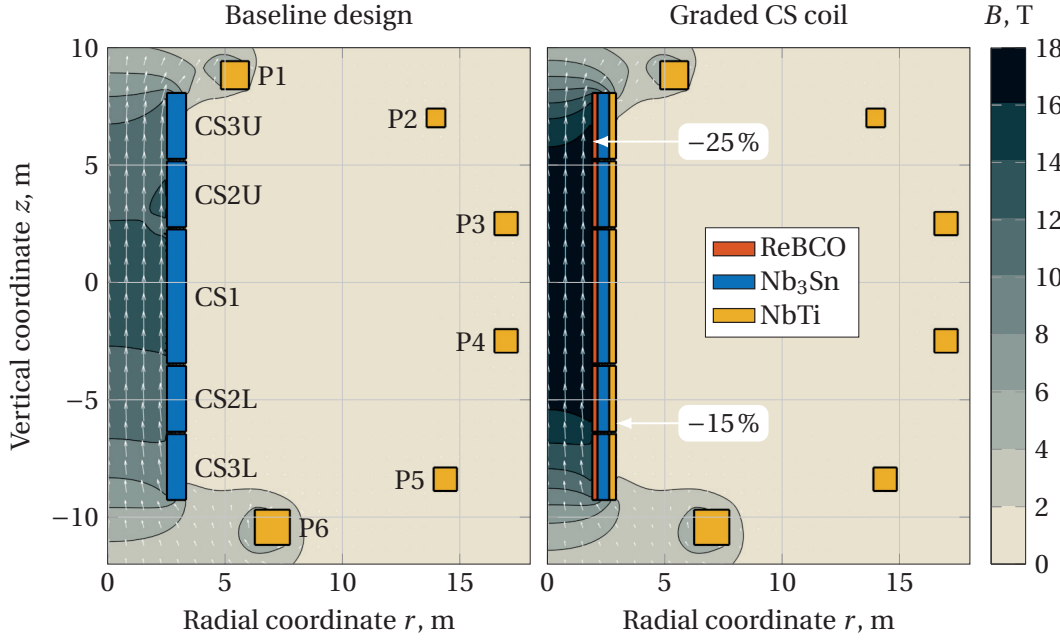
Figure 7.2: Magnetic field generated by the central solenoid and PF coils for the two design options.

with grading.

Magnitude of the magnetic field in the midplane of the system (i.e. $z = 0$) is compared in figure 7.3 for the two options. It reaches the maximum value at the inner radius a_1 and decreases almost linearly, when passes through the CS1 module till its outer radius a_2. The effect of the PF coils on the field generated inside the central solenoid is moderate, of the order of 0.5 T (compare the solid and dashed lines in figure 7.3). Note that the maximum field at the location of Nb_3Sn is increased from 12.3 T in the baseline design to 14.2 T in the graded solenoid. The maximum field for the NbTi layers is about 5.2 T.

The magnetic flux through the solenoid is calculated as $\Phi = \int_0^{a_2} B_z(r,0)2\pi r\,dr$. As the field profile in the midplane $B_z(r,0)$ can be approximated by a constant value B_0 for r from 0 to a_1 and by a linear decrease to zero for r from a_1 to a_2, the magnetic flux is also estimated as:

$$\Phi = B_0 \frac{\pi a_1^2}{12}\left(3 + \left(1 + \frac{2a_2}{a_1}\right)^2\right) \tag{7.1}$$

The obtained magnetic flux is about 330 Wb for both options.

The distribution of the magnetic field and its orientation, θ, at the inner radius of the graded solenoid, $r = 1.9$ m, is presented in figure 7.4. The magnetic field is almost parallel to the broad side of the cable for the inner modules, $\theta \sim 90°$ for CS1, and deviate up to 30° from the vertical direction at the outermost modules, $\theta \sim 60°$ at the
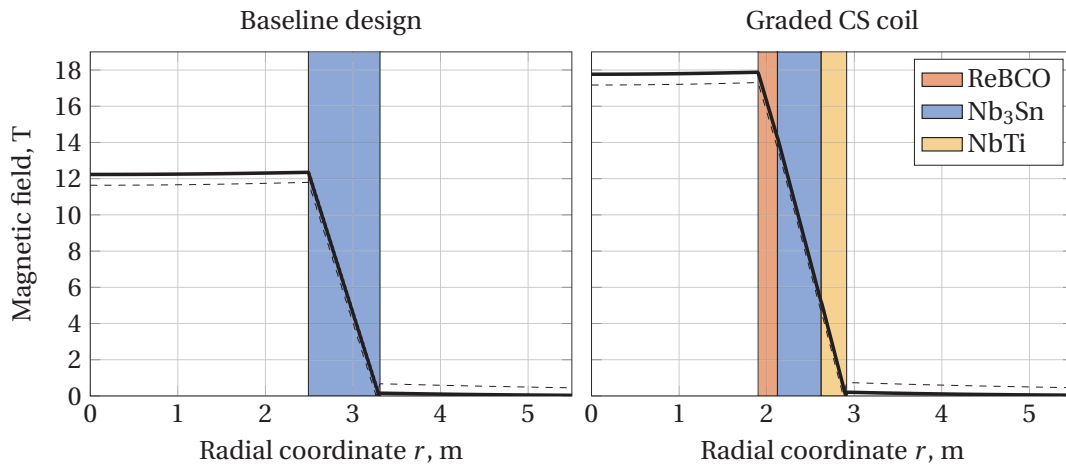
Figure 7.3: Magnetic field in the midplane of the system for the two design options. Dashed lines show the field generated only by the central solenoid.
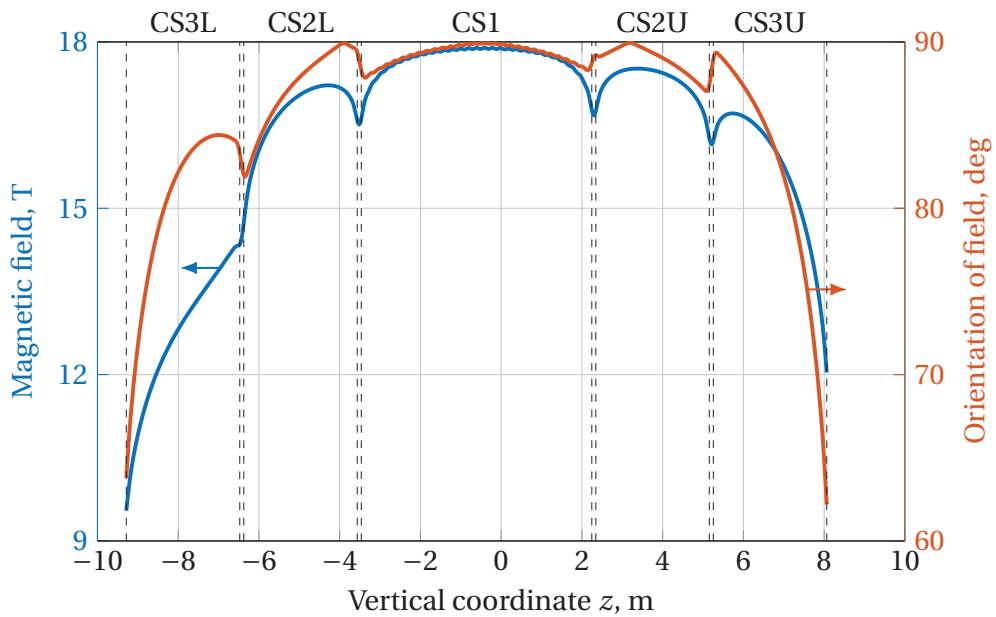
Figure 7.4: Magnitude and orientation of the magnetic field along the vertical direction for the graded solenoid at its inner radius.

edges of CS3L and CS3U. However, because of the strand twisting in the cable, it is not foreseen to align the tapes in the cable such that the perpendicular component can be excluded, what would significantly increase I_c of the tape. Nonetheless, the orientation of the magnetic field strongly affects the AC loss performance of flat cables. This will be further discussed in the next section. As the magnetic field at the CS3L module is below 14.3 T and the analysed pre-magnetization stage is expected to provide the peak field conditions, the CS3L module can be made using only the LTS cables.

7.2 Design and properties of the CS cable

According to the preliminary design study of the graded central solenoid, its innermost layers are made of HTS cables rated for ≈ 53 kA at 18 T. The amount of steel in the cables is mainly dictated by the mechanical analysis of the system, based on the criteria for allowable stress intensity in steel of 660 MPa, 2/3 of the yield stress of steel [117]. During the design iterations, the cross-section of steel varies typically in the range from 2000 mm^2 to 3000 mm^2 [115]. An average value of 2500 mm^2 is used below. Note that in the following discussion we deviate from the cable specifications presented in [115], which are based on the parameters of the SuperOx tapes. Instead, the design of short prototypes is evaluated here using the parameters of the SST tapes, which are planned to use in the manufacturing. The corresponding $j_c(B, T)$ parametrization is discussed below in this section.

Aiming at better understanding of the cyclic load degradation obtained in the first prototypes (see section 4.6.4), two design options for the HTS cables are elaborated, for which annealing of the copper profiles is taken as a basic distinctive feature. This follows the results obtained on single strands subjected to a cyclic loading, suggesting that the preliminary annealing can be at the origin of the degradation (see section 3.9).

The critical bending radius of the strand with non-annealed copper profiles is about twice larger than if annealing is used (section 3.7), which requires to reduce the number of strands in order to maintain similar values of the cable twist-pitch for both cable options (section 4.2.1). As a result, $N = 12$ is set for the annealed option and $N = 6$ for the non-annealed one. The main design parameters and the cross-section of the cables are shown in figures 7.5 and 7.6, where a steel cross-section of 2500 mm^2 is used for both options. Due to the difference in the aspect ratio of the cables, they are referred to as 'flat' and 'round'.

As the critical current of bent strands degrades faster against cyclic loading than that of straight (see sections 3.9 and 4.7), an increase of the strand bending radius R is considered as the most effective approach to avoid degradation of the cable performance during the cycling test. Hence, R at the cable edge is relatively high,

Stage	Parameter	Value
Tape	Width of tape w	3.3 mm
	Thickness of tape d_t	0.07 mm
Strand	Number of tapes n_t	28
	Slot width	3.6 mm
	Slot height	3.6 mm
	Split line	$\parallel$ to c-axis
	Diameter D	7.0 mm
	Twist-pitch h	400 mm
	Annealing of profiles	Yes
Cable	Number of strands N	12
	Thickness of core g	5.0 mm
	Twist-pitch L	1000 mm
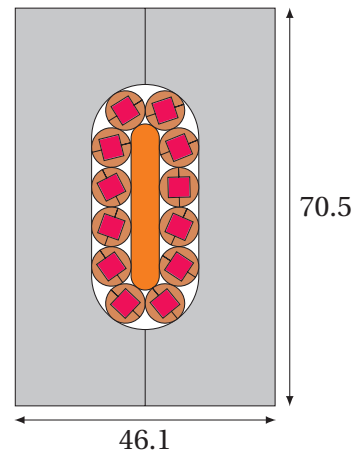
Figure 7.5: Design parameters and cross-section of the 'flat' cable for CS coils.

Stage	Parameter	Value
Tape	Width of tape w	4.8 mm
	Thickness of tape d_t	0.07 mm
Strand	Number of tapes n_t	42
	Slot width	5.2 mm
	Slot height	5.0 mm
	Split line	$\parallel$ to c-axis
	Diameter D	10.0 mm
	Twist-pitch h	500 mm
	Annealing of profiles	No
Cable	Number of strands N	6
	Thickness of core g	10.0 mm
	Twist-pitch L	1000 mm
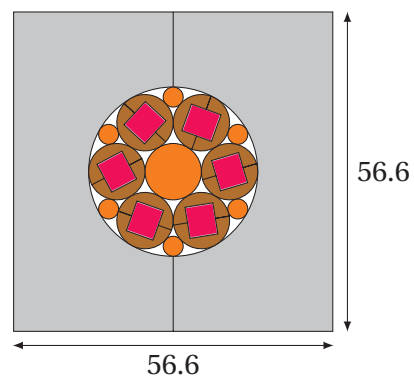
Figure 7.6: Design parameters and cross-section of the 'round' cable for CS coils.

0.85 m for the flat and 2.78 m for the round option, about 2.4 and 7.7 times larger than in the first prototypes. The values of the critical bending radius R_c are still required for both cable options to evaluate the corresponding R/R_c ratio, which is about 1.5 in the first samples.

When the cables are bent at 1.9 m, corresponding to the inner radius of the graded central solenoid, the bottom estimate for R is about 0.34 m for the flat and 0.43 m for the round cable (see section 4.2.1). Depending on R_c, a correction of these values might still be needed, which can be done by increasing the cable twist-pitch L. The average transverse pressure at the midplane of strands for the operation at 53 kA/18 T is estimated about 23 MPa and 48 MPa, which is acceptable due to the increased diameters of the strands.

The total cross-section of copper in the cables, S_{cu}, is about 470 mm^2. For the round cable this value is achieved by additional use of minor copper rods of about 3.6 mm of diameter, increasing S_{cu} by ≈ 60 mm^2. According to the mechanical analysis, similar to that in section 4.2.2, these copper rods also reduce the peak stress by ≈ 40 %, assuming that they are in a tight contact with the strands and the steel jacket. However, the contact may become loose due to finite manufacturing tolerances. Even in that case, reduction of the transverse loading on strands is still expected due to an efficient redistribution of the stresses.

The remaining main properties of the cross-section for the flat and round cables are as follows: the cable space – 750 mm^2 and 710 mm^2, the void fraction – 19 % and 14 %, the copper current density – about 110 A/mm^2 for both.

The cables are based on two widths of the tape, 3.3 mm and 4.8 mm, and 70 μm thickness. These values correspond to the selected manufacturer of tapes, the company SST. The following parameters are used for the $j_c(B, T)$ scaling law: $\alpha = 1.52$, $\beta = 2.33$, $p = 0.50$, $q = 1.70$, $B_0 = 120$ T, $T_c = 93$ K (see appendix A.1). The total width of the tape present in the cable cross-section is about 1109 mm for the flat cable and 1210 mm for the round. These values correspond to slightly higher j_c performance of the 3.3 mm tape than that of the 4.8 mm one, obtained in the measurements at 12 T/4.2 K. Thus, the prefactor A of the scaling law is set to 3969 kA/mm^2 and 3616 kA/mm^2, respectively.

The parameters of the $j_c(B, T)$ scaling law, defined above, allow us to assess the T_{cs} performance of the cables, similar to what was done for the first cable prototypes in section 4.5. In a sample composed of the flat and round cables to be tested in SULTAN, the distance between the respective centers is about 55 mm. The main parameters of the SULTAN test facility are given in appendix A.4.

The results of the T_{cs} calculation for the reference field 18 T and the peak field of SULTAN 10.9 T are presented in figure 7.7. For the 53 kA/18 T operating conditions, the temperature margin at 5 K is about 4 K. As the SULTAN sample can be measured
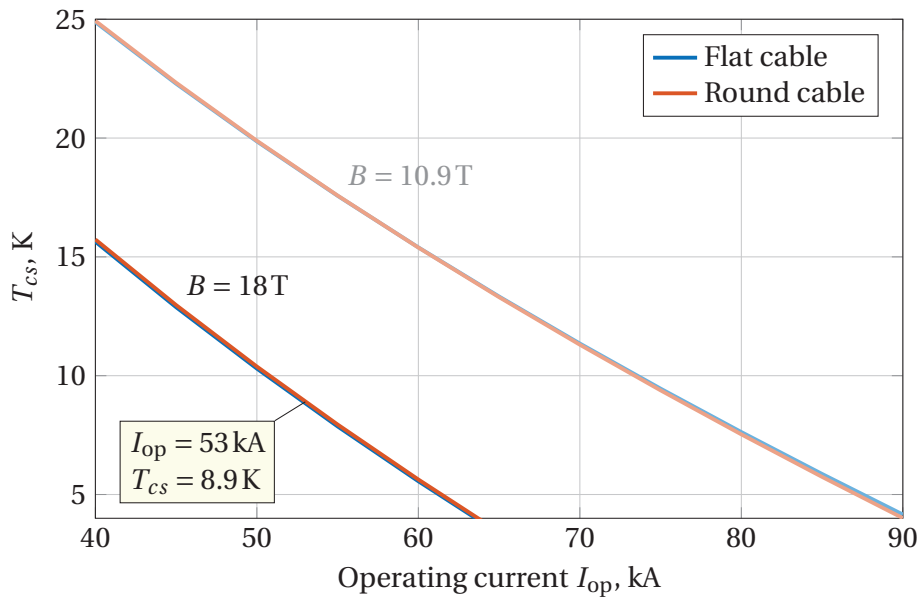
Figure 7.7: T_{cs} of the flat and round cable in a SULTAN sample as a function of operating current for the reference field in the CS1 module and the peak field of the SULTAN test facility.

only up to 10.9 T external field, an electromagnetic load, similar to that at 53 kA/18 T, should be developed at about 88 kA. This value is near the expected critical current of the cables at 5 K and 10.9 T.

The AC energy loss of the cables in the AC test of SULTAN, where a sinusoidal AC field is applied, can be assessed directly from the cable design parameters using equation (5.6) for the hysteresis loss and equations (5.10) to (5.12) for the coupling loss. As shown in figure 7.8, a significant reduction of the total loss is expected for the new cables compared with that of the first prototype. This is achieved only by adjusting the geometry parameters, while the values for the inter-strand resistances are not changed and taken as $R_a = 15\,\mu\Omega\cdot$m and $R_c = 1.5\,\mu\Omega\cdot$m. If a further loss reduction is necessary, R_a and R_c can be increased by plating of copper and/or using the mixed matrix composites.

Although an AC field parallel to the broad side of the cable is very rarely used in the SULTAN measurements, this orientation is mostly present in the CS1 module (see figure 7.4). As one can see from the right plot in figure 7.8, the computed values of the AC losses in the round cable are independent from the field orientation and are noticeably lower for the elongated cables in the case of parallel field. The AC losses are still slightly larger in the flat cable than in the round. This difference originates in the time constant of the inter-strand coupling loss, which is about twice larger in the flat cable ($\tau \approx 43\,$ms) than in the round ($\tau \approx 23\,$ms), while the shape factors are
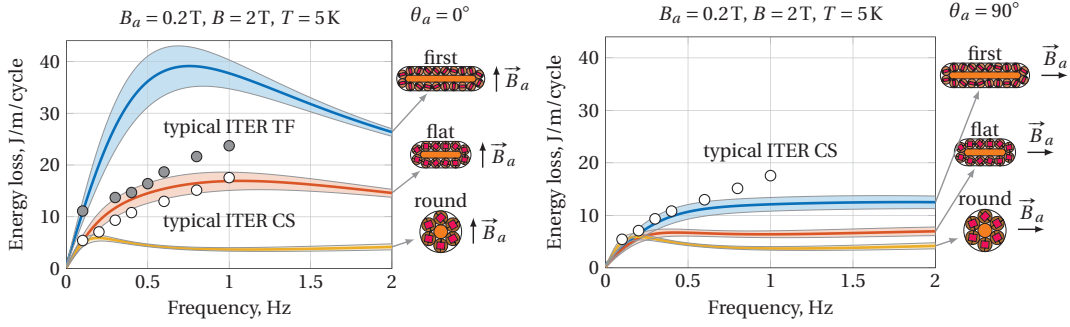
Figure 7.8: AC energy loss of the flat and round cable compared against the first cable prototype and typical data for the ITER TF and CS cables. The results are presented for a field perpendicular (left) and parallel to the broad side of the cables (right).

almost identical. At higher frequencies this situation is the opposite, the round cable becomes 'lossier' than the flat one. The provided results should only be considered as a first estimate of the AC energy loss, which mostly serves to identify the proper 'directions' in the minimization of the total loss.

Note that some of the loss curves have a double peak shape. This occurs when the intra- and inter-strand coupling losses are comparable in absolute values, but the frequencies of the peak loss are different. When only one peak is present, the dominant contribution is due to the inter-strand coupling currents.

For the CS1 module operating at a relatively low ramp-rate, such that the duration of the pulse is much longer than any of the time constants, the total power loss due to the coupling currents is estimated as $P = \dot{B}^2 Sn\tau/\mu_0$, where $Sn\tau \approx NS_{\mathrm{strand}}n_1\tau_1 + S_{\mathrm{cable}}n_2\tau_2$ is the sum of the intra- and inter-strand contributions. In a parallel field, $Sn\tau \approx 57\,\mathrm{mm}^2 \cdot \mathrm{s}$ for the flat cable and $\approx 98\,\mathrm{mm}^2 \cdot \mathrm{s}$ for the round.

Finally, we calculate the hot spot temperature during a quench using the numerical model presented in chapter 6 and considering an adiabatic situation for the cable and the steel jacket. The two cable options are similar in terms of amount of material in their cross-sections, containing $2500\,\mathrm{mm}^2$ of steel and about $600\,\mathrm{mm}^2$ of the cable domain. Copper occupies about 78 % in the cable, the remaining fractions are for YBCO (~0.2 %), Hastelloy (~10 %), SnPb solder (~11 %) and silver (~0.2 %).

The main input parameters of the model are set as follows: $T_0 = 5\,\mathrm{K}$, $B_0 = 18\,\mathrm{T}$ and $I_0 = 53\,\mathrm{kA}$ for the operating conditions; $Q = 2 \cdot \mathrm{MQE}$, $l_p = 0.1\,\mathrm{m}$ and $t_p = 0.1\,\mathrm{m}$ for the heat pulse; $V_{\mathrm{th}} = 100\,\mathrm{mV}$ and $t_{\mathrm{discharge}} = 1.1\,\mathrm{s}$ for the current dump. The time constant of the current dump, τ, is not specified for the DEMO CS coils and it was decided to perform a parametric study for this parameter in the range from 5 s to 25 s. This range is roughly based on the ITER experience, suggesting that the terminal voltage across the CS module during a magnet discharge, V_{max}, can be chosen in the range from $\approx 10\,\mathrm{kV}$ to $\approx 30\,\mathrm{kV}$ [118, 119]. Thus, τ is simply estimated as LI_0/V_{max}, where $L \approx 6\,\mathrm{H}$
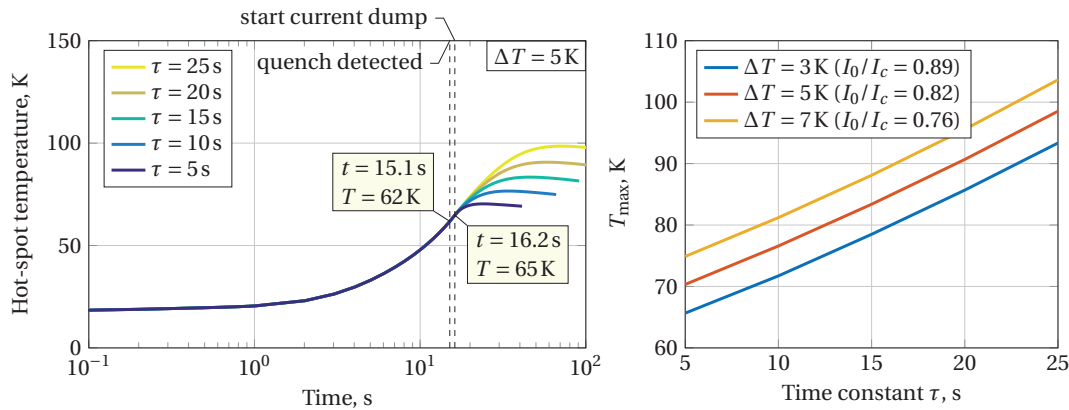
Figure 7.9: Left: hot-spot temperature as a function of time for the temperature margin $\Delta T = 5\,\mathrm{K}$. Right: peak temperature as a function of the time constant τ.

for the CS1 module.

The values of the minimum quench energy are somewhat similar to those presented in figure 6.3. It is about 170 J, 120 J and 40 J for $I_0/I_c = 0.75$, 0.8 and 0.9, respectively. As $I_0 = 53\,\mathrm{kA}$ is already specified in the present study, the I_0/I_c ratio was varied by changing the I_c of the cable.

The results of the calculation are shown in figure 7.9. A relatively slow build-up of the hot spot temperature is obtained, which is due to the large thermal capacity of the cable. The quench is detected 15 s after the heater is switched off. The hot spot temperature reaches about 62 K at that moment and increases to 65 K at the beginning of the current dump, which is then simulated during 5τ.

The maximum temperature $T_{\max}$ during the simulation is well below the allowable limit of 150 K, within the entire range studied for τ. $T_{\max}$ increases moderately for the increasing values of the temperature margin ΔT, which is due to a slower longitudinal propagation of the high temperature zone.

As a layer winding is envisaged for the graded CS modules, the regions with significantly larger ΔT are not expected for the HTS cables, because they are located only in a high field zone. Unlike the layer winding, it may become challenging to protect an entire coil made by pancake winding, as regions with high ΔT will inevitably be present in a low field zone of the winding pack.

7.3 Cost considerations

The ratio between the cost per unit length of superconductor and its critical current – the price-performance ratio – depends strongly on the operating conditions. Although

this parameter qualitatively describes the 'attractiveness' of the superconductor for a certain application, it is necessary to specify in addition the non-copper current density j_{non-cu} of the given conductor, which is defined for the cross-section without taking into account the stabilizing copper. For instance, a very cheap superconductor with a low j_{non-cu} value still cannot be used as it would require too much space to produce the required field.

Let us consider three main superconductors for a simple estimate: NbTi, Nb_3Sn and ReBCO. Their cost is roughly 1 \$/m, 5 \$/m and 30 \$/m, respectively. The critical current density of NbTi and Nb_3Sn is calculated as proposed in the reference document for DEMO magnets [94], and that of ReBCO is taken for the SST tape, discussed in the previous section. The LTS wires are considered of 1 mm diameter and the HTS tape – of 4.8 mm width and 70 μm thickness, corresponding to the SST tape used in the round cable (see previous section). In order to obtain j_{non-cu}, the cu:non-cu ratio is set as 1.6:1 for the NbTi wire, 1:1 for the Nb_3Sn wire, 20:50 for the ReBCO tape. The cross-section of the superconductor S_{sc} is about 0.30 mm^2, 0.26 mm^2 and 0.005 mm^2, respectively. Note that S_{sc} is equal to the non-cu cross-section for NbTi and lower for the other two options, due to a presence of such non-superconducting domains as diffusion barriers in the Nb_3Sn wires and Hastelloy, silver and buffer layers in the ReBCO tape.

The comparison of the price-performance ratio and j_{non-cu} for NbTi, Nb_3Sn and ReBCO is provided in figure 7.10 for the operating temperature $T_0 = 5$ K and magnetic field in the range from 1 T to 25 T. As superconductors should operate at certain temperature margin between the current-sharing and operating temperatures, $\Delta T = T_{cs} - T_0$, the results are presented as bands with the chosen values of ΔT indicated for the edge curves. Note an increasing impact of ΔT on the width of the band when the magnetic field approaches the irreversibility field, which is about 9 T for NbTi, 27 T for Nb_3Sn and above 100 T for ReBCO at 5 K.

At relatively low fields, $B \lesssim 5$ T, j_{non-cu} is similar for all three options and the price-performance ratio is the lowest for NbTi, making it the most appealing one for low field applications. The optimal field range for use of Nb_3Sn is from about 6 T up to 15 T, where the upper limit is mostly defined by the values of j_{non-cu}. Unlike large fusion magnets, Nb_3Sn still has a potential for application at slightly larger fields in small magnets, where the requirement on j_{non-cu} is less strict. The price-performance ratio of ReBCO for $B \gtrsim 16$ T is comparable to or lower than that of the LTS superconductors and high values of j_{non-cu} are still retained. Hence, application of ReBCO at such fields is fully justified.

$T_0 = 5\,\mathrm{K}$
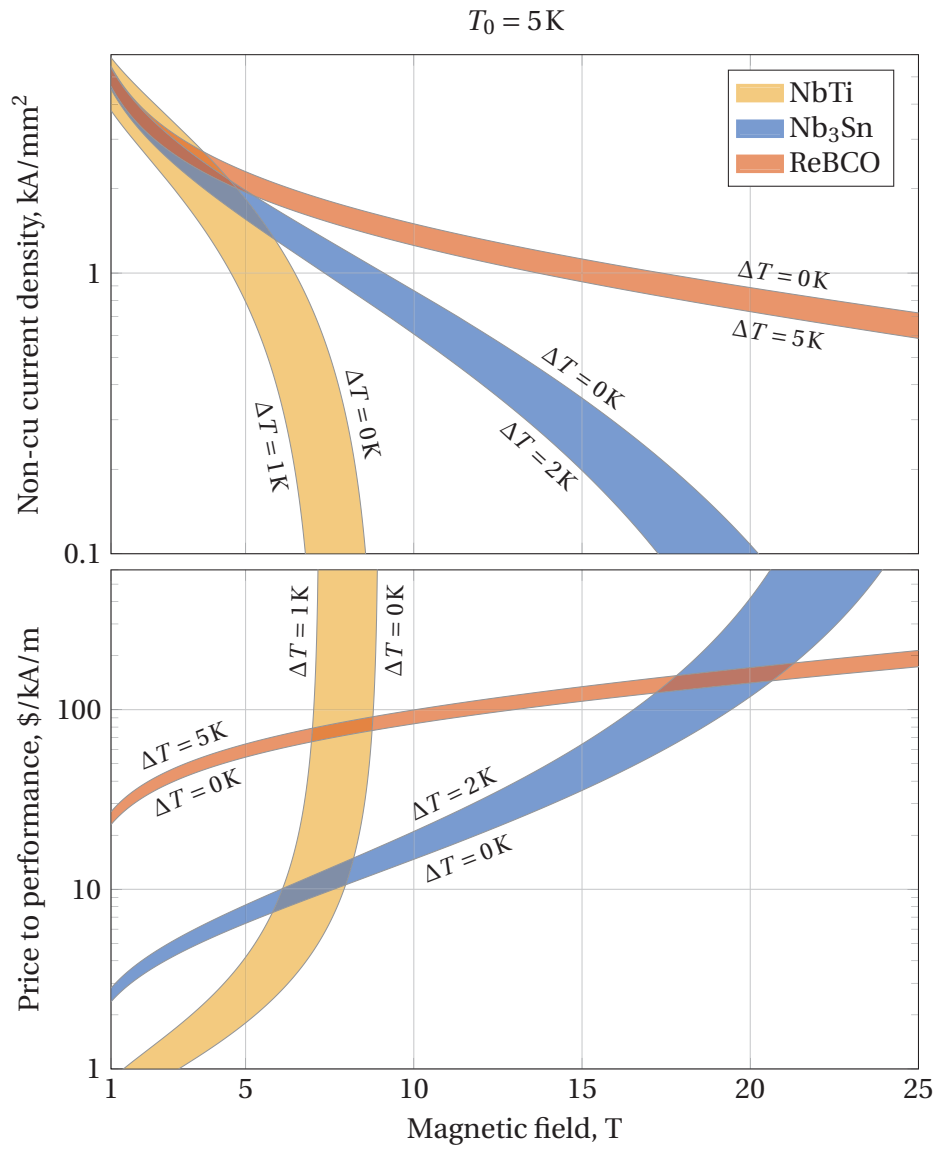
Figure 7.10: Non-cu current density (top) and price-performance ratio (bottom) for the three main superconductors at 5 K and in a wide range of magnetic fields.

7.4 Conclusion

In the preliminary design of the graded CS1 module for DEMO (EU reference design 2015) with the layer wound ReBCO cables at the inner radial section, Nb_3Sn at the central section and NbTi at the outermost one, it is possible to generate the same magnetic flux as in the reference design, while reducing the inner radius from 2.5 m to 1.9 m and the outer radius from 3.3 m to 2.9 m. An optimization of the other modules of the graded central solenoid should be still performed, as some of them are operated at relatively low fields, where the use of HTS cables is not necessary.

The two proposed designs of 53 kA/18 T HTS cable prototypes, based on the annealed and non-annealed copper profiles, fulfill the main mechanical, electrical and hot spot temperature requirements. Trying to avoid the cyclic load degradation in the new prototypes, the bending radius of strands at the cable edges is significantly increased if compared with the first cable prototypes. The reduction of the AC loss, by factor 2 to 4, is also expected and it can be further reduced by increasing the inter-strand resistance, which was not addressed in the present assessment.

Use of the HTS materials becomes compatible in terms of price with Nb_3Sn at 5 K and 16 T, where both have the price-performance ratio about 150 \$/kA/m. A high temperature margin, $\Delta T \sim 5\,K$, can be achieved in HTS at the low increase of the price-performance ratio even at higher magnetic fields.

If the HTS cables are used in the central solenoid of the same dimensions as in the baseline design, the generated magnetic flux can be increased by a factor of 1.5, corresponding to an increase of the peak field from about 12 T to 18 T. Both options for the central solenoid – either with the reduced dimensions and the same magnetic flux or with the same dimensions and the increased flux – provide significant changes to fusion machine, thus the design choice should be based on the assessment of its overall performance.

8 Conclusion

The main objective of this thesis – the development of the coated conductor cabling concept for fusion magnets – was split into the two main stages. Firstly, starting at the level of a thin single tape, we focus on the first cabling stage – the strand – which typically comprises ten to forty tapes. Then, we concentrate on the second cabling stage – a specified arrangement of strands within the cable space. This results in several hundreds of tapes included in the cable, which corresponds to the amount of HTS needed for cables in fusion magnets.

The electrical and electromechanical properties of the proposed design of the strand – a stack of tapes twisted and soldered together with two semicircular copper profiles – were investigated. Thanks to soldering, the inter-tape resistance between tapes is very low: about 20 nΩ·m at 77 K and 4 nΩ·m at 4.2 K for the adjacent tapes in the stack. As a result, the strands exhibit a pure power-law voltage-current transition when operated in DC, which implies that the current distribution between tapes is uniform. The DC measurements of the strand critical current performed at high field and low temperature confirmed that the strand design is feasible for applications to fusion magnets. The two main issues that arise from similar measurements of other cabling concepts – the mechanical reinforcement against Lorentz force and the thermal stabilization at overloading conditions – are successfully addressed in the proposed design. A critical current of 3 kA was achieved on the two 16-tape samples at 12 T/4.2 K, in-line with the expectations and without thermal or cyclic degradation of the performance. However, taking a broader view than the application to fusion, the stacking of tapes is not advisable for low field applications as the self-field effect provides a strong reduction of the overall critical current.

Between the two options to twist the strand – first twist then solder or first solder then twist – the latter one should be avoided due to the strain accumulation effect. When the twisting is applied before soldering, the minimum permissible value of the strand twist-pitch is mostly defined by the properties of a single tape and, typically, is of the order of 100 mm. As is inevitable when using soldering, the I_c value of the strand is very vulnerable to bending deformations. A critical value of the bending radius, defined at a certain value of the I_c degradation, can be reduced almost twice (lower is better), when the copper profiles are preliminary annealed. However, the preliminary annealing reduces also the critical values of the transverse loading (higher is better), especially when the strands are under a cyclic loading. We observe no cyclic

load degradation in the strands with non-annealed profiles. Thus, annealing of the copper profiles plays a crucial role on the strand electromechanical properties and its overall impact on the cable properties is still a matter of further investigations.

The cable arrangement is based on the Rutherford cable design – a fully transposed two-layered assembly of round strands – with additional central copper core. The main purpose of using the central core is to reduce the strand bending radius at the cable edge. The cable design was implemented in the manufacturing of two cable prototypes, rated for 60 kA at 12 T and made of 20 SuperPower and 20 SuperOx 16-tape strands (in total, 320 tapes were arranged in each prototype). During the manufacturing, the I_c value of the strands was measured at 77 K after soldering and after cabling. In both situations the results deviate from the expected values by $\lesssim 5\,\%$. No major issues were obtained working on the terminations and jacketing of the prototypes. Based on the manufacturing process of the 2.5 m-long prototypes, carried out at laboratory scale, no technological obstacles are expected for an industrialization of the process.

A typical test program for fusion cables, including T_{cs}, I_c, AC loss and cycling tests, has been carried out on the two prototypes in the EDIPO test facility. Their T_{cs} and I_c performances follow the predicted values within a few percent. We conclude that the feasibility of the proposed cable design for fusion is experimentally demonstrated. Unlike LTS cables, the temperature margin of several kelvins can be achieved at relatively high operating currents, $I/I_c \sim 0.85$.

The main issue arising from the measurements is the progressive degradation of the cable performance during the cycling test, where the operating current was varied from 0 kA to 50 kA at 12 T. At the end of the test, after about 2000 electromagnetic cycles, the I_c degradation reaches $\approx 10\,\%$ for SuperPower and $\approx 20\,\%$ for SuperOx. Comparing with the performance of single strands under a cyclic loading, annealing of the copper profiles might be at the origin of this fatigue phenomenon. A visual inspection and I_c measurements performed after the EDIPO test on the SuperOx prototype revealed also a high non-uniformity of the degradation. Although on average higher degradation is present at the cable edges, non-damaged regions are still present locally, at the tape level. Presumably, this arises from issues with the soldering process, resulting in voids in the strand volume, which become locations of higher stress intensity.

The AC loss properties of the cable design have been investigated both numerically and experimentally. Scaling laws have been identified for each type of loss contributions – namely, hysteresis loss in the stacks and coupling losses at the strand and cable levels – and validated against the corresponding experimental datasets. They are recommended as a first estimate of the energy loss in a time-varying magnetic field.

The issues related with a potential quench in the cable have been addressed via numerical modelling. The design of the first prototypes with 950 mm^2 of steel fulfils the

protection requirement of 150 K on the jacket over a broad range of operating currents at 12 T. It is recommended to perform the quench analysis during the design study of the next prototypes because this allows identifying the required amount of copper in the cable. The results obtained for the first prototypes suggest that the copper cross-section can be reduced by ~25 % still fulfilling the protection requirement.

Presently, using HTS cables in high fields is one of their most appealing applications as they allow operating above a limit of about 15 T, where Nb_3Sn cables are no longer efficient. An increase of the peak field on the central solenoid leads to the two attractive possibilities: either the same magnetic flux can be produced by the solenoid with smaller dimensions or higher magnetic flux is generated when the dimensions are kept unchanged. While the first option provides with a potential to reduce dimensions, and in turn cost, of an entire fusion device, the second option allows for a longer plasma burn. To minimize the cost impact due to the implementation of expensive HTS cables in the system, a grading of the superconductor – positioning of HTS, Nb_3Sn and NbTi cables in high, medium and low field regions, respectively – should be envisaged for the solenoid.

The design studies of the new cable prototypes for the application in the innermost layers of the graded solenoid, operating at 53 kA and 18 T, resulted in the two possible options, the 'round' and 'flat' cables. While both fulfil the main mechanical, electrical and protection requirements, the key distinction between them is whether the preliminary annealing of the copper profiles is used or not. When both prototypes will be tested in the SULTAN test facility, the results should provide us with a better understanding of the cyclic load degradation, which is the remaining issue of the proposed cable design. According to the present understanding of this issue, an increase of the strand bending radius by a factor of 2.4 for the round and 7.7 for the flat cables if compared with the first prototypes, was applied as the most effective measure to avoid the cyclic load degradation.

Using the HTS cables in fusion magnets is the only design option when it comes to high field applications. The two main issues of the HTS conductor technology – difficulties with the manufacturing long tapes (i.e. several hundreds of meters) with uniform I_c and a relatively high cost – are both addressed in the proposed cable design and its application in the graded CS module. Using soldering in the strand design practically eliminates an issue with the presence of defects along the tape length. Secondly, the HTS materials at high magnetic fields becomes comparable to, or even cheaper than Nb_3Sn wires in terms of the price-performance ratio, which fully justifies their application.

Finally, the salient findings obtained in this work are summarized in the table below.

Table 8.1: Outline of the salient findings of the thesis.

Topic	Finding	Key reference point
Strand, 1$^{\text{st}}$ cabling stage	Suitability for high field applications	figure 3.9
	I_c reduction due to the self-field	figure 3.8
	Low inter-tape resistance	figure 3.3
	Limits for twisting	figure 3.13
	Limits for bending	figure 3.17
	Limits for transverse loading	figure 3.23
	Fatigue phenomenon	figure 3.26
Cable, 2$^{\text{nd}}$ cabling stage	Geometry description	eq. (4.2), (4.3)
	Mechanical limits for manufacturing	eq. (4.9), (4.13)
	Feasibility of manufacturing	section 4.4
	Suitability for fusion magnets	figures 4.26 and 4.27
	Cyclic load degradation	sections 4.6.4 and 4.7
Numerical modelling	Scaling laws for AC losses	eq. (5.6), (5.11), (5.12)
	Potential reduction of S_{cu}	figure 6.8
	Size reduction of DEMO central solenoid	figure 7.2
	Cable design proposals for 53 kA at 18 T	figures 7.5 and 7.6
	Cost-effective use of HTS	figure 7.10

A Appendixes

A.1 Scaling law of the critical current density

The chosen scaling law of the critical current in a magnetic field perpendicular to the tape (i.e. along the c-axis of tape) requires a set of 7 parameters $(A, \alpha, \beta, p, q, B_0, T_c)$ to describe the field-temperature dependence. For given values of the magnetic field B and temperature T, the dimensionless parameters $t = T/T_c$ and $b = B/B_{\mathrm{irr}}(T)$ are used as follows:

$$j_c(B, T) = \frac{A}{B} b_{\mathrm{irr}}^\beta b^p (1-b)^q$$

$$b_{\mathrm{irr}}(t) = (1-t)^\alpha$$

(A.1)

where the irreversibility field is defined as $B_{\mathrm{irr}}(T) = B_0 (1-t)^\alpha$. In case if $t > 1$ or $b > 1$, $j_c = 0$ should be set explicitly.

Expression (A.1) allows to define the lift-factor as $\mathrm{lf}(B, T) = j_c(B, T)/j_c(\mathrm{sf}, 77\,\mathrm{K})$, where the self-field parameter sf is needed to specify the bottom limit for B: $B(B < \mathrm{sf}) = \mathrm{sf}$. Note that similarly to how the absolute values of j_c are scaled with A, the values of $\mathrm{lf}(B, T)$ can be adjusted by changing the parameter sf.

The scaling parameters for the SuperOx tape were obtained by fitting the data for the tape (field perpendicular to the wide face of the tape) provided by the manufacturer and measured at ENEA. The SuperPower parameters were obtained by fitting the data published in [120]. The lift-factors for SuperPower and SuperOx and the corresponding fits are reported in figure A.1, where sf = 10.1 mT and 7.9 mT are used, respectively.

The angular dependence of the critical current at 4.2 K and high magnetic field is reported in figure A.2. The data for SuperPower is from [83], the data for SuperOx have been measured at 5 T, 9 T and 12 T. Due to a similar shape of the curves for both SuperPower and SuperOx at different magnitudes of the field, an interpolation function based on these data is used to describe the angular dependence in the calculations.
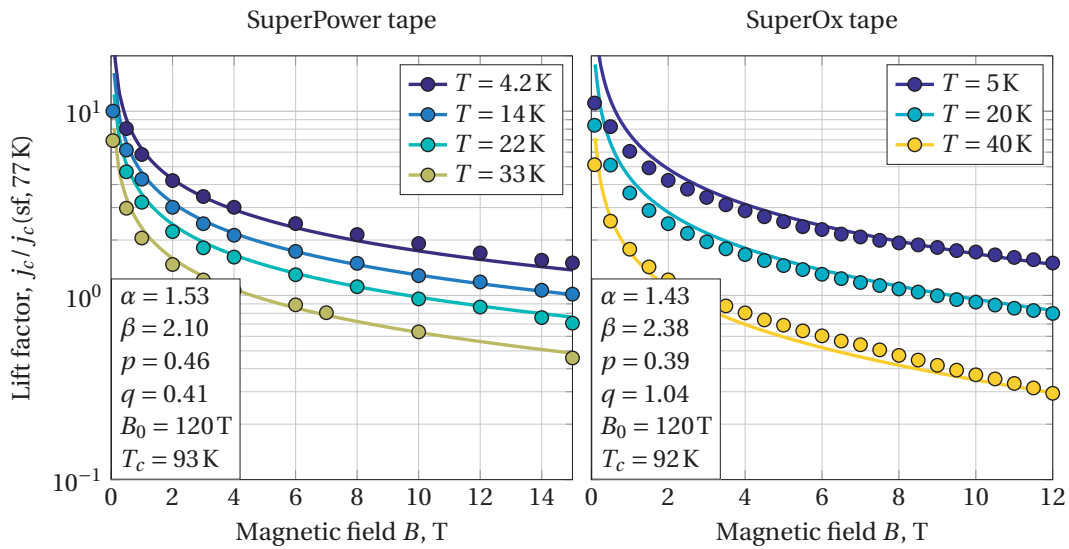
Figure A.1: Lift factor versus magnetic field at different temperatures. Left: SuperOx tape measured at ENEA, Italy. Right: SuperPower tape, data published in [120]. The fit lines and the values of the fit parameters are also reported.
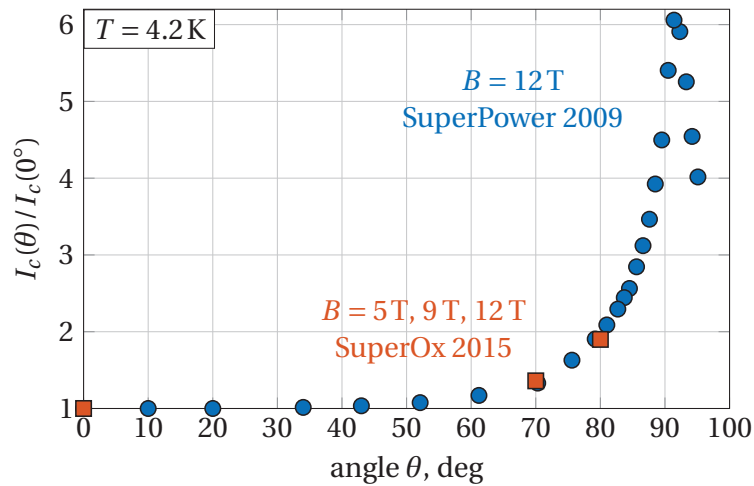
Figure A.2: Angular dependence of the critical current at 4.2 K: data for SuperOx have been measured at 5 T, 9 T and 12 T; data for SuperPower – at 12 T (from [83]).

A.2 Superconductors in electrical circuits

A set of N discrete superconducting elements that are electrically connected either in parallel or in series is considered. Each element has its own critical current I_{c_k} and a transition exponent n_k. I_c and n are corresponding effective values for the whole set. The total voltage V due to the total transport current I and voltage at each element V_k due to the current I_k is written as:

$$V = E_c l \left(\frac{I}{I_c} \right)^n$$
$$V_k = E_c l_k \left(\frac{I_k}{I_{c_k}} \right)^{n_k}$$

(A.2)

where $E_c = 1\,\mu\text{V/cm}$ is the voltage threshold, l and l_k are the total and each element lengths. When the connection between the elements is specified, the purpose of the calculation is to deduce I_c and n from the given values of I_{c_k} and n_k.

A.2.1 Parallel connection

When all the N elements are connected in parallel the following equations can be written:

$$\begin{cases} I = \sum_{k=1}^{N} I_k \\ V = V_k \end{cases}$$

(A.3)

Assuming also that $l = l_k$, these two equations and (A.2) lead to:

$$I = \sum_{k=1}^{N} I_{c_k} \left(\frac{I}{I_c} \right)^{\frac{n}{n_k}}$$

(A.4)

I_c and n can be deduced by setting $I = I_c$ in the equation (A.4) and in the derivative over I of that equation as follows:

$$I_c = \sum_{k=1}^{N} I_{c_k}$$
$$n = \frac{I_c}{\sum_{k=1}^{N} \dfrac{I_{c_k}}{n_k}}$$

(A.5)

A.2.2 Serial connection

When all the N elements are connected serially the following equations can be written:

$$
\begin{cases}
I = I_k \\
V = \sum_{k=1}^{N} V_k
\end{cases}
\tag{A.6}
$$

Combining them with expressions in (A.2) results in:

$$
l \left(\frac{I}{I_c} \right)^n = \sum_{k=1}^{N} l_k \left(\frac{I}{I_{c_k}} \right)^{n_k}
\tag{A.7}
$$

I_c and n can be deduced by setting $I = I_c$ in the equation (A.4) and in the derivative over I of that equation as follows:

$$
\begin{aligned}
1 &= \sum_{k=1}^{N} \frac{l_k}{l} \left(\frac{I_c}{I_{c_k}} \right)^{n_k} \\
n &= \sum_{k=1}^{N} n_k \frac{l_k}{l} \left(\frac{I_c}{I_{c_k}} \right)^{n_k}
\end{aligned}
\tag{A.8}
$$

Note that the first expression is the implicit function for I_c. If $n_k = 1$ for all the elements (i.e. linear transitions), the well-known result for the resistors in series will be obtained.

A.3 Magnetic field calculation

A.3.1 Long straight conductors

Contribution to the total vector potential and magnetic field from the long straight conductor with the infinitesimal cross-section $du \times dv$ and current density j at the point remote by (x, y) from the conductor can be expressed as:

$$
\begin{aligned}
\mathrm{d}A_z(x, y) &= -\frac{\mu_0 j}{4\pi} \ln\left(x^2 + y^2 \right) \mathrm{d}u\,\mathrm{d}v \\
\mathrm{d}\vec{B}(x, y) &= \frac{\mu_0 j}{2\pi} \frac{\{-y, x, 0\}}{x^2 + y^2} \mathrm{d}u\,\mathrm{d}v
\end{aligned}
\tag{A.9}
$$

Then, the total vector potential and magnetic field generated by a current element that has the rectangular bar geometry centred at the origin (infinitely long in z-direction, with s and d dimensions in xy-plane) and uniform distribution of the current I (i.e.

$j = I/(sd)$) can be expressed as:

$$A_z(x, y) = \int_{u=-s/2}^{s/2} \int_{v=-d/2}^{d/2} \mathrm{d}A_z(x-u, y-v) = -\frac{\mu_0 I}{4\pi sd} z(f)$$

$$\vec{B}(x, y) = \left\{ \frac{\partial A_z}{\partial y}, -\frac{\partial A_z}{\partial x}, 0 \right\} = \frac{\mu_0 I}{4\pi sd} \{-z(g_x), z(g_y), 0\}$$

(A.10)

where the functions f, g_x, g_y and functional operator z have the following definitions:

$$z(h) = h_{(1,1)} - h_{(-1,1)} - h_{(1,-1)} + h_{(-1,-1)}$$

$$h_{(p,q)} = h(x + p \cdot s/2, y + q \cdot d/2)$$

$$f(u, v) = -3uv + uv \ln(u^2 + v^2) + u^2 \arctan\frac{v}{u} + v^2 \arctan\frac{u}{v}$$

(A.11)

$$g_x(u, v) = u \ln(u^2 + v^2) + 2v \arctan\frac{u}{v}$$

$$g_y(u, v) = g_x(v, u)$$

Considering the two identical current elements centred at the positions (x_1, y_1) and (x_2, y_2), average vector potential and magnetic field generated by the first element with the current I over the cross-section of the second can be obtained by direct integration of (A.10):

$$\langle A_z \rangle (\Delta x, \Delta y) = -\frac{\mu_0 I}{4\pi s^2 d^2} Z(F)$$

$$\langle \vec{B} \rangle (\Delta x, \Delta y) = \frac{\mu_0 I}{4\pi s^2 d^2} \{-Z(G_x), Z(G_y), 0\}$$

(A.12)

where $\Delta x = x_2 - x_1$, $\Delta y = y_2 - y_1$. The functions F, G_x, G_y and functional operator Z have the following definitions:

$$Z(H) = 4H_{(0,0)} + H_{(1,1)} + H_{(-1,-1)} + H_{(-1,1)} + H_{(1,-1)} -$$

$$- 2(H_{(0,1)} + H_{(1,0)} + H_{(-1,0)} + H_{(0,-1)})$$

$$H_{(p,q)} = H(\Delta x + p \cdot s, \Delta y + q \cdot d)$$

$$F(u, v) = -\frac{25}{24} u^2 v^2 - \frac{1}{24}(u^4 + v^4 - 6u^2 v^2) \ln(u^2 + v^2) +$$

$$+ \frac{1}{3}\left(u^3 v \arctan\frac{v}{u} + uv^3 \arctan\frac{u}{v}\right)$$

(A.13)

$$G_x(u, v) = -\frac{1}{6}(v^3 - 3u^2 v) \ln(u^2 + v^2) + uv^2 \arctan\frac{u}{v} + \frac{1}{3} u^3 \arctan\frac{v}{u}$$

$$G_y(u, v) = G_x(v, u)$$

Hence, the matrix of the mutual inductances of the current elements per unit length is written as $C = \langle A_z \rangle / I$. The matrices for the magnetic field components are written
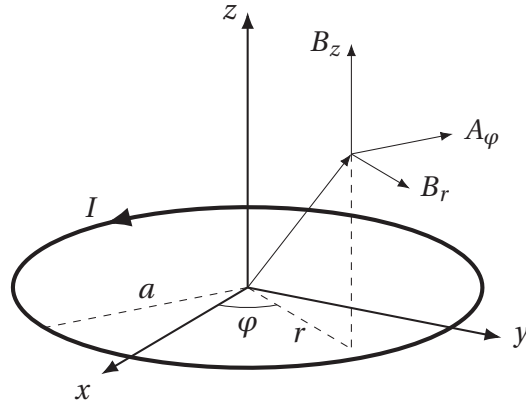
Figure A.3: Sketch of the magnetic field and vector potential generated by a ring-shaped conductor with the radius a and current I.

as $M_x = \langle B_x \rangle / I$, $M_y = \langle B_y \rangle / I$. When the two current elements have different cross-sections, a general form of the expression (A.12) must be used. This is given in [121].

A.3.2 Ring-shaped conductors

For the ring-shaped conductor of radius a centred at the origin and with the axis along the z direction (see illustration in figure A.3), the vector potential is axial symmetric and can be written in terms of the cylindrical coordinates (r, z) as:

$$
\begin{aligned}
A_\varphi(r, z) &= \frac{\mu_0 I}{\pi} \sqrt{\frac{a}{mr}} \left(\left(1 - m/2\right) K - E \right) \\
K &= \int_0^{\pi/2} \frac{\mathrm{d}\theta}{\sqrt{1 - m \sin^2 \theta}} \\
E &= \int_0^{\pi/2} \sqrt{1 - m \sin^2 \theta} \, \mathrm{d}\theta \\
m &= \frac{4ar}{(a + r)^2 + z^2}
\end{aligned}
\tag{A.14}
$$

where K and E are the complete elliptic integrals of the first and second kind, I is the current in the conductor. The cylindrical components of the magnetic field are

expressed as:

$$
\begin{aligned}
B_z(r,z) &= \frac{1}{r}\frac{\partial}{\partial r}\left(r A_\varphi\right) = \frac{\mu_0 I}{2\pi} \frac{1}{\sqrt{(a+r)^2 + z^2}}\left(K + \frac{a^2 - r^2 - z^2}{(a-r)^2 + z^2}E\right)\\
B_r(r,z) &= -\frac{\partial A_\varphi}{\partial z} = \frac{\mu_0 I}{2\pi} \frac{z}{r\sqrt{(a+r)^2 + z^2}}\left(-K + \frac{a^2 + r^2 + z^2}{(a-r)^2 + z^2}E\right)\\
B_\varphi(r,z) &= 0
\end{aligned}
\tag{A.15}
$$

Note that the field lines are given by: $r A_\varphi(r,z) = \text{const.}$

Finally, let us consider solenoids with a uniform current density in the round winding. Field in the center B_0 of the solenoid, which has the inner radius a_1, outer radius a_2 and height $2b$, can be obtained by integrating equation (A.15) as follows [122]:

$$
\begin{aligned}
B_0 &= \int_S \mathrm{d}B_z(0,z) = \frac{\mu_0 j}{2} \int_{a_1}^{a_2}\int_{-b}^{b} \frac{a^2}{\left(a^2 + z^2\right)^{3/2}}\,\mathrm{d}a\,\mathrm{d}z = \mu_0 j a_1 F\left(\frac{a_2}{a_1}, \frac{b}{a_1}\right),\\
&\text{where } F(\alpha,\beta) = \beta \ln\left(\frac{\alpha + \sqrt{\alpha^2 + \beta^2}}{1 + \sqrt{1 + \beta^2}}\right),
\end{aligned}
\tag{A.16}
$$

$j = I_\Sigma / S$ is an average current density in the winding and I_Σ the total current flowing in the solenoid cross-section $S = 2b(a_2 - a_1)$.

The distribution of the magnetic field along the central axis of the solenoid can be deduced from the symmetry considerations. The magnetic fields for the points located at the distance z top and bottom from the solenoid center are identical, $B(-z) = B(z)$. Therefore, B_0 of the solenoid with the height $2(z + b)$ can be written as B_0 of the solenoid with the height $2(z - b)$ plus twice $B(z)$, assuming that a_1, a_2 and j of these solenoids are the same. This allows to express $B(z)$ as follows:

$$
B(z) = \frac{\mu_0 j a_1}{2}\left(F\left(\frac{a_2}{a_1}, \frac{b+z}{a_1}\right) + F\left(\frac{a_2}{a_1}, \frac{b-z}{a_1}\right)\right)
\tag{A.17}
$$

Considering a set of N coaxial solenoids, the total magnetic field on axis can be calculated from the superposition principle as $\sum_{k=1}^{N} B_k(z - z_{0_k})$, where the contribution from each solenoid B_k is calculated using equation (A.17) for the corresponding parameters $(j_k, a_{1_k}, a_{2_k}, b_k)$ and z_{0_k} is the distance between the center of the k-th solenoid and the origin.

A.4 SULTAN and EDIPO test facilities

There are two major test facilities at the Swiss Plasma Center (SPC) for testing and evaluating forced-flow high current cables: SULTAN (German acronym for SUpraLeiter TestANlage) and EDIPO (acronym for European DIPOle). The main properties and photograph of the facilities are presented in table A.1. Typical studies in the facilities include experiments on critical current, AC losses and fatigue effects.

In SULTAN the magnetic field is generated by three concentric pairs of superconducting split coils (each pair is the split solenoid), in EDIPO – by the two tilted heads race-track coils [123]. The test facilities are suitable to conduct experiments on both LTS and HTS conductors. In case of HTS sample, the operating temperature can be extended up to 50 K using an HTS adapter that limits the heat flow to the transformer and the counter-flow heat exchanger to re-cool the helium flow return to the cryoplant [62].

A test sample has a hairpin-like geometry: it can be made either of one conductor bent 180 degrees at the center or of two conductors connected together at the bottom terminations. At the top end the sample has two terminations that are connected either directly to the superconducting NbTi transformer or through the HTS adapter, if operation above 10 K is of interest. The total length of the sample can be from 2.5 m to 3.5 m. To achieve operating currents up to 100 kA with the magnetic flux pump, the total resistance of the sample must be kept very low, $\lesssim 10\,\mathrm{n\Omega}$ [61].

The cryogenic system is operated with a forced flow of supercritical helium: the mass flow can be set in the range from 0 to 10 g/s, the maximum pressure is 10 bar. The mass flow of helium is regulated separately in each conductor section.

Measurements of AC loss are performed in a sinusoidal magnetic field using a gas flow calorimetric method: a power loss of the conductors is assessed from increase of the helium enthalpy.

Fatigue effects are studied by applying the operating current in a cyclic manner in a high magnetic field. This allows assessing the conductor performance as a function of number of the electromagnetic load cycles.

Measurements of the prototype conductor reported in this work have been carried out in EDIPO. However, the facility is no longer available from summer 2016.

Table A.1: The main properties of the EDIPO and SULTAN test facilities. EDIPO is situated on the left in the photograph, SULTAN – on the right.

Property	EDIPO	SULTAN
Maximum DC field	12.35 T	10.89 T
Homogeneous field length ($\pm 1\%$)	910 mm	425 mm
Minimum charging time	14 min	40 min
Sample size in test well	89 mm × 138 mm	92 mm × 142 mm
Current leads	HTS – 17.2 kA	3 pairs, copper
AC field length	1100 mm	390 mm
Max AC field amplitude / frequency	± 0.31 T / 0.8 Hz	± 0.42 T / 6 Hz
Transient field (single pulse)	n.a.	≤ 4 T / 140 ms
Maximum sample current	100 kA	100 kA
Available flux in transformer	2.97 V·s	1.65 V·s
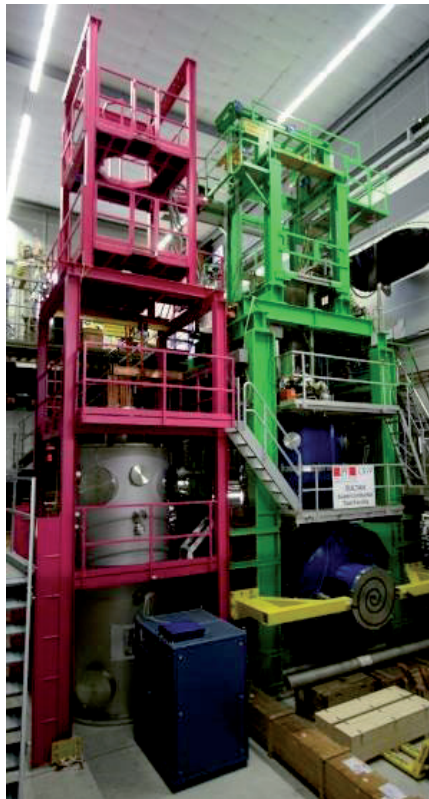
A.5 Partition of tapes for the cable prototypes

The tapes from SuperPower and SuperOx used for the fabrication of the two cable prototypes were delivered as spools, see photographs in the first row in figure A.4. Some of them were cut in shorter pieces in order to reduce non-homogeneity of the critical current along the length of the every entire piece. As a result, the list of the tape pieces, their lengths and the critical currents at 77 K/self-field and 4.2 K/12 T (perpendicular to tape) are listed in table A.2 for SuperPower and SuperOx.

To manufacture 20 SuperPower and 20 SuperOx strands, the tapes from each manufacturer were distributed according to the 'partition maps' shown in tables A.3 and A.4. The numbers in the tables correspond to the number of the spool from which the tape should be taken.

Photographs of the manufacturing and cabling of the strands are presented in the second and third rows in figure A.4.
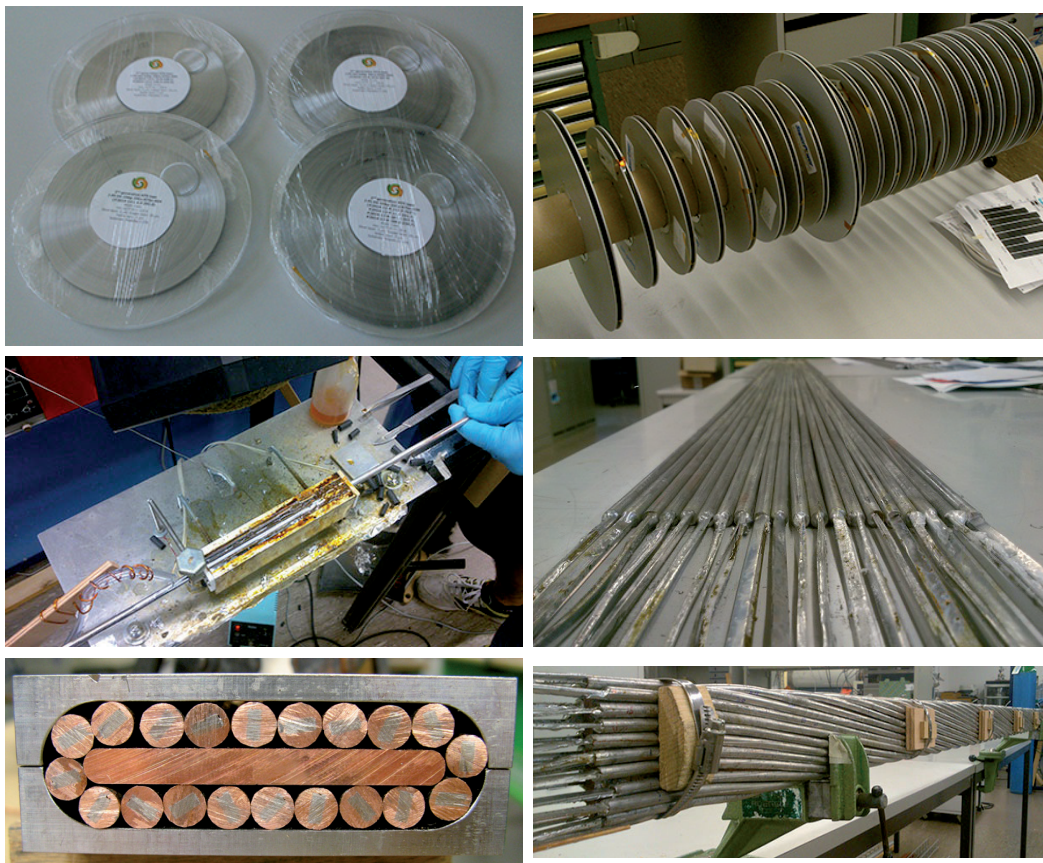
Figure A.4: Manufacturing steps of the cable prototypes: top row – spools with SuperOx (left) and SuperPower (right) tapes; central row – manufacturing of the strands; bottom row – cabling of the strands.

Table A.2: Properties of the SuperPower and SuperOx spools. Measurements at 4.2 K/12 T have been performed on short samples from all the SuperOx spools and from the SuperPower spools #1-16. Lift factors of the remaining spools are estimated to the most probable value of the measured ones.

	SuperPower spool		Lift factor	I_c, A	
#	Name	Length, m		s.f., 77 K	12 T, 4.2 K
1	M4-169-1 MS 959.9m	65.0	2.69	85	229
2	M4-158-3 BS	12.8	1.89	96	181
3	M4-169-1 MS 834.9m	60.0	2.32	75	174
4	M4-157-2 FS 1040-1075	13.0	1.78	97	173
5	M3-1030-1 FS 583-617	12.8	1.41	124	175
6	M3-1030-1 FS 681-716	12.6	1.41	125	176
7	M3-1036-2 BS 316-352	36.0	1.67	110	184
8	M3-1036-2 BS 710-745	35.0	1.67	100	167
9	M4-157-2 FS 1125-1160	35.0	1.78	98	174
10	M4-191-3 0912	20.0	1.64	85	139
11	M4-191-3 0912	30.0	1.64	75	123
12	M4-156-1 MS	35.0	1.87	98	183
13	M3-772-1 BS	40.0	1.17	103	121
14	M4-157-2 MS 937-958	20.0	1.86	122	227
15	M4-157-2 MS 920-937	17.0	1.86	116	216
16	M4-141-2 FS	17.6	1.43	77	110
17	M3-1111-2 0104	50.0	1.90	125	238
18	M4-150-1 FS	18.0	1.90	130	247
19	M3-1048-2 0508	39.0	1.90	124	236
20	M4-168-1 FS	13.6	1.90	123	234
21	M4-153-3 MS	35.0	1.90	120	228
22	M3-1089-2 0505	15.4	1.90	120	228
23	M4-150-1 FS	5.0	1.90	116	220
24	M4-171-2 BS	39.0	1.90	116	220
25	M4-149-3 MS 1713-1728	14.9	1.90	110	209
26	M4-150-1 FS	5.0	1.90	108	205
27	M4-211-5 0912	13.0	1.90	106	201
28	M3-1084-2 0104	12.8	1.90	105	200
29	M4-155-1 BS	36.0	1.90	103	196
30	M4-149-3 MS	5.0	1.90	102	194
31	M4-149-3 MS	8.0	1.90	91	173
32	M4-150-1 FS	5.0	1.90	89	169
33	M4-194-3 BS	16.8	1.90	115	219
34	thick spool #2	57.2	1.90	83	158

	SuperOx spool		Lift factor	I_c, A	
#	Name	Length, m		s.f., 77 K	12 T, 4.2 K
1	14-centre (25.6-148.1)	122.5	1.25	144	180
2	14-centre (149.4-235.5)	86.1	1.25	141	177
3	14-left (4.0-245.0)	241.0	1.23	151	185
4	13-right (11.4-181.1)	169.7	1.36	150	203
5	13-right (253.7-352.1)	98.4	1.37	148	203
6	13-right (181.1-207.4)	26.3	1.37	142	194
7	13-right (208.8-238.7)	29.9	1.38	151	209
8	14-right (18.5-257.4)	238.9	1.26	158	199

Table A.3: Partition map for the SuperPower tapes.

#	Length, m	Strand

#	Length, m	1	2	3	4	5	6	7	8	9	10	11	12	13	14	15	16	17	18	19	20
1	2.21	17	17	17	17	19	17	17	1	19	19	1	17	19	17	19	19	17	31	19	19
2	2.24	21	21	1	21	21	24	24	24	24	21	24	24	21	24	24	21	21	24	21	21
3	2.27	9	24	9	29	9	29	9	24	9	9	29	9	29	29	9	29	29	33	29	9
4	2.30	18	18	24	18	17	17	17	18	17	19	19	17	17	19	17	17	19	29	17	17
5	2.33	9	29	19	19	15	12	14	19	7	15	12	14	15	12	15	6	12	9	12	19
6	2.36	8	8	21	8	8	33	8	13	8	8	17	34	8	17	22	21	22	8	8	13
7	2.39	33	7	24	25	24	9	24	25	12	12	22	25	29	25	24	26	22	23	24	9
8	2.42	7	2	13	9	30	20	9	4	3	33	4	3	21	33	32	31	22	33	22	21
9	2.45	10	10	34	11	13	16	20	13	23	16	11	21	13	16	13	13	16	16	11	16
10	2.48	15	15	15	10	14	14	11	10	10	11	11	11	11	11	11	10	34	14	10	10
11	2.51	13	13	13	1	13	13	13	5	13	8	25	13	20	31	20	30	8	2	32	33
12	2.54	28	5	25	16	28	5	7	2	1	7	8	20	28	6	8	2	7	28	28	26
13	2.57	27	6	5	19	6	5	6	18	27	14	27	27	29	18	2	14	27	29	14	18
14	2.60	7	7	7	7	4	12	29	29	7	12	7	12	4	7	12	7	12	12	4	12
15	2.63	3	3	3	3	3	3	3	3	3	3	3	3	3	3	3	3	3	3	3	3
16	2.66	1	1	1	1	1	1	1	1	1	1	1	1	1	1	1	1	1	1	1	1

Table A.4: Partition map for the SuperOx tapes.

#	Length, m	1	2	3	4	5	6	7	8	9	10	11	12	13	14	15	16	17	18	19	20
1	2.21	4	4	4	4	4	4	4	4	4	4	4	4	4	4	4	4	4	4	4	4
2	2.24	1	1	1	1	1	1	1	1	1	1	1	1	1	1	1	1	1	1	1	1
3	2.27	2	2	2	2	2	2	2	2	2	2	2	2	2	2	2	2	2	2	2	2
4	2.30	8	8	8	8	3	3	3	8	8	8	8	8	8	8	8	8	3	8	8	8
5	2.33	4	4	5	5	4	4	4	5	4	4	5	5	4	4	5	5	4	5	5	5
6	2.36	8	5	5	5	8	8	8	5	5	8	5	5	5	8	5	8	8	8	8	8
7	2.39	1	2	1	1	1	1	1	1	2	1	1	1	2	1	1	2	1	1	2	2
8	2.42	4	4	4	4	4	4	4	4	4	4	4	4	4	4	4	4	4	4	4	4
9	2.45	3	8	8	8	8	8	8	8	8	8	8	8	8	8	8	3	8	8	8	8
10	2.48	2	2	1	1	2	2	2	1	2	2	1	1	2	2	1	1	2	1	1	1
11	2.51	8	8	8	8	8	8	8	8	8	3	8	8	8	3	8	8	8	8	8	8
12	2.54	7	6	6	6	7	7	7	6	6	7	6	6	6	7	6	7	7	6	7	7
13	2.57	3	3	1	1	3	3	3	1	3	3	1	1	3	3	1	3	3	3	3	3
14	2.60	4	4	4	4	4	4	4	4	4	4	4	4	4	4	4	4	4	4	4	4
15	2.63	8	8	8	8	8	8	8	8	8	8	8	8	8	8	8	8	8	8	3	3
16	2.66	5	5	5	5	5	5	5	5	5	5	5	5	5	5	5	5	5	5	5	5

Bibliography

[1] D. MacKay, *Sustainable energy - without the hot air* (UIT Cambridge, England, 2009).

[2] P. Taylor, *Energy technology perspectives 2010: scenarios & strategies to 2050* (International Energy Agency, Paris, 2010), 706 pp.

[3] J. P. Freidberg, *Plasma physics and fusion energy* (Cambridge University Press, Cambridge, 2007).

[4] T. J. Dolan, ed., *Magnetic fusion technology*, Vol. 19, Lecture Notes in Energy (Springer London, London, 2013).

[5] *ITER project – the way to new energy*, `http://www.iter.org`.

[6] D. Maisonnier, I. Cook, P. Sardain, R. Andreani, L. Di Pace, R. Forrest, et al., *A conceptual study of commercial fusion power plants*, (European Fusion Development Agreement, Apr. 2005).

[7] *ITER and fusion energy*, `http://iter.rma.ac.be/`.

[8] N. Mitchell and A. Devred, "The ITER magnet system: configuration and construction status", Fusion Engineering and Design, 9155 (2017).

[9] P. Bruzzone, "Superconductivity and fusion energy—the inseparable companions", Superconductor Science and Technology **28**, 024001 (2015).

[10] L. Muzzi, G. De Marzi, A. Di Zenobio, and A. della Corte, "Cable-in-conduit conductors: lessons from the recent past for future developments with low and high temperature superconductors", Superconductor Science and Technology **28**, 053001 (2015).

[11] B. Stepanov, P. Bruzzone, K. Sedlak, and R. Wesche, "Statistics of test results for the ITER Nb_3Sn and NbTi conductors in the SULTAN facility", IEEE Transactions on Applied Superconductivity, 1–1 (2016).

[12] M. Breschi, D. Macioce, and A. Devred, "Performance analysis of the toroidal field ITER production conductors", Superconductor Science and Technology **30**, 055007 (2017).

[13] C. Calzolaio, "Irreversible degradation in Nb_3Sn cable in conduit conductors", PhD thesis (2013).

[14] C. Sanabria, P. J. Lee, W. Starch, I. Pong, A. Vostner, M. C. Jewell, et al., "Evidence that filament fracture occurs in an ITER toroidal field conductor after cyclic lorentz force loading in SULTAN", Superconductor Science and Technology **25**, 075007 (2012).

[15] N. Martovetsky, T. Isono, D. Bessette, Y. Takahashi, Y. Nunoya, Y. Nabara, et al., "ITER central solenoid insert test results", IEEE Transactions on Applied Superconductivity, 1–1 (2016).

[16] P. Bruzzone, K. Sedlak, B. Stepanov, R. Wesche, L. Muzzi, M. Seri, et al., "Design, manufacture and test of a 82 kA react&wind TF conductor for DEMO", IEEE Transactions on Applied Superconductivity, 1–1 (2016).

[17] L. Muzzi, L. Affinito, S. Chiarelli, V. Corato, A. della Corte, A. D. Zenobio, et al., "Design, manufacture, and test of an 80 kA-class Nb_3Sn Cable-In-Conduit conductor with rectangular geometry and distributed pressure relief channels", IEEE Transactions on Applied Superconductivity **27**, 1–6 (2017).

[18] *European consortium for the development of fusion energy*, https://www.euro-fusion.org/.

[19] J. G. Bednorz and K. A. Müller, "Possible high T_c superconductivity in the Ba-La-Cu-O system", Zeitschrift für Physik B Condensed Matter **64**, 189–193 (1986).

[20] D. Larbalestier, A. Gurevich, D. M. Feldmann, and A. Polyanskii, "High-T_c superconducting materials for electric power applications", Nature **414**, 368–377 (2001).

[21] D. C. Larbalestier, J. Jiang, U. P. Trociewitz, F. Kametani, C. Scheuerlein, M. Dalban-Canassy, et al., "Isotropic round-wire multifilament cuprate superconductor for generation of magnetic fields above 30 T", Nature Materials **13**, 375–381 (2014).

[22] Y. Kamihara, T. Watanabe, M. Hirano, and H. Hosono, "Iron-Based layered superconductor $La[O_{1-x}F_x]FeAs$ (x=0.05-0.12) with T_c=26 K", Journal of the American Chemical Society **130**, 3296–3297 (2008).

[23] Y. Iwasa, *Case studies in superconducting magnets* (Springer US, Boston, MA, 2009), 682 pp.

[24] C. Barth, G. Mondonico, and C. Senatore, "Electro-mechanical properties of REBCO coated conductors from various industrial manufacturers at 77 K, self-field and 4.2 K, 19 T", Superconductor Science and Technology **28**, 045011 (2015).

[25] H. Maeda and Y. Yanagisawa, "Recent developments in High-Temperature superconducting magnet technology", IEEE Transactions on Applied Superconductivity **24**, 1–12 (2014).

[26] M. Takayasu, L. Chiesa, L. Bromberg, and J. V. Minervini, "HTS twisted stacked-tape cable conductor", Superconductor Science and Technology **25**, 014011 (2012).

[27] D. C. van der Laan, X. F. Lu, and L. F. Goodrich, "Compact $GdBa_2Cu_3O_{7-\delta}$ coated conductor cables for electric power transmission and magnet applications", Superconductor Science and Technology **24**, 042001 (2011).

[28] D. C. van der Laan, D. Abraimov, A. A. Polyanskii, D. C. Larbalestier, J. F. Douglas, R. Semerad, et al., "Anisotropic in-plane reversible strain effect in YGdBa-CuO coated conductors", Superconductor Science and Technology **24**, 115010 (2011).

[29] W. Goldacker, A. Frank, R. Heller, S. I. Schlachter, B. Ringsdorf, K.-P. Weiss, et al., "ROEBEL assembled coated conductors (RACC): preparation, properties and progress", IEEE Transactions on Applied Superconductivity **17**, 3398–3401 (2007).

[30] J. v. Nugteren, "High temperature superconductor accelerator magnets", PhD thesis (University of Twente, 2016).

[31] C. Barth, "High temperature superconductor cable concepts for fusion magnets", PhD thesis (Karlsruhe Institute of Technology, 2013).

[32] C. Barth, M. Takayasu, N. Bagrets, C. M. Bayer, K.-P. Weiss, and C. Lange, "Temperature-and field dependent characterization of a twisted stacked-tape cable", Superconductor Science and Technology **28**, 045015 (2015).

[33] C. Barth, D. C. v. d. Laan, N. Bagrets, C. M. Bayer, K.-P. Weiss, and C. Lange, "Temperature- and field-dependent characterization of a conductor on round core cable", Superconductor Science and Technology **28**, 065007 (2015).

[34] C. M. Bayer, P. V. Gade, C. Barth, A. Preuß, A. Jung, and K. P. Weiß, "Mechanical reinforcement for RACC cables in high magnetic background fields", Superconductor Science and Technology **29**, 025007 (2016).

[35] C. M. Bayer, "Characterization of high temperature superconductor cables for magnet toroidal field coils of the DEMO fusion power plant", PhD thesis (Karlsruhe Institute of Technology, 2017).

[36] D. Uglietti, R. Wesche, and P. Bruzzone, "Fabrication trials of round strands composed of coated conductor tapes", IEEE Transactions on Applied Superconductivity **23**, 4802104 (2013).

[37] N. J. Long, "Model for the angular dependence of critical currents in technical superconductors", Superconductor Science and Technology **21**, 025007 (2008).

[38] D. K. Hilton, A. V. Gavrilin, and U. P. Trociewitz, "Practical fit functions for transport critical current versus field magnitude and angle data from (RE)BCO coated conductors at fixed low temperatures and in high magnetic fields", Superconductor Science and Technology **28**, 074002 (2015).

[39] P. M. Leys, M. Klaeser, F. Schleissinger, and T. Schneider, "Analysis of the anisotropic critical current behaviour of HTS coated conductors", Journal of Physics: Conference Series **507**, 022013 (2014).

[40] N. A. Mineev and I. A. Rudnev, "Angular distributions of the critical current of ReBCO coated conductors in magnetic field up to 5 T", Progress in Superconductivity and Cryogenics **17**, 6–9 (2015).

[41] X. Zhang, Z. Zhong, H. S. Ruiz, J. Geng, and T. A. Coombs, "General approach for the determination of the magneto-angular dependence of the critical current of YBCO coated conductors", Superconductor Science and Technology **30**, 025010 (2017).

[42] L. Rostila, L. Söderlund, R. Mikkonen, and J. Lehtonen, "Modelling method for critical current of YBCO tapes in cable use", Physica C: Superconductivity **467**, 91–95 (2007).

[43] V. M. R. Zermeño, K. Habelok, M. Stępień, and F. Grilli, "A parameter-free method to extract the superconductor's $J_c(B,\theta)$ field-dependence from in-field current–voltage characteristics of high temperature superconductor tapes", Superconductor Science and Technology **30**, 034001 (2017).

[44] N. V. Bykovsky, S. S. Fetisov, A. A. Nosov, V. V. Zubko, and V. S. Vysotsky, "Analysis of critical current reduction in self-field in stacked twisted 2G HTS tapes", Journal of Physics: Conference Series **507**, 022001 (2014).

[45] C. Bayer, C. Barth, P. V. Gade, K.-P. Weiss, and R. Heller, "FBI measurement facility for high temperature superconducting cable designs", IEEE Transactions on Applied Superconductivity **24**, 1–4 (2014).

[46] K. Ilin, K. A. Yagotintsev, C. Zhou, P. Gao, J. Kosse, S. J. Otten, et al., "Experiments and FE modeling of stress-strain state in ReBCO tape under tensile, torsional and transverse load", Superconductor Science and Technology **28**, 055006 (2015).

[47] C. Basaran and J. Jiang, "Measuring intrinsic elastic modulus of Pb/Sn solder alloys", Mechanics of Materials **34**, 349–362 (2002).

[48] R. P. Reed and A. F. Clark, eds., *Materials at low temperatures* (American Society for Metals, Metals Park, Ohio, 1983), 590 pp.

[49] K.-P. Weiss, W. Goldacker, and M. Nannini, "Finite element analysis of torsion experiments on HTSC tapes", IEEE Transactions on Applied Superconductivity **21**, 3102–3106 (2011).

[50] C. Barth, K.-P. Weiss, and W. Goldacker, "Influence of shear stress on current carrying capabilities of high temperature superconductor tapes", IEEE Transactions on Applied Superconductivity **21**, 3098–3101 (2011).

[51] M. Takayasu, L. Chiesa, L. Bromberg, and J. Minervini, "Electrical and mechanical characteristics of HTS twisted Stacked-Tape cable conductor", IEEE Transactions on Applied Superconductivity, 1–1 (2017).

[52] S. Timoshenko and J. N. Goodier, *Theory of elasticity* (McGraw-Hill, New York, 1970).

[53] R. P. Reed and R. P. Mikesell, *Low temperature mechanical properties of copper and selected copper alloys* (National Bureau of Standards, 1967).

[54] *Mechanical properties of copper and copper alloys at low temperatures*, `https://www.copper.org/resources/properties/144_8/`.

[55] R. d. Borst and M. A. Crisfield, eds., *Nonlinear finite element analysis of solids and structures*, 2nd ed (Wiley, Hoboken, NJ, 2012), 516 pp.

[56] N.-H. Kim, *Introduction to nonlinear finite element analysis* (Springer US, Boston, MA, 2015).

[57] C. Calzolaio, G. Mondonico, A. Ballarino, B. Bordini, L. Bottura, L. Oberli, et al., "Electro-mechanical properties of PIT Nb_3Sn wires under transverse stress: experimental results and FEM analysis", Superconductor Science and Technology **28**, 055014 (2015).

[58] G. A. Costello, *Theory of wire rope*, red. by F. F. Ling, E. F. Gloyna, and W. Howard, Mechanical Engineering Series (Springer New York, New York, NY, 1997).

[59] C. T. Crowe, D. F. Elger, B. C. Williams, and J. A. Roberson, *Engineering fluid mechanics*, 9th ed (Wiley, Hoboken, N.J, 2008), 553 pp.

[60] E. Abbena, S. Salamon, and A. Gray, *Modern differential geometry of curves and surfaces with Mathematica* (CRC press, 2006).

[61] G. Pasztor, B. Blau, A. Fuchs, B. Jakob, and C. Marinucci, "Design, fabrication and testing of a 100 kA superconducting transformer for the SULTAN test facility", in Proceedings 15th international conference on magnet technology, Vol. 2 (1998), pp. 839–842.

[62] R. Wesche, P. Bruzzone, D. Uglietti, N. Bykovsky, and M. Lewandowska, "Upgrade of SULTAN/EDIPO for HTS cable test", Physics Procedia **67**, 762–767 (2015).

[63] S. W. Van Sciver, *Helium cryogenics* (Springer New York, New York, NY, 2012).

[64] J. W. Ekin, *Experimental techniques for low-temperature measurements: cryostat design, material properties, and superconductor critical-current testing* (Oxford University Press, Oxford; New York, 2006).

[65] N. Bykovsky, D. Uglietti, R. Wesche, and P. Bruzzone, "Strain management in HTS high current cables", IEEE Transactions on Applied Superconductivity **25**, 4800304 (2015).

[66] C. P. Bean, "Magnetization of high-field superconductors", Reviews of Modern Physics **36**, 31–38 (1964).

[67] M. R. Halse, "AC face field losses in a type II superconductor", J. Phys. D: Appl. Phys **3**, 717 (1970).

[68] E. Pardo, J. Souc, and L. Frolek, "Electromagnetic modelling of superconductors with a smooth current-voltage relation: variational principle and coils from a few turns to large magnets", Superconductor Science and Technology **28**, 044003 (2015).

[69] F. Grilli, E. Pardo, A. Stenvall, D. N. Nguyen, Weijia Yuan, and F. Gomory, "Computation of losses in HTS under the action of varying magnetic fields and currents", IEEE Transactions on Applied Superconductivity **24**, 78–110 (2014).

[70] E. Brandt and M. Indenbom, "Type-II-superconductor strip with current in a perpendicular magnetic field", Physical Review B **48**, 12893–12906 (1993).

[71] E. H. Brandt, "Superconductors of finite thickness in a perpendicular magnetic field: strips and slabs", Physical Review B **54**, 4246 (1996).

[72] Y. Mawatari, "Critical state of periodically arranged superconducting-strip lines in perpendicular fields", Physical Review B **54**, 13215–13221 (1996).

[73] F. Grilli, S. Ashworth, and S. Stavrev, "Magnetization AC losses of stacks of YBCO coated conductors", Physica C: Superconductivity **434**, 185–190 (2006).

[74] F. Grilli, R. Brambilla, and L. Martini, "Modeling High-Temperature superconducting tapes by means of edge finite elements", IEEE Transactions on Applied Superconductivity **17**, 3155–3158 (2007).

[75] W. T. Norris, "Calculation of hysteresis losses in hard superconductors carrying ac: isolated conductors and edges of thin sheets", Journal of Physics D: Applied Physics **3**, 489 (1970).

[76] K.-H. Müller, "Self-field hysteresis loss in periodically arranged superconducting strips", Physica C: Superconductivity **289**, 123–130 (1997).

[77] G. P. Mikitik, Y. Mawatari, A. T. S. Wan, and F. Sirois, "Analytical methods and formulas for modeling high temperature superconductors", IEEE Transactions on Applied Superconductivity **23**, 8001920–8001920 (2013).

[78] E. M. Gyorgy, R. B. van Dover, K. A. Jackson, L. F. Schneemeyer, and J. V. Waszczak, "Anisotropic critical currents in Ba2YCu3O7 analyzed using an extended bean model", Applied Physics Letters **55**, 283 (1989).

[79] N. Mineev and I. Rudnev, "Measurements and numerical simulations of trapped field in a stack of HTS tapes", IEEE Transactions on Applied Superconductivity **26**, 1–4 (2016).

[80] Y. Fukuda, K. Toyota, K. Kajikawa, M. Iwakuma, and K. Funaki, "Field angle dependence of AC losses in stacked Bi-2223/Ag sheathed tapes", IEEE Transactions on Applied Superconductivity **13**, 3610–3613 (2003).

[81] Z. Jiang, N. Amemiya, K. Kakimoto, Y. Iijima, T. Saitoh, K. Suzuki, et al., "Total AC loss characteristics in a stacked YBCO conductor", IEEE Transactions on Applied Superconductivity **17**, 2442–2445 (2007).

[82] M. Polak, J. Kvitkovic, P. Mozola, E. Usak, P. N. Barnes, and G. A. Levin, "Frequency dependence of hysteresis loss in YBCO tapes", Superconductor Science and Technology **20**, S293–S298 (2007).

[83] D. Uglietti, H. Kitaguchi, Seyong Choi, and T. Kiyoshi, "Angular dependence of critical current in coated conductors at 4.2 K and magnet design", IEEE Transactions on Applied Superconductivity **19**, 2909–2912 (2009).

[84] F. Grilli, V. M. Zermeno, and M. Takayasu, "Numerical modeling of twisted stacked tape cables for magnet applications", Physica C: Superconductivity and its Applications **518**, 122–125 (2015).

[85] V. E. Sytnikov, G. G. Svalov, S. G. Akopov, and I. B. Peshkov, "Coupling losses in superconducting transposed conductors located in changing magnetic fields", Cryogenics **29**, 926–930 (1989).

[86] A. P. Verweij, "Electrodynamics of superconducting cables in accelerator magnets", PhD thesis (University of Twente, 1995).

[87] A. Akhmetov, "Network models of superconducting cables and the results of the matrix approach to their description", Physica C: Superconductivity **310**, 309–315 (1998).

[88] S. Russenschuck, *Field computation for accelerator magnets: analytical and numerical methods for electromagnetic design and optimization* (Wiley-VCH-Verl, Weinheim, 2010), 757 pp.

[89] A. E. Ruehli, "Inductance calculations in a complex integrated circuit environment", IBM journal of research and development **16**, 470–481 (1972).

[90] F. W. Grover, *Inductance calculations: working formulas and tables* (Instrument Society of America, Research Triangle Park, N.C., 1981).

[91] A. Campbell, "A general treatment of losses in multifilamentary superconductors", Cryogenics **22**, 3–16 (1982).

[92] G. Ries, "AC-losses in multifilamentary superconductors at technical frequencies", IEEE Transactions on Magnetics **13**, 524–526 (1977).

[93]   L. Dresner, *Stability of superconductors* (Plenum Press, New York, 1995).

[94]   V. Corato, R. Bonifetto, P. Bruzzone, D. Ciazynski, M. Coleman, E. Galo, et al., *Common operating values for DEMO magnets design for 2016*, EUROFUSION WPMAG-REP(16) 16565 (June 21, 2016).

[95]   L. Bottura, *Solid materials database of CryoSoft*, `https://supermagnet.sourceforge.io/solids.html`.

[96]   A. D. Berger, *Stability of superconducting cables with twisted stacked YBCO coated conductors*, PSFC/RR-11-15 (2012).

[97]   L. Bottura, *Cryosoft*, `http://cryosoftsupport.wixsite.com/cryosoft`.

[98]   L. Bottura, "A numerical model for the simulation of quench in the ITER magnets", Journal of Computational Physics **125**, 26–41 (1996).

[99]   V. D. Arp, R. D. McCarthy, and D. G. Friend, *Thermophysical properties of helium-4 from 0.8 to 1500 K with pressures to 2000 MPa*, NIST Technical Note 1334 (revised) (1998).

[100] V. Arp, J. M. Persichetti, and C. Guo-bang, "The gruneisen parameter in fluids", Journal of fluids engineering **106**, 193–200 (1984).

[101] F. P. Incropera, ed., *Fundamentals of heat and mass transfer*, 6th ed (John Wiley, Hoboken, NJ, 2007), 997 pp.

[102] K. Takahata, H. Tamura, and T. Mito, "Thermal contact conductance between the bundle and the conduit in Cable-in-Conduit conductors", IEEE Transactions on Appiled Superconductivity **14**, 1477–1480 (2004).

[103] Y. Wachi, M. Ono, and T. Hamajima, "Heat transfer characteristics of the supercritical helium in a cable-in-conduit conductor", IEEE Transactions on Applied Superconductivity **5**, 568–571 (1995).

[104] F. W. Dittus and L. M. K. Boelter, "Heat transfer in automobile radiators of the tubular type", International Communications in Heat and Mass Transfer **12**, 3–22 (1985).

[105] R. H. Winterton, "Where did the dittus and boelter equation come from?", International journal of heat and mass transfer **41**, 809–810 (1998).

[106] P. J. Giarratano, V. D. Arp, and R. V. Smith, "Forced convection heat transfer to supercritical helium", Cryogenics **11**, 385–393 (1971).

[107] K. Sedlak, P. Bruzzone, X. Sarasola, B. Stepanov, and R. Wesche, "Design and R&D for the DEMO toroidal field coils based on Nb_3Sn react and wind method", IEEE Transactions on Applied Superconductivity, 1–1 (2016).

[108] K. Sedlak, P. Bruzzone, and M. Lewandowska, "Thermal-hydraulic and quench analysis of the DEMO toroidal field winding pack WP1", Fusion Engineering and Design, 9245 (2017).

[109] B. J. Maddock and G. B. James, "Protection and stabilisation of large superconducting coils", in Proceedings of the institution of electrical engineers, Vol. 115 (1968), pp. 543–547.

[110] M. N. Wilson, *Superconducting magnets* (Clarendon Press ; Oxford University Press, 1983).

[111] A. V. Zlobin, "Superconducting magnets - principles, operation, and applications", in J. G. Webster, *Wiley encyclopedia of electrical and electronics engineering* (John Wiley & Sons, Inc., Hoboken, NJ, USA, Dec. 15, 2014), pp. 1–19.

[112] R. Wenninger and G. Federici, *EU DEMO1 2015 – reference design*, EFDA-D-2MDKFH (Apr. 23, 2015).

[113] B. Meszaros and H. Hurzlmeier, *EU DEMO1 2015 – DEMO TOKAMAK COMPLEX*, EFDA-D-2D3FBF (May 8, 2015).

[114] R. Ambrosino and A. Albanese, *Reference flat-top equilibria for DEMO with aspect ratio 3.1*, EFDA-D-2AQ5GP (May 18, 2015).

[115] R. Wesche and X. Sarasola, *CS winding pack design and analysis*, EFDA-D-2MRPVA (Jan. 16, 2017).

[116] R. Wesche, N. Bykovsky, X. Sarasola, K. Sedlak, B. Stepanov, D. Uglietti, et al., "Central solenoid winding pack design for DEMO", Fusion Engineering and Design **121**, 9404 (2017).

[117] F. Nunio, A. Panin, and M. E. Biancolini, *Reference basis for mechanical & thermal analysis of TFC*, EFDA-D-2MC8T4 (Oct. 3, 2015).

[118] M. Coatanea-gouachet, "Quench detection and behaviour in case of quench in the ITER magnet systems", PhD thesis (Aix-Marseille University, 2012).

[119] N. N. Martovetsky and A. L. Radovinsky, "ITER CS quench detection system and its qualification by numerical modeling", IEEE Transactions on Applied Superconductivity **24**, 1–4 (2014).

[120] D. Turrioni, E. Barzi, M. Lamm, R. Yamada, A. Zlobin, and A. Kikuchi, "Study of HTS wires at high magnetic fields", IEEE Transactions on Applied Superconductivity **19**, 3057–3060 (2009).

[121] E. Pardo, A. Sanchez, D.-X. Chen, and C. Navau, "Theoretical analysis of the transport critical-state ac loss in arrays of superconducting rectangular strips", Physical Review B **71**, 134517 (2005).

[122] D. B. Montgomery, *Solenoid magnet design* (Wiley-Interscience, New York, 1969), 312 pp.

[123] P. Bruzzone, B. Stepanov, D. Uglietti, R. Wesche, and K. Sedlak, "EDIPO: the test facility for High-Current High-Field HTS superconductors", IEEE Transactions on Applied Superconductivity **26**, 9500106 (2016).

List of Figures

List of Tables

Acknowledgements

Nikolay Bykovsky

⌂ *Sommerhaldenstrasse 49*
5200 Brugg
Switzerland

☏ *+41 78 771 96 55*

✉ nikolay.bykovsky@psi.ch

Curriculum vitae

Education & Work Experience

2013 – P. T.	**PhD in Physics** "HTS high current cable for fusion application" under supervision of Pierluigi Bruzzone at EPFL – Swiss Plasma Center; exam date 03/10/2017.
2012 – 2013	**Engineer** at Russian Scientific R&D Cable Institute (JSC "VNIIKP"), Podolsk (Moscow region).
2007 – 2013	**MSc in Physics & Engineering** "Current carrying element made of stacked-twisted tapes" under supervision of Vitaly Vysotsky at National Research Nuclear University MEPhI (Moscow Engineering Physics Institute); average score: 5/5.

Key achievements

2017	Plenary presentation at MT–25 conference, 'Young Scientist' session 🏆
2016	IEEE CSC Graduate Study Fellowship in Applied Superconductivity 🏆
2016	Runner up in the SNF Best MT-24 Contributed Preprint Contest 🏆
2016	Best poster award at Heraeus seminar

Skills & Knowledge

|	
Experimental:	$I_c(B, T)$ measurements: 4 point probe and VSM methods.
	Electro-mechanical tests: bending, twisting, transverse pressure.
	AC loss measurements: electrical, calorimetric and VSM methods.
	Advanced techniques: Hall probe and Rogowski coil measurements.
	Instrument control and data acquisition: GPIB, NI, analog interfaces.
	Design and construction of experimental setups and large scale HTS samples.
	Long-length pre-tinning and soldering.
Numerical:	Magnetic field calculations / I_c and T_{cs} performance assessment / Finite element analysis / Electrical network models / Quench simulations / Optimization problems / Tikhonov regularization / Reduction of large datasets / Signal processing / Parametric analysis / Computational and differential geometry.
Programming:	MATLAB (7 years), Python (1 year), Fortran (1 year), LaTeX (3 years)
CAD:	SolidWorks (2 years), Kompas–3D (3 years)
Languages:	Russian (native), English (advanced), German (intermediate)

References

Dr. Pierluigi Bruzzone
PhD thesis supervisor
Head of superconductivity group at
EPFL – Swiss Plasma Center
5232 Villigen-PSI, Switzerland
✉ pierluigi.bruzzone@psi.ch

Prof. Vitaly Vysotsky
Master's thesis supervisor
Head of department in Russian Scientific
R&D Cable Institute (JSC "VNIIKP")
Shosse Entuziastov 5, 111024 Moscow, Russia
✉ vysotsky@ieee.org
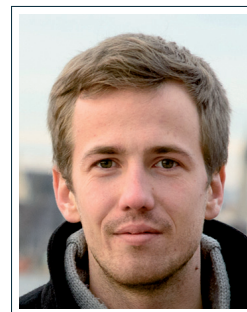
Publications

[1] P. Bruzzone, K. Sedlak, D. Uglietti, N. Bykovsky, L. Muzzi, G. De Marzi, G. Celentano, et al., "LTS and HTS high current conductor development for DEMO", Fusion Engineering and Design **96-97**, 77–82 (2015).

[2] P. Bruzzone, R. Wesche, D. Uglietti, and N. Bykovsky, "High temperature superconductors for fusion at the Swiss Plasma Center", Nuclear Fusion **57**, 085002 (2017).

[3] N. V. Bykovsky, S. S. Fetisov, A. A. Nosov, V. V. Zubko, and V. S. Vysotsky, "Analysis of critical current reduction in self-field in stacked twisted 2G HTS tapes", Journal of Physics: Conference Series **507**, 022001 (2014).

[4] N. Bykovsky, D. Uglietti, R. Wesche, and P. Bruzzone, "Strain management in HTS high current cables", IEEE Transactions on Applied Superconductivity **25**, 4800304 (2015).

[5] N. Bykovsky, D. Uglietti, R. Wesche, and P. Bruzzone, "Design optimization of round strands made by twisted stacks of HTS tapes", IEEE Transactions on Applied Superconductivity **26**, 4201207 (2016).

[6] N. Bykovsky, D. Uglietti, R. Wesche, and P. Bruzzone, "Design of the HTS fusion conductors for TF and CS coils", IEEE Transactions on Applied Superconductivity **26**, 6600104 (2016).

[7] N. Bykovsky, D. Uglietti, K. Sedlak, B. Stepanov, R. Wesche, and P. Bruzzone, "Performance evolution of 60 kA HTS cable prototypes in the EDIPO test facility", Superconductor Science and Technology **29**, 084002 (2016).

[8] N. Bykovsky, G. D. Marzi, D. Uglietti, P. Bruzzone, and L. Muzzi, "Magnetization loss for stacks of ReBCO tapes", Superconductor Science and Technology **30**, 024010 (2017).

[9] N. Bykovsky, D. Uglietti, R. Wesche, and P. Bruzzone, "Cyclic load effect on round strands made by twisted stacks of HTS tapes", Fusion Engineering and Design **121**, 9402 (2017).

[10] S. S. Fetisov, A. A. Nosov, V. V. Zubko, N. V. Bykovsky, S. Y. Zanegin, V. S. Vysotsky, G. G. Svalov, et al., "First model power cables made of russian 2G HTS wires and their test results", Journal of Physics: Conference Series **507**, 032063 (2014).

[11] S. Fetisov, D. Sotnikov, S. Y. Zanegin, N. Bykovsky, I. Radchenko, V. Zubko, and V. Vysotsky, "Current density distribution in 2G HTS tape in an external magnetic field", Physics Procedia **67**, 931–938 (2015).

[12] D. Uglietti, N. Bykovsky, R. Wesche, and P. Bruzzone, "Development of HTS conductors for fusion magnets", IEEE Transactions on Applied Superconductivity **25**, 1–6 (2015).

[13] D. Uglietti, N. Bykovsky, K. Sedlak, B. Stepanov, R. Wesche, and P. Bruzzone, "Test of 60 kA coated conductor cable prototypes for fusion magnets", Superconductor Science and Technology **28**, 124005 (2015).

[14] V. Vysotsky, S. Fetisov, V. Zubko, S. Zanegin, A. Nosov, S. M. Ryabov, N. V. Bykovsky, et al., "Development and test results of HTS windings for superconducting transformer with 1 MVA rated power", IEEE Transactions on Applied Superconductivity, 5500105 (2016).

[15] R. Wesche, P. Bruzzone, D. Uglietti, N. Bykovsky, and M. Lewandowska, "Upgrade of SULTAN/EDIPO for HTS cable test", Physics Procedia **67**, 762–767 (2015).

[16] R. Wesche, N. Bykovsky, D. Uglietti, K. Sedlak, B. Stepanov, and P. Bruzzone, "Commissioning of HTS adapter and heat exchanger for testing of high current HTS conductors", IEEE Transactions on Applied Superconductivity, 1–1 (2016).

[17] R. Wesche, K. Sedlak, N. Bykovsky, P. Bruzzone, L. Zani, and M. Coleman, "Winding pack proposal for the TF and CS coils of european DEMO", IEEE Transactions on Applied Superconductivity **26**, 1–6 (2016).

[18] R. Wesche, N. Bykovsky, X. Sarasola, K. Sedlak, B. Stepanov, D. Uglietti, and P. Bruzzone, "Central solenoid winding pack design for DEMO", Fusion Engineering and Design **121**, 9404 (2017).

SWISS PLASMA CENTER

ÉCOLE POLYTECHNIQUE FÉDÉRALE DE LAUSANNE

State-of-the-art magnets of fusion devices, which are based on low temperature superconductors (LTS), have almost reached their technological limits. Further progress can be made using novel high temperature superconductors (HTS). While LTS conductors can be manufactured in a favorable geometry of round wires, the most promising HTS materials are only available as thin tapes. Thus, cable technology transfer from LTS to HTS is challenging.

In this research we aim at demonstrating experimentally the applicability of HTS materials for fusion magnets. As a result of full-scale R&D activity at the Swiss Plasma Center, 60 kA-class HTS cable prototypes have been manufactured and successfully tested at high background magnetic fields, up to 12 T. Use of HTS cables can open access to fields above 15 T in fusion magnets and has potential to reduce the overall dimensions and cost of fusion devices.